Untersuchung (ultra-)dünner Filme und Beschichtungen aus dem rekombinanten Spinnenseidenprotein eADF4(C16) für die biomedizinische Anwendung

Dissertation

zur Erlangung des akademischen Grades

Doktor der Naturwissenschaften (Dr. rer. nat.)

in der Bayreuther Graduiertenschule für Mathematik und Naturwissenschaften

(BayNAT)

der Universität Bayreuth

vorgelegt von

Diplom-Chemiker
Christian Bruno Borkner

aus Mönchengladbach

Bayreuth 2018

Für meine Familie.

Die vorliegende Arbeit wurde in der Zeit von Juli 2012 bis August 2018 in Bayreuth am Lehrstuhl für Biomaterialien, Fakultät für Ingenieurwissenschaften, Universität Bayreuth, unter der Betreuung von Herrn Professor Dr. Thomas Scheibel in Bayreuth angefertigt und bei der Bayreuther Graduiertenschule für Mathematik und Naturwissenschaften (BayNAT) der Universität Bayreuth im Promotionsprogramm Polymerwissenschaft eingereicht.

Vollständiger Abdruck der von der Bayreuther Graduiertenschule für Mathematik und Naturwissenschaften (BayNAT) der Universität Bayreuth genehmigten Dissertation zur Erlangung des akademischen Grades eines Doktors der Naturwissenschaften (Dr. rer. nat.).

Dissertation eingereicht am: 03.09.2018

Zulassung durch das Leitungsgremium: 27.09.2018

Wissenschaftliches Kolloquium: 10.05.2019

Amtierender Direktor der BayNAT: Prof. Dr. Dirk Schüler

Prüfungsausschuss:

Prof. Dr. Thomas Scheibel	(Gutachter)
Prof. Dr. Georg Papastavrou	(Gutachter)
Prof. Dr. Markus Retsch	(Vorsitz)
Prof. Dr. Hans-Werner Schmidt	

Inhaltsverzeichnis

Zusammenfassung

Obwohl Biomaterialien schon seit langer Zeit genutzt werden, ist die systematische Biomaterialwissenschaft ein noch recht junger Wissenschaftsbereich mit einer 60- bis 70-jährigen Geschichte. Seide wird seit Jahrtausenden für Textilien verwenden und insbesondere Spinnenseide wurde schon vor Jahrhunderten von Polynesiern bei der Fischerei sowie in der Antike als Wundauflage und als Nahtmaterial verwendet. Aus heutiger Sicht ist die Biomaterialwissenschaft ein Zusammenwirken verschiedener Fachbereiche und das Verständnis der physikalischen und chemischen Wechselwirkungen zwischen komplexen biologischen Systemen und synthetischen oder modifizierten natürlichen Materialien nimmt einen hohen Stellenwert ein. Die Biokompatibilität spielt hierbei eine große Rolle. Doch es bedarf einer genauen Betrachtung, die abhängig vom jeweiligen Anwendungsgebiet (z.B. Hartgewebe, Weichgewebe, Herz-Kreislauf-System) des Biomaterials ist. Biokompatibilität kann in zwei Bereiche – die Strukturkompatibilität und die Oberflächenkompatibilität – gegliedert werden. Bei der Strukturkompatibilität wird z.B. die Struktur, Form und Mechanik eines Implantats an das Verhalten des Gewebes im Wirtsorganismus betrachtet. Werden die chemischen, physikalischen, biologischen und morphologischen Oberflächeneigenschaften eines Materials an das Wirtsgewebe angepasst, spricht man von Oberflächenkompatibilität.

Die Oberflächeneigenschaften eines Biomaterials sind somit entscheidend für seine Biokompatibilität und Wechselwirkung mit dem Wirtssystem. Durch seine gute Verfügbarkeit und gute Biokompatibilität ist das rekombinante Spinnenseidenprotein eADF4(C16) ein interessantes Material zur Steuerung und Modifizierung der Oberflächeneigenschaften von Biomaterialien. Spinnenseide ist nicht hämolytisch oder zytotoxisch und auch die beim Abbau der Seidenproteine entstehenden Produkte (Peptide und Aminosäuren) sind nicht toxisch und können vom Körper resorbiert werden. Es tritt keine Immunantwort auf und Zellen zeigen nur eine geringe Interaktion mit glatten eADF4(C16)-Filmen und ihren Oberflächen. eADF4(C16) ist daher gut als Beschichtungsmaterial für Implantate (z.B. Silikonbrustimplantate) oder auch Katheter geeignet.

In der vorliegenden Arbeit wurde ein Prozess entwickelt, um glatte Polymeroberflächen, wie z.B. von Kathetern (aus Silikon, Polyurethan (PU) und Polytetrafluoroethylen (PTFE)), mit eADF4(C16) zu beschichten. Die Beschichtungen, die sich durch ihre Schichtdicke von < 100 nm von bisher untersuchten Silikonimplantatbeschichtungen aus Spinnenseide mit einer Schichtdicke im Mikrometerbereich unterscheiden, wurden hinsichtlich ihrer Stabilität, Biokompatibilität und ihrer Zelladhäsionseigenschaften untersucht.

Die in dieser Arbeit verwendeten polymeren Biomaterialien (PTFE, PU und Silikon) haben hydrophobe Oberflächen und wurden vor dem Tauchbeschichtungsprozess im Sauerstoffplasma hydrophilisiert. Um die Haftung der eADF4(C16)-Beschichtung auf der plasmabehandelten Oberfläche zur erhöhen, wurde eine Vermittlerschicht aus dem polykationischen Polymer Polyethylenimin (PEI) bzw. dem positiv geladenen rekombinanten Spinnenseidenprotein eADF4(κ16) auf die hydrophilisierte Polymeroberflächen aufgebracht. Die Beschichtungen zeigen keine Delamination bei Biegebelastung und die Oberflächenkontaktwinkel liegen für diese Beschichtungen deutlich unter dem für gegossene eADF4(C16)-Filme mit einer Dicke von 1 bis 2 μm.

Sinkt die Schichtdicke eines Films oder einer Beschichtung, so steigt auch die spezifische Oberfläche je Volumen. Erreicht ein Material Abmessungen von < 100 nm in mindestens einer Dimension, so spricht man von Nanomaterialien, die im Vergleich zum *bulk*-Material verschiedene Eigenschaften aufweisen. Es konnte gezeigt werden, dass sich die Oberflächeneigenschaften (*hier*: Oberflächenkontaktwinkel) abhängig von der Schichtdicke ändern. Zusätzlich wurden die strukturellen Eigenschaften (β-Faltblattanteil) schichtdickenabhängig untersucht. Betrachtet man die Aminosäuresequenz von eADF4(C16), so lässt sich das Protein als eine sich wiederholende Abfolge eines alaninreichen hydrophoben und eines glycinreichen hydrophilen Blockes beschreiben und kann aus polymerwissenschaftlicher Sicht als AB-Multiblockcopolymer beschrieben werden. Auf Basis der gesammelten Daten über die Schichtdickenabhängigkeit des β-Faltblattanteils und der Oberflächeneigenschaften zusammen mit den bereits beschriebenen Multiblockcopolymereigenschaften des Proteins wurde ein schichtdickenabhängiges Assemblierungs- und Phasenseparationsmodell von der nur einige Nanometer dicken Proteinlage bis zum *bulk*-Material vorgeschlagen.

Zusätzlich wurde die Bioabbaubarkeit dünner eADF4(C16)-Beschichtungen untersucht. Die eADF4(κ16)/eADF4(C16)-Beschichtungen auf Silikonkathetern zeigten eine sehr gute Stabilität in Puffer und wiesen in Wundheilungsumgebung eine langsame Bioabbaubarkeit sowie eine gute Stabilität der Beschichtungen gegenüber mechanischer Belastung auf.

Neben der Beschichtungsstabilität spielt auch die Zellinteraktion mit den Beschichtungsoberflächen eine bedeutende Rolle für die Biokompatibilität des Materials und seine spezifische Anwendung. Auf mit eADF4(C16) beschichteten Katheteroberflächen war eine geringe Zelladhäsion von BALB/3T3 Fibroblasten, B50 neuronalen Zellen, HaCaT Keratinocyten sowie C2C12 Myoblasten zu beobachten. Dünne eADF4(C16) Beschichtungen bieten somit für biomedizinische Anwendungen, in denen keine Wirtsreaktion auftreten soll und Zellen nicht mit der Oberfläche interagieren sollen, eine gute Möglichkeit zur Einstellung der Oberflächeneigenschaften bei gleichzeitig geringem Materialeinsatz.

Zusätzlich wurden mit eADF4(C2) funktionalisierte bakterielle Nanopartikeln (MamC-C2 Magnetosomen) untersucht. Magnetosomen werden von magnetotaktischen Bakterien zur Orientierung entlang der Feldlinien des Erdmagnetfeldes gebildet. Im Modellorganismus *Magnetospirillum gryphiswaldense* bestehen sie aus einem Magnetitkern und einer Phospholipid-Doppelschicht (Magnetosomen-Membran). Im Fall von MamC-C2 Magnetosomen ist eine zweifache Wiederholung des C-Moduls des Spinnenseidenproteins eADF4(C16) über das Ankerprotein MamC in der Biomembran verankert und bildet mit dieser zusammen eine den Partikel kolloidal stabilisierende Hülle. QCM-D Experimente haben gezeigt, dass eine intermolekulare Wechselwirkung zwischen MamC-C2 Magnetosomen und eADF4(C16) besteht und MamC-C2 Magnetosomen als Nukleationskeime für die Assemblierung von eADF4(C16)-Fibrillen dienen können.

Summary

Although biomaterials have been used for a long time, systematic biomaterial science is a relatively young research area with a just 60- to 70-year history. Silk has been used for textiles for millennia and spider silk was used for centuries by Polynesians for fishing and in ancient times as wound dressing and even as suture material. From today's perspective, biomaterials science is a collaboration of different disciplines and the understanding of the physical and chemical interactions between complex biological systems and synthetic or modified natural materials is important. Biocompatibility plays an important role, but careful consideration is needed depending on the particular field of application (e.g., hard tissue, soft tissue, cardiovascular system) of the biomaterial. Biocompatibility can be divided into two areas - structural compatibility and surface compatibility. In structural compatibility structure, shape and mechanics of an implant are adapted to the behavior of the tissue in the host organism. If the chemical, physical, biological and morphological surface properties of a material are adapted to the host tissue, it’s called surface compatibility.

Surface properties of a biomaterial are crucial for its biocompatibility and its interaction with the host system. Due to its good availability and biocompatibility, the recombinant spider silk protein eADF4(C16) is a very interesting material to control and modify surface properties of biomaterials. Spider silk is not hemolytic or cytotoxic, and its degradation products (peptides and amino acids) are non-toxic and can be body-resorbed. There is no immune response, and cells show only weak interaction with smooth eADF4(C16) films and surfaces. eADF4(C16) is well suited as a coating material for implants (e.g., silicone breast implants) or catheters.

In the present work, a process to coat smooth polymer surfaces like catheters (made of silicone, polyurethane (PU) and polytetrafluoroethylene (PTFE)) with eADF4(C16) has been developed. The coatings differ in their thickness from previously published silicone implant coatings with micron-sized layer thickness. The new nano-coatings were characterized concerning stability, biocompatibility and cell adsorption properties.

The polymeric biomaterials used in this work have hydrophobic surfaces and were hydrophilized in oxygen plasma prior to dip-coating with eADF4(C16). To increase the adhesion of eADF4(C16) to plasma treated surfaces, a layer of the polycationic polymer

polyethyleneimine (PEI) or the positively charged recombinant spider silk protein eADF4(κ16) was applied to the hydrophilized polymeric biomaterial surface. Coatings show no delamination upon bending load. The surface contact angles of the coatings were significantly smaller than contact angles determined for eADF4(C16) films with a thickness of 1 µm to 2 µm.

Therefore, the hypothesis that the surface properties of silk coatings change depending on layer thickness was investigated. If the layer thickness of a film or a coating decreases, the specific surface area per volume increases. Materials with dimensions of < 100 nm in at least one direction in space are called nanomaterial and show different properties compared to bulk materials. In addition to surface wetting properties, also structural features (β-sheet fraction) were investigated depending on film thickness. Considering the amino acid sequence of eADF4(C16), the protein comprises repeats of a polyalanin-rich hydrophobic and a glycine-rich hydrophilic block. From a polymer science point of view, this protein therefore can be described as an AB multiblock copolymer. Based on the data and the polymer-like properties of eADF4(C16), a film-thickness-dependent assembly and phase separation model from the protein layer of only a few nanometer in thickness up to the bulk material was proposed and described.

In addition, eADF4(κ16)/eADF4(C16) coatings show very good stability in buffer and slow biodegradability in a wound healing environment. Interaction of cells with the coating surface also plays a significant role for biocompatibility of the material and its specific application. BALB/3T3 fibroblasts, B50 neuronal cells, HaCaT keratinocytes and C2C12 myoblasts showed only low cell adhesion on eADF4(C16) coated catheter surfaces. For biomedical applications, where no host response is supposed to occur and cells should not interact with the surface, thin eADF4 (C16) coatings are a good option to adjust surface properties and minimize the materials usage.

In addition, eADF4(C2) functionalized bacterial nanoparticles (MamC-C2 magnetosomes) were investigated. Magnetotactic bacteria form magnetosomes to orient along the field lines of the Earth's magnetic field. In the model organism *Magnetospirillum gryphiswaldense* they consist of a magnetite core and a phospholipid bilayer (magnetosome membrane). Spider silk proteins (two times repeat of the C module in case of MamC-C2) were incorporated in the biomembrane using the anchor protein

MamC and form a shell, which increased colloidal stability of the particles. QCM-D experiments indicated an intermolecular interaction between MamC-C2 magnetosomes and eADF4(C16), and MamC-C2 magnetosomes can serve as nucleation site for eADF4(C16) fibril assembly.

1. Einleitung

1.1. Biomaterialien

1.1.1. Einführung

Die Wissenschaft der Biomaterialien ist aus heutiger Sicht ein Zusammenwirken verschiedener Fachbereiche. Einen hohen Stellenwert in der Biomaterialforschung nimmt das Verständnis der physikalischen und chemischen Wechselwirkungen zwischen komplexen biologischen Systemen und synthetischen oder modifizierten natürlichen Materialien ein. Aufgrund ihrer Komplexität muss die Biomaterialforschung als multidisziplinäres Forschungsfeld betrachtet werden.

Einzelne Fachrichtungen definieren den Begriff Biomaterial unterschiedlich. Von *D. F. Williams* wurden 1999 in *The Williams Dictionary of Biomaterials* verschiedene Definitionen aus der Biologie und der Biomaterialwissenschaft zusammengefasst.[1] In der Biologie sind Biomaterialien feste Materialen, wie zum Beispiel Chitin, Fibrin oder Knochen, die in lebenden Organismen vorkommen und von ihnen hergestellt werden.[2] Um auch synthetische Materialien zu berücksichtigen, benötigt es im Rahmen der Materialwissenschaft hingegen einer anderen Formulierung der Definition eines Biomaterials.

Die *European Society of Biomaterials* erarbeitete folgende Definition:

> *Ein Biomaterial ist ein nicht lebensfähiges Material, das in einem Medizinprodukt verwendet wird und bestimmungsgemäß in Wechselwirkung mit biologischen Systemen steht.*
>
> *(Engl.: A biomaterial is a "nonviable material used in a medical device, intended to interact with biological systems." – Williams, 1987)*[3]

Diese Definition wurde im Rahmen der Veröffentlichung *Biomaterial-Tissue Interfaces: European Conference on Biomaterials* überarbeitet, um die Beschränkung auf nicht lebensfähige Materialien aufzuheben und eine Verbindung zur beabsichtigten Funktion des Biomaterials herauszustellen:

> *Ein Biomaterial ist ein Material, das an der Schnittstelle zum biologischen System den Zweck erfüllt Gewebe, Organe oder Funktionen des Körpers auszuwerten, zu behandeln, zu verstärken oder zu ersetzen.*
>
> *(Engl.: A Biomaterial is a "material intended to interface with biological systems to evaluate, treat, augment or replace any tissue, organ or function of the body." – Doherty, Williams, Williams, Lee, 1992)*[4]

Diese Formulierung lässt die Anwendung des Begriffes in der Materialwissenschaft von der Synthese über die Charakterisierung von Biomaterialien bis zur Wechselwirkung mit der Wirtsumgebung in verschiedensten Anwendungsbereichen, wie beispielsweise der Geweberekonstruktion oder bei künstlichen Organen und Implantaten, zu. Durch das Wirken des Biomaterials an der Schnittstelle zum biologischen System tritt zwangsläufig auch eine Wirtsantwort auf das Biomaterial auf (Fremdkörperreaktion; *Engl.: foreign-body response*). Ein weiterer wichtiger Begriff, der daher einer Definition bedarf, ist die Biokompatibilität. Nach *Williams* (*Biomaterial-Tissue Interfaces: European Conference on Biomaterials*; *Consensus Conference II)* ist Biokompatibilität wie folgt definiert:

> *"Biokompatibilität" ist die Fähigkeit eines Materials in einer spezifischen Anwendung mit der zugehörigen Wirtsantwort zu funktionieren.*
>
> *(Engl.: "Biocompatibility" is the ability of a material to perform with an appropriate host response in a specific application. – Williams, 1987)*[3]

Das Verständnis der Biokompatibilität eines Materials ist sehr wichtig, doch bedarf es einer genauen Betrachtung abhängig vom jeweiligen Anwendungsgebiet (z.B. Hartgewebe, Weichgewebe, Herz-Kreislauf-System) des Biomaterials. Die Biokompatibilität kann in zwei Bereiche – die Strukturkompatibilität und die Oberflächenkompatibilität – gegliedert werden. Bei der Strukturkompatibilität wird z.B. die Struktur, Form und Mechanik eines Implantats an das Verhalten des Gewebes im Wirtsorganismus angepasst. Werden die chemischen, physikalischen, biologischen und morphologischen Oberflächeneigenschaften eines Materials an das Wirtsgewebe angepasst, spricht man von Oberflächenkompatibilität. Neben der Biokompatibilität sind weitere wesentliche Aspekte in der Biomaterialwissenschaft die Toxikologie (sowie Pathobiologie und –biochemie) des Materials, die mechanischen und physischen

Anforderungen und Belastungen des Materials abhängig von der Wirtsumgebung, die Wechselwirkung in funktioneller Gewebestruktur und die durch das Biomaterial hervorgerufenen bzw. beeinflussten Entzündungs- und Heilungsvorgänge (physiologisch, pathologisch; Fremdkörperreaktion). Neben diesen Vorgängen kann es in der Wirtsumgebung auch zum Abbau beziehungsweise zur chemischen Veränderung des Grundmaterials kommen. Wichtig ist hier, dass nicht nur das Grundmaterial, sondern auch die entstehenden Abbauprodukte biokompatibel, d.h. vor allem nicht toxisch und nicht immunogen, sind.

Die Eigenschaften des Grundmaterials (*Engl.: bulk*), vor allem die mechanischen Eigenschaften, werden nicht nur durch den atomaren Aufbau, sondern auch durch die Mikrostruktur des Materials bestimmt. So können beispielsweise polymere Materialien durch unterschiedliche Anordnung von Phasen im Material unterschiedliche mechanische Eigenschaften aufweisen. Weitere Eigenschaften des Grundmaterials sind z. B. die optischen Eigenschaften (z. B. bei optische Linsen, Hornhautgewebe, Biosensoren) und elektrische sowie thermische Leitfähigkeit (z. B. bei Bioelektroden, Biosensoren).

Die Art und Weise wie das Biomaterial mit seiner Wirtsumgebung wechselwirkt, hängt zu einem großen Teil von den chemischen und physikalischen Eigenschaften der Biomaterialoberfläche ab. Die Moleküle im Biomaterial wechselwirken miteinander über verschiedene Kräfte (u.a. Van-der-Waals Kräfte, ionische Wechselwirkungen, Wasserstoffbrückenbindungen, metallische Bindungen, kovalente Bindungen). Die Oberflächenatome haben jedoch durch ihre Exposition an der Grenzfläche zum umgebenden Medium weniger Wechselwirkungsmöglichkeiten miteinander und sind nun asymmetrisch ausgebildet. Oberflächen besitzen daher im Vergleich zum *bulk* eine besondere Reaktivität und besondere Oberflächeneigenschaften. Diese haben einen wichtigen Einfluss auf die Biokompatibilität des Materials. So werden z. B. Protein- sowie Zelladhäsion auf einem Biomaterial direkt durch die Eigenschaften der Oberfläche beeinflusst. Die Unterschiede zwischen Grundmaterial und Oberfläche lassen sich wie folgt zusammenfassen: Die Masse, durch die die Oberfläche gebildet wird, ist im Vergleich zum Grundmaterial sehr klein. Die Oberfläche besitzt eine zum Grundmaterial verschiedene Reaktivität und Oberflächenmoleküle weisen eine beträchtliche Mobilität im Vergleich zu Molekülen des Grundmaterials auf. Außerdem werden Oberflächen schnell kontaminiert.[5]

1.1.2. Wasser und Biomaterialien

Eine bedeutende Rolle in der Interaktion mit Biomaterialien und der Wechselwirkung der Biomaterialoberfläche mit der Umgebung nimmt Wasser ein. An der Grenzfläche zwischen Wasser und Luft werden die Wassermoleküle durch die Kohäsionskräfte zusammengehalten. Die Oberflächenspannung ist ein Maß für diese Kraft zwischen den Wassermolekülen. Neben diesen Eigenschaften ist Wasser ein Lösungsmittel für Proteine, Zucker, Salze und viele organische Flüssigkeiten, Lipide und Tenside. Werden Ionen und Moleküle hydratisiert, umgibt sie eine Schicht Wasser. Diese Wasserschicht hat im Vergleich zum *bulk*-Wasser verschiedene Eigenschaften und stört auch die Eigenschaften des diese hydratisierten Ionen umgebenden Wassers.[6] Auf diesen Effekten beruht auch die Wirkung der kosmotropen und chaotropen Salze.[7-14]

Wasser ist das Molekül, das noch vor der Adsorption von Proteinen oder Zellen mit der Biomaterialoberfläche wechselwirkt. Wassermoleküle adsorbieren auf der Materialoberfläche und strukturieren sich dort unter Optimierung der Energie für das System. Diese Wasserschicht (1-4 Wassermoleküle) ermöglicht erst den Transport weiterer Moleküle, wie von Proteinen, und ist die primäre Bedingung für die Wechselwirkung eines Biomaterials mit seiner Wirtsumgebung. Ein Molekül interagiert zu allererst mit dem an der Oberfläche gebundenen Wasser. Die Ordnung des Systems ist durch das an die Oberfläche gebundene Wasser hoch (niedrige Entropie). Bindet nun ein Proteinmolekül an die Oberfläche, wird Oberflächenwasser freigesetzt und die Entropie steigt. Das Oberflächenwasser kann jedoch auch so stark an die Oberfläche gebunden sein, dass keine Verdrängung des Wassers und somit auch keine Proteinadsorption stattfinden kann. Weitere Aspekte der Proteinadsorption werden in Kapitel 1.1.3.2 beschrieben.

1.1.3. Eigenschaften von (polymeren) Biomaterialien

1.1.3.1. (Bio-)Abbaubarkeit und Resorption

Die Biokompatibilität eines Biomaterials hängt, wie schon in Kapitel 1.1.1 beschrieben, auch von der Biokompatibilität seiner Zersetzungs- und Abbauprodukte ab. Neben hochgradig stabilen, nicht-abbaubaren Materialien, die sich nicht in der Zeitspanne ihrer erwarteten Einsatzdauer zersetzen,[15] werden zunehmend auch abbaubare Materialien, wie z.B. Polyhydroxyessigsäure als resorbierbares medizinisches Nahtmaterial, eingesetzt.[16-18] Die Zersetzung eines Materials wird nach der *American Society of Testing Materials ASTM* als „Änderung in der chemischen Struktur, den physikalischen Eigenschaften oder dem Erscheinungsbild eines Materials“ definiert.[1] Es treten jedoch verschiedenste Effekte auf, die unabhängig voneinander zur Freisetzung von Fremdmolekülen und Teilen des Biomaterials führen können. Man unterscheidet hier zwischen verschiedenen Zersetzungsarten wie der chemischen Zersetzung, der Erosion, der Bioabbaubarkeit, der Bioerosion, Oberflächenerosion und der *bulk*-Erosion.[19] Diese Begriffe sind folgendermaßen definiert:

- *Chemische Zersetzung*: Brechen kovalenter Bindungen, beispielsweise durch Hydrolyse, Redoxprozesse oder photooxidativen Abbau.[19]
- *Erosion*: physikalische Änderung von Größe, Form oder Masse des Materials, beispielsweise durch Lösen, Abtragen, oder mechanischen Verschleiß.[1,19]
- *Bioerosion*: Umwandlung eines in Wasser unlöslichen Materials in ein lösliches Material unter physiologischen Bedingungen.[19]
- *Bulk-Erosion*: Die Einwanderung des Wassers in den *bulk* ist schneller als die Oberflächenerosion. Das Material erodiert „von innen“.[19]
- *Bioabbaubarkeit*: Abbau durch biologische Systeme (z.B. Enzyme, Zellen, Mikroorganismen).[1,19]
- *Oberflächenerosion*: Erosion eines Polymers von der Oberfläche her. Die Umwandlung an der Oberfläche ist schneller als die Infiltration des *bulk* mit Wassermolekülen.[19]

Auch bei Zersetzungs- oder Erosionsvorgängen, vor allem in der Wirtsumgebung, spielen Wassermoleküle eine Schlüsselrolle. Bei hydrolytischen und auch enzymatischen Prozessen müssen zuerst Wassermoleküle mit den funktionellen Gruppen des Biomaterials wechselwirken. Die Hydrophobizität, die Kristallinität und somit die damit zusammenhängende mögliche Wasseraufnahme bzw. Möglichkeit zur Interaktion mit Wasser sind entscheidende Faktoren für die Abbaubarkeit bzw. Resorbierbarkeit vor allem von polymeren Biomaterialien.

Durch die Wirtsumgebung und die auftretenden Zersetzungsmechanismen können auch im Biomaterial vorhandene Verunreinigungen freigesetzt werden. Mögliche Verunreinigungen des Polymers sind Initiatoren, Monomerrückstände, Oligomere und Nebenprodukte, Lösungsmittelrückstande oder auch Additive. Neben solchen durch die Herstellung bedingten Faktoren kann auch die Verarbeitung des Materials, wie z.B. Sterilisationsmethoden (z.B. Temperatur, Druck, oxidative Prozesse), oder auch nur die Art der Lagerung (z.B. Feuchtigkeit) zu einer (oberflächlichen) Veränderung bzw. Zersetzung des Materials führen. Diese sind ein nicht zu vernachlässigender Faktor bei der Beurteilung der Biokompatibilität eines Biomaterials, da durch sie auch die Oberflächeneigenschaften des Materials verändert werden können.

Um die biologische Antwort auf ein Biomaterial zu verstehen, müssen auch Oberflächeneigenschaften wie die Morphologie und die Rauigkeit, die Oberflächenbenetzbarkeit und die Oberflächenchemie (atomar, supramolekular & makromolekular) im Zusammenhang mit der Wirtsantwort verstanden werden.

1.1.3.2. Proteinadsorption

In vielen Einsatzgebieten kommen Biomaterialien abhängig von der Anwendung intra- sowie extrakorporal in direkten Kontakt mit Proteinen aus der Wirtsumgebung. Da kein Biomaterial mit einer absolut proteinresistenten Oberfläche bekannt ist, ist die Proteinadsorption auf den exogenen Biomaterialoberflächen als ein wichtiger Faktor bei der Einschätzung der Biokompatibilität des Materials zu betrachten. Zusätzlich ist die Proteinadsorption unmittelbar mit der Zelladhäsion verknüpft. In der Regel weisen Oberflächen mit einer hohen Proteinadsorption ebenfalls eine hohe Zelladhäsion auf und proteinresistente Oberflächen geringe bis keine Zelladhäsion. Durch das Abschwächen bzw. Verhindern von unspezifischer Proteinadsorption, z.B. durch Verringerung der Oberflächenenergie des Biomaterials, kann die Biokompatibilität eines Biomaterials verbessert werden. Die Oberflächen werden dadurch für Körperflüssigkeiten „unsichtbar“.[20,21] Es hat sich jedoch gezeigt, dass es in physiologischer Umgebung auch bzw. insbesondere auf sehr hydrophoben Oberflächen mit geringer Oberflächenenergie, wie beispielsweise Polytetrafluoroethylen (PTFE), zu einer deutlichen oft irreversiblen Proteinadsorption kommt und diese mit einer Denaturierung des Proteins auf der Oberfläche einhergehen kann.[22-27]

Das sogenannte Berg-Gesetz beschreibt anhand der Hydrophilie bzw. Hydrophobizität welche Oberfläche Proteinadsorption fördert.[28,29] So können Proteine auf hydrophilen Oberflächen ($\theta < 65°$) das oberflächengebundene Wasser nicht verdrängen und daher auch nicht adsorbieren. Auf hydrophoben Oberflächen ist das konträre Verhalten zu beobachten, jedoch kann das Berg-Gesetz in der Regel nur auf makroskopische Oberflächen und nicht auf nanoskalige Oberflächen, wie z.B. Nanopartikeloberflächen, angewendet werden.[30]

Im Allgemeinen tendieren Proteine zur Ausbildung von adsorbierten Monolagen, d.h. Proteine adsorbieren nicht unspezifisch auf ihren eigenen Monolagen. Der Grund hierfür liegt darin, dass das Hydrationswasser der adsorbierten Proteinmoleküle an der Grenzfläche Monolage/Proteinlösung nicht verdrängt wird und keine starke Wechselwirkung zwischen den bereits adsorbierten Molekülen und den Proteinmolekülen in Lösung ausgebildet werden kann.[31]

Um bioinerte Oberflächen designen und die Biokompatibilität von Biomaterialien erhöhen und steuern zu können, ist es essenziell, die Triebkräfte der Proteinadsorption zu verstehen. Proteinadsorption ist ein kinetischer Vorgang, bei dem sich die Proteinschicht über die Zeit verändert. In einem ersten Schritt binden Proteine lose an die Oberflächen. Es folgen diverse De- und Adsorptionsvorgänge (Vroman Effekt), bei dem die ursprünglich adsorbierten Proteine durch Proteine mit einer höheren Affinität zur Oberfläche ersetzt werden.[32-36] Dieser Vorgang ist möglich, solange die adsorbierten Proteine erneut hydratisiert werden können und nicht vollständig denaturieren. Neben den auftretenden kinetischen Effekten ist Proteinadsorption ein thermodynamischer Vorgang und lässt sich vereinfacht mit der Gibbs-Gleichung beschreiben (Gleichung 1).[21] ΔG_{ads} ist die freie Adsorptionsenthalpie, ΔH_{ads} die Adsorptionsenthalpie, ΔS_{ads} die Adsorptionsentropie und T die Temperatur.

$$\Delta G_{ads} = \Delta H_{ads} - T\Delta S_{ads}$$

Gleichung 1

Die thermodynamischen Effekte der Proteinadsorption sind in Tabelle 1 zusammengefasst. Kommt ein Proteinmolekül mit der Biomaterialoberfläche in Kontakt, interagiert es zuerst mit dem an der Oberfläche gebundenen Wasser (vgl. Kapitel 1.1.2). Die daraus resultierende Triebkraft für die Proteinadsorption ist der Entropiegewinn ($\Delta S_{ads} > 0$) durch die Freisetzung von oberflächengebundenem Wasser. Auch durch die

Denaturierung und Dehydratisierung des Proteins kommt es zu einem Entropiegewinn ($\Delta S_{ads} > 0$).[37] Liegt in Lösung eine geringe Ionenstärke vor, so binden kationische Proteine an anionische Oberflächen und anionische Proteine an kationische Oberflächen. Die Triebkraft ist hier die Enthalpie durch die Ausbildung langreichweitiger ionischer Wechselwirkungen ($\Delta H_{ads} < 0$) und der Entropiegewinn durch die Freisetzung von Gegenionen des Proteins ($\Delta S_{ads} > 0$). Diese Wechselwirkungen sind bei physiologischen Bedingungen zu einem großen Teil vernachlässigbar, da die ionischen Proteingruppen bei der vorhandenen hohen Ionenstärke abgeschirmt werden.[37] Auch die Ausbildung kurzreichweitiger Van-der-Waals Wechselwirkungen des Proteins mit der Oberfläche begünstigen die Proteinadsorption ($\Delta H_{ads} < 0$). Die Dehydration der Oberfläche und des Proteins führt zwar zu einem Entropiegewinn, doch durch den positiven Beitrag zur Adsorptionsenthalpie wirken diese Vorgänge, ebenso wie die Entfaltung des Proteins, der Proteinadsorption entgegen. Auch wird die Ordnung des Systems durch die Proteinadsorption wieder erhöht ($\Delta S_{ads} < 0$).

Tabelle 1: Thermodynamik der Proteinadsorption.

Die Proteinadsorption begünstigend ($\Delta G_{ads} < 0$)		**Der Proteinadsorption entgegenwirkend ($\Delta G_{ads} > 0$)**	
$\Delta H_{ads} < 0$	$\Delta S_{ads} > 0$	$\Delta H_{ads} > 0$	$\Delta S_{ads} < 0$
Van-der Waals Wechselwirkungen	Desorption von Oberflächenwasser	Dehydration der Oberfläche und des Proteins	Proteinadsorption
Ionische Wechselwirkungen	Denaturierung und Dehydration des Proteins	Proteinentfaltung	Exponierung hydrophober Proteine und Sequenzbestandteile
	Freisetzung von Gegenionen		

In den letzten zwei Jahrzehnten beschäftigten sich verschiedene Forschungsgruppen mit der Interaktion von Proteinen mit Polymerbeschichtungen und Biomaterialien und der Herstellung proteinresistenter Oberflächen.[30,38,39] So wurde beschrieben, dass die physikochemischen Prozesse der Proteinadsorption von einem komplexen Zusammenspiel der Konformationsfreiheitsgrade der (schaltbaren und auf äußere Einflüsse reagierenden) Polymerschichten und von diversen polaren und unpolaren Interaktionsmechanismen beeinflusst werden.[30,40] Von *Whiteside und Mitarbeitern* wurden systematische Studien zur Struktur-Eigenschaftsbeziehung durch Vergleich der chemischen Struktur von selbstassemblierenden Monolagen und ihrem Potential zur Unterdrückung von Proteinadsorption durchgeführt.[41,42] Aus diesen Studien wurden die sogenannten *Whiteside*-Regeln aufgestellt, die auf molekularer Ebene die Charakteristiken proteinresistenter Monolagen beschreiben:

1. Anwesenheit polarer funktionaler Gruppen (z.B. Hydrophilie)
2. Anwesenheit von Akzeptor-Gruppen für Wasserstoffbrückenbindungen
3. Abwesenheit von Donor-Gruppen für Wasserstoffbrückenbindungen
4. Abwesenheit von Nettoladung

Biomaterialien werden trotz der Abwesenheit von biologischen Motiven, auf die das Immunsystem reagiert, vom Wirtsorganismus erkannt. Dies ist in der Adsorption von Adhäsionsproteinen auf die Biomaterialoberflächen begründet. Die Integrinrezeptoren der meisten Zellen erkennen die auf der Biomaterialoberfläche adsorbierten Adhäsionsproteine. Dies führt zu einem biologisch erkennbaren Material.[43] Im folgenden Kapitel wird nun näher auf die Interaktion von Zellen mit Biomaterialien eingegangen.

1.1.3.3. Zellinteraktion

Die Biokompatibilität eines Biomaterials beruht neben den schon beschriebenen Effekten auch auf der Interaktion der Biomaterialoberflächen mit Zellen.[44] Die Zellen-Oberflächeninteraktion wird durch verschiedene Faktoren, wie die Oberflächenchemie, die Topographie und den Elastizitätsmodul bzw. die Steifheit des Substrats beeinflusst.

Zellen adhärieren *in vivo* über Fokale Adhäsionen. Das sind Zellverbindungen, die das Zytoskelett einer Zelle mechanisch an das Substrat (Extrazelluläre Matrix) koppeln. Kleine Fokale Adhäsionen, wie sie in migrierenden Zellen zu finden sind, bestehen unter anderem aus transmembranen Integrinen (Zell-Adhäsions-Glykoprotein-Rezeptoren) und binden an extrazelluläre Motive der ECM Proteine (z.B. Kollagen, Fibronectin).[44,45] Die mechanischen Eigenschaften des Mikromilieus um die Zellen werden ebenfalls durch Fokale Adhäsionen abgetastet.[46,47] Die Stimulation der Zellen durch mechanische Reize wird heute als wichtiger Einflussfaktor für die Zellaktivität betrachtet. Dies beinhaltet die Proliferation, Migration und Differenzierung.[48]

Um die Interaktion von Zellen mit Biomaterialien zu beeinflussen, können spezifische molekulare Erkennungsmotive verwendet werden, welche auf die Biomaterialoberfläche aufgebracht werden. Typische Beispiele für zellbindende Peptide sind beispielsweise YIGSR (aus Laminin)[49] oder die RGD-Sequenz (z.B. in Fibronectin)[50,51] als minimales Erkennungsmotiv der Integrine. Neben der Funktionalisierung der Biomaterialoberflächen kann die Affinität zwischen Zellen und Biomaterial auch durch Beschichtung oder Funktionalisierung der Biomaterialoberfläche mit Proteinen aus der ECM erhöht werden. Ein Problem kann hierbei die schnelle Abbaubarkeit der ECM-Proteine darstellen. Wird die Beschichtung aus ECM-Proteinen schneller abgebaut, als die Trägerstruktur, kann es zur Abstoßung oder auch Verkapselung durch den Wirtsorganismus kommen.[44]

Bei Abwesenheit dieser spezifischen Wechselwirkungsmechanismen wird die Zell-Biomaterial-Wechselwirkung durch unspezifisch auf die Biomaterialoberfläche adsorbierte Proteine vermittelt.[52] Dies beruht auf den physikochemischen Eigenschaften der Oberflächen, insbesondere dem Zetapotential bzw. der Ladungsdichte und der Grenzflächenspannung der Oberfläche (Benetzbarkeit).[53] *In vitro* zeigte sich, dass die Zelladhäsion durch eine positiv geladene Polymermatrix verbessert wird. Auf negativ geladenen Oberflächen war die Zelladhäsion deutlich verringert.[44,54-56] Auch durch die Benetzbarkeit/Hydrophobizität der Oberfläche wird die Zelladhäsion beeinflusst. Die Hydrophobizität hat, wie im vorigen Kapitel beschrieben, einen direkten Einfluss auf die Proteinadsorption. Auf hydrophoben Oberflächen wird die Konformation der adsorbierten Proteine geändert. Durch diese Konformationsänderungen kann es zu einer veränderten Zugänglichkeit von Zelladhäsionsmotiven kommen.[57,58] Auf Oberflächen mit Wasserkontaktwinkeln θ von 55°-60° tritt die maximale Zelladhäsion verschiedener Zelltypen auf.[44,56,58,59] Neben stark hydrophoben Oberflächen ($\theta >$ 90 °C) ist die Zelladhäsion auch auf stark hydrophilen Oberflächen vermindert ($\theta <$ 30 °C).[53,60]

Weitere Faktoren, die die Zelladhäsion beeinflussen, sind die Oberflächentopografie und Oberflächenrauigkeit, die auch in direktem Zusammenhang mit der Benetzbarkeit stehen.[61] In der Literatur wurde bereits der Einfluss der Oberflächenstruktur auf die

Migration, Morphologie und die Ausrichtung adhärenter Zellen beschrieben.[44,62,63] Zellen orientieren sich beispielsweise entlang von Fasern (Kontaktführung, *Engl.: contact guidance*).[64-66] Betrachtet man die Zellinteraktion mit Vliesen, so lässt sich ein Einfluss des Faserdurchmessers auf die Zelladhäsion beobachten.[67] Auf Vliesen wird die Zelladhäsion hauptsächlich durch morphologische Wechselwirkung zwischen den Zellen und der Matrixtopographie vermittelt.

1.1.4. Polymere Biomaterialien

Es gibt verschiedene Arten von Biomaterialien, die in den unterschiedlichsten Gebieten Anwendung finden (z.B. Polymere, Metalle, Keramiken/Gläser/Glaskeramiken, Kompositmaterialien). Diese Materialien werden je nach Möglichkeit und Anforderung in unterschiedliche Morphologien, wie z.B. Hydrogele, Schäume, texturierte und poröse Materialien, Gewebe, Fasern, Vliese, etc. prozessiert. Im Folgenden werden als Biomaterial gebräuchliche synthetische Polymere vorgestellt: Polydimethylsiloxan (PDMS; Silikone), Polyurethane (PU) und (expandiertes) Polytetrafluoroethylen ((e)PTFE; z.B. Teflon® & GoreTex®).

1 Polysiloxan

2 Polydimethylsiloxan

Abbildung 1. Grundwiederholungseinheiten von Silikonen. Siloxanrückgrat **1** mit variablem Rest R und Polydymethylsiloxan **2** mit R = CH_3.

Es gibt lineare, cyclische, verzweigte und vernetzte Polysiloxane.[68] Lineare Silikone (Abbildung 1) sind in der Regel Flüssigkeiten, die durch Quervernetzung (z.B. durch Alkoxysilane) und Füllmaterialien (z.B. Silicapartikel) stabilisiert werden müssen. Silikone haben eine lange Tradition in der Körperpflege als auch als Biomaterial in medizinischen Anwendungen und werden schon seit den 1940er Jahren beispielsweise als Trägermaterial in der Kosmetik, in Deodorants, Haarwaschmitteln und Material für medizinische Schläuche sowie Prothesen verwendet. Durch ihre Flexibilität, die geringen Ermüdungseigenschaften und die hohe Biokompatibilität und Biohaltbarkeit, vor allem in der Langzeitanwendung, eignen sie sich gut für die Verwendung in Fingergelenken, Herzklappen, als Brustimplantate, zur Ohr-, Kinn- und Nasenrekonstruktion sowie für Katheter (z.B. transurethrale Blasenkatheter, wie der Teleflex® Rüsch Brillant Ballonkatheter). Silikone sind außerdem nicht toxisch und haben eine hohe chemische Beständigkeit und widerstehen tiefen und hohen Temperaturen. Der Glasübergang liegt typischerweise bei unter -120 °C. Dies ist für Biomaterialien insofern wichtig, dass eine Sterilisation (hier: Autoklavieren) sowie eine kühle Lagerung möglich ist, ohne das Material und seine Eigenschaften zu verändern. Aufgrund ihrer hohen Transparenz, der hohen Gaspermeabilität und ihrer mechanischen Eigenschaften finden Silikonhydrogele auch in ophthalmologischen Anwendungen, wie z.B. als Mehrtages-Kontaktlinsenmaterial, Anwendung.[69]

Durch ihre hydrophobe Oberfläche kommt es jedoch zu einer schnellen und starken Proteinadsorption bei Gewebekontakt.[70,71] Dies kann zu pathophysiologischen Komplikationen, wie einer schnellen Bildung von Narbengewebe und der Verkapselung des Materials im Körper, z.B. periprosthetische Kapselfibrosen bei Silikon-Brustimplantaten, führen.[72] Es gibt verschiedene Ansätze die Proteinadsorption auf Silikonen zu verringern und so wurden Silikone beispielsweise mit kurzen Polyethylenglykolen (PEG) versehen.[69]

Ein weiteres in medizinischen Geräten und Produkten häufig eingesetztes Material sind Polyurethane. PU **5** sind robuste Polymere auf Isocyanatbasis mit geringen Materialermüdungseigenschaften.[73,74] Sie entstehen durch Polyadditionsreaktion von Polyisocyanaten **3** mit Polyolen **4** (Abbildung 2 A).[75,76]

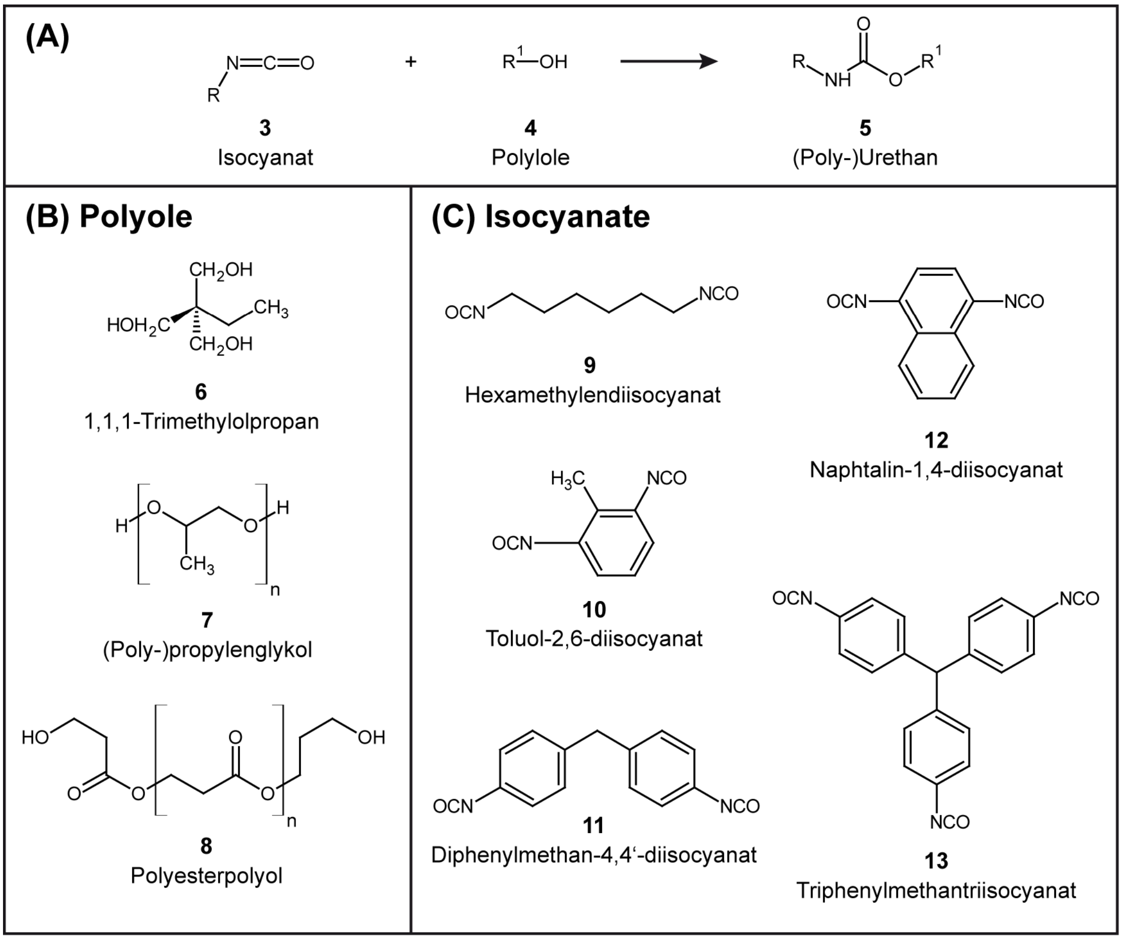

Abbildung 2. Bildung von Urethanen aus Isocyanaten und Polyolen (A). Die Chemie der Polyurethane bietet vielfältige Möglichkeiten zur Beeinflussung der Polymereigenschaften durch Wahl der Monomere. Beispielhaft sind verschiedene Monomere für (B) Polyole und (C) Isocyanate gezeigt.

Die Eigenschaften (hart, weich, bioabbaubar, etc.) der Polyurethane können durch die Wahl der Monomere auf die Anwendung maßgeschneidert werden und es lassen sich segmentierte Polyurethane mit alternierenden harten glasartigen bzw. kristallinen und weichen gummiartigen Blöcken herstellen.[73] Dadurch kann PU als thermoplastisches Elastomer hergestellt werden.[76] Es wird eine große Fülle von Polyolen als Monomer eingesetzt. Hier bietet sich eine Fülle an Variationsmöglichkeiten, beispielsweise durch den Einsatz von Triolen wie 1,1,1-Trimethylolpropan **6** zur Erhöhung des Vernetzungsgrades. Es werden aber auch polymere Polyole wie beispielsweise Polypropylenglykole **7** und Polyesterpolyole **8** (Abbildung 2 B), aber auch Polyetherdiole, wie PEG, eingesetzt. Verwendete Isocyanate sind beispielsweise Diisocyanate wie Hexamethylendiisocyanat **9** und Toluoldiisocyanate **10** oder auch Triisocyanate wie Triphenylmethantriisocyanat **13** (Abbildung 2 C).

Von *Akutsu et al.* wurde schon 1959 über die biomedizinische Anwendung von PU als Herzklappen[77,78] und kurze Zeit später über PUs als Pumpendiaphragma in künstlichen Herzen berichtet.[74] PUs sind sehr universell einsetzbar und werden beispielsweise als Leitungsisolierung von Herzschrittmachern, als Gefäßersatzmaterial, für Wundauflagen und als Katheter eingesetzt, aber auch eine Verwendung als Kleber, Beschichtung, Dichtmittel, (harte und weiche) Schäume und Textilfaser ist möglich.

Die letzte Gruppe an Polymeren, die hier vorgestellt wird, sind hochgradig fluorierte Kohlenwasserstoffe wie z.B. PTFE **15** und Polyvinylidenfluorid **16** (PVDF; Arkema: Kynar®).

15
Polytetrafluoroethylen
PTFE

16
Polyvinylidenfluorid
PVDF

Abbildung 3. Grundwiederholungseinheiten von fluorierten Kohlenwasserstoffen. Polytetrafluoroethylen (PTFE) **15** und Polyvinylidenfluorid (PVDF) **16**.

Sie sind annähernd chemisch inert, extrem hydrophob, lösungsmittelstabil und besitzen eine hohe thermische und chemische Stabilität. Durch die hohe Ionisierungsenergie und die geringe Polarisierbarkeit treten nur schwache intermolekulare Kräfte auf. Dies führt zu einer geringen Grenzflächenenergie, was wichtig in Bezug auf die Anwendung dieser Materialien an Grenzflächen wie z.B. der Implantat/Wirtsorganismus-Grenzfläche ist. Zusätzlich besitzen diese Materialien einen geringen Reibungskoeffizienten und somit eine hohe Schmierfähigkeit sowie eine hohe Sauerstoffpermeabilität. Biomedizinische Anwendungen von fluorierten Kohlenwasserstoffen sind (kardiovaskuläre, dentale, okulare, kraniofaziale, urologische und abdominale) Dauerimplantate, luminale Zugänge (v.a. Katheter in vielfältigen Formen) und andere medizinische Schläuche & biotechnologische Komponenten wie z.B. Membranen.[79-82] Haupteinsatzgebiete von (e)PTFE sind medizinische Schläuche, Katheter (z.B. Venenverweilkatheter; BD

Venflon®), Gefäßersatzmaterialien, aber auch Netze/Gitter/Gewebe sowie Naht- und Implantatmaterialien.[83]

Fluorierte Kohlenwasserstoffe sind zwar chemisch annähernd inert, aber nicht inert gegenüber biologischer Wirtsreaktion (v.a. Proteinadsorption und Blutgerinnung). Serum Albumin und Fibrinogen sowie Blutserumproteine im Allgemeinen zeigen ein sehr starkes Adsorptionsverhalten an diese Materialoberflächen. Durch die hohe Adsorptionsneigung von Serum Albumin an die Oberfläche der fluorierten Kohlenwasserstoffe bildet sich direkt nach dem Kontakt mit Blut eine adsorbierte Schicht aus Serum Albumin. Diese Schicht blockiert die Adhäsion der meisten Zellen und Proteine und ist der Grund für die gute Resistenz gegen Bio-Fouling.[80,84-88] Soll die Zelladhäsion verbessert werden, können zelladhäsive Proteine wie Kollagen oder Fibronectin vor dem Kontakt mit der Wirtsumgebung auf die Oberfläche der fluorierten Kohlenwasserstoffe adsorbiert werden.[89,90] Fluorierte Kohlenwasserstoffe sind demnach nicht biologisch inert, sondern intrinsisch reaktiv. Proteine haben eine hohe Adsorptionsneigung auf diesen Oberflächen und zeigen eine hohe intrinsische Blutkoagulation in Serum und Plasma.

1.2. Spinnenseide

Neben den zuvor vorgestellten synthetischen Polymeren gibt es auch natürliche bzw. naturidente Polymere, wie Seiden. Diese sind Strukturproteine mit hoch repetitiver Aminosäuresequenz und gehören einer Klasse von Proteinmaterialien an, die von Arthropoden produziert wird.[91-93] Die Seiden der Webspinnen (*Araneae*) gehören, wie die Seide der Raupe des Maulbeerspinners (*Bombyx mori*) und die Seide aus den Eierstielen der Florfliegen (*Chrysopidae*), zu den β-kristallinen Seiden.[94] Weibliche Radnetzspinnen (*Araneodiae*), wie beispielsweise *Nephila clavipes* aus der Gattung der Seidenspinnen (*Nephila*) sowie die *Araneus gemmoides* und die Europäische Gartenkreuzspinne *Araneus diadematus* aus der Gattung der Kreuzspinnen (*Araneus*), können in bis zu sieben Seidendrüsen verschiedene Seidentypen mit verwendungsspezifischen Eigenschaften herstellen.[95-100] Die unterschiedlichen Seiden sind nach der Drüse benannt, aus der sie gesponnen werden.

Seidenfäden aus der großen Ampullendrüse (*Engl.: major ampullate;* MA Seide) werden von der Spinne als Rahmen des Netzes sowie als Abseilfaden verwendet.[101] Die Proteine haben eine Größe von > 300 kDa[102-104] und weisen eine hohe Zugfestigkeit, eine moderate Elastizität sowie eine sehr hohe Tenazität (Zähigkeit) auf.[93,105-110] Die Seiden aus der kleinen Ampullendrüse (*Engl.: minor ampullate*, MI Seide; > 250 kDa[103]) haben ähnliche mechanische Eigenschaften wie MA Seide und bilden die Hilfsspirale, die das Netz während des Baus stabilisiert.[111-113] In der *Flagelliform*-Drüse werden hochelastische Seidenfäden für die Fangspirale hergestellt.[113-117] Um das Netz an den verschiedensten Substraten (Holz, Stein, Glas, u.v.m.) zu befestigen und verschiedene Seidenfäden miteinander zu verbinden wird ein hochspezialisiertes Klebeprotein in der *Pyriform*-Drüse produziert.[100,118,119] Eine weiteres Klebeprotein wird in der *Aggregate*-Drüse produziert. Die *Aggregate*-Seide ist ein Gemisch aus klebrigen Glykoproteinen und kleinen hochhygroskopischen Peptiden. Mit diesem Gemisch werden die Fäden der Fangspirale beschichtet, die so ihre guten Klebeeigschaften als auch ihre Elastizität erhält.[120-127] *Cylindriform*- bzw. *Tubiliform*-Seide bilden die äußere Schale der Eihülle[128-137] und *Aciniform*-Seide wird für die weiche innere Eihülle sowie zum Einwickeln der Beute verwendet.[97,137-140]

1.2.1. Struktur und Aufbau des Abseilfadens

Es gibt bereits zahlreiche Untersuchungen und systematische Übersichtsartikel zur Biologie[115,141-143], Struktur[143-145] und den mechanischen Eigenschaften[105,109,146-148] von Spinnenseiden. Abbildung 4 zeigt den schematischen Aufbau (hierarchisches Modell) des Abseilfadens der Radnetzspinnen. Ein fibrillärer Kernbereich aus MA Seide, welche aus den Proteinen MaSp1 (*Engl: **ma**jor ampullate **sp**idroin*) und MaSp2 besteht, ist in MI Seide eingebettet und wird von einer Glykoprotein- sowie einer äußeren Lipidhülle umschlossen.[94,144,149-152] Die äußere Hülle aus Glykoproteinen dient aufgrund der hygroskopischen Eigenschaften als Schutz vor Austrocknung, wie schon für die Aggregat-Seide beschrieben wurde und die Lipidschicht dient zum Schutz vor bakterieller Besiedlung.[153]

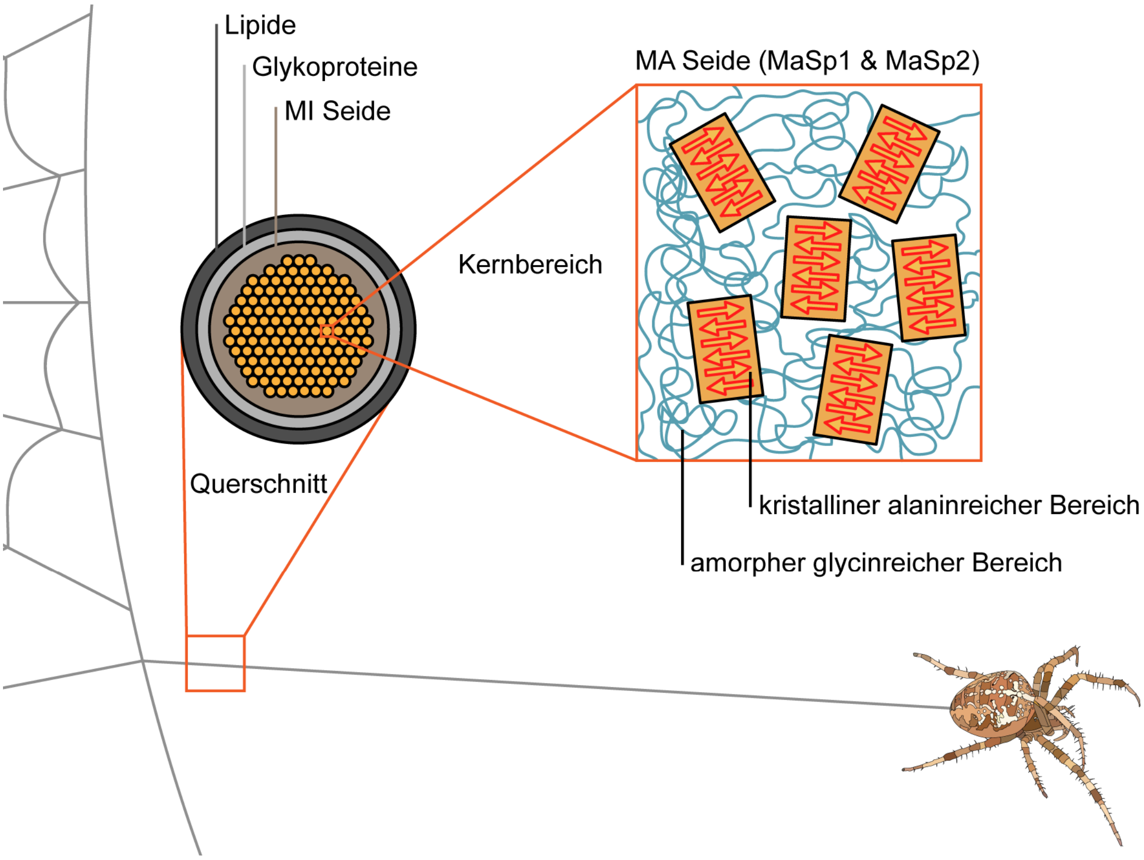

Abbildung 4. Schematischer Aufbau des Abseilfadens der Radnetzspinnen.

Die nano- und submikro-Fibrillen im Kernbereich bestehen aus MA Seide bzw. Spidroinen (*Engl:* ***spid**er **f**ibroin*), welche hauptsächlich Glycin, Alanin und Prolin beinhalten. MA Seiden werden abhängig von ihrem Prolingehalt und ihrer Hydrophobizität in zwei Klassen eingeteilt: MaSp1 hat einen niedrigen und MaSp2 einen hohen Prolingehalt.[154] MA Spidroine bestehen grundsätzlich aus einer repetitiven Kerndomäne. Diese besteht aus Aminosäuresequenzen von 20-40 Aminosäuren (AS), die bis zu 100 mal wiederholt werden.[98,138,155] Die Fibrillen im Kernbereich bestehen aus hochgeordneten nanokristallinen Bereichen mit einer mittleren Größe von mindestens 2 nm x 5 nm x 7 nm, die in eine amorphe Matrix eingebettet sind.[152,156-161] Diese kristallinen Bereiche sind entlang der Faserachse ausgerichtet und bestehen aus antiparallelen β-Faltblättern deren Ausrichtung aufgrund der Scherung und Streckung während des Spinnprozesses erfolgt.[162] Der β-Faltblattanteil in MA Seide beträgt 11-46 % bei *N. clavipes*,[163-165] 34-35 % bei *A. diadematus*[166] und 46 % bei *N. edulis*[167] und ist somit vergleichbar mit dem β-Faltblattanteil von *B. mori* (40-55 %).[105,163,164]

Antiparallele *β*-Faltblätter werden durch Polyalanine (A_n; n = 4-12) und Glycin-Alanin Wiederholungen $(GA)_n$ sowie benachbarte GGA Blöcke gebildet.[164,165] Ein Dreiphasenmodell, in dem eine Interphase aus GXG (X = Q, Y, L, R) die in der amorphen Matrix eingebetteten *β*-Faltblattkristalle umgibt und als Übergang zwischen dem kristallinen und dem amorphen Bereich fungiert, wurde vorgeschlagen.[165,168] Die *β*-Faltblätter können sich inter- sowie intramolekular ausbilden, wirken somit als Quervernetzer im Faden und sind für die hohe Zugfestigkeit des Abseilfadens verantwortlich.[94,157] Die hohe Zähigkeit wird jedoch erst durch die Dehnbarkeit, welche durch die amorphe Matrix vermittelt wird, erreicht. Die amorphe Matrix besteht aus *β*-Schleifen und -Spiralen (GPGXX; X = Q, G, Y) sowie 3_1-Helices (GGX; X = Y, L, Q).[115,143,169,170]

Die repetitive Kerndomäne wird von einer N-terminalen und einer C-terminalen nicht-repetitiven funktionalen Domäne flankiert. Diese Domänen sind zwischen den Spezies hoch konserviert und vermitteln die Lagerungs- und Assemblierungseigenschaften der Spinnenseidenproteine.[128,171-177]

1.3. Rekombinante Spinnenseidenproteine - Biopolymere

Im Gegensatz zur Seide von *B. mori*, die aus den Kokons der Seidenraube gewonnen wird, kann die Seide von Radnetzspinnen nicht in ausreichenden Mengen durch Herstellung in Seidenfarmen gewonnen werden, denn Spinnen zeigen territoriales und kannibalisches Verhalten[99,137,153,171,172,178] und produzieren in Gefangenschaft Seide von geringerer Qualität.[142,179,180] Als eine Alternative zu natürlichen Quellen wurde die biotechnologische Spinnenseidenproteinproduktion etabliert.[181,182]

1.3.1. Herstellung

Eine umfassende systematische Übersicht über natürliche und synthetische Spinnenseidengene und die Seidenproteinproduktion wird bei *Heidebrecht und Scheibel* gegeben.[183]

Verschiedene Ansätze zur rekombinanten Seidenherstellung in verschiedenen Wirtsorganismen sind aufgrund des repetitiven Charakters der Gensequenz gescheitert.

Eine erfolgreiche Methode war die Entwicklung von auf natürlichen Motiven basierender synthetischer Sequenzen, die an die Kodonverwendung (*Engl.: codon usage*) des Wirtssystems wie Bakterien (z.B. *Escherichia coli*) oder Hefen (z.B. *Pichia pastoris*) angepasst sind.[114,184,185] Abbildung 5 zeigt ein Schema der rekombinanten Herstellung von Spinnenseide, wie es für die Herstellung der auf der Konsensussequenz der MaSp2 Proteine *A. diadematus* Fibroin 3 und 4 (ADF3, ADF4) der Europäischen Gartenkreuzspinne basierenden rekombinanten Proteine eADF3 (*engineered* ADF3) und eADF4 angewendet wird. Nach Rückübersetzung und Gendesign, Anpassung des Molekulargewichts und der Kodonverwendung an die Wirtsorganismen, wird die Transgen-DNA in die Plasmid-DNA eingefügt. Diese Konstrukte können nun in *E. coli* exprimiert und anschließend gereinigt werden. Damit erlaubt es die biotechnologische Produktion Seidenproteine mit absoluter Kontrolle über die Primärstruktur und das Molekulargewicht für die weitere technische Verarbeitung in ausreichender Menge herzustellen.

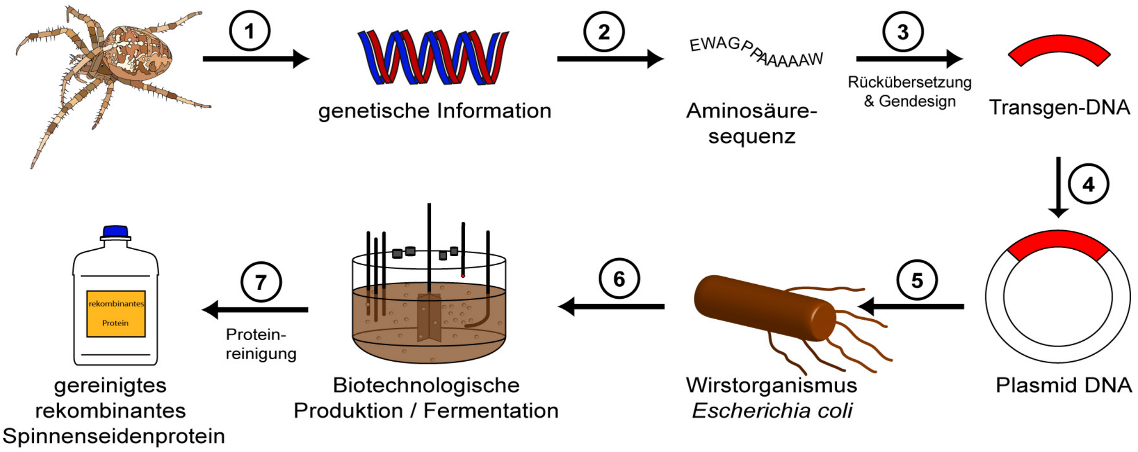

Abbildung 5. Schema der rekombinanten Herstellung von Spinnenseide. (1) Gewinnung der genetischen Information, (2) Entschlüsselung der extrahierten DNA, (3) Rückübersetzung und Gendesign, (4) Ligation der Transgen-DNA in Plasmid-DNA, (5) Transfer in den Wirtsorganismus, (6) biotechnologische Produktion / Fermentation, (7) Proteinreinigung. Mit Genehmigung modifiziert und abgedruckt aus C. B. Borkner, M. B. Elsner, T. Scheibel, Coatings and Films Made of Silk Proteins. *ACS Applied Materials & Interfaces* **2014**, *6*, 15611-15625. Copyright 2014 American Chemical Society.

In dieser Arbeit werden rekombinante Spinnenseidenproteine basierend auf der Konsensussequenz der repetitiven Kerndomäne von ADF4 verwendet. Diese Aminosäuresequenz wird C-Modul genannt (Abbildung 6). Wird das C-Modul 16 mal wiederholt, so erhält man das rekombinante Spinnenseidenprotein eADF4(C16) (M = 47,7 kDa). Dieses Protein trägt im Vergleich zum natürlichen Vorbild keine funktionalen terminalen Domänen. Die biotechnologische Produktion ermöglicht die genetische Modifikation der Proteine, wodurch die Ladung des bei physiologischem pH negativ geladenen eADF4(C16) (pI = 3,48) durch Austausch der Glutaminsäure (E) im C-Modul mit Lysin (K) E → K geändert werden kann. Durch 16-fache Wiederholung dieses nun κ-Modul genannten Sequenzmotivs erhält man das bei physiologischem pH positiv geladene rekombinante Spinnenseidenprotein eADF4(κ16) (pI = 9,52).[186]

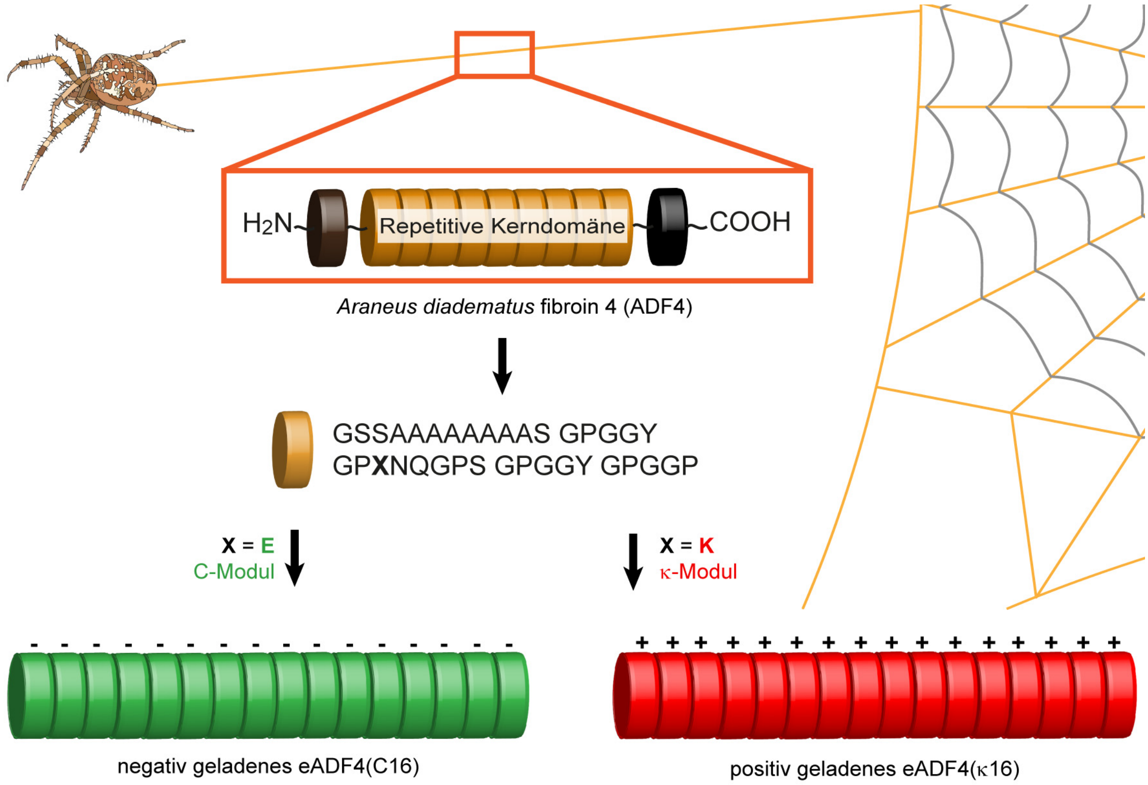

Abbildung 6. Schematische Darstellung und Aminosäuresequenz des C-Moduls sowie des κ-Moduls und der rekombinanten Spinnenseidenproteine eADF4(C16) und eADF4(κ16). Bei physiologischem pH ist eADF4(C16) (pI = 3,48) negativ und eADF4(κ16) (pI = 9,52) positiv geladen.

1.3.2. Blockcopolymere

Blockcopolymere sind Copolymere, in denen die verschiedenen Monomere blockförmig angeordnet sind. Je nach Anordnung der Blöcke unterscheidet man in Diblockcopolymere $(A)_n(B)_m$, Triblockcopolymere $(A)_n(B)_m(A)_p$ oder $(A)_n(B)_m(C)_p$ und Multiblockcopolymere $–[(A)_n(B)_m]_p–$.[75]

1.3.2.1. Mikrophasenseparation

Weisen die Blöcke im Copolymer unterschiedliche Löslichkeiten auf, so versuchen gleiche Blöcke die gegenseitige Wechselwirkung zu maximieren und verschiedene Blöcke diese zu minimieren.[187] Dies führt zur Selbstassemblierung und Separation/Entmischung von Blockcopolymeren in Mikrodomänen unter Ausbildung einer möglichst kleinen Grenzfläche zwischen den Polymerblöcken.[188,189] Hier muss zwischen Makro- und Mikrophasenseparation unterschieden werden. In verdünnter Lösung wechselwirken die Polymere und ihre Blöcke mit dem Lösungsmittel und es kommt oberhalb der kritischen Mizellenkonzentration (*Engl.: critical micelle concentration*, cmc) zur Makrophasenseparation (Mizellenbildung), vergleichbar mit der Mizellenbildung, die bei Tensiden beobachtet wird. Steigt die Konzentration weiter an, so können sich auch lyotrop-flüssigkristalline Phasen bilden.[188-190] Dieses Phasenverhalten von Polymermischungen wird thermodynamisch durch Gleichung 2 beschrieben. ΔG_m ist die freie Mischungsenthalpie, ΔH_m die Mischungsenthalpie, ΔS_m die Mischungsentropie und T die Temperatur.

$$\Delta G_m = \Delta H_m - T\Delta S_m \qquad \textbf{Gleichung 2}$$

Polymere bzw. Blockcopolymerblöcke sind nur dann vollständig mischbar, wenn ΔG_m negative Werte annimmt ($\Delta G_m < 0$). Da die Blöcke in Blockcopolymeren oft chemisch sehr verschieden sind, sind deren intermolekulare Wechselwirkungen ebenfalls sehr verschieden, d.h. es treten keine spezifischen Wechselwirkungen, wie z.B. Wasserstoffbrückenbindungen oder Ladungswechselwirkungen, auf ($\Delta H_m > 0$). Durch die kovalente Bindung zwischen den unterschiedlichen Blöcken kann bei Blockcopolymeren in hohen Konzentrationen keine Makrophasenseparation wie bei Tensiden stattfinden. Es kommt wie in der Festphase zu einer Mikrophasenseparation, bei der gleiche Blöcke bevorzugt miteinander interagieren.

Die Selbstkonsistente Molekularfeldtheorie (*Engl.: self-consistent mean field theory*; SCMT) beschreibt das Phasenverhalten von AB-Diblockcopolymeren durch das Produkt des Flory-Huggins Wechselwirkungsparameters χ mit dem Polymerisationsgrad N und dem relativen Anteil f eines Blockes. Der relative Anteil eines Blockes, hier f_A, ergibt sich aus $f_A = N_A/N$ und es gilt $f_A + f_B = 1$.[191] Der Flory-Huggins Wechselwirkungsparameter χ_{AB} beschreibt die Wechselwirkung der Wiederholungseinheiten A und B des Blockcopolymers. Er ist umgekehrt proportional zur Temperatur T ($\chi \sim T^{-1}$), d.h. mit steigender Temperatur nehmen entropische Effekte zu und χ wird kleiner (Gleichung 3). C_1 und C_2 sind experimentell bestimmbare Konstanten und abhängig vom bestimmten Blockcopolymer, d.h. von seiner Blockzusammensetzung.[192-194]

$$\chi_{AB} = \frac{C_1}{T} + C_2 \qquad \textbf{Gleichung 3}$$

Abbildung 7 zeigt ein theoretisches Phasendiagramm eines Blockcopolymers abhängig von χN und f eines Blockes.

Es können verschiedene Phasen auftreten: kubisch raumzentriert (*Engl: body centered cubic*, BCC), kubisch flächenzentriert (*Engl.: face-centered cubic*, FCC), hexagonal gepackte Zylinder (HEX), gyroidale Strukturen und lamellare Strukturen (LAM).[189,195,196] Die Größe der Mikrodomänen und die charakteristischen Abstände der Wiederholungseinheiten liegen in einem Größenbereich von 10 nm bis 100 nm.[197,198]

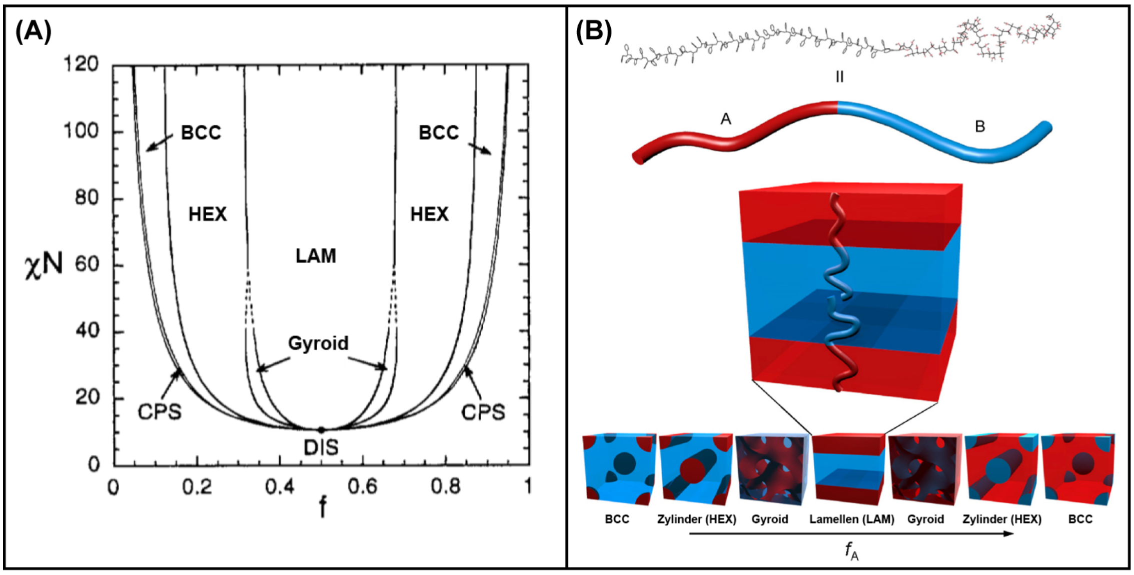

Abbildung 7. (A) Theoretisches Phasendiagramm von Blockcopolymeren. BCC: kubisch raumzentriert (*Engl.: body-centered cubic*), HEX: hexagonal gepackte Zylinder, LAM: lamellare Strukturen, CPS: dichteste Kugelpackung (*Engl.: closed packed spheres*) bzw. kubisch flächenzentriert (*Engl.: face centered cubic*, FCC), DIS: ungeordnet (*Engl.: disordered*). Mit Genehmigung modifiziert und abgedruckt aus M. W. Matsen, F. S. Bates, Unifying Weak- and Strong-Segregation Block Copolymer Theories. *Macromolecules* **1996**, *29*, 1091-1098. Copyright 2014 American Chemical Society. **(B)** Schematische Darstellung thermodynamisch stabiler Diblockcopolymerphasen. Das A-B Diblockcopolymer, wie z.B. das oben gezeigte PS-*b*-PMMA Molekül, ist hier als einfaches Piktogramm eines zweifarbigen Strangs dargestellt. Die Stränge untergehen Selbstorganisation um den Kontakt zwischen den Blöcken zu minimieren. Die Struktur wird hauptsächlich durch den Volumenbruch der Blöcke (f_A) bestimmt. Mit Genehmigung übersetzt und abgedruckt aus S. B. Darling, Directing the Self-Assembly of Block Copolymers. *Progress in Polymer Science* **2007**, *32*, 1152-1204, Copyright 2007 Elsevier Ltd, mit Genehmigung von Elsevier.

1.3.2.2. (Ultra-) dünne Blockcopolymerfilme

Im *bulk* wird die Struktur noch hauptsächlich durch die molekularen Eigenschaften des Blockcopolymers, wie Kettenlänge, Volumenanteile der Blöcke, Mischbarkeit der Blöcke und Temperatur, bestimmt. Geht man von der Polymerschmelze bzw. *bulk*-Festphase hin zu dünnen Schichten, so überwiegt die Zahl der Moleküle an bzw. nahe den Grenzflächen im Gegensatz zum *bulk*. Die Grenzflächen spielen eine zentrale Rolle bei der Orientierung und Anordnung der Polymermoleküle in Mikrodomänen.[188,198-200] Die Mikrodomänenstruktur in dünnen Filmen wird also wesentlich von den Grenzflächen Polymer/Substrat und Polymer/Luft sowie von der Schichtdicke bestimmt. Durch die Verschiedenheit der Blöcke im Blockcopolymerfilm wird sich ein Block bevorzugt an die Grenzfläche Substrat/Polymer anlagern und so zu einer niedrigeren Grenzflächenspannung γ führen. Die Kraft an der Substrat/Polymer-Grenzfläche wird als

Oberflächenfeld bezeichnet und korreliert mit der Differenz der Grenzflächenspannung $\gamma_A - \gamma_B$ der beiden Blöcke A und B. Es lagert sich bevorzugt der Block an die Oberfläche an, der zur Bildung der niedrigeren Grenzflächenspannung führt. Gerade im direkten Bereich der Grenzflächen kann der Abstand der durch die verschiedenen Blöcke gebildeten Layer von dem im *bulk* abweichen.[201] Betrachtet man nun zusätzlich zur Affinität der Blöcke A und B zur Substrat/Polymer-Grenzfläche auch die Affinität zur Polymer/Luft-Grenzfläche, kann es zur Ausbildung sogenannter symmetrischer und asymmetrischer Systeme kommen (Abbildung 8). In symmetrischen Systemen lagert sich der gleiche Block (z.B. Block A) bevorzugt an beiden Grenzflächen an. Dies führt im optimalen Fall zu Filmen mit einer Schichtdicke d, die ein ganzzahliges Vielfaches n der Mikrodomänengröße L_0 beträgt.

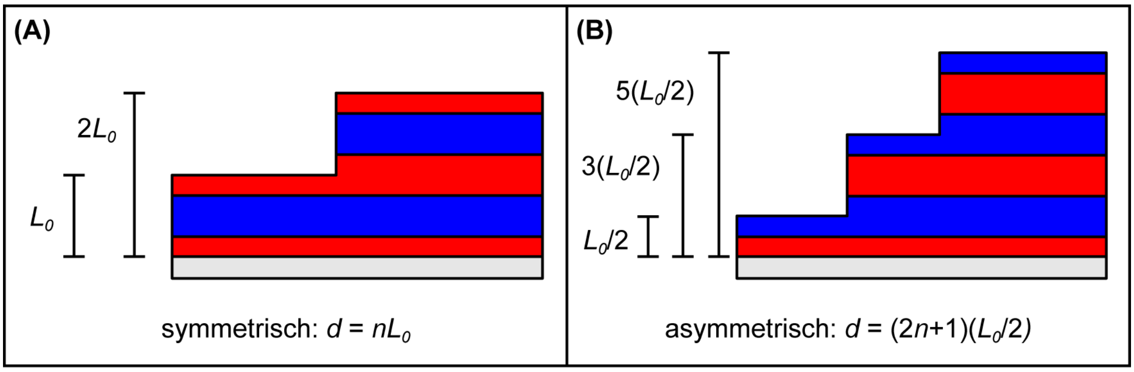

Abbildung 8. Schematische Darstellung der (A) symmetrischen und (B) asymmetrischen Terrassierung in dünnen lamellaren Blockcopolymerfilmen. Die Schichtdicke d hängt von einem ganzzahligen Vielfachen n und der Mikrodomänengröße L_0 ab.

Abbildung 8 A zeigt das symmetrische System beispielhaft für die lamellare Phase. Haben die Blöcke eine unterschiedliche Affinität zur Substrat/Polymer- und Polymer/Luft-Grenzfläche, so kommt es im Idealfall zur Ausbildung eines asymmetrischen Systems (Abbildung 8 B). Die Quantisierung der Filmdicke wird auch Terrassierung (*Engl.: terracing*) genannt.[188,199] Die Ausbildung dieser Idealstrukturen wird in der Regel durch Tempern oberhalb der Glastemperatur oder durch Behandlung mit Lösungsmitteln erreicht.

Es wurde schon über verschiedene deutlich vom *bulk* abweichende Strukturen berichtet.[202-205] Im Allgemeinen treten in dünnen Blockcopolymerfilmen verschiedene Strukturen auf. So können lamellare Strukturen, wie liegende (Abbildung 9 A) und senkrecht zur Oberfläche stehende (Abbildung 9 B) Lamellen, deren Verlaufrichtung parallel zur Oberfläche ist, auftreten. Zylindrische Nanodomänen, die parallel zur Oberfläche verlaufen, sind in Abbildung 9 C gezeigt. Neben stehenden, senkrecht zur Oberfläche ausgerichtete, hexagonal gepackte Zylindern (Abbildung 9 D) treten auch sphärische Strukturen (Abbildung 9 E) auf.

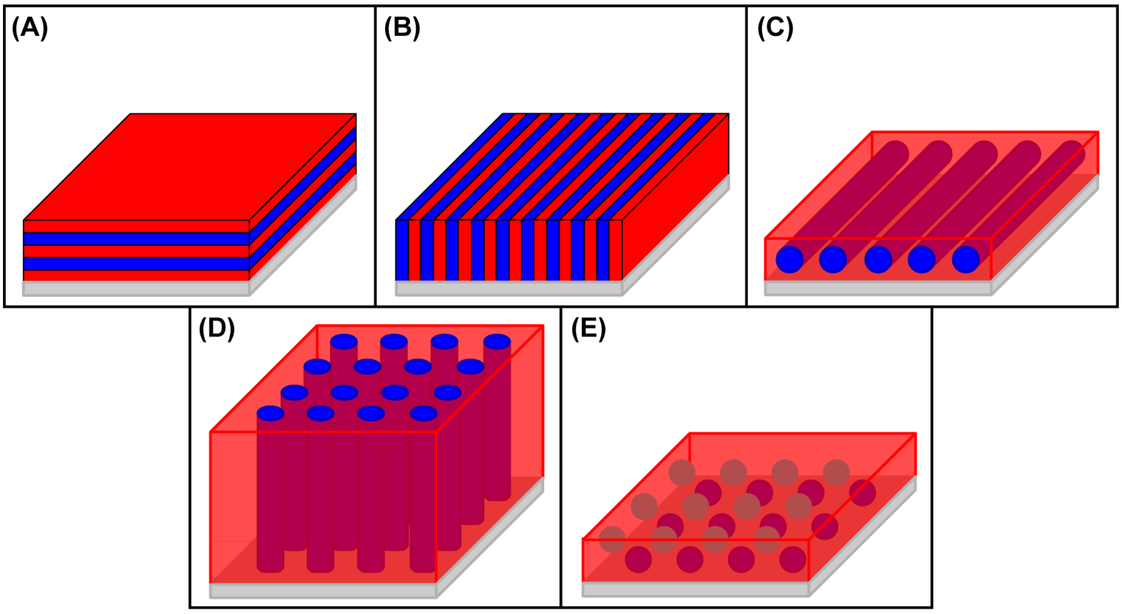

Abbildung 9. Schematische Darstellung verschiedener Mikrophasen und deren Orientierung in dünnen Filmen relativ zur Substratoberfläche. (A) Liegende Lamellen parallel zum Substrat, (B) senkrecht zum Substrat stehende Lamellen mit parallel zum Substrat liegender Ausbreitungsrichtung, (C) parallel zum Substrat liegende Zylinder, (D) senkrecht zum Substrat stehende Zylinder und (E) Kugeln.

Knoll et al. berichteten über die Abhängigkeit der in dünnen Blockcopolymerfilmen gebildeten Morphologien und Mikrostrukturen von der Schichtdicke und dem Oberflächenfeld am Beispiel eines Poly(styrol-*b*-butadien-*b*-styrol) Triblockcopolymers (SBS).[206] Dieses Polymer bildet im *bulk* zylindrische Strukturen aus. SBS wurde mittels Rotationsbeschichtung auf polierte Siliziumsubstrate aufgebracht und anschließend mit Chloroformdampf behandelt, um die Mikrostrukturbildung zu erreichen. In einem

Schichtdickenbereich von null bis 60 nm konnten diverse Mikrostrukturen beobachtet werden (Abbildung 10 a, b).

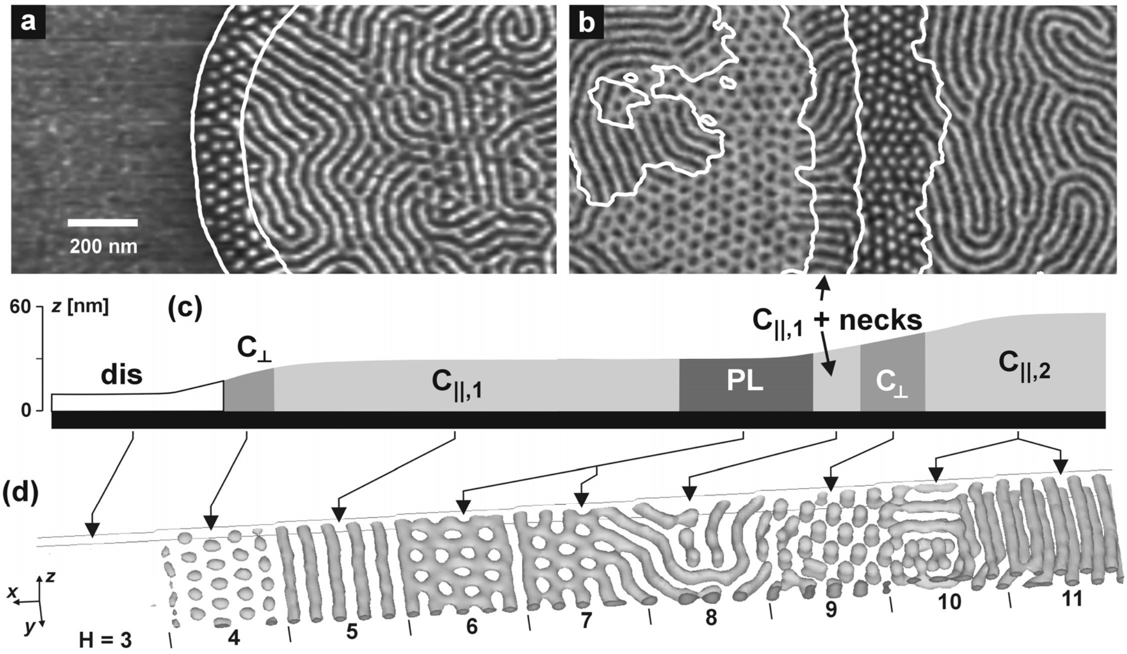

Abbildung 10. (a, b) TM-AFM Phasenbilder dünner SBS Filme auf Siliziumsubstraten nach Behandlung in Chloroformatmosphäre. (c) Schematisches Höhenprofil der Phasenbilder aus (a, b). (d) Simulation eines $A_3B_{12}A_3$ Blockcopolymers. Mit Genehmigung abgedruckt aus A. Knoll, A. Horvat, K. S. Lyakhova, G. Krausch, G. J. A. Sevink, A. V. Zvelindovsky, R. Magerle, Phase Behavior in Thin Films of Cylinder-Forming Block Copolymers. *Physical Review Letterts*. **2002**, 89, 035501-1 – 035501-4. Copyright 2002 by the American Physical Society.

Diese wiesen große Übereinstimmung mit dem simulierten Verhalten eines $A_3B_{12}A_3$ Blockcopolymers auf (Abbildung 10 c, d). Für sehr dünne Schichten ($d < 10$ nm; in der Simulation $H = 3$ Gittereinheiten) wurde eine unstrukturierte Phase (*Engl.: disordered*, dis) beobachtet. Erhöht man die Schichtdicke auf bis zu 30 nm durchläuft man einen Übergang von kurzen stehenden Zylindern ($C_\perp$; $H = 4$) über parallele Zylinder ($C_{\parallel,1}$, $H = 5$) zu perforierten Lamellen (PL, $H = 6$) und einer Mischphase ($H = 7$) von perforierten Lamellen (PL) und parallelen Zylindern ($C_{\parallel,1}$). Bei weiter ansteigenden Schichtdicken von $d > 30$ nm werden weitere Phasen beobachtet. Bei $H = 8$ tritt eine Mischphase von Zylindern und Wellen bzw. Hälsen auf, gefolgt von stehenden Zylindern ($C_\perp$; $H = 9$) und zwei aufeinanderliegenden Schichten aus parallelen Zylindern (($C_{\parallel,1}$,

$H = 10, 11, 12$). Das simulierte Phasendiagramm zeigt eine große Übereinstimmung mit experimentell ermittelten Daten.[206,207]

Die Ausrichtung von Mikrodomänen kann auf vielfältige Art und Weise beeinflusst werden. Haben beispielsweise beide Blöcke des Blockcopolymers eine annähernd gleiche Affinität zu den Grenzflächen, so richten sich die Mikrodomänen des Blockcopolymers in dünnen Filmen aus entropischen Gründen senkrecht zur Oberfläche aus. Auch durch kontrolliertes Abdampfen und die Verwendung verschiedener Lösungsmittel kann die Ausrichtung der Mikrodomänen beeinflusst werden. So hat die Abdampfrate sowie die Löslichkeit der einzelnen Blockcopolymerblöcke im gewählten Lösungsmittel einen direkten Einfluss auf die Struktur der Mikrodomänen.[200,208]

1.3.2.3. Spinnenseide als Multiblockcopolymer

Im Ampullenbeutel der Spinndrüse der Radnetzspinnen liegen die über den C-Terminus mit einer Disulfidbrücke kovalent verbundenen Proteine als Dimere vor. Durch den hydrophilen Charakter der terminalen Domänen und den im Vergleich hydrophoberen Charakter des repetitiven Kerns tritt Mikrophasenseparation auf und es bilden sich mizellenartige Strukturen, bei der die terminalen Domänen an die Grenzfläche Mizelle/Puffer orientiert sind. Die MA Spidroine sind im Mizelleninneren teilweise vorstrukturiert und weisen flüssigkristalline Eigenschaften auf. Diese Makrophasenseparation ermöglicht die Lagerung der MA Proteine in Konzentrationen von bis zu 50 % (w/v).[172,209] Dieser Effekt wird auch für die Herstellung hochkonzentrierter Seidenlösungen aus rekombinanten Spinnenseidenproteinen genutzt, welche eine C-terminale Domäne tragen. Aus diesen Lösungen ist die Herstellung künstlich nassgesponnener Fasern mit einer Zähigkeit im Bereich des natürlichen Abseilfadens möglich.[210]

Betrachtet man ausschließlich die Aminosäuresequenz des auf ADF4 basierenden C-Moduls, so lässt sich dieses Modul ähnlich zu einem Blockcopolymer in zwei Blöcke mit unterschiedlichen Eigenschaften unterteilen. Der erste Block ist alaninreich und hydrophob, der zweite Block glycinreich und hydrophil (Abbildung 11). So kann das rekombinante Spinnenseidenprotein eADF4(C16) aus polymerwissenschaftlicher Sicht auch als AB-Multiblockcopolymer mit einer 16-fachen Wiederholung des hydrophoben alaninreichen und hydrophilen glycinreichen Blocks beschrieben werden.

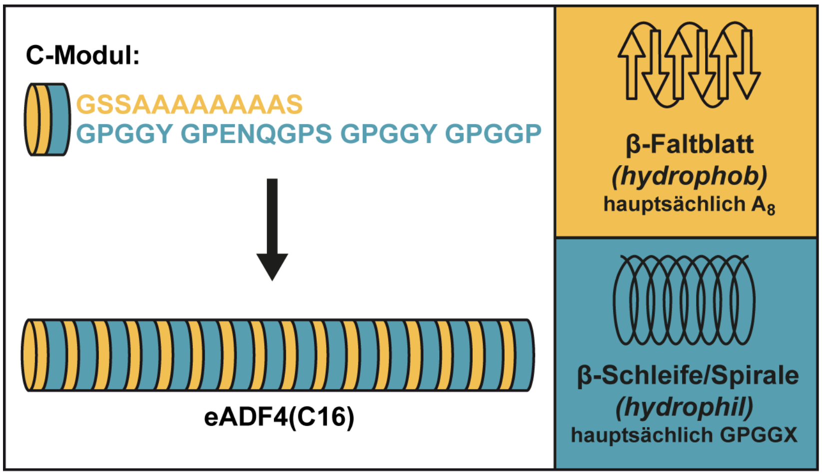

Abbildung 11. Einteilung des C-Moduls in einen hydrophoben alaninreichen und einem hydrophilen glycinreichen Block sowie schematische Darstellung von eADF4(C16) als AB-Multiblockcopolymer mit 16-facher Wiederholung der Blockabfolge AB angelehnt an den Multiblockcopolymercharakter des Proteins. Mit Genehmigung modifiziert und abgedruckt aus C. B. Borkner, S. Lentz, M. Müller, A. Fery, T. Scheibel, Ultrathin Spider Silk Films: Insight into Spider Silk Assembly on Surfaces. *ACS Applied Polymer Materials* **2019**, *1*, 3366-3374. Copyright 2019 American Chemical Society.

Mikrophasenseparation, ähnlich zu Blockcopolymeren, konnte schon für natürliche und gentechnisch konstruierte Seidenproteine,[211,212] *B. mori* Seidenfibroin[213,214] und auf Seidenproteinen basierenden (Multi-)Blockcopolymere[215,216] beobachtet werden. Schon in den 1990er Jahren wurde für dünne Filme die Struktur und das Phasenseparationsverhalten von Seidenprotein der Seidenspinnerraupe *B. mori* an der Wasser/Luft-Grenzfläche beschrieben.[217-219]

Basierend auf den Primärstrukturelementen von MaSp1 wurden von *Rabotyagova et al.* blockcopolymerartige rekombinante Spinnenseidenproteine hergestellt. Diese Proteine (HBA_x, x = 1, 2, 6) bestehen aus einem Histidin-Tag (H) für die Proteinreinigung, einem hydrophoben kristallinen pAla/Glycin-reichen Block (A), der β-Faltblätter bildet, und einem weniger kristallinen glycinreichen Block (B).[220] In Langmuir Blodget Filmen zeigten diese Proteine eine Separation der hydrophilen und hydrophoben Blöcke an der Luft/Wasser und Luft/Festkörper-Grenzfläche abhängig vom Oberflächendruck.[221] Die Untersuchung der Sekundärstruktur in gegossenen Filmen aus HBA_3 und HAB_3 zeigte außerdem eine Abhängigkeit dieser von der Primärstruktur aufgrund der unterschiedlichen Anzahl an Wiederholungen des polyalaninreichen Blocks A.[222,223] Die Erhöhung der Anzahl der AB-Wiederholungseinheiten von $H(AB)_2$ auf $H(AB)_{12}$ führte zu einer Strukturänderung vom ungeordneten zum lamellaren Zustand.[224]

Für gegossene eADF4(C16) Filme mit einer Dicke von 1 µm – 2 µm wurde von *Wohlrab et al.* basierend auf dem Phasenseparationsverhalten von Blockcopolymeren, ein Mikrophasenseparationsmodell in Abhängigkeit von der Substrathydrophilie (Oberflächenfeld) entwickelt (Abbildung 12).[225]

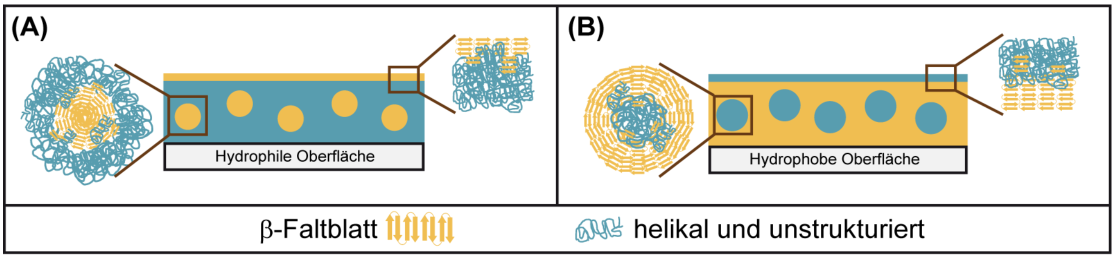

Abbildung 12. Modell zur Mikrophasenseparation von eADF4(C16) auf Oberflächen und Substrateinfluss auf die Sekundärstruktur des Proteins. Ein hydrophiles Substrat führt zu einem verringerten Anteil an β-Faltblättern, jedoch werden diese an der Film/Luft-Grenzfläche exponiert, was zu einer hydrophoben Oberfläche führt. Auf hydrophoben Substraten ist die Oberfläche des Films an der Film/Luft-Grenzfläche hydrophiler. Modifiziert und abgedruckt aus S. Wohlrab, K. Spieß, T. Scheibel, Varying Surface Hydrophobicities of Coatings Made of Recombinant Spider Silk Proteins. *Journal of Materials Chemistry* **2012**, *22*, 22050-22054. Mit Genehmigung von The Royal Society of Chemistry. Copyright 2012 The Royal Society of Chemistry.

Der hydrophobe und hydrophile Block des C-Moduls separieren in diesen Filmen. Die Substrat/eADF4(C16)-Grenzfläche hat einen signifikanten Einfluss auf die Oberflächenbenetzbarkeit der gegossenen Seidenfilme. Auf Filmen, die auf hydrophilen Substraten (z.B. Glas) gegossen wurden, wurden im Vergleich zu hydrophoben Substraten (z.B. Polystyrol (PS), Polytetrafluoroethylen (PTFE)) größere Wasserkontaktwinkel (hydrophober) gemessen. Beispielsweise haben aus Hexafluoroisopropanol (HFIP) auf das hydrophobe Substrat PTFE gegossene Filme hydrophile Kontaktwinkel von 41,7° ± 6,3°. Diese Filme können vom PTFE-Substrat abgelöst werden und zeigen auf der zum Substrat hingewandten Seite einen deutlich hydrophoberen Wasserkontaktwinkel von 74,4° ± 5,8°. Dies spricht ebenfalls für eine blockcopolymerähnliche Mikrophasenseparation. Auf hydrophilen Oberflächen lagern sich hydrophobe β-Faltblatt-Domänen in eine amorphe Matrix ein und separieren an die eADF4(C16)/Luft-Grenzfläche, was zu dem hydrophoberen Kontaktwinkel führt (Abbildung 12 A). Auf hydrophoben Substraten zeigt sich das inverse Verhalten (Abbildung 12 B). Dieses Modell wurde durch Sekundärstrukturanalyse und selektiven enzymatischen Abbau der amorphen Bereiche bestätigt.[225]

Die Gentechnik hat es erlaubt Biopolymere, wie synthetische Spinnenseidenproteine, zu designen und herzustellen. So wurde ein fundamentales Verständnis der Struktur-Funktions-Eigenschaftsbeziehung in Proteinen ermöglicht.[226]

1.3.3. Spinnenseide als Biomaterial

Die Menschen nutzen die Seide der Raupe des Maulbeerspinners (*B. mori*) schon seit Jahrtausenden für Textilien und seit mehreren Jahrzehnten als Nahtmaterial.[227] Auch Spinnenseide wurde schon vor Jahrhunderten von Polynesiern bei der Fischerei verwendet[228] und als Biomaterial fand Spinnenseide bereits in der Antike als Wundauflage, Verband und sogar als Nahtmaterial Verwendung.[229,230]

Diese Nutzung von Seidenraupen- und Spinnenseiden basiert auf den besonderen mechanischen Eigenschaften und der biologischen Verträglichkeit.[231,232] Auch das rekombinante Spinnenseidenprotein eADF4(C16) ist nicht toxisch,[72,233] löst eine geringe bis keine Immunantwort im Körper aus[72,233] und weist eine langsame Bioabbaubarkeit auf.[233-235] Steuerung der Interaktion mit Zellen ist durch Modifikation der rekombinanten Spinnenseidenmoleküle[236] sowie durch Anpassung der Oberflächenmorphologie[237] möglich (Abbildung 13).

In Zellkultur (*in vitro*) zeigte sich, dass Spinnenseiden nicht hämolytisch oder zytotoxisch sind.[235,238-240] Auch die beim (enzymatischen) Abbau der Seidenproteine entstehenden Abbauprodukte (Peptide und Aminosäuren) sind nicht toxisch und können vom Körper resorbiert werden.[234] Diese Eigenschaften qualifizieren Spinnenseide zum Einsatz als Biomaterial. Spinnenseidenproteine, wie das rekombinante eADF4(C16), lassen sich in verschiedene Morphologien wie Fibrillen, Fasern, Vliese, Partikel, Kapseln, Filme und Hydrogele prozessieren und können so in verschiedenen Bereichen Anwendung finden.[99]

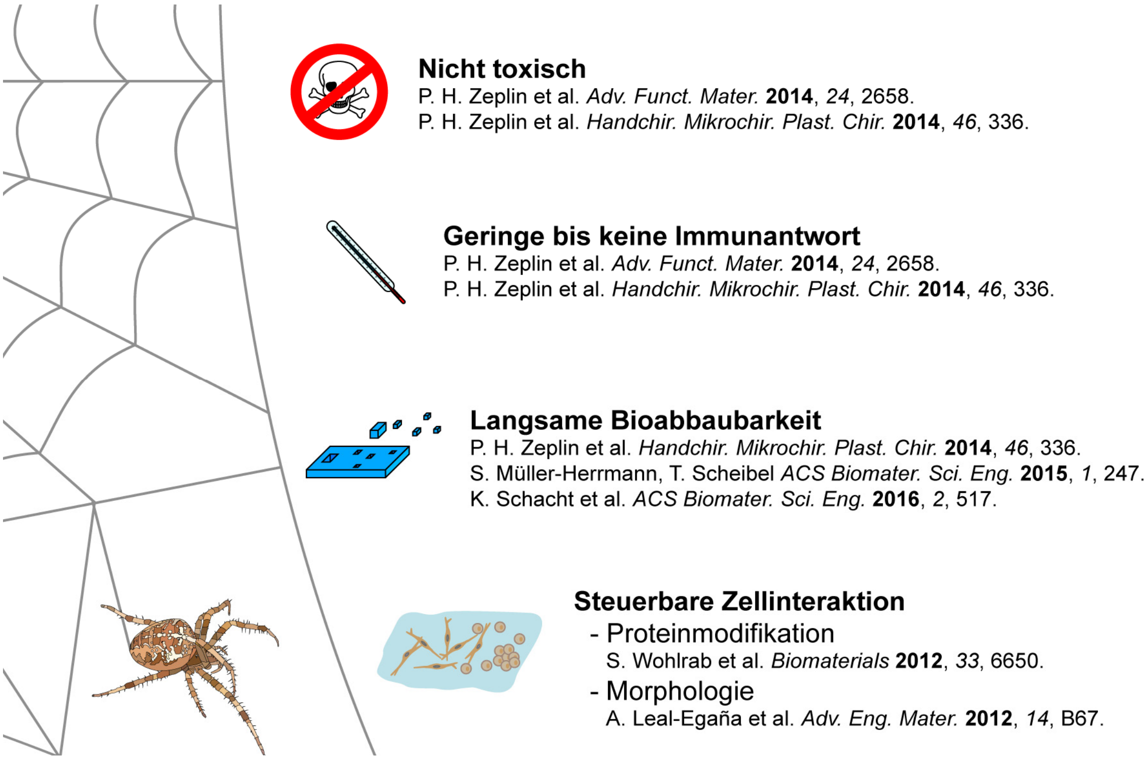

Abbildung 13. Darstellung der für die biomedizinische Anwendung von (rekombinanten) Spinnenseidenproteinen qualifizierenden Eigenschaften.

So wurden Spinnenseidenpartikel aus eADF4(C16)-basierten Proteinen als Wirkstofftransportsystem für die Aufnahme in Zellen hergestellt und erfolgreich charakterisiert.[239,241] Schäume aus eADF4(C16) und eADF4(C16)-RGD zeigen Potential als Material in der Geweberekonstruktion[235,242] und Vliese wurden für Wundabdeckungen Beschichtungen und Gerüststrukturen verwendet.[237] Zur kardialen Gewebekonstruktion kann das positiv geladene Spinnenseidenprotein eADF4(κ16) verwendet werden.[243] Abbildung 14 zeigt schematisch, wie die Zelladhäsion durch unterschiedliche Seidenmorphologien beeinflusst wird. Auf gegossenen glatten eADF4(C16)-Filmen zeigen BALB/3T3 Fibroblasten nur schwache Zelladhäsion und bilden hauptsächlich kugelige Zellmorphologien und Zellaggregate (Abbildung 14 A).[236,237] Es gibt verschiedene Faktoren, die dieses Verhalten von Zellen hervorrufen. So ist das Protein eADF4(C16), wie die Zellmembran, unter physiologischen Bedingungen und in Zellkulturmedium negativ geladen, wodurch es zu elektrostatische Abstoßung kommt.[28,60] Zudem sind in eADF4(C16) keine Zellerkennungsmotive vorhanden. Auf dem rekombinanten Spinnenseidenprotein 4RepCT (positive Nettoladung) zeigen Fibroblasten Zelladhäsion vergleichbar mit der Positivkontrolle.[244]

Werden rekombinante Spinnenseidenproteine wie eADF4(C16) und 4RepCT jedoch mit zellbindenden Peptiden (z.B. eADF4(C16)-RGD) modifiziert (chemisch oder genetisch), weisen diese Filme eine deutlich verbesserte Zelladhäsion und Spreitung auf.[236,245-247]

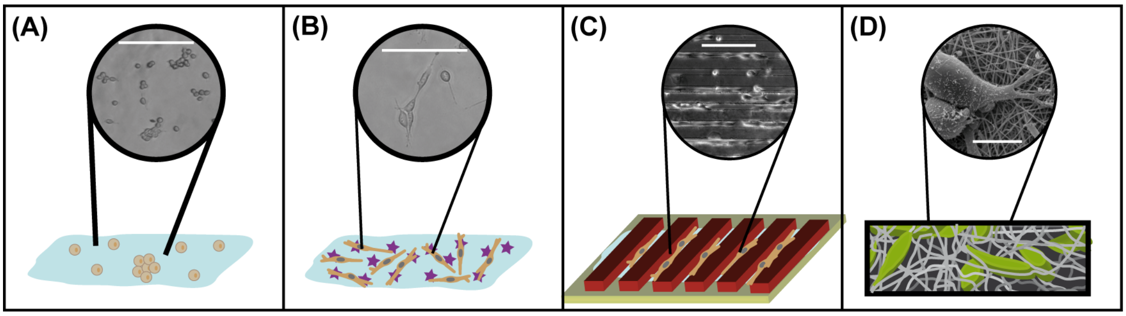

Abbildung 14. Zelladhäsion auf unterschiedlichen Seidenmorphologien sowie auf modifizierten Seidenfilmen. (A) Zellen wurden auf flache eADF4(C16)-Filme ausgesäht und es wurde schwache Zellädhäsion und kugelige/runde Zellmorphologie der BALB/3T3 Fibroblasten beobachtet. (B) RGD-modifizierte eADF4(C16)-Filme weisen eine verbesserte Zellädhäsion und Zellspreitung auf. Die Oberflächentopographie kann durch (C) Musterung oder (D) Herstellung von Vliesen verändert werden. Beide Vorgehensweisen haben einen großen Einfluss auf die Zelladhäsion und Orientierung. Maßstabsbalken: (A-C) 200 µm; (D) 10 µm.[237,244,248-252] Mit Genehmigung modifiziert und abgedruckt aus C. B. Borkner, M. B. Elsner, T. Scheibel, Coatings and Films Made of Silk Proteins. *ACS Applied Materials and Interfaces* **2014**, *6*, 15611-15625. Copyright 2014 American Chemical Society.

Eine weitere Möglichkeit die Zelladhäsion auf Filmen aus rekombinanten Seidenproteinen zu verbessern ist die Funktionalisierung der Filmoberfläche mit Makromolekülen aus der ECM. So wurden eADF4(C16)-Filme mit Glycopolymeren funktionalisiert. Die Glycopolymere binden Proteine aus der ECM und führen zur Ausbildung einer biomimetischen Beschichtung auf den Seidenfilmen, wodurch die Zelladhäsion verbessert wird.[253] Auch die Topographie der Oberflächen hat einen entscheidenden Einfluss auf die Zelladhäsion, Proliferation, Polarität und Morphologie der gebundenen Zellen. Während Zellen in der Regel auf glatten Seidenfilmen schlecht adhärieren, können durch Strukturierung der Oberfläche diese Eigenschaften verbessert werden und Zellen lassen sich entlang von Mikrostrukturen ausrichten (Abbildung 14 C). Eine weitere Möglichkeit die Wechselwirkung mit Zellen zu verbessern ist die Herstellung von Vliesen. So zeigen BALB/3T3 Fibroblasten auf Vliesen aus eADF4(C16) und 4RepCT verbesserte Zelladhäsion (Abbildung 14 D).[237,244] Die Interaktion mit Zellen ist hier abhängig vom Faserdurchmesser. Für eADF4(C16)-Vliese wurde gezeigt, dass Adhäsion und Proliferation (BALB/3T3 Fibroblasten) mit steigendem Faserduchmesser (150 µm bis 680 µm) steigt.

Durch die hohe Biokompatibilität von eADF4(C16) und die geringe Fibroblastenadhäsion und Proliferation eignet sich das Spinnenseidenprotein gut für Implantatbeschichtungen. Beschichtungen aus eADF4(C16) wurden auf Silikon-Brustimplantate aufgebracht. Dazu wurden die Implantate mit eADF4(C16) aus Ameisensäure mehrfach tauchbeschichtet bis eine Schichtdicke von ca. 1 µm erreicht war. Fibroblasten sind im Prozess der Fibrosenbildung involviert und zeigen auf diesen eADF4(C16) beschichteten Silikonimplantaten deutlich verringerte Proliferationsraten im Vergleich zu unbeschichteten Implantaten. Die ebenfalls an der Fibrose beteiligten primären humanen Monocyten weisen eine signifikante Verringerung der Differenzierung in CD68-positive Makrophagen (Histocyten) auf.[72] Die Implantate wurden für 12 Monate in Spraque-Dawley Ratten implantiert und zeigten eine gute Verträglichkeit mit dem Wirtsorganismus. Es traten keine Wundheilungsstörungen auf. Durch die eADF4(C16)-Beschichtung konnte die Bildung von fibroblastenreichem periprosthetischem Gewebe und mehrlagig angeordneten Histocyten deutlich reduziert werden. Zusätzlich waren die Entzündungsparameter bei Verwendung von eADF4(C16) beschichteten Implantaten im Vergleich zu unbeschichteten Implantaten verringert. Die Seidenbeschichtung wird langsam abgebaut, jedoch konnte im Rahmen des Versuches noch nach 12 Monaten Implantationszeit eine durchgehende Beschichtung auf den Implantaten nachgewiesen werden.[72,233]

2. Zielsetzung

Das aus dem Abseilfaden der Europäischen Gartenkreuzspinne (*A. diadematus*) abgeleitete rekombinante Spinnenseidenprotein eADF4(C16) ist nicht toxisch, löst nur eine geringe Immunantwort aus, ist langsam bioabbaubar und die Zellinteraktion mit dem Material kann durch Variation der Morphologie bzw. direkte Modifikation des Proteins gesteuert werden. Filme aus eADF4(C16) sind demnach biokompatibel und eignen sich Aufgrund der geringen Zelladhäsion und Proliferation für die Beschichtung von Biomaterialien wie z.B. Silikon-Brustimplantaten.[72,233]

Bei der Langzeitanwendung von Implantaten oder auch medizinischen Schläuchen kann es zu Komplikationen durch eine Wirtsantwort auf das Biomaterial kommen. Solche pathophysiologischen Komplikationen sind beispielsweise eine schnelle Bildung von Narbengewebe und die Verkapselung des Materials im Körper, wie z.B. bei einer periprosthetischen Kapselfibrose (z.B. bei Silikon-Brustimplantaten). Silikon-Brustimplantate weisen in der Regel eine schwammartige und raue Oberflächenstruktur auf. Daher ist es möglich diese Oberflächen direkt mit Spinnenseide aus Lösung zu beschichten und die Seidenbeschichtung haftet in diesem Fall aufgrund von mechanischer Adhäsion auf der Oberfläche des Implantats. Möchte man hydrophobe und glatte Oberflächen aus wässriger Lösung mit rekombinantem Spinnenseidenprotein beschichten, so muss die schlechte Benetzbarkeit der Oberfläche beachtet werden. Auch ist die mechanische Adhäsion einer Seidenschicht auf glatten Oberflächen im Vergleich zu der schwammartigen Oberflächenstruktur von Silikon-Brustimplantaten deutlich verringert.

In dieser Arbeit sollte ein Tauchbeschichtungsprozess entwickelt werden, um glatte Oberflächen, z.B. von medizinischen Schläuchen, mit dem rekombinanten Spinnenseidenprotein eADF4(C16) zu beschichten. Die daraus resultierenden dünnen Beschichtungen mit einer Schichtdicke von unter 100 nm wurden hinsichtlich ihrer Eigenschaften wie Stabilität, Homogenität, Rauigkeit, Benetzungseigenschaften sowie Zelladhäsion und –proliferation, untersucht und charakterisiert. Für Blockcopolymere ist bekannt, dass ein schichtdickenabhängiges Assemblierungs- und Phasenseparationsverhalten in (ultra-)dünnen Schichten auftritt. Von *Wohlrab et al.* wurde für eADF4(C16) ein substratabhängiges Phasenseparationsmodell für Filme im Mikrometerbereich aufgestellt und es konnte gezeigt werden, dass eADF4(C16) Blockcopolymer-charakteristiken aufweist und sich die Primärstruktur (Aminosäuresequenz) von eADF4(C16) durch den vorhandenen hydrophilen und hydrohoben Block ähnlich einem AB-Multiblockcopolymer beschreiben lässt. Eine weitere zu untersuchende Hypothese war, ob die Phasenseparation von eADF4(C16)-Filmen ebenfalls eine Schichtdicken-abhängigkeit aufweist. Diese Hypothese sollte durch Charakterisierung der Sekundärstruktur und der Oberflächeneigenschaften von (ultra-) dünnen eADF4(C16)-Filmen von der Proteinlage mit einer Dicke von nur einigen Nanometern bis zum *bulk* untersucht werden. Ein entsprechendes Phasenseparationsmodell von eADF4(C16) Nanofilmen bis hin zu den von *Wohlrab et al.* beschriebenen *bulk*-Filmen mit einer Schichtdicke im Mikrometerbereich sollte erstellt, vorgeschlagen und diskutiert werden.

3. Synopsis

Obwohl vielfältige Prozessierungsmöglichkeiten für (Bio-) Polymere bekannt sind und einige Methoden wie Filmgießen, Rotationsbeschichtung und nanolithographische Techniken auch für verschiedene Seidenproteine (Fibroin, Spinnenseiden) angewendet wurden, sind kaum Informationen über das Assemblierungs- und Phasenseparationsverhalten von rekombinanten Spinnenseidenproteinen vorhanden, die in (ultra-) dünne Filme prozessiert wurden. Die vorliegende Arbeit umfasst vier Publikationen (Teilarbeiten), welche sich mit der Prozessierung von Spinnenseide, v.a. des rekombinanten Spinnenseidenproteins eADF4(C16), in dünne Filme und Beschichtungen für die biomedizinische Anwendung und den Eigenschaften dieser dünnen Filme beschäftigen. Abbildung 15 zeigt eine schematische Übersicht über den Inhalt der Dissertationsschrift und gibt einen ersten Überblick über den Zusammenhang der Teilarbeiten (siehe Kapitel 6).

Der erste Teil der Dissertation (Kapitel 6, Teilarbeit I, Coatings and Films Made of Silk Proteins) ist ein systematischer Übersichtsartikel, der den Stand der Forschung über die Prozessierungsmöglichkeiten von verschiedenen natürlichen und rekombinanten *β*-kristallinen Seidenproteinen in unterschiedliche Morphologien aufzeigt. Der Fokus wird hier auf Filme und Beschichtungen und ihre biomedizinische sowie optische und (bio-) sensorische Anwendung gelegt.

Der zweite Teil der Dissertation (Kapitel 6, Teilarbeit II, Surface Modification of Polymeric Biomaterials Using Recombinant Spider Silk Proteins) befasst sich mit der Entwicklung eines Beschichtungsprozesses, um glatte polymere Biomaterialoberflächen für die medizinische Anwendung mit eADF4(C16) zu beschichten. Die Beschichtungen wurden hinsichtlich ihrer Stabilität, Biokompatibilität und ihrer Zelladhäsionseigenschaften untersucht und unterscheiden sich von vorher veröffentlichten Silikonimplantatbeschichtungen mit einer Schichtdicke im Mikrometerbereich[72,233] vor allem durch ihre geringere Dicke von unter 100 nm.

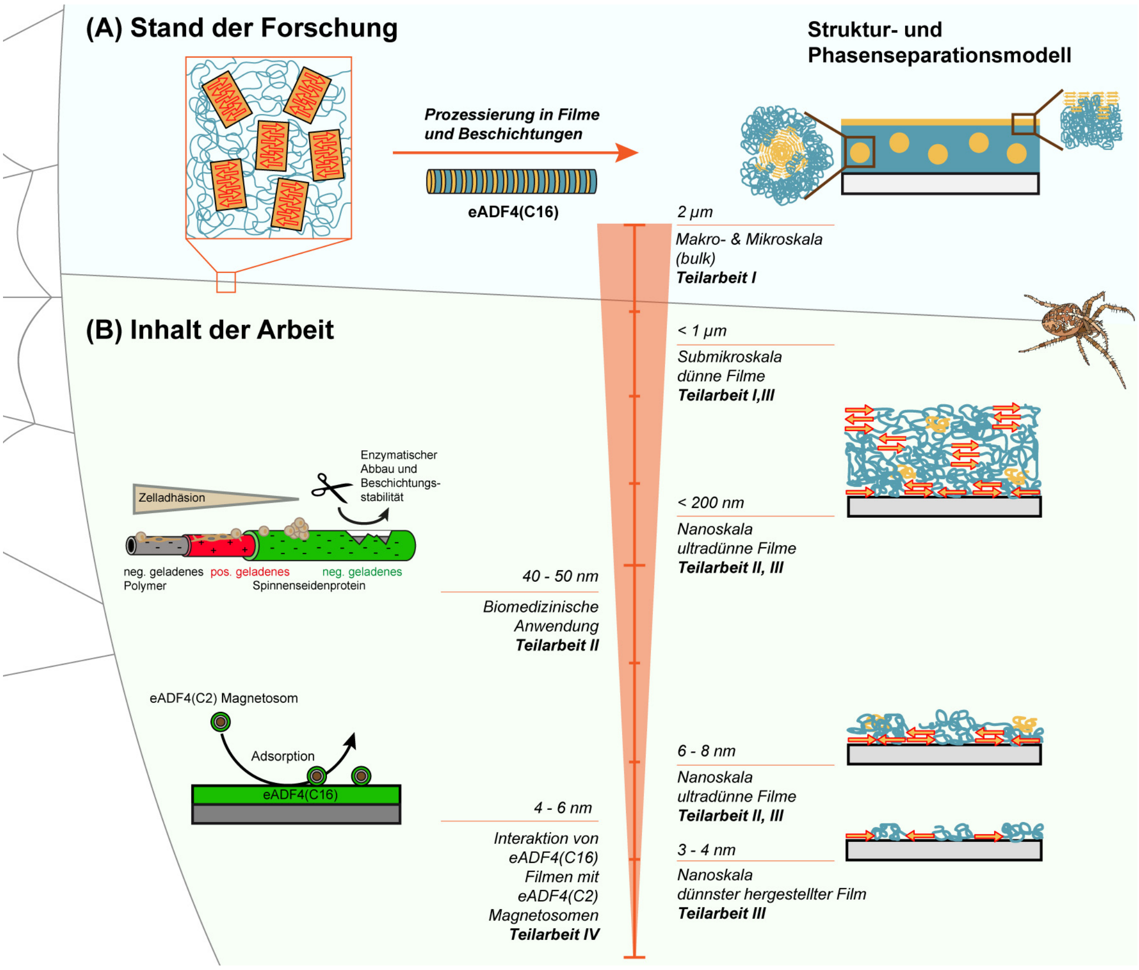

Abbildung 15. Struktur der Arbeit aufgeteilt in (A) Stand der Forschung vom natürlichen Vorbild des Abseilfadens und Prozessierung und Charakterisierung des multiblockcopolymerähnlichen rekombinanten Spinnenseidenproteins eADF4(C16) in *bulk*-Filmen sowie (B) Entwicklung eines schichtdickenabhängigen Phasenseparations- und Strukturmodells von der Makro- bzw. Mikroskala bis zur Nanoskala und in dieser Arbeit untersuchte Anwendungsbeispiele entsprechender Filme. In Teilen mit Genehmigung modifiziert und abgedruckt aus: C. B. Borkner, M. B. Elsner, T. Scheibel, Coatings and Films Made of Silk Proteins. *ACS Applied Materials and Interfaces* **2014**, *6*, 15611-15625. Copyright 2014 American Chemical Society. C. B. Borkner, S. Wohlrab, E. Möller, G. Lang, T. Scheibel, Surface Modification of Polymeric Biomaterials Using Recombinant Spider Silk Proteins. *ACS Biomaterials Science & Engineering* **2017**, *3*, 767-775. Copyright 2016 American Chemical Society.

Der Dritte Teil der Arbeit (Kapitel 6, Teilarbeit III: Ultrathin Spider Silk Films: Insights into Spider Silk Assembly on Surfaces) beschäftigt sich mit den strukturellen Eigenschaften sowie den Oberflächeneigenschaften von nano- und submikroskaligen eADF4(C16)-Filmen und schließt somit die Lücke zum *bulk*-Material sowie mikroskaligen Filmen. Es wurden Filme in einem Bereich von 3-4 nm Schichtdicke bis hin zum Mikrometerbereich hergestellt und die Separation der hydrophilen und hydrophoben Sequenzblöcke schichtdickenabhängig untersucht. Aus den auf der

Phasenseparation dieser Sequenzblöcke basierenden Oberflächenkontaktwinkeln und den schichtdickenabhängigen Daten zur Sekundärstrukturbildung (insbesondere dem relativen *β*-Faltblatt Anteil) wurde ein schichtdickenabhängiges Phasenseparationsmodell entwickelt.

Der vierte Teil der Arbeit (Kapitel 6, Teilarbeit IV: *In Vivo* Coating of Bacterial Magnetic Nanoparticles by Magnetosome Expression of Spider Silk-Inspired Peptides) beschreibt die Expression von Spinnenseidenmotiven in *M. gryphiswaldense*, die Charakterisierung der Magnetosomen sowie die Untersuchung der Adsorptionseigenschaften der mit eADF4(C2) modifizierten Nanopartikel auf eADF4(C16) Filmen. Die Wechselwirkung von eADF4(C2) mit eADF4(C16) wurde genutzt, um gezielt eADF4(C16) Fibrillen auf den eADF4(C2) modifizierten Magnetosomen zu assemblieren.

In den folgenden Abschnitten werden die wichtigsten Ergebnisse und Schlussfolgerungen der in Kapitel 6 dargestellten Publikationen dargestellt und diskutiert. Weiterführende Ergebnisse und detaillierte experimentelle Informationen sind den Publikationen zu entnehmen.

3.1. Seidenbeschichtungen

Bei der biomedizinischen Anwendung polymerer Biomaterialien (vgl. Kapitel 1.1.4) kann es aufgrund der Oberflächeneigenschaften dieser Materialien zu je nach Anwendungsgebiet unerwünschten Nebeneffekten durch Proteinadsorption (vgl. Kapitel 1.1.3.2) und Zellinteraktion (vgl. Kapitel 1.1.3.3) kommen.

Seidenproteine können entweder aus natürlichen Quellen oder biotechnologisch gewonnen werden. So wird *B. mori* Seide aus Kokons des Maulbeerspinners durch Degummierung mit 0,02 M Na_2CO_3 und Denaturierung mittels stark chaotroper Reagenzien (z.B. 9 M LiBr) gewonnen. Die biotechnologische Herstellung von Spinnenseiden in *E. coli* (vgl. Kapitel 1.3.1) hingegen ermöglicht die direkte Modifizierung der Proteine auf genetischer Ebene, um gewünschte Materialeigenschaften zu erzielen und auf verschiedene Anwendungen maßzuschneidern.[254] Das rekombinante Spinnenseidenprotein kann nun auf verschiedene Weise prozessiert werden (Kapitel 6, Teilarbeit I, Figure 2). Dazu muss das gereinigte und getrocknete rekombinante Seidenprotein in Lösung überführt werden. Als Lösungs- bzw. Denaturierungsmittel finden unterschiedliche Stoffe wie ionische Flüssigkeiten, starke Säuren, organische (fluorierte) Lösungsmittel sowie chaotrope Salze Anwendung. In den in dieser Arbeit beschriebenen Anwendungen findet Ameisensäure als Lösungsmittel zur Herstellung (ultra-) dünner Filme mittels Rotationsbeschichtungen (Teilarbeit III) und 6 M Guanidinthiocyanat (GdnSCN) als Denaturierungsreagenz zur Herstellung von Proteinlösungen in verschiedenen Puffern für die Tauchbeschichtung Verwendung (Teilarbeit II).

Bei der Beschichtung von polymeren Oberflächen mit wässrigen Spinnenseidenlösungen treten verschiedene Probleme auf. Die in dieser Arbeit verwendeten polymeren Biomaterialien PTFE, PU und Silikon haben hydrophobe, d.h. mit wässrigen Beschichtungslösungen und auch Ameisensäure schlecht benetzbare Oberflächen (Kapitel 6, Teilarbeit II, Figure 2). Eine Möglichkeit Polymeroberflächen zu hydrophilisieren, d.h. die Benetzbarkeit mit Wasser zu erhöhen, ist die Behandlung der Oberflächen im Sauerstoffplasma. Hierbei werden hochenergetische funktionelle Gruppen durch die Reaktion der Polymeroberfläche mit der reaktiven Plasmaspezies erzeugt. Der Hydrophilisierungseffekt kann zusätzlich durch Topographieänderung aufgrund der Plasmabehandlung verstärkt werden.[255-257] Die so hydrophilisierte Oberfläche kann in einem Tauchbeschichtungsprozess mit Spinnenseidenproteinen beschichtet werden. Da die hydrophilisierte Oberfläche mit der Zeit ihre Hydrophilie verliert,[257] muss die Beschichtung unmittelbar nach der Plasmabehandlung der Polymeroberflächen erfolgen. Die Plasmabehandlung der Oberflächen führt zu einer stärker negativen Oberflächenladung des Polymers.[258]

Die wässrige eADF4(C16)-Beschichtungslösung wurde durch Dialyse des denaturierten Proteins gegen Ammoniumhydrogencarbonat-Puffer (20 mM, pH 9) hergestellt. Bei direkter Beschichtung der plasmabehandelten Polymere mit eADF4(C16) (in Ammoniumhydrogencarbonat-Puffer, pH 9) kommt es aufgrund des pI(eADF4(C16)) von 3,48 und der daraus in NH_4HCO_3-Puffer (pH 9) resultierenden negativen Ladung des Proteins zu elektrostatischer Abstoßung zwischen der Oberfläche und eADF4(C16). Die Seidenbeschichtungen sind inhomogen und delaminieren bei geringster mechanischer Belastung. Wird konzentrierte Ameisensäure als Lösungsmittel für eADF4(C16) verwendet, erhält man homogenere aber ebenso gegenüber mechanischer Belastung instabile Filme.

Um die Adhäsion zwischen der Polymeroberfläche und dem Spinnenseidenprotein eADF4(C16) zu verbessern, wurde eine positiv geladene Vermittlerschicht aus dem polykationischen Polymer Polyethylenimin (PEI) auf die im Sauerstoffplasma hydrophilisierte polymere Biomaterialoberflächen aufgebracht. Hierzu wird das zu beschichtende Objekt unmittelbar nach der Plasmabehandlung in wässriger PEI-Lösung (1 % w/v) inkubiert. Durch die elektrostatische Wechselwirkung zwischen der Oberfläche und PEI bildet sich eine positiv geladene Schicht des Polyelektrolyts auf dem zu beschichtenden Material. Diese Schicht vermittelt nun die Adhäsion des negativ geladenen Spinnenseidenproteins eADF4(C16) auf den Oberflächen. Da PEI ein die Zellmembran penetrierendes Polymer ist und toxisch auf Zellen wirken kann, wurde PEI durch das positiv geladene Spinnenseidenprotein eADF4(κ16) ersetzt. Diese eADF4(κ16)/eADF4(C16)-Beschichtungen wurden auf Silikonoberflächen aufgebracht (Kapitel 6, Teilarbeit II, Figure 1 & S1) und zeigen keine Delamination bei Biegebelastung (Kapitel 6, Teilarbeit II, Figure 3 & S3). Die Schichtdicke liegt für Proteinbeschichtungen auf Silikon bei $d_{PEI/eADF4(C16)} = 43{,}1\ \mathrm{nm} \pm 9{,}7\ \mathrm{nm}$ bzw. $d_{eADF4(\kappa16)/eADF4(C16)} = 46{,}0\ \mathrm{nm} \pm 11{,}4\ \mathrm{nm}$. Die Rauigkeiten lagen mit $R_a = 13{,}5\ \mathrm{nm} \pm 2{,}5\ \mathrm{nm}$ für PEI/eADF4(C16) und $R_a = 13{,}7\ \mathrm{nm} \pm 2{,}9\ \mathrm{nm}$ für eADF4(κ16)/eADF4(C16) (Kapitel 6, Teilarbeit II, Figure S2) in der gleichen Größenordnung wie für bei *Wohlrab et al.*[225] beschriebene gegossene Filme und wiesen mittlere Oberflächenkontaktwinkel von 66° bis 69° auf. *Wohlrab et al.* untersuchten die Oberflächenkontaktwinkel von aus Ameisensäure gegossenen eADF4(C16) Filme auf Glas, PTFE und PS. Da Vergleichswerte von auf PDMS gegossenen eADF4(C16)-Filmen nicht vorhanden sind, werden die Oberflächenkontaktwinkel der Seidenbeschichtungen mit auf Glas gegossenen eADF4(C16)-Filmen verglichen. Die in dieser Arbeit ermittelten Oberflächenkontaktwinkel liegen deutlich unter dem für auf Glas gegossene eADF4(C16) Mikrofilme ermittelten Oberflächenkontaktwinkel von ca. 90° (*Wohlrab et al.*).[225]

Eine mögliche Erklärung für die unterschiedlichen Kontaktwinkel auf dünnen Seidenbeschichtungen der Polymerschläuche und gegossenen Filmen kann wie von *Wohlrab et al.* beschrieben das verwendete Substrat sein. Betrachtet man jedoch auch die Schichtdickenunterschiede der durch Tauchbeschichtung und Filmgießen hergestellten Filme, so lässt sich ebenfalls die Hypothese aufstellen, dass sich die

Oberflächeneigenschaften schichtdickenabhängig verändern. Sinkt die Schichtdicke, so steigt auch die spezifische Oberfläche je Volumen. Erreicht ein Material Abmessungen von < 100 nm in mindestens einer Dimension, so spricht man von Nanomaterialien, die im Vergleich zum *bulk*-Material verschiedene Eigenschaften aufweisen.

Abbildung 16 zeigt die auf beschichteten Kathetern ermittelten Oberflächenkontaktwinkel (Kapitel 6, Teilarbeit II) im Vergleich zu (ultra-) dünnen eADF4(C16)-Filmen (auf Si-Wafern) (Kapitel 6, Teilarbeit III). Die Seidenfilme wurden mittels Rotationsbeschichtung (eADF4(C16) gelöst in konz. Ameisensäure) auf die Si-Wafer-Substrate aufgebracht und weisen schichtdickenunabhängig eine mittlere Rauigkeit von $R_a < 1{,}0$ nm auf (Kapitel 6, Teilarbeit III, Figure 2).

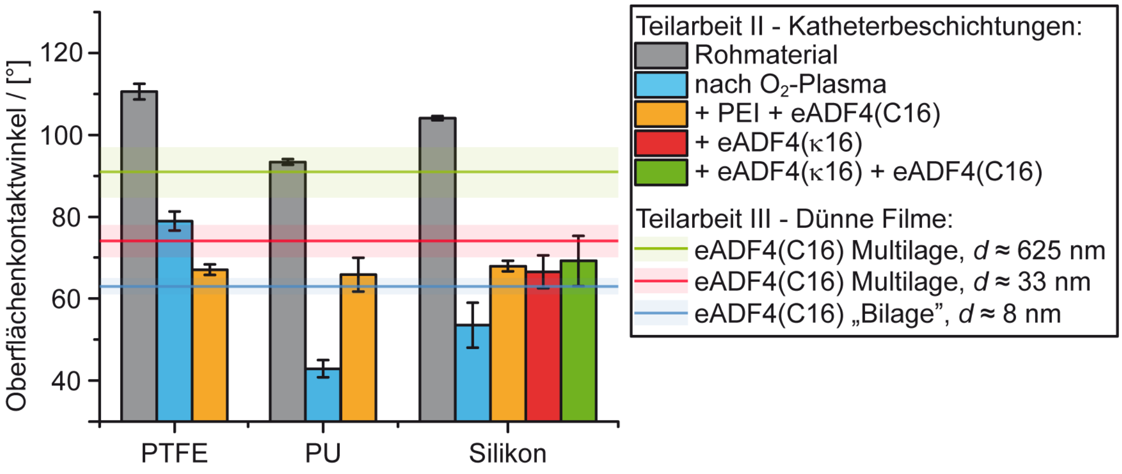

Abbildung 16. Oberflächenkontaktwinkel von in einem Tauchbeschichtungsprozess mit einer Seidenbeschichtung versehenen Polymerschläuchen im Vergleich zum Rohmaterial (Teilarbeit II) und durch Rotationsbeschichtung hergestellten dünnen eADF4(C16)-Filmen (Teilarbeit III). Es wurde der Wasserkontaktwinkel (Methode des liegenden Tropfens) ermittelt. Der Kontaktwinkel auf plasmabehandelten Oberflächen wurde unmittelbar nach der Plasmabehandlung ermittelt. Alle Seidenbeschichtungen zeigen unabhängig vom verwendeten Haftvermittler (PEI oder eADF4(κ16)) vergleichbare Kontaktwinkel. PEI: Polyethylenimin, PU: Polyurethan, PTFE: Polytetrafluoroethylen. Mit Genehmigung abgedruckt und modifiziert aus C. B. Borkner, S. Wohlrab, E. Möller, G. Lang, T. Scheibel, Surface Modification of Polymeric Biomaterials Using Recombinant Spider Silk Proteins. ACS Biomaterials Science & Engineering **2017**, *3*, 767-775. Copyright 2016 American Chemical Society.

Die Nomenklatur der Filme Anhand ihrer Dicke/Anzahl der Proteinlagen („Monolage"/„Bilage"/Multilage) der hergestellten Beschichtungen bezieht sich in dieser Arbeit auf die Referenzgröße der Beschichtung mit einer Schichtdicke von 3-4 nm. Sie liegt im Größenbereich zwischen der Höhe eines *β*-sheet Nanokristalls ($d \approx 5$ nm), wie er für *B. mori* Fibroin beschrieben wurde, und seiner Nanofibrillen ($d \approx 2$ nm)[259] bzw. der molekularer Monolage ($d \approx 1{,}5$ nm).[260] Diese Beschichtung war die dünnste homogene mittels Rotationsbeschichtung herstellbare Beschichtung und wird in dieser Arbeit als „Monolage“ bezeichnet und darf nicht mit molekularen Monolagen wie beispielsweise Selbstassemblierenden Monolagen (SAMs) verwechselt werden, da sie aus mehreren Moleküllagen besteht.

Der Kontaktwinkel liegt für Schichten mit einer Dicke von ca. 8 nm („Bilage“) bei $\theta_{bi} = 63° \pm 2°$ und somit geringfügig unter dem Kontaktwinkel der Katheterbeschichtungen. Mit steigender Schichtdicke steigt der Kontaktwinkel an ($\theta_{d=33nm} = 74° \pm 4°$; $\theta_{d=625nm} = 91° \pm 6°$) und erreicht die Größenordnung wie für auf Glassubstraten aus Ameisensäure gegossener eADF4(C16) Filme (*Wohlrab et al.*[225]). Der Kontaktwinkel zeigt eine deutliche Abhängigkeit von der Schichtdicke des Seidenfilms. Der Vergleich dieser Daten berücksichtigt jedoch nicht den Einfluss der verschiedenen Substrate, Lösungsmittel und Unterschiede in der Oberflächenrauigkeit auf den Oberflächenkontaktwinkel der Beschichtungen auf polymeren Kathetern im Vergleich zu (ultra-) dünnen Filmen auf Silizium. Dies erklärt den Unterschied in den absoluten Kontaktwinkeln für gleiche Schichtdicken zwischen aus wässriger Lösung hergestellten Katheterbeschichtungen und den aus Ameisensäure hergestellten (ultra-) dünnen Schichten.

3.2. Phasenseparation in (ultra-)dünnen Filmen

Neben den schichtdickenabhängigen Oberflächeneigenschaften (Kontaktwinkel) wurden die strukturellen Eigenschaften schichtdickenabhängig untersucht. Dazu wurde der relative β-Faltblattanteil (B) von eADF4(C16) Filmen im Schichtdickenbereich von 3-4 nm („Monolage“) bis hin zum Mikrometerbereich vor (*Engl.*: *before post treatment*, *bpt*) und nach Nachbehandlung (*Engl.*: *after post treatment*, *apt*) mit Methanol untersucht (Kapitel 6, Teilarbeit III). Filme bis 600 nm Schichtdicke wurden durch Rotationsbeschichtung und Mikrofilme durch Gießen hergestellt.

B wird aus der Amid I-Bande eines FTIR-Spektrum des Proteins ermittelt. Die Amid I-Bande ist hauptsächlich eine Superposition von C=O Streckschwingungen des

Proteinrückgrats unterschiedlicher Schwingungsenergien.[261-264] Sie wird in ihrer Vibrationsenergie durch die chemische und strukturelle Umgebung der jeweiligen Carbonylgruppe der Peptidbindung beeinflusst, d.h. sie hängt direkt von der Sekundärstruktur des Proteinrückgrats ab und kann daher zur quantitativen Analyse der verschiedenen Sekundärstrukturen verwendet werden. Durch Fourier-Selbstentfaltung und anschließende Peakanpassung an die entfaltete Amid-I Bande können die relativen Sekundärstrukturanteile bestimmt werden (vgl. Kapitel 6, Teilarbeit III, Figure 3).[261-263,265]

eADF4(C16) „Monolagen“ (d = 3-4 nm) haben ein B_{bpt} von 14,2 % ± 2,7 %. Erhöht man die Schichtdicke auf eine „Bilage“, so sinkt B_{bpt} leicht auf 12,7 % ± 1,8 % und steigt anschließend wieder mit steigender Schichtdicke an, bis ein Sättigungswert von B_{bpt} = 18 % bis 21 % im Bereich $d > 65$ nm erreicht ist. Obwohl die Signifikanz dieses Unterschieds zwischen „Mono-“ und „Bilage“ gering ist, soll trotzdem Augenmerk auf diese leichte Abnahme von B_{bpt} von der „Mono-“ zur „Bilage“ gelegt werden, die einen Hinweis auf ein Minimum in B_{bpt} gibt, das sich durch die intra- und intermolekularen Wechselwirkungen des Proteins mit Proteinmolekülen und der Oberfläche erklären ließe. Während der Rotationsbeschichtung bildet sich ein dünner Film der Spinnenseidenlösung auf dem Substrat. Das Lösungsmittel (*hier*: konz. Ameisensäure) dampft ab und es bildet sich ein fester, jedoch aufgrund der schnellen Trocknung vorwiegend unstrukturierter Spinnenseidenfilm (geringer B_{bpt}). Ein möglicher Erklärungsansatz für ein höheres B_{bpt} der „Monolage“ im Vergleich zur „Bilage“ ist, dass die erste adsorbierte vorwiegend unstrukturierte Schicht hydrophobe Wechselwirkungen mit der Oberfläche des Substrates ausbildet. Solch eine Wechselwirkung beruht auf der Verdrängung von Wasser von der Protein- und Substratoberfläche. Dadurch können Carbonylgruppen des Proteinrückgrats mit der Siliziumoxidschicht der Oberfläche interagieren, was zu einer möglichen Veränderung der Schwingungsenergie der C=O Bindung führen kann. In der „Bilage“ wird dieser aufgrund der hydrophoben Substrat-Protein Interaktion höhergeordneten ersten Proteinschicht eine vorwiegend unstrukturierte zweite Schicht hinzugefügt, was zu einer Abnahme in B_{bpt} führt. Bei steigender Schichtdicke steigt wiederum die Wahrscheinlichkeit für inter- und intramolekulare Wechselwirkung der Moleküle, da diese (bis auf die Moleküle an den Grenzflächen) nun in alle drei Raumrichtungen interagieren können und B_{bpt} steigt mit steigender Schichtdicke wieder an. Durch

Nachbehandlung der Seidenfilme in Methanolatmosphäre wird *β*-Faltblattbildung induziert und B_{apt} steigt kontinuierlich mit steigender Schichtdicke. Basierend auf der alternierenden Abfolge hydrophober und hydrophiler Sequenzblöcke kann das rekombinante Spinnenseidenprotein eADF4(C16) als AB-Multiblockcopolymer beschrieben werden (vgl. Kapitel 1.3.2.3). Auf Basis der Oberflächeneigenschaften (Kontaktwinkelanalyse) und der ermittelten relativen *β*-Faltblattanteile vor und nach Nachbehandlung wurde unter Berücksichtigung der Proteineigenschaften und der Theorie der Phasenseparation von Blockcopolymeren (vgl. Kapitel 1.3.2.1) ein schichtdickenabhängiges Phasenseparationsmodell für eADF4(C16) vorgeschlagen und diskutiert (vgl. Kapitel 6, Teilarbeit III, Figure 4). Die Benetzungseigenschaften von nachbehandelten eADF4(C16)-Filmen sind ein Indikator für die Struktureigenschaften des Proteins an der Protein/Luft-Grenzfläche. Abbildung 17 zeigt eine schematische Darstellung des schichtdickenabhängigen Phasenseparationsverhaltens von eADF4(C16) in nachbehandelten Filmen und verdeutlicht den Zusammenhang mit den Oberflächenbenetzungseigenschaften (Kontaktwinkel). Für Details wird auf Teilarbeit III (Kapitel 6) verwiesen.

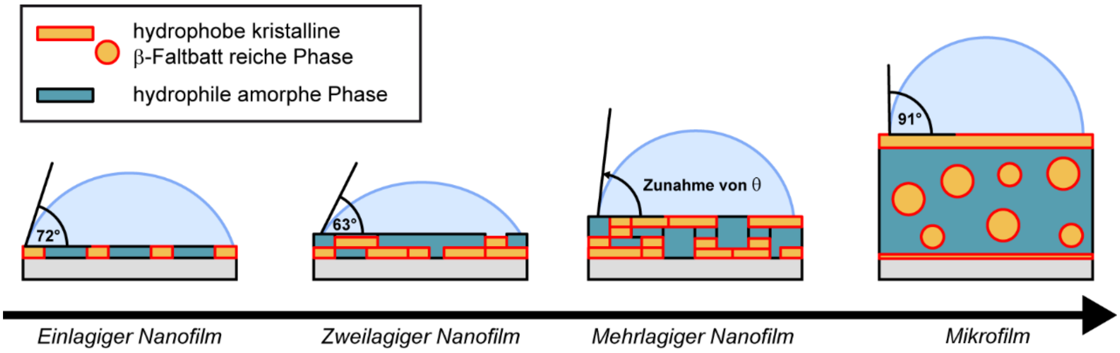

Abbildung 17. Schematische Darstellung des schichtdickenabhängigen Phasenseparationsverhaltens und der zugehörigen Oberflächenkontaktwinkel. Einlagige Nanofilme weisen eine 2D-Separation der hydrophilen und hydrophoben Phase auf. „Bilagige“ Nanofilme zeigen eine Ala-reiche Phase an der Substrat/Protein-Grenzfläche, was zu einer Exposition der hydrophilen Phase an der Protein/Luft-Grenzfläche und somit einem niedrigeren Kontaktwinkel im Vergleich zur „Monolage“ führt. Mit steigender Zahl an Proteinlagen nimmt der Kontaktwinkel wieder zu. In solchen multilagigen Nanofilmen steigt die Wahrscheinlichkeit der Interaktion der Seidenmoleküle in alle drei Raumrichtungen und die hydrophoben Ala reichen Bereiche separieren zunehmend an der Protein/Luft-Grenzfläche. Mikrofilme zeigen Phasenseparationsverhalten wie von *Wohlrab et al.* berichtet. Mit Genehmigung modifiziert und abgedruckt aus C. B. Borkner, S. Lentz, M. Müller, A. Fery, T. Scheibel, Ultrathin Spider Silk Films: Insight into Spider Silk Assembly on Surfaces. ACS Applied Polymer Materials **2019**, *1*, 3366-3374. Copyright 2019 American Chemical Society.

In der „Monolage“ sind die vorwiegend unstrukturierten hydrophilen und die hydrophoben Blöcke statistisch verteilt. Die hydrophoben pAla-Bereiche interagieren vorwiegend mit dem Substrat und werden von der hydrophilen Phase umgeben. Phasenseparation kann in der „Monolage“ nur in der *xy*-Ebene auftreten, wodurch die Wechselwirkungsmöglichkeiten der pAla-Blöcke begrenzt werden. Für die „Monolage“ konnte ein Kontaktwinkel von 72° ± 6° ermittelt werden. Für die „Bilage“ sinkt der Oberflächenkontaktwinkel auf 63° ± 2°. Hier sei nochmal auf die bereits erwähnte geringe Signifikanz der Abnahme von B_{bpt} von der „Mono-“ zur „Bilage“ (bei alleiniger Betrachtung) verwiesen. Betrachtet man jedoch die Abnahme von B_{bpt} im Zusammenhang mit der Abnahme des Kontaktwinkels von der „Mono-“ zur „Bilage“, so ergibt sich folgende Erklärung: Durch die größere Affinität des hydrophoben Blocks zur Substratoberfläche und der nun möglichen Bildung dichter pAla-pAla Interaktionen in *z*-Richtung zwischen den einzelnen Lagen in der „Bilage“ kommt es zu einer Anreicherung des hydrophoben Blocks an der Substratoberfläche und des hydrophilen Blocks an der Protein/Luft-Grenzfläche von der „Mono-“ zur „Bilage“, wodurch der Oberflächenkontaktwinkel sinkt.

Das Maximum in B_{apt} ist bereits bei einer Schichtdicke zwischen 90 nm und 250 nm erreicht. Ist der maximale β-Faltblattanteil erreicht, können sich jedoch mit steigender Schichtdicke immer noch größere kristalline Bereiche ausbilden, deren mizellarer Charakter mit steigender Schichtdicke ansteigt.[225] Durch die mit der Schichtdicke zunehmende Mikrophasenseparation kommt es in mehrlagigen eADF4(C16)-Filmen mit steigender Schichtdicke zu einer erneuten Zunahme des Oberflächenkontaktwinkels, bis ein Maximalwert von 91 ± 6° bei einer Schichtdicke von ~600 nm erreicht ist. Der Kontaktwinkel liegt hier in der gleichen Größenordnung wie für auf Glassubstraten aus Ameisensäure gegossene eADF4(C16) Filme (*Wohlrab et al.*[225]). Der hydrophobe pAla-reiche Block separiert bevorzugt an die Substrat/Protein- sowie Protein/Luft-Grenzflächen und bildet mizellenartige Strukturen eingebettet in die hydrophile amorphe Matrix.

Dieses schichtdickenabhängige eADF4(C16)-Phasenseparationsmodell schließt somit die Lücke zum *bulk*-Material, dessen Phasenseparationsverhalten in mikrometerdicken Filmen von *Wohlrab et al.*[225] (vgl. 1.3.2.3, Abbildung 12) beschrieben wurde.

3.3. Eigenschaften dünner Seidenbeschichtungen

Seide findet aufgrund ihrer Eigenschaften als Biomaterial (z.B. als Implantatbeschichtung) Anwendung (vgl. Kapitel 1.3.3). Neben der Stabilität solcher Beschichtungen gegenüber mechanischer Belastung, ist die Bioabbaubarkeit eine wichtige Eigenschaft von Biomaterialien (vgl. Kapitel 1.1.3.1). Bisher wurde die Bioabbaubarkeit von eADF4(C16) in Lösung, als Mikro-Filme, Partikel und Vliese[234] sowie von Hydrogelen[235] untersucht.

In dieser Arbeit wurde die Bioabbaubarkeit dünner eADF4(C16) Beschichtungen untersucht. Dazu wurden eADF4(κ16)/eADF4(C16)-Beschichtungen auf Silikonkathetern analog zu dem von *Müller-Herrmann und Scheibel*[234] für eADF4(C16) etablierten Modellsystem mit Protease Typ XIV (PXIV, *Streptomyces griseus*; Modell für Verdauumgebung) und Kollagenase Typ IA (*Engl.: collagenase type IA*, CHC, *Clostridium histolyticum*; Modellenzym für Wundheilungsumgebung) verdaut (Kapitel 6, Teilarbeit II, Figure 4). PXIV, eine Mischung aus mindestens 10 Proteasen, ist im pH-Bereich von pH 5,0 bis 9,0 stabil und zeigt seine optimale Aktivität bei pH 7 bis 8.[266] Durch die geringe Spezifität wird beispielsweise Casein zu mehr als 70 % in einzelne Aminosäuren verdaut und PXIV ist dabei deutlich effektiver als Trypsin oder Chymotrypsin.[266,267] CHC ist eine Kollagenase, deren optimaler pH-Bereich bei pH 6,3 bis 8,8 liegt. Sie wird bei pH 7,4 verwendet und hat eine hohe Spezifität.[268,269] Die Erkennungssequenz ist R-PX↓GP-R, in der X meistens eine neutrale Aminosäure ist. Die Schnittstelle liegt zwischen X und G.[268] Die Spinnenseidenbeschichtungen auf Silikonkathetern zeigten eine sehr gute Stabilität in Puffer. Durch PXIV wurde eADF4(C16) nach 6 Tagen und eADF4(κ16) nach 4 Tagen vollständig abgebaut. Beide Proteine zeigen jedoch eine höhere Stabilität in Wundheilungsumgebung. Zusammengefasst weisen eADF4(k16)/eADF4(C16)-Beschichtungen demnach eine langsame Bioabbaubarkeit in Wundheilungsumgebung sowie eine gute Stabilität gegenüber mechanischer Belastung, wie sie bei der biomedizinischen Anwendung polymerer Schläuche auftritt, auf.

Neben der Beschichtungsstabilität spielt auch die Proteinadsorption sowie Zellinteraktion mit den Beschichtungsoberflächen eine bedeutende Rolle für die Biokompatibilität des Materials und seine spezifische Anwendung. Die Interaktion von µm-dicken eADF4(C16)-Filmen mit Zellen wurde in den letzten Jahren detailliert untersucht (vgl. Kapitel 1.3.3). Im Rahmen von Teilarbeit II wurde die Adhäsion von BALB/3T3 Fibroblasten auf seidenbeschichtetem PTFE, PU und Silikon nach 24 h Inkubation untersucht. Auf den Rohmaterialien zeigen Fibroblasten eine schlechte Zelladhäsion. Wird eine Haftvermittlerschicht aus Polyethylenimin (PEI) aufgebracht steigt die Zelladhäsion. Auf eADF4(C16) beschichteten Katheteroberflächen ist eine geringe Zelladhäsion im 24 h Versuch im Vergleich mit der nichtbehandelten Zellkulturplatte (*Engl.: non-treated cellculture plate*, NTCP) zu beobachten und eADF4(C16)-RGD vermittelt eine bessere Zelladhäsion im Vergleich zu eADF4(C16) (Kapitel 6, Teilarbeit II, Figure 5). Auch im 6-Tage Adhäsionsexperiment zeigte sich eine geringe Zelladhäsion auf der eADF4(κ16)/eADF4(C16) beschichteten Silikonkatheteroberfläche. Auf der Haftvermittlerschicht (eADF4(κ16) & PEI) hingegen zeigen BALB/3T3 Fibroblasten eine höhere Zelladhäsion (Kapitel 6, Teilarbeit II, Figure 6). Dies konnte auf PDMS-Modelloberflächen für die Proliferation (6 d) von BALB/3T3 Fibroblasten bestätigt (Kapitel 6, Teilarbeit II, Table 1) und reproduziert werden (Abbildung 18). Neben der Adhäsion von BALB/3T3 Fibroblasten wurde die Adhäsion von B50 neuronalen Zellen (Kapitel 6, Teilarbeit II, Figure S5), HaCaT Keratinocyten (Kapitel 6, Teilarbeit II, Figure S6) sowie C2C12 Myoblasten (Kapitel 6, Teilarbeit II, Figure S7) untersucht. Alle Zelltypen zeigen ein zu Fibroblasten analoges Adhäsionsverhalten. Solche durch Tauchbeschichtung hergestellten Seidenbeschichtungen, wie sie auf Katheter aufgebracht wurden, zeigen mit gegossenen Mikrofilmen vergleichbare Zelladhäsionseigenschaften (vgl. Kapitel 1.3.3).[232,236,237,248] Dünne eADF4(C16) Beschichtungen bieten somit für biomedizinische Anwendungen, in denen keine Wirtsreaktion auftreten soll und Zellen nicht mit der Oberfläche interagieren sollen, eine gute Möglichkeit zur Einstellung der Oberflächeneigenschaften bei gleichzeitig geringem Materialeinsatz.

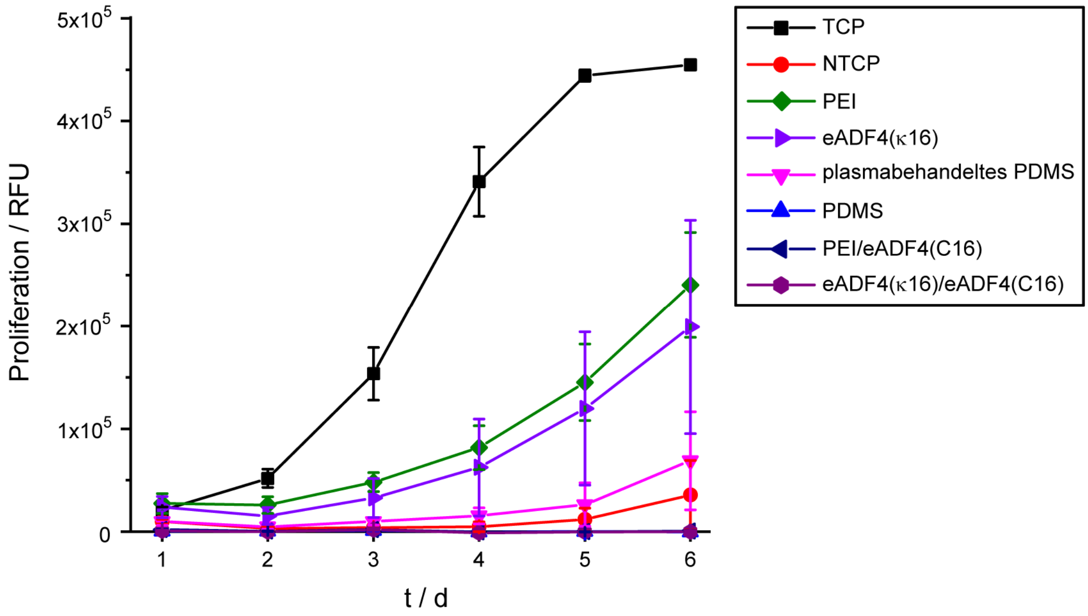

Abbildung 18. Proliferation von BALB/3T3 Fibroblasten (5000 Zellen/cm²) auf Seidenbeschichtungen und Referenzsubstraten über 6 Tage. Die Beschichtungen (PEI; eADF4(κ16),PEI/eADF4(C16), eADF4(κ16)/eADF4(C16)) wurden auf plasmabehandeltes PDMS aufgebracht. TCP: behandelte Zellkulturplatte (*Engl.: treated cell culture plate*); NTCP: unbehandelte Zellkulturplatte (*Engl.: non-treated cell culture plate*); PEI: Polyethylenimin, PDMS: Polydimethylsiloxan.

Zusätzlich zu den Eigenschaften dünner Filme wurde die Interaktion von eADF4(C2) funktionalisierten bakteriellen Nanopartikeln (MamC-C2 Magnetosomen) mit ultradünnen eADF4(C16) Filmen untersucht (Kapitel 6, Teilarbeit IV). Magnetosomen werden von magnetotaktischen Bakterien zur Orientierung entlang der Feldlinien des Erdmagnetfeldes gebildet.[270,271] Im Modellorganismus *Magnetospirillum gryphiswaldense* bestehen sie aus einem Magnetitkern und einer Phospholipid-Doppelschicht, der sogenannten Magnetosomen-Membran. Letztere enthält einen Großteil der für die Magnetosomen-Biosynthese relevanten Proteinkomponenten.[272] Magnetosomen-Membran (Mam-) Proteine erlauben die Darstellung von Fremdproteinen auf der Magnetosomen-Oberfläche, welche als Hybridproteine (bestehend aus Mam-Protein und Fremdprotein) als translationelle Fusion exprimiert werden können.[273-275]

Im Falle von MamC-C2 Magnetosomen ist das Spinnenseidenprotein über das Ankerprotein MamC in der Biomembran verankert und bildet mit ihr zusammen eine den Partikel kolloidal stabilisierende Hülle. Im Rahmen dieser Arbeit wurde eine Methode zur qualitativen empirischen Kontrolle von Magnetosomsuspensionen entwickelt. Im FTIR Spektrum kann man zwei charakteristische Bereiche erkennen. Im

Wellenzahlbereich von ca. 1750 cm^{-1} bis 1710 cm^{-1} liegt der für Carbonsäuren und ihre Ester, wie sie in Phospholipiden vorkommen, charakteristische Absorptionsbereich.[276] eADF4(C16) zeigt seine Amid I Bande im Bereich von ca. 1690 cm^{-1} bis 1600 cm^{-1}. Aus im Wellenzahlbereich von 1765 cm^{-1} bis 1585 cm^{-1} auf die maximale Absorption normierten FTIR-Spektren der Magnetosomen lässt sich das Intensitätsverhältnis der maximalen Absorption der Proteinabsorption und der Phospholipidmembran ermitteln (Kapitel 6, Teilarbeit IV, Figure S9). Im Zusammenhang mit SDS-PAGE und Western-Blot Analyse der Membranbestandteile konnte gezeigt werden, dass die FTIR-Analyse der Magnetosomen einen guten Hinweis auf die Batchqualität, d.h. das Vorhandensein einer intakten Magnetosomenmembran, geben kann.

In QCM-D Messungen wurden MamC-C2 Magnetosomen über eADF4(C16)-Beschichtungen geleitet und die Interaktion der Partikel mit der Oberfläche untersucht (Abbildung 19 A). Dazu wurden Wildtyp (*wt*) Magnetosomen bzw. MamC-C2 Magnetosomen in 10 mM 2-(4-(2-Hydroxyethyl)-1-piperazinyl)-ethansulfonsäure (HEPES) mit 1 mM Ethylendiamintetraessigsäure (EDTA) über eADF4(C16) Oberflächen geleitet. Es zeigte sich, dass die Adsorptionsraten von MamC-C2 gegenüber *wt* Magnetosomen erhöht waren. Dies lässt auf eine intermolekulare Wechselwirkung von in der Magnetosomenmembran verankertem eADF4(C2) und eADF4(C16) auf der QCM-D Chipoberfläche schließen.

Humenik et al. beschrieben den Einfluss chaotroper und kosmotroper Salze auf die Fibrillisierung von eADF4(C16).[277] Die Nukleation konnte durch Impfen mit vorstrukturierten Fibrillen deutlich beschleunigt werden und die Verwendung von Submikro-Partikeln, die ebenfalls als Nukleationskeime wirken, führte zu Fibrillienwachstum ausgehend von der Partikeloberfläche.[277] *Humenik et al.* zeigten, dass die Assemblierung der eADF4(C16)-Fibrillen an diversen C-Modul basierten Oberflächen wie z.B. eADF4(C16)-Partikeln oder eADF4(C)n-Keimen (n = 2 bis 16), möglich ist.[278] Basierend auf dieser Schlussfolgerung und der nachgewiesenen Interaktion von MamC-C2 Magnetosomen mit eADF4(C16)-Oberflächen, können MamC-C2 Magnetosomen als Nukleationskeime für eADF4(C16)-Fibrillisierung verwendet werden (Abbildung 19 B).

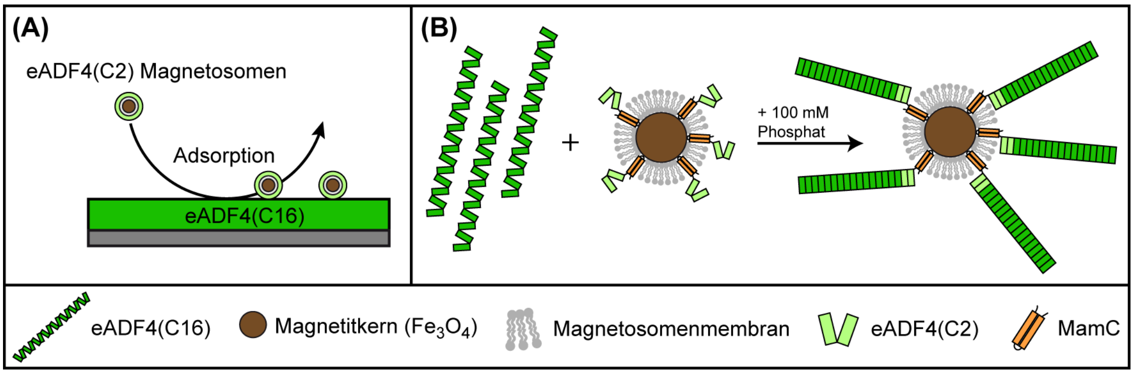

Abbildung 19. Schematische Darstellung der (A) Adsorption eADF4(C2)-Magnetosompartikeln auf eADF4(C16) beschichteten QCM-D Resonatoren (in 10 mM HEPES, 1 mM EDTA) und (B) Fibrillisierung von eADF4(C16) auf eADF4(C2) Magnetosomen in Anwesenheit von 100 mM Kaliumphosphat.

Dazu wurden die MamC-C2 bzw. *wt* Magnetosomen in einer eADF4(C16)-Lösung in Anwesenheit von 100 mM Phosphat inkubiert. Im Gegensatz zu *wt* Magnetosomen, bei denen die Fibrillisierung nur in der die *wt* Magnetosomen umgebenden Seidenlösung stattfand, konnte bei den MamC-C2 Magnetosomen Fibrillenbildung ausgehend von der Partikeloberfläche nachgewiesen werden. Das Fibrillenwachstum schien dabei gleichermaßen von einzelnen Partikeln als auch von in Ketten angeordneten Magnetosomen auszugehen.

4. Literaturverzeichnis

(1) Williams, D. F., *The Williams Dictionary of Biomaterials*. 1st ed.; Liverpool University Press: Liverpool, 1999.

(2) Walker, P. M. B., *Larousse Dictionary of Science and Technology*. 1st ed.; Larousse: Edinburgh, 1995.

(3) Williams, D. F., *Definitions in Biomaterials: Proceedings of a Censensus Conference of the European Society for Biomaterials*. Elsevier: Amsterdam, 1987; Vol. 4.

(4) Doherty, P. J.; Williams, R. L.; Williams, D. F.; Lee, A. J. C., *Biomaterial-Tissue Interfaces: Proceedins of the Ninth European Conference on Biomaterials*. Elsevier: Amsterdam, 1992; Vol. 10.

(5) Ratner, B. D., Chapter I.1.5 Surface Properties and Surface Characterization of Biomaterials. In *Biomater. Sci.*, 3rd ed.; Rattner, B. D.; Hoffman, A. S.; Schoen, F. J.; Lemons, J. E., Eds. Elsevier Academic Press: San Diego, CA, 2013; pp 34-55.

(6) Marcus, Y. Effect of Ions on the Structure of Water: Structure Making and Breaking. *Chem. Rev.* **2009**, *109*, 1346-1370.

(7) Ratner, B. D., Chapter I.1.6 Role of Water in Biomaterials. In *Biomater. Sci.*, 3rd ed.; Rattner, B. D.; Hoffman, A. S.; Schoen, F. J.; Lemons, J. E., Eds. Elsevier Academic Press: San Diego, CA, 2013; pp 55-59.

(8) Hofmeister, F. Zur Lehre von der Wirkung der Salze. Zweithe Mittheilung. *Arch. Exp. Pathol. Pharmakol.* **1888**, *24*, 247-260.

(9) Baldwin, R. L. How Hofmeister Ion Interactions Affect Protein Stability. *Biophys. J.* **1996**, *71*, 2056-2063.

(10) Boström, M.; Williams, D. R. M.; Stewart, P. R.; Ninham, B. W. Hofmeister Effects in Membrane Biology: The Role of Ionic Dispersion Potentials. *Phys. Rev. E* **2003**, *68*.

(11) Boström, M.; Williams, D. R. M.; Ninham, B. W. Special Ion Effects: Why the Properties of Lysozyme in Salt Solutions Follow a Hofmeister Series. *Biophys. J.* **2003**, *85*, 686-694.

(12) Boström, M.; Williams, D. R. M.; Ninham, B. W. Specific Ion Effects: The Role of Co-Ions in Biology. *Europhys. Lett.* **2003**, *63*, 610-615.

(13) Boström, M.; Craig, V. S. J.; Albion, R.; Williams, D. R. M.; Ninham, B. W. Hofmeister Effects in pH Measurements: Role of Added Salt and Co-Ions. *J. Phys. Chem. B* **2003**, *107*, 2875-2878.

(14) Zhang, Y.; Furyk, S.; Bergbreiter, D. E.; Cremer, P. S. Specific Ion Effects on the Water Solubility of Macromolecules: PNIPAM and the Hofmeister Series. *J. Am. Chem. Soc.* **2005**, *127*, 14505-10.

(15) Coury, A. J., Chapter II.4.2 Chemical and Biochemical Degradation of Polymers Intended to be Biostable. In *Biomater. Sci.*, 3rd ed.; Rattner, B. D.; Hoffman, A. S.; Schoen, F. J.; Lemons, J. E., Eds. Elsevier Academic Press: San Diego, CA, 2013; pp 696-715.

(16) Göpferich, A. Mechanisms of Polymer Degradation and Erosion. *Biomaterials* **1996**, *17*, 103-114.

(17) Herrmann, J. B.; Kelly, R. J.; Higgins, G. A. Polyglycolic Acid Sutures: Laboratory and Clinical Evaluation of a New Absorbable Suture Material. *Arch. Surg.* **1970**, *100*, 486-490.

(18) Lin, C.-C.; Anseth, K. S., Chapter II.4.3 The Biodegradation of Biodegradable Polymeric Biomaterials. In *Biomater. Sci.*, 3rd ed.; Rattner, B. D.; Hoffman, A. S.; Schoen, F. J.; Lemons, J. E., Eds. Elsevier Academic Press: San Diego, CA, 2013; pp 716-728.

(19) Treiser, M.; Abramson, S.; Langer, R.; Kohn, J., Chapter I.2.6 Degradable and Resorbable Biomaterials. In *Biomater. Sci.*, 3rd ed.; Rattner, B. D.; Hoffman, A. S.; Schoen, F. J.; Lemons, J. E., Eds. Elsevier Academic Press: San Diego, CA, 2013; pp 179-195.

(20) Meyers, S. R.; Grinstaff, M. W. Biocompatible and Bioactive Surface Modifications for Prolonged *In Vivo* Efficacy. *Chem. Rev.* **2012**, *112*, 1615-1632.

(21) Ratner, B. D.; Hoffman, A. S., Chapter I.2.10 Non-Fouling Surfaces. In *Biomater. Sci.*, 3rd ed.; Rattner, B. D.; Hoffman, A. S.; Schoen, F. J.; Lemons, J. E., Eds. Elsevier Academic Press: San Diego, CA, 2013; pp 55-59.

(22) Chandy, T.; Das, G. S.; Wilson, R. F.; Rao, G. H. R. Use of Plasma Glow for Surface-Engineering Biomolecules to Enhance Bloodcompatibility of Dacron and PTFE Vascular Prosthesis. *Biomaterials* **2000**, *21*, 699-712.

(23) Hoffman, A. S. A General Classification Scheme for Hydrophilic and Hydrophobic Biomaterial Surfaces. *J. Biomed. Mater. Res.* **1986**, *20*, ix-xi.

(24) Horbett, T. A.; Brash, J. L., Proteins at Interfaces: Current Issues and Future-Prospects. In *ACS Symposium Series: Proteins at Interfaces - Physiochemical and Biochemical Studies*, Horbett, T. A.; Brash, J. L., Eds. American Chemical Society: Washington, DC, 1987; Vol. 343, pp 1-33.

(25) Horbett, T. A.; Brash, J. L., Proteins at Interfaces: An Overview. In *ACS Symposium Series: Proteins at Interfaces II - Fundamentals and Applications*, Horbett, T. A.; Brash, J. L., Eds. American Chemical Society: Washington, DC, 1995; Vol. 602, pp 1-25.

(26) Dash, P. R.; Read, M. L.; Barrett, L. B.; Wolfert, M.; Seymour, L. W. Factors Affecting Blood Clearance and *In Vivo* Distribution of Polyelectrolyte Complexes for Gene Delivery. *Gene Ther.* **1999**, *6*, 643-650.

(27) Owens III, D. E.; Peppas, N. A. Opsonization, Biodistribution, and Pharmacokinetics of Polymeric Nanoparticles. *Int. J. Pharm.* **2006**, *307*, 93-102.

(28) Vogler, E. A. Structure and Reactivity of Water at Biomaterial Surfaces. *Adv. Colloid Interface Sci.* **1998**, *74*, 69-117.

(29) Berg, J. M.; Eriksson, L. G. T.; Claesson, P. M.; Børve, K. G. N. Three-Component Langmuir-Blodgett Films with a Controllable Degree of Polarity. *Langmuir* **1994**, *10*, 1225-1234.

(30) Wei, Q.; Becherer, T.; Angioletti-Uberti, S.; Dzubiella, J.; Wischke, C.; Neffe, A. T.; Lendlein, A.; Ballauff, M.; Haag, R. Protein Interactions with Polymer Coatings and Biomaterials. *Angew. Chem., Int. Ed.* **2014**, *53*, 8004-8031.

(31) Horbett, T. A. Principles Underlying the Role of Adsorbed Plasma Proteins in Blood Interactions with Foreign Materials. *Cardiovasc. Pathol.* **1993**, *2*, S137-S148.

(32) Casals, E.; Pfaller, T.; Duschl, A.; Oostingh, G. J.; Puntes, V. Time Evolution of the Nanoparticle Protein Corona. *ACS Nano* **2010**, *4*, 3623-3632.

(33) Lundqvist, M.; Stigler, J.; Cedervall, T.; Berggård, T.; Flanagan, M. B.; Lynch, I.; Elia, G.; Dawson, K. The Evolution of the Protein Corona around Nanoparticles: A Test Study. *ACS Nano* **2011**, *5*, 7503-7509.

(34) Vroman, L.; Adams, A. L. Findings with Recording Ellipsometer Suggesting Rapid Exchange of Specific Plasma Proteins at Liquid/Solid Interfaces. *Surf. Sci.* **1969**, *16*, 438-446.

(35) Jung, S.-Y.; Lim, S.-M.; Albertorio, F.; Kim, G.; Gurau, M. C.; Yang, R. D.; Holden, M. A.; Cremer, P. S. The Vroman Effect: A Molecular Level Description of Fibrinogen Displacement. *J. Am. Chem. Soc.* **2003**, *125*, 12782-12786.

(36) Noh, H.; Vogler, E. A. Volumetric Interpretation of Protein Adsorption: Competition from Mixtures and the Vroman Effect. *Biomaterials* **2007**, *28*, 405-422.

(37) Hoffman, A. S. Non-Fouling Surface Technologies. *J. Biomater. Sci. Polym. Ed.* **1999**, *10*, 1011-1014.

(38) Norde, W.; Horbett, T. A.; Brash, J. L., Proteins at Interfaces III: Introductory Ovierview. In *ACS Symposium Series: Proteins at Interfaces III - State of the Art*, Norde, W.; Horbett, T. A.; Brash, J. L., Eds. American Chemical Society: Washington, DC, 2012; Vol. 1120, pp 1-34.

(39) Müller, C.; Lüders, A.; Hoth-Hannig, W.; Hannig, M.; Ziegler, C. Initial Bioadhesion on Dental Materials as a Function of Contact Time, pH, Surface Wettability, and Isoelectric Point. *Langmuir* **2010**, *26*, 4136-4141.

(40) Stuart, M. A. C.; Huck, W. T. S.; Genzer, J.; Müller, M.; Ober, C.; Stamm, M.; Sukhorukov, G. B.; Szleifer, I.; Tsukruk, V. V.; Urban, M.; Winnik, F.; Zauscher, S.; Luzinov, I.; Minko, S. Emerging Applications of Stimuli-Responsive Polymer Materials. *Nat. Mater.* **2010**, *9*, 101-113.

(41) Ostuni, E.; Chapman, R. G.; Holmlin, R. E.; Takayama, S.; Whitesides, G. M. A Survey of Structure-Property Relationships of Surfaces that Resist the Adsorption of Protein. *Langmuir* **2001**, *17*, 5605-5620.

(42) Chapman, R. G.; Ostuni, E.; Takayama, S.; Holmlin, R. E.; Yan, L.; Whitesides, G. M. Surveying for Surfaces that Resist the Adsorption of Proteins. *J. Am. Chem. Soc.* **2000**, *122*, 8303-8304.

(43) Horbett, T. A., Chapter II.1.2 Adsorbed Proteins on Biomaterials. In *Biomater. Sci.*, 3rd ed.; Rattner, B. D.; Hoffman, A. S.; Schoen, F. J.; Lemons, J. E., Eds. Elsevier Academic Press: San Diego, CA, 2013; pp 394-408.

(44) Leal-Egaña, A.; Díaz-Cuenca, A.; Boccaccini, A. R. Tuning of Cell-Biomaterial Anchorage for Tissue Regeneration. *Adv. Mater.* **2013**, *25*, 4049-57.

(45) Margadant, C.; Monsuur, H. N.; Norman, J. C.; Sonnenberg, A. Mechanisms of Integrin Activation and Trafficking. *Curr. Opin. Cell Biol.* **2011**, *23*, 607-614.

(46) Prager-Khoutorsky, M.; Lichtenstein, A.; Krishnan, R.; Rajendran, K.; Mayo, A.; Kam, Z.; Geiger, B.; Bershadsky, A. D. Fibroblast Polarization is a Matrix-Rigidity-Dependent Process Controlled by Focal Adhesion Mechanosensing. *Nat. Cell Biol.* **2011**, *13*, 1457-1465.

(47) Hoffman, B. D.; Grashoff, C.; Schwartz, M. A. Dynamic Molecular Processes Mediate Cellular Mechanotransduction. *Nature* **2011**, *475*, 316-323.

(48) Young, J. L.; Engler, A. J. Hydrogels with Time-Dependent Material Properties Enhance Cardiomyocyte Differentiation *In Vitro*. *Biomaterials* **2011**, *32*, 1002-1009.

(49) Salber, J.; Gräter, S.; Harwardt, M.; Hofmann, M.; Klee, D.; Dujic, J.; Jinghuan, H.; Ding, J.; Kippenberger, S.; Bernd, A.; Groll, J.; Spatz, J. P.; Möller, M. Influence of Different ECM Mimetic Peptide Sequences Embedded in a Nonfouling Environment on the Specific Adhesion of Human-Skin Keratinocytes and Fibroblasts on Deformable Substrates. *Small* **2007**, *3*, 1023-1031.

(50) Pierschbacher, M. D.; Ruoslahti, E. Cell Attachment Activity of Fibronectin can be Duplicated by Small Synthetic Fragments of the Molecule. *Nature* **1984**, *309*, 30-33.

(51) Bellis, S. L. Advantages of RGD Peptides for Directing Cell Association with Biomaterials. *Biomaterials* **2011**, *32*, 4205-4210.

(52) Roach, P.; Eglin, D.; Rohde, K.; Perry, C. C. Modern Biomaterials: A Review-Bulk Properties and Implications of Surface Modifications. *J. Mater. Sci.: Mater. Med.* **2007**, *18*, 1263-1277.

(53) Bacakova, L.; Filova, E.; Parizek, M.; Ruml, T.; Svorcik, V. Modulation of Cell Adhesion, Proliferation and Differentiation on Materials Designed for Body Implants. *Biotechnol. Adv.* **2011**, *29*, 739-767.

(54) Kim, J.; Kim, D.-H.; Lim, K. T.; Seonwoo, H.; Park, S. H.; Kim, Y.-R.; Kim, Y.; Choung, Y.-H.; Choung, P.-H.; Chung, J. H. Charged Nanomatrices as Efficient Platforms for Modulating Cell Adhesion and Shape. *Tissue Eng., Part C* **2012**, *18*, 913-923.

(55) Healy, K. E.; Thomas, C. H.; Rezania, A.; Kim, J. E.; McKeown, P. J.; Lom, B.; Hockberger, P. E. Kinetics of Bone Cell Organization and Mineralization on Materials with Patterned Surface Chemistry. *Biomaterials* **1996**, *17*, 195-208.

(56) Anselme, K. Osteoblast Adhesion on Biomaterials. *Biomaterials* **2000**, *21*, 667-681.

(57) Hlady, V.; Buijs, J. Protein Adsorption on Solid Surfaces. *Curr. Opin. Biotechnol.* **1996**, *7*, 72-77.

(58) Lensen, M. C.; Schulte, V. A.; Salber, J.; Diez, M.; Menges, F.; Moller, M. Cellular Responses to Novel, Micropatterned Biomaterials. *Pure Appl. Chem.* **2008**, *80*, 2479-2487.

(59) Ruardy, T. G.; Schakenraad, J. M.; van der Mei, H. C.; Busscher, H. J. Adhesion and Spreading of Human Skin Fibroblasts on Physicochemically Characterized Gradient Surfaces. *J. Biomed. Mater. Res.* **1995**, *29*, 1415-1423.

(60) Vogler, E. A. Water and the Acute Biological Response to Surfaces. *J. Biomater. Sci., Polym. Ed.* **1999**, *10*, 1015-1045.

(61) Anselme, K.; Bigerelle, M.; Noel, B.; Dufresne, E.; Judas, D.; Iost, A.; Hardouin, P. Qualitative and Quantitative Study of Human Osteoblast Adhesion on Materials with Various Surface Roughnesses. *J. Biomed. Mater. Res.* **2000**, *49*, 155-166.

(62) Harrison, R. G. On the Stereotropism of Embryonic Cells. *Science* **1911**, *34*, 279-281.

(63) Meyle, J.; Gültig, K.; Wolburg, H.; von Recum, A. F. Fibroblast Anchorage to Microtextured Surfaces. *J. Biomed. Mater. Res.* **1993**, *27*, 1553-1557.

(64) Weiss, P. Erzwingung Elementarer Strukturverschiedenheiten am *In Vitro* Wachsenden Gewebe. *Wilhelm Roux' Arch. Entwicklungsmech. Org.* **1929**, *116*, 438-554.

(65) Weiss, P. Experiments on Cell and Axon Orientation *In Vitro*: The Role of Colloidal Exudates in Tissue Organization. *J. Exp. Zool.* **1945**, *100*, 353-386.

(66) Bettinger, C. J.; Langer, R.; Borenstein, J. T. Engineering Substrate Topography at the Micro- and Nanoscale to Control Cell Function. *Angew. Chem., Int. Ed.* **2009**, *48*, 5406-5415.

(67) Christopherson, G. T.; Song, H.; Mao, H.-Q. The Influence of Fiber Diameter of Electrospun Substrates on Neural Stem Cell Differentiation and Proliferation. *Biomaterials* **2009**, *30*, 556-564.

(68) Colas, A.; Curtis, J., Chapter I.2.2.B. Silicones. In *Biomater. Sci.*, 3rd ed.; Rattner, B. D.; Hoffman, A. S.; Schoen, F. J.; Lemons, J. E., Eds. Elsevier Academic Press: San Diego, CA, 2013; pp 82-91.

(69) Chen, H.; Brook, M. A.; Sheardown, H. Silicone Elastomers for Reduced Protein Adsorption. *Biomaterials* **2004**, *25*, 2273-2282.

(70) Bartzoka, V.; McDermott, M. R.; Brook, M. A. Protein-Silicone Interactions. *Adv. Mater.* **1999**, *11*, 257-259.

(71) Anderson, J. M.; Ziats, N. P.; Azeez, A.; Brunstedt, M. R.; Stack, S.; Bonfield, T. L. Protein Adsorption and Macrophage Activation on Polydimethylsiloxane and Silicone Rubber. *J. Biomater. Sci., Polym. Ed.* **1995**, *7*, 159-169.

(72) Zeplin, P. H.; Maksimovikj, N. C.; Jordan, M. C.; Nickel, J.; Lang, G.; Leimer, A. H.; Römer, L.; Scheibel, T. Spider Silk Coatings as a Bioshield to Reduce Peroprosthetic Fibrous Capsule Formation. *Adv. Funct. Mater.* **2014**, *24*, 2658-2666.

(73) Petrović, Z. S.; Ferguson, J. Polyurethane Elastomers. *Prog. Polym. Sci.* **1991**, *16*, 695-836.

(74) Boretos, J. W.; Pierce, W. S. Segmented Polyurethane: A New Elastomer for Biomedical Applications. *Science* **1967**, *158*, 1481-1482.

(75) Tieke, B., *Makromolekulare Chemie*. 2nd ed.; WILEY-VCH: Weinheim, 2005.

(76) Heath, D. E.; Cooper, S. L., Chapter I.2.2.A. Polyurethanes. In *Biomater. Sci.*, 3rd ed.; Rattner, B. D.; Hoffman, A. S.; Schoen, F. J.; Lemons, J. E., Eds. Elsevier Academic Press: San Diego, CA, 2013; pp 79-82.

(77) Akutsu, T.; Dreyer, B.; Kolff, W. J. Polyurethane Artificial Heart Valves in Animals. *J. Appl. Physiol.* **1959**, *14*, 1045-1048.

(78) Kolff, W. J.; Akutsu, T.; Dreyer, B.; Norton, H. Artificial Heart in the Chest and Use of Polyurethane for Making Hearts, Valves and Aortas. *Trans. - Am. Soc. Artif. Intern. Organs* **1959**, *5*, 298-299.

(79) Ratner, B. D. New Ideas in Biomaterials Science - A Path to Engineered Biomaterials. *J. Biomed. Mater. Res.* **1993**, *27*, 837-850.

(80) Legeais, J. M.; Werner, L. P.; Legeay, G.; Briat, B.; Renard, G. *In Vivo* Study of a Fluorocarbon Polymer-Coated Intraocular Lens in a Rabbit Model. *J. Cataract Refract. Surg.* **1998**, *24*, 371-379.

(81) Valdevit, A.; Türegün, M.; Kambic, H.; Siemionow, M.; Zins, J. Cranial Defect Repair Using e-PTFE: Part I. Evaluation of Bone Stiffness. *J. Biomed. Mater. Res.* **2000**, *53*, 62-66.

(82) Reid, G.; Busscher, H. J.; Sharma, S.; Mittelman, M. W.; McIntyre, S. Surface Properties of Catheters, Stents and Bacteria Associated with Urinary Tract Infections. *Surf. Sci. Rep.* **1995**, *21*, 251-273.

(83) Liu, F.; Grainger, D. W., Chapter I.2.2.C. Fluorinated Biomaterials. In *Biomater. Sci.*, 3rd ed.; Rattner, B. D.; Hoffman, A. S.; Schoen, F. J.; Lemons, J. E., Eds. Elsevier Academic Press: San Diego, CA, 2013; pp 92-103.

(84) Kesler, K. A.; Herring, M. B.; Arnold, M. P.; Glover, J. L.; Park, H. M.; Helmus, M. N.; Bendick, P. J. Enhanced Strength of Endothelial Attachment on Polyester Elastomer and Polytetrafluoroethylene Graft Surfaces with Fibronectin Substrate. *J. Vasc. Surg.* **1986**, *3*, 58-64.

(85) Kempczinski, R. F.; Rosenman, J. E.; Pearce, W. H.; Roedersheimer, L. R.; Berlatzky, Y.; Ramalanjaona, G. Endothelial Cell Seeding of a New PTFE Vascular Prothesis. *J. Vasc. Surg.* **1985**, *2*, 424-429.

(86) Dekker, A.; Reitsma, K.; Beugeling, T.; Bantjes, A.; Feijen, J.; Vanaken, W. G. Adhesion of Endothelial Cells and Adsorption of Serum Proteins on Gas Plasma-Treated Polytetrafluoroethylene. *Biomaterials* **1991**, *12*, 130-138.

(87) Schmidt, S.; Decleer, W.; Wagner, U.; Kindermann, D.; Pringle, K.; Krebs, D. An Approach to Fetal Surgery - Endoscopic Use of Excimer Laser. *Eur. J. Obstet. Gynecol. Reprod. Biol.* **1991**, *42*, S84-S86.

(88) van Kooten, T. G.; Schakenraad, J. M.; van der Mei, H. C.; Busscher, H. J. Influence of Substratum Wettability on the Strength of Adhesion of Human Fibroblasts. *Biomaterials* **1992**, *13*, 897-904.

(89) McClary, K. B.; Ugarova, T.; Grainger, D. W. Modulating Fibroblast Adhesion, Spreading, and Proliferation Using Self-Sssembled Monolayer Films of Alkylthiolates on Gold. *J. Biomed. Mater. Res.* **2000**, *50*, 428-439.

(90) Koenig, A. L.; Gambillara, V.; Grainger, D. W. Correlating Fibronectin Adsorption with Endothelial Cell Adhesion and Signaling on Polymer Substrates. *J. Biomed. Mater. Res., Part A* **2003**, *64A*, 20-37.

(91) Craig, C. L. Evolution of Arthropod Silks. *Annu. Rev. Entomol.* **1997**, *42*, 231-267.

(92) Sutherland, T. D.; Young, J. H.; Weisman, S.; Hayashi, C. Y.; Merritt, D. J. Insect Silk: One Name, Many Materials. *Annu. Rev. Entomol.* **2010**, *55*, 171-188.

(93) Vollrath, F.; Porter, D. Spider Silk as Archetypal Protein Elastomer. *Soft Matter* **2006**, *2*, 377-385.

(94) Lintz, E. S.; Scheibel, T. R. Dragline, Egg Stalk and Byssus: A Comparison of Outstanding Protein Fibers and Their Potential for Developing New Materials. *Adv. Funct. Mater.* **2013**, *23*, 4467-4482.

(95) Vollrath, F.; Knight, D. P. Liquid Crystalline Spinning of Spider Silk. *Nature* **2001**, *410*, 541-548.

(96) Stauffer, S. L.; Coguill, S. L.; Lewis, R. V. Comparison of Physical Properties of Three Silks from *Nephila clavipes* and *Araneus gemmoides*. *J. Arachnol.* **1994**, *22*, 5-11.

(97) Vollrath, F. Spider Webs and Silks. *Sci. Am.* **1992**, *266*, 70-76.

(98) Guerette, P. A.; Ginzinger, D. G.; Weber, B. H.; Gosline, J. M. Silk Properties Determined by Gland-Specific Expression of a Spider Fibroin Gene Family. *Science* **1996**, *272*, 112-115.

(99) Hardy, J. G.; Römer, L. M.; Scheibel, T. R. Polymeric Materials Based on Silk Proteins. *Polymer* **2008**, *49*, 4309-4327.

(100) Humenik, M.; Scheibel, T.; Smith, A. Spider Silk: Understanding the Structure-Function Relationship of a Natural Fiber. *Prog. Mol. Biol. Transl. Sci.* **2011**, *103*, 131-185.

(101) ap Rhisiart, A.; Vollrath, F. Design Features of the Orb Web of the Spider, *Araneus diadematus*. *Behavioral Ecology* **1994**, *5*, 280-287.

(102) Jackson, C.; O'Brien, J. P. Molecular Weight Distribution of *Nephila Clavipes* Dragline Silk. *Macromolecules* **1995**, *28*, 5975-5977.

(103) Candelas, G. C.; Cintron, J. A Spider Fibroin and Its Synthesis. *J. Exp. Zool.* **1981**, *216*, 1-6.

(104) Mello, C. M.; Senecal, K.; Yeung, B.; Vouros, P.; Kaplan, D., Initial Characterization of *Nephila clavipes* Dragline Protein. In *Silk Polymers*, Kaplan, D.; Adams, W. W.; Farmer, B.; Viney, C., Eds. American Chemical Society: Washington, DC, 1994; Vol. 544, pp 67-79.

(105) Gosline, J. M.; Guerette, P. A.; Ortlepp, C. S.; Savage, K. N. The Mechanical Design of Spider Silks: From Fibroin Sequence to Mechanical Function. *J. Exp. Biol.* **1999**, *202*, 3295-3303.

(106) Dunaway, D. L.; Thiel, B. L.; Viney, C. Tensile Mechanical Property Evaluation of Natural and Epoxide-Treated Silk Fibers. *J. Appl. Polym. Sci.* **1995**, *58*, 675-683.

(107) Viney, C. Natural Silks: Archetypal Supramolecular Assembly of Polymer Fibres. *Supramol. Sci.* **1997**, *4*, 75-81.

(108) Gosline, J. M.; Pollak, C. C.; Guerette, P. A.; Cheng, A.; Demont, M. E.; Denny, M. W. Elastomeric Network Models for the Frame and Viscid Silks from the Orb Web of the Spider *Araneus diadematus*. *Silk Polymers* **1994**, *544*, 328-341.

(109) Gosline, J.; Lillie, M.; Carrington, E.; Guerette, P.; Ortlepp, C.; Savage, K. Elastic Proteins: Biological Roles and Mechanical Properties. *Philos. Trans. R. Soc., B* **2002**, *357*, 121-132.

(110) Blackledge, T. A.; Summers, A. P.; Hayashi, C. Y. Gumfooted Lines in Black Widow Cobwebs and the Mechanical Properties of Spider Capture Silk. *Zoology* **2005**, *108*, 41-46.

(111) Tillinghast, E. K.; Townley, M. A., Silk Glands of Araneid Spiders - Selected Morphological and Physiological-Aspects. In *Silk Polymers*, Kaplan, D.; Adams, W. W.; Farmer, B.; Viney, C., Eds. American Chemical Society: Washington, DC, 1994; Vol. 544, pp 29-44.

(112) Riekel, C.; Vollrath, F. Spider Silk Fibre Extrusion: Combined Wide- and Small-Angle X-Ray Microdiffraction Experiments. *Int. J. Biol. Macromol.* **2001**, *29*, 203-210.

(113) Dicko, C.; Knight, D.; Kenney, J. M.; Vollrath, F. Secondary Structures and Conformational Changes in Flagelliform, Cylindrical, Major, and Minor Ampullate Silk Proteins. Temperature and Concentration Effects. *Biomacromolecules* **2004**, *5*, 2105-2115.

(114) Scheibel, T. Spider Silks: Recombinant Synthesis, Assembly, Spinning, and Engineering of Synthetic Proteins. *Microb. Cell Fact.* **2004**, *3*, 14.

(115) Winkler, S.; Kaplan, D. L. Molecular Biology of Spider Silk. *Rev. Mol. Biotechnol.* **2000**, *74*, 85-93.

(116) Becker, N.; Oroudjev, E.; Mutz, S.; Cleveland, J. P.; Hansma, P. K.; Hayashi, C. Y.; Makarov, D. E.; Hansma, H. G. Molecular Nanosprings in Spider Capture-Silk Threads. *Nat. Mater.* **2003**, *2*, 278-283.

(117) Bini, E.; Knight, D. P.; Kaplan, D. L. Mapping Domain Structures in Silks from Insects and Spiders Related to Protein Assembly. *J. Mol. Biol.* **2004**, *335*, 27-40.

(118) Kovoor, J.; Zylberberg, L. Fine Structural Aspects of Silk Secretion in a Spider (*Araneus diadematus*). I. Elaboration in the Pyriform Glands. *Tissue Cell* **1980**, *12*, 547-556.

(119) Kovoor, J.; Zylberberg, L. Fine Structural Aspects of Silk Secretion in a Spider. II. Conduction in the Pyriform Glands. *Tissue Cell* **1982**, *14*, 519-530.

(120) Vollrath, F.; Tillinghast, E. K. Glycoprotein Glue Beneath a Spider Web's Aqueous Coat. *Naturwissenschaften* **1991**, *78*, 557-559.

(121) Vollrath, F. Spider Silk: Thousands of Nano-Filaments and Dollops of Sticky Glue. *Curr. Biol.* **2006**, *16*, R925-R927.

(122) Hu, X. Y.; Yuan, J.; Wang, X. D.; Vasanthavada, K.; Falick, A. M.; Jones, P. R.; La Mattina, C.; Vierra, C. A. Analysis of Aqueous Glue Coating Proteins on the Silk Fibers of the Cob Weaver, *Latrodectus hesperus*. *Biochemistry* **2007**, *46*, 3294-3303.

(123) Schildknecht, H.; Kunzelmann, P.; Krauß, D.; Kuhn, C. Über die Chemie der Spinnwebe, I - Arthropodenabwehrstoffe, LVII. *Naturwissenschaften* **1972**, *59*, 98-99.

(124) Townley, M. A.; Bernstein, D. T.; Gallagher, K. S.; Tillinghast, E. K. Comparative Study of Orb Web Hygroscopicity and Adhesive Spiral Composition in Three Araneid Spiders. *J. Exp. Zool.* **1991**, *259*, 154-165.

(125) Vollrath, F.; Fairbrother, W. J.; Williams, R. J. P.; Tillinghast, E. K.; Bernstein, D. T.; Gallagher, K. S.; Townley, M. A. Compounds in the Droplets of the Orb Spiders Viscid Spiral. *Nature* **1990**, *345*, 526-528.

(126) Edmonds, D. T.; Vollrath, F. The Contribution of Atmospheric Water-Vapor to the Formation and Efficiency of a Spiders Capture Web. *Proc. R. Soc. Biol. Sci. Ser. B* **1992**, *248*, 145-148.

(127) Vollrath, F.; Edmonds, D. T. Modulation of the Mechanical Properties of Spider Silk by Coating with Water. *Nature* **1989**, *340*, 305-307.

(128) Rising, A.; Hjalm, G.; Engstrom, W.; Johansson, J. N-Terminal Nonrepetitive Domain Common to Dragline, Flagelliform, and Cylindriform Spider Silk Proteins. *Biomacromolecules* **2006**, *7*, 3120-3124.

(129) Bittencourt, D.; Souto, B. M.; Verza, N. C.; Vineck, F.; Dittmar, K.; Silva, P. I.; Andrade, A. C.; da Silva, F. R.; Lewis, R. V.; Rech, E. L. Spidroins from the Brazilian Spider *Nephilengys cruentata* (Araneae: Nephilidae). *Comp. Biochem. Physiol., Part B: Biochem. Mol. Biol.* **2007**, *147*, 597-606.

(130) Garb, J. E.; Hayashi, C. Y. Modular Evolution of Egg Case Silk Genes across Orb-Weaving Spider Superfamilies. *Proc. Natl. Acad. Sci. U. S. A.* **2005**, *102*, 11379-11384.

(131) Hu, X.; Vasanthavada, K.; Kohler, K.; McNary, S.; Moore, A. M. F.; Vierra, C. A. Molecular Mechanisms of Spider Silk. *Cell. Mol. Life Sci.* **2006**, *63*, 1986-1999.

(132) Hu, X. Y.; Kohler, K.; Falick, A. M.; Moore, A. M. F.; Jones, P. R.; Sparkman, O. D.; Vierra, C. Egg Case Protein-1 - A New Class of Silk Proteins with Fibroin-Like Properties from the Spider *Latrodectus hesperus*. *J. Biol. Chem.* **2005**, *280*, 21220-21230.

(133) Hu, X. Y.; Kohler, K.; Falick, A. M.; Moore, A. M. F.; Jones, P. R.; Vierra, C. Spider Egg Case Core Fibers: Trimeric Complexes Assembled from TuSp1, ECP-1, and ECP-2. *Biochemistry* **2006**, *45*, 3506-3516.

(134) Hu, X. Y.; Lawrence, B.; Kohler, K.; Falick, A. M.; Moore, A. M. F.; McMullen, E.; Jones, P. R.; Vierra, C. Araneoid Egg Case Silk: A Fibroin with Novel Ensemble Repeat Units from the Black Widow Spider, *Latrodectus hesperus*. *Biochemistry* **2005**, *44*, 10020-10027.

(135) Huang, W.; Lin, Z.; Sin, Y. M.; Li, D.; Gong, Z.; Yang, D. Characterization and Expression of a cDNA Encoding a Tubuliform Silk Protein of the Golden Web Spider *Nephila antipodiana*. *Biochimie* **2006**, *88*, 849-858.

(136) Barghout, J. Y. J.; Thiel, B. L.; Viney, C. Spider (*Araneus diadematus*) Cocoon Silk: A Case of Non-Periodic Lattice Crystals with a Twist? *Int. J. Biol. Macromol.* **1999**, *24*, 211-217.

(137) Hakimi, O.; Knight, D. P.; Knight, M. M.; Grahn, M. F.; Vadgama, P. Ultrastructure of Insect and Spider Cocoon Silks. *Biomacromolecules* **2006**, *7*, 2901-2908.

(138) Hayashi, C. Y.; Blackledge, T. A.; Lewis, R. V. Molecular and Mechanical Characterization of Aciniform Silk: Uniformity of Iterated Sequence Modules in a Novel Member of the Spider Silk Fibroin Gene Family. *Mol. Biol. Evol.* **2004**, *21*, 1950-1959.

(139) Vasanthavada, K.; Hu, X.; Falick, A. M.; La Mattina, C.; Moore, A. M. F.; Jones, P. R.; Yee, R.; Reza, R.; Tuton, T.; Vierra, C. Aciniform Spidroin, a Constituent of Egg Case Sacs and Wrapping Silk Fibers from the Black Widow Spider *Latrodectus hesperus*. *J. Biol. Chem.* **2007**, *282*, 35088-35097.

(140) La Mattina, C.; Reza, R.; Hu, X.; Falick, A. M.; Vasanthavada, K.; McNary, S.; Yee, R.; Vierra, C. A. Spider Minor Ampullate Silk Proteins Are Constituents of Prey Wrapping Silk in the Cob Weaver *Latrodectus hesperus*. *Biochemistry* **2008**, *47*, 4692-700.

(141) Gührs, K.-H.; Weisshart, K.; Grosse, F. Lessons from Nature – Protein Fibers. *Rev. Mol. Biotechnol.* **2000**, *74*, 121-134.

(142) Vollrath, F. Biology of Spider Silk. *Int. J. Biol. Macromol.* **1999**, *24*, 81-88.

(143) Smith, A.; Scheibel, T., Hierarchical Protein Assemblies as a Basis for Materials. In *Materials Design Inspired by Nature: Function Through Inner Architecture*, Fratzl, P.; Dunlop, J. W. C.; Weinkamer, R., Eds. The Royal Society of Chemistry: Cambridge, 2013; Vol. 4, pp 256-281.

(144) Römer, L.; Scheibel, T. The Elaborate Structure of Spider Silk – Structure and Function of a Natural High Performance Fiber. *Prion* **2008**, *2*, 154-161.

(145) Eisoldt, L.; Thamm, C.; Scheibel, T. Review the Role of Terminal Domains During Storage and Assembly of Spider Silk Proteins. *Biopolymers* **2012**, *97*, 355-361.

(146) Cranford, S. W.; Tarakanova, A.; Pugno, N. M.; Buehler, M. J. Nonlinear Material Behaviour of Spider Silk Yields Robust Webs. *Nature* **2012**, *482*, 72-76.

(147) Elices, M.; Plaza, G. R.; Pérez-Rigueiro, J.; Guinea, G. V. The Hidden Link Between Supercontraction and Mechanical Behavior of Spider Silks. *J. Mech. Behav. Biomed. Mater.* **2011**, *4*, 658-669.

(148) Liu, Y.; Shao, Z. Z.; Vollrath, F. Relationships between Supercontraction and Mechanical Properties of Spider Silk. *Nat. Mater.* **2005**, *4*, 901-905.

(149) Nova, A.; Keten, S.; Pugno, N. M.; Redaelli, A.; Buehler, M. J. Molecular and Nanostructural Mechanisms of Deformation, Strength and Toughness of Spider Silk Fibrils. *Nano Lett.* **2010**, *10*, 2626-2634.

(150) Frische, S.; Maunsbach, A. B.; Vollrath, F. Elongate Cavities and Skin-Core Structure in Nephila Spider Silk Observed by Electron Microscopy. *J. Microsc. (Oxf.)* **1998**, *189*, 64-70.

(151) Augsten, K.; Muhlig, P.; Herrmann, C. Glycoproteins and Skin-Core Structure in *Nephila clavipes* Spider Silk Observed by Light and Electron Microscopy. *Scanning* **2000**, *22*, 12-15.

(152) Papadopoulos, P.; Sölter, J.; Kremer, F. Hierarchies in the Structural Organization of Spider Silk - A Quantitative Model. *Colloid Polym. Sci.* **2009**, *287*, 231-236.

(153) Sponner, A.; Vater, W.; Monajembashi, S.; Unger, E.; Grosse, F.; Weisshart, K. Composition and Hierarchical Organisation of a Spider Silk. *PLoS One* **2007**, *2*, e998.

(154) Liu, Y.; Sponner, A.; Porter, D.; Vollrath, F. Proline and Processing of Spider Silks. *Biomacromolecules* **2008**, *9*, 116-121.

(155) Ayoub, N. A.; Garb, J. E.; Tinghitella, R. M.; Collin, M. A.; Hayashi, C. Y. Blueprint for a High-Performance Biomaterial: Full-Length Spider Dragline Silk Genes. *PLoS One* **2007**, *2*, e514.

(156) van Beek, J. D.; Hess, S.; Vollrath, F.; Meier, B. H. The Molecular Structure of Spider Dragline Silk: Folding and Orientation of the Protein Backbone. *Proc. Natl. Acad. Sci. U. S. A.* **2002**, *99*, 10266-10271.

(157) Grubb, D. T.; Jelinski, L. W. Fiber Morphology of Spider Silk: The Effects of Tensile Deformation. *Macromolecules* **1997**, *30*, 2860-2867.

(158) Yang, Z.; Grubb, D. T.; Jelinski, L. W. Small-Angle X-Ray Scattering of Spider Dragline Silk. *Macromolecules* **1997**, *30*, 8254-8261.

(159) Kümmerlen, J.; van Beek, J. D.; Vollrath, F.; Meier, B. H. Local Structure in Spider Dragline Silk Investigated by Two-Dimensional Spin-Diffusion Nuclear Magnetic Resonance. *Macromolecules* **1996**, *29*, 2920-2928.

(160) Simmons, A. H.; Michal, C. A.; Jelinski, L. W. Molecular Orientation and Two-Component Nature of the Crystalline Fraction of Spider Dragline Silk. *Science* **1996**, *271*, 84-87.

(161) Riekel, C.; Müller, M.; Vollrath, F. *In Situ* X-Ray Diffraction During Forced Silking of Spider Silk. *Macromolecules* **1999**, *32*, 4464-4466.

(162) Wagner, J. A.; Patil, S. P.; Greving, I.; Lämmel, M.; Gkagkas, K.; Seydel, T.; Müller, M.; Markert, B.; Gräter, F. Stress-Induced Long-Range Ordering in Spider Silk. *Sci. Rep.* **2017**, *7*, 15273.

(163) Fu, C.; Shao, Z.; Vollrath, F. Animal Silks: Their Structures, Properties and Artificial Production. *Chem. Commun.* **2009**, *0*, 6515-6529.

(164) Lefèvre, T.; Rousseau, M.-E.; Pézolet, M. Protein Secondary Structure and Orientation in Silk as Revealed by Raman Spectromicroscopy. *Biophys. J.* **2007**, *92*, 2885-2895.

(165) Paquet-Mercier, F.; Lefèvre, T.; Auger, M.; Pézolet, M. Evidence by Infrared Spectroscopy of the Presence of Two Types of β-Sheets in Major Ampullate Spider Silk and Silkworm Silk. *Soft Matter* **2013**, *9*, 208-215.

(166) Keerl, D.; Scheibel, T. Characterization of Natural and Biomimetic Spider Silk Fibers. *Bioinspired, Biomimetic Nanobiomater.* **2012**, *1*, 83-94.

(167) Ene, R.; Papadopoulos, P.; Kremer, F. Quantitative Analysis of Infrared Absorption Coefficient of Spider Silk Fibers. *Vib. Spectrosc.* **2011**, *57*, 207-212.

(168) Anton, M. A.; Kossack, W.; Gutsche, C.; Figuli, R.; Papadopoulos, P.; Ebad-Allah, J.; Kuntscher, C.; Kremer, F. Pressure-Dependent FTIR-Spectroscopy on the Counterbalance between External and Internal Constraints in Spider Silk of *Nephila pilipes*. *Macromolecules* **2013**, *46*, 4919-4923.

(169) Thiel, B. L.; Viney, C. *β*-Sheets and Spider Silk. *Science* **1996**, *273*, 1480-1481.

(170) Fahnestock, S. R.; Irwin, S. L. Synthetic Spider Dragline Silk Proteins and their Production in *Escherichia coli*. *Appl. Microbiol. Biotechnol.* **1997**, *47*, 23-32.

(171) Garb, J. E.; Ayoub, N. A.; Hayashi, C. Y. Untangling Spider Silk Evolution with Spidroin Terminal Domains. *BMC Evol. Biol.* **2010**, *10:243*, 1-16.

(172) Eisoldt, L.; Smith, A.; Scheibel, T. Decoding the Secrets of Spider Silk. *Mater. Today* **2011**, *14*, 80-86.

(173) Bauer, J.; Scheibel, T. Dimerization of the Conserved N-Terminal Domain of a Spider Silk Protein Controls the Self-Assembly of the Repetitive Core Domain. *Biomacromolecules* **2017**, *18*, 2521-2528.

(174) Motriuk-Smith, D.; Smith, A.; Hayashi, C. Y.; Lewis, R. V. Analysis of the Conserved N-terminal Domains in Major Ampullate Spider Silk Proteins. *Biomacromolecules* **2005**, *6*, 3152-3159.

(175) Askarieh, G.; Hedhammar, M.; Nordling, K.; Saenz, A.; Casals, C.; Rising, A.; Johansson, J.; Knight, S. D. Self-Assembly of Spider Silk Proteins is Controlled by a pH-Sensitive Relay. *Nature* **2010**, *465*, 236-238.

(176) Hagn, F.; Eisoldt, L.; Hardy, J. G.; Vendrely, C.; Coles, M.; Scheibel, T.; Kessler, H. A Conserved Spider Silk Domain Acts as a Molecular Switch that Controls Fibre Assembly. *Nature* **2010**, *465*, 239-242.

(177) Hagn, F.; Thamm, C.; Scheibel, T.; Kessler, H. pH-Dependent Dimerization and Salt-Dependent Stabilization of the N-terminal Domain of Spider Dragline Silk-Implications for Fiber Formation. *Angew. Chem., Int. Ed.* **2011**, *50*, 310-313.

(178) Fox, L. R. Cannibalism in Natural-Populations. *Annu. Rev. Ecol. Syst.* **1975**, *6*, 87-106.

(179) Madsen, B.; Shao, Z. Z.; Vollrath, F. Variability in the Mechanical Properties of Spider Silks on Three Levels: Interspecific, Intraspecific and Intraindividual. *Int. J. Biol. Macromol.* **1999**, *24*, 301-306.

(180) Guehrs, K.-H.; Schlott, B.; Grosse, F.; Weisshart, K. Environmental Conditions Impinge on Dragline Silk Protein Composition. *Insect Mol. Biol.* **2008**, *17*, 553-564.

(181) Tokareva, O.; Michalczechen-Lacerda, V. A.; Rech, E. L.; Kaplan, D. L. Recombinant DNA Production of Spider Silk Proteins. *Microb. Biotechnol.* **2013**, *6*, 651-663.

(182) Kaplan, D. L.; Scheibel, T., Recombinant Silk Production in Bacteria In *Reference Module in Materials Science and Materials Engineering*, Elsevier Inc.: Amsterdam, 2016; pp 8615-8618.

(183) Heidebrecht, A.; Scheibel, T. Recombinant Production of Spider Silk Proteins. *Adv. Appl. Microbiol.* **2013**, *82*, 115-153.

(184) Huemmerich, D.; Helsen, C. W.; Quedzuweit, S.; Oschmann, J.; Rudolph, R.; Scheibel, T. Primary Structure Elements of Spider Dragline Silks and their Contribution to Protein Solubility. *Biochemistry* **2004**, *43*, 13604-13612.

(185) Vendrely, C.; Scheibel, T. Biotechnological Production of Spider-Silk Proteins Enables New Applications. *Macromol. Biosci.* **2007**, *7*, 401-409.

(186) Doblhofer, E.; Scheibel, T. Engineering of Recombinant Spider Silk Proteins Allows Defined Uptake and Release of Substances. *J. Pharm. Sci.* **2015**, *104*, 988-994.

(187) Binder, K. Phase-Transitions in Polymer Blends and Block-Copolymer Melts: Some Recent Developments. *Adv. Polym. Sci.* **1994**, *112*, 181-299.

(188) Darling, S. B. Directing the Self-Assembly of Block Copolymers. *Prog. Polym. Sci.* **2007**, *32*, 1152-1204.

(189) Förster, S.; Plantenberg, T. From Self-Organizing Polymers to Nanohybrid and Biomaterials. *Angew. Chem.* **2002**, *41*, 689-714.

(190) Kita-Tokarczyk, K.; Junginger, M.; Belegrinou, S.; Taubert, A. Amphiphilic Polymers at Interfaces. *Adv. Polym. Sci.* **2011**, *242*, 151-201.

(191) Leibler, L. Theory of Microphase Separation in Block Co-Polymers. *Macromolecules* **1980**, *13*, 1602-1617.

(192) Bates, F. S. Polymer-Polymer Phase-Behavior. *Science* **1991**, *251*, 898-905.

(193) Bates, F. S.; Fredrickson, G. H. Block Copolymer Thermodynamics - Theory and Experiment. *Annu. Rev. Phys. Chem.* **1990**, *41*, 525-557.

(194) Fredrickson, G. H.; Bates, F. S. Dynamics of Block Copolymers: Theory and Experiment. *Annu. Rev. Mater. Sci.* **1996**, *26*, 501-550.

(195) Matsen, M. W.; Bates, F. S. Unifying Weak- and Strong-Segregation Block Copolymer Theories. *Macromolecules* **1996**, *29*, 1091-1098.

(196) Mai, Y.; Eisenberg, A. Self-Assembly of Block Copolymers. *Chem. Soc. Rev.* **2012**, *41*, 5969-5985.

(197) Tawfick, S.; De Volder, M.; Copic, D.; Park, S. J.; Oliver, C. R.; Polsen, E. S.; Roberts, M. J.; Hart, A. J. Engineering of Micro- and Nanostructured Surfaces with Anisotropic Geometries and Properties. *Adv. Mater.* **2012**, *24*, 1628-1674.

(198) Krausch, G.; Magerle, R. Nanostructured Thin Films via Self-Assembly of Block Copolymers. *Adv. Mater.* **2002**, *14*, 1579-1583.

(199) Fasolka, M. J.; Mayes, A. M. Block Copolymer Thin Films: Physics and Applications. *Annu. Rev. Mater. Res.* **2001**, *31*, 323-355.

(200) Segalman, R. A. Patterning With Block Copolymer Thin Films. *Mater. Sci. Eng., R* **2005**, *48*, 191-226.

(201) Stein, G. E.; Kramer, E. J.; Li, X. F.; Wang, J. Layering Transitions in Thin Films of Spherical-Domain Block Copolymers. *Macromolecules* **2007**, *40*, 2453-2460.

(202) Karim, A.; Singh, N.; Sikka, M.; Bates, F. S.; Dozier, W. D.; Felcher, G. P. Ordering in Asymmetric Poly (Ethylene-Propylene)-Poly (Ethylethylene) Diblock Copolymer Thin-Films. *J. Chem. Phys.* **1994**, *100*, 1620-1629.

(203) Radzilowski, L. H.; Carvalho, B. L.; Thomas, E. L. Structure of Minimum Thickness and Terraced Free-Standing Films of Block Copolymers. *J. Polym. Sci., Part B: Polym. Phys.* **1996**, *34*, 3081-3093.

(204) Konrad, M.; Knoll, A.; Krausch, G.; Magerle, R. Volume Imaging of an Ultrathin SBS Triblock Copolymer Film. *Macromolecules* **2000**, *33*, 5518-5523.

(205) Harrison, C.; Park, M.; Chaikin, P.; Register, R. A.; Adamson, D. H.; Yao, N. Depth Profiling Block Copolymer Microdomains. *Macromolecules* **1998**, *31*, 2185-2189.

(206) Knoll, A.; Horvat, A.; Lyakhova, K. S.; Krausch, G.; Sevink, G. J. A.; Zvelindovsky, A. V.; Magerle, R. Phase Behavior in Thin Films of Cylinder-Forming Block Copolymers. *Phys. Rev. Lett.* **2002**, *89*, 035501.

(207) Knoll, A.; Magerle, R.; Krausch, G. Phase Behavior in Thin Films of Cylinder-Forming ABA Block Copolymers: Experiments. *J. Chem. Phys.* **2004**, *120*, 1105-1116.

(208) Kim, G.; Libera, M. Morphological Development in Solvent-Cast Polystyrene-Polybutadiene-Polystyrene (SBS) Triblock Copolymer Thin Films. *Macromolecules* **1998**, *31*, 2569-2577.

(209) Eisoldt, L.; Hardy, J. G.; Heim, M.; Scheibel, T. R. The Role of Salt and Shear on the Storage and Assembly of Spider Silk Proteins. *J. Struct. Biol.* **2010**, *170*, 413-419.

(210) Heidebrecht, A.; Eisoldt, L.; Diehl, J.; Schmidt, A.; Geffers, M.; Lang, G.; Scheibel, T. Biomimetic Fibers Made of Recombinant Spidroins with the Same Toughness as Natural Spider Silk. *Adv. Mater.* **2015**, *27*, 2189-2194.

(211) Rammensee, S.; Slotta, U.; Scheibel, T.; Bausch, A. R. Assembly Mechanism of Recombinant Spider Silk Proteins. *Proc. Natl. Acad. Sci. U. S. A.* **2008**, *105*, 6590-6595.

(212) Hermanson, K. D.; Huemmerich, D.; Scheibel, T.; Bausch, A. R. Engineered Microcapsules Fabricated from Reconstituted Spider Silk. *Adv. Mater.* **2007**, *19*, 1810-1815.

(213) Hu, X.; Lu, Q.; Kaplan, D. L.; Cebe, P. Microphase Separation Controlled *β*-Sheet Crystallization Kinetics in Fibrous Proteins. *Macromolecules* **2009**, *42*, 2079-2087.

(214) Gebhardt, R.; Vendrely, C.; Burghammer, M.; Riekel, C. Characterization of the Boundary Zone of a Cast Protein Drop: Fibroin *β*-Sheet and Nanofibril Formation. *Langmuir* **2009**, *25*, 6307-6311.

(215) Rathore, O.; Sogah, D. Y. Nanostructure Formation Through *β*-Sheet Self-Assembly in Silk-Based Materials. *Macromolecules* **2001**, *34*, 1477-1486.

(216) Rabotyagova, O. S.; Cebe, P.; Kaplan, D. L. Protein-Based Block Copolymers. *Biomacromolecules* **2011**, *12*, 269-289.

(217) Muller, W. S.; Samuelson, L. A.; Fossey, S. A.; Kaplan, D. L. Formation and Characterization of Langmuir Silk Films. *Langmuir* **1993**, *9*, 1857-1861.

(218) Valluzi, R.; Gido, S. P.; Muller, W.; Kaplan, D. L. Orientation of Silk III at the Air-Water Interface. *Int. J. Biol. Macromol.* **1999**, *24*, 237-242.

(219) Valluzi, R.; Gido, S. P.; Zhang, W.; Muller, W. S.; Kaplan, D. L. Trigonal Crystal Structure of *Bombyx mori* Silk Incorporating a Threefold Helical Chain Conformation Found at the Air-Water Interface. *Macromolecules* **1996**, *29*, 8606-8614.

(220) Rabotyagova, O. S.; Cebe, P.; Kaplan, D. L. Self-Assembly of Genetically Engineered Spider Silk Block Copolymers. *Biomacromolecules* **2009**, *10*, 229-236.

(221) Krishnaji, S. T.; Huang, W.; Rabotyagova, O.; Kharlampieva, E.; Choi, I.; Tsukruk, V. V.; Naik, R.; Cebe, P.; Kaplan, D. L. Thin Film Assembly of Spider-like Block Copolymers. *Langmuir* **2010**, *27*, 1000-1008.

(222) Krishnaji, S. K.; Huang, W.; Cebe, P.; Kaplan, D. L. Influence of Solution Parameters on Phase Diagram of Recombinant Spider Silk-Like Block Copolymers. *Macromol. Chem. Phys.* **2014**, *215*, 1230-1238.

(223) Krishnaji, S. T.; Bratzel, G.; Kinahan, M. E.; Kluge, J. A.; Staii, C.; Wong, J. Y.; Buehler, M. J.; Kaplan, D. L. Sequence-Structure-Property Relationships of Recombinant Spider Silk Proteins: Integration of Biopolymer Design, Processing and Modeling. *Adv. Funct. Mater.* **2013**, *23*, 241-253.

(224) Tokareva, O. S.; Lin, S.; Jacobsen, M. M.; Huang, W.; Rizzo, D.; Li, D.; Simon, M.; Staii, C.; Cebe, P.; Wong, J. Y.; Buehler, M. J.; Kaplan, D. L. Effect of Sequence Features on Assembly of Spider Silk Block Copolymers. *J. Struct. Biol.* **2014**, *186*, 412-419.

(225) Wohlrab, S.; Spieß, K.; Scheibel, T. Varying Surface Hydrophobicities of Coatings Made of Recombinant Spider Silk Proteins. *J. Mater. Chem.* **2012**, *22*, 22050-22054.

(226) Tokareva, O.; Jacobsen, M.; Buehler, M.; Wong, J.; Kaplan, D. L. Structure-Function-Property-Design Interplay in Biopolymers: Spider Silk. *Acta Biomater.* **2014**, *10*, 1612-1626.

(227) Altman, G. H.; Diaz, F.; Jakuba, C.; Calabro, T.; Horan, R. L.; Chen, J.; Lu, H.; Richmond, J.; Kaplan, D. L. Silk-Based Biomaterials. *Biomaterials* **2003**, *24*, 401-416.

(228) Pratt, A. E., *Two years among New Guinea cannibals*. J. B. Lippincott Company: Philadelphia, 1906.

(229) Newman, J.; Newman, C. Oh What a Tangled Web: The Medicinal Uses of Spider Silk. *Int. J. Dermatol.* **1995**, *34*, 290-292.

(230) Gerritsen, V. B. The Tiptoe of an Airbus. *Protein Spotlight* **2002**, *24*, 1-2.

(231) Hakimi, O.; Knight, D. P.; Vollrath, F.; Vadgama, P. Spider and Mulberry Silkworm Silks as Compatible Biomaterials. *Composites, Part B* **2007**, *38*, 324-337.

(232) Aigner, T. B.; DeSimone, E.; Scheibel, T. Biomedical Applications of Recombinant Silk-Based Materials. *Adv. Mater.* **2018**, *30*, 1704636.

(233) Zeplin, P. H.; Berninger, A. K.; Maksimovikj, N. C.; van Gelder, P.; Scheibel, T.; Walles, H. Verbesserung der Biokompatibilitat von Silikonimplantaten durch Spinnenseidenbeschichtung: Immunhistochemische Untersuchungen zum Einfluss auf die Kapselbildung. *Handchir. Mikrochir. Plast. Chir.* **2014**, *46*, 336-341.

(234) Müller-Herrmann, S.; Scheibel, T. Enzymatic Degradation of Films, Particles, and Nonwoven Meshes Made of a Recombinant Spider Silk Protein. *ACS Biomater. Sci. Eng.* **2015**, *1*, 247-259.

(235) Schacht, K.; Vogt, J.; Scheibel, T. Foams Made of Engineered Recombinant Spider Silk Proteins as 3D Scaffolds for Cell Growth. *ACS Biomater. Sci. Eng.* **2016**, *2*, 517-525.

(236) Wohlrab, S.; Müller, S.; Schmidt, A.; Neubauer, S.; Kessler, H.; Leal-Egaña, A.; Scheibel, T. Cell Adhesion and Proliferation on RGD-Modified Recombinant Spider Silk Proteins. *Biomaterials* **2012**, *33*, 6650-6659.

(237) Leal-Egaña, A.; Lang, G.; Mauerer, C.; Wickinghoff, J.; Weber, M.; Geimer, S.; Scheibel, T. Interactions of Fibroblasts with Different Morphologies Made of an Engineered Spider Silk Protein. *Adv. Eng. Mater.* **2012**, *14*, B67-B75.

(238) Kuhbier, J. W.; Coger, V.; Mueller, J.; Liebsch, C.; Schlottmann, F.; Bucan, V.; Vogt, P. M.; Strauss, S. Influence of Direct or Indirect Contact for the Cytotoxicity and Blood Compatibility of Spider Silk. *J. Mater. Sci.: Mater. Med.* **2017**, *28*, 127.

(239) Schierling, M. B.; Doblhofer, E.; Scheibel, T. Cellular Uptake of Drug Loaded Spider Silk Particles. *Biomater. Sci.* **2016**, *4*, 1515-1523.

(240) Leal-Egaña, A.; Scheibel, T. Silk-Based Materials for Biomedical Applications. *Biotechnol. Appl. Biochem.* **2010**, *55*, 155-167.

(241) Kumari, S.; Bargel, H.; Anby, M. U.; Lafargue, D.; Scheibel, T. Recombinant Spider Silk Hydrogels for Sustained Release of Biologicals. *ACS Biomater. Sci. Eng.* **2018**, *4*, 1750-1759.

(242) Schacht, K.; Scheibel, T. Controlled Hydrogel Formation of a Recombinant Spider Silk Protein. *Biomacromolecules* **2011**, *12*, 2488-2495.

(243) Petzold, J.; Aigner, T. B.; Touska, F.; Zimmermann, K.; Scheibel, T.; Engel, F. B. Surface Features of Recombinant Spider Silk Protein eADF4(κ16)-Made Materials are Well-Suited for Cardiac Tissue Engineering. *Adv. Funct. Mater.* **2017**, *27*, 1701427.

(244) Widhe, M.; Bysell, H.; Nystedt, S.; Schenning, I.; Malmsten, M.; Johansson, J.; Rising, A.; Hedhammar, M. Recombinant Spider Silk as Matrices for Cell Culture. *Biomaterials* **2010**, *31*, 9575-9585.

(245) Widhe, M.; Johansson, U.; Hillerdahl, C.-O.; Hedhammar, M. Recombinant Spider Silk with Cell Binding Motifs for Specific Adherence of Cells. *Biomaterials* **2013**, *34*, 8223-8234.

(246) Bini, E.; Foo, C. W. P.; Huang, J.; Karageorgiou, V.; Kitchel, B.; Kaplan, D. L. RGD-Functionalized Bioengineered Spider Dragline Silk Biomaterial. *Biomacromolecules* **2006**, *7*, 3139-3145.

(247) Tasiopoulos, C. P.; Widhe, M.; Hedhammar, M. Recombinant Spider Silk Functionalized with a Motif from Fibronectin Mediates Cell Adhesion and Growth on Polymeric Substrates by Entrapping Cells during Self-Assembly. *ACS Appl. Mater. Interfaces* **2018**, *10*, 14531-14539.

(248) Bauer, F.; Wohlrab, S.; Scheibel, T. Controllable Cell Adhesion, Growth and Orientation on Layered Silk Protein Films. *Biomater. Sci.* **2013**, *1*, 1244-1249.

(249) Tien, L. W.; Gil, E. S.; Park, S.-H.; Mandal, B. B.; Kaplan, D. L. Patterned Silk Film Scaffolds for Aligned Lamellar Bone Tissue Engineering. *Macromol. Biosci.* **2012**, *12*, 1671-1679.

(250) Foo, C. W. P.; Patwardhan, S. V.; Belton, D. J.; Kitchel, B.; Anastasiades, D.; Huang, J.; Naik, R. R.; Perry, C. C.; Kaplan, D. L. Novel Nanocomposites from Spider Silk-Silica Fusion (Chimeric) Proteins. *Proc. Natl. Acad. Sci. U. S. A.* **2006**, *103*, 9428-9433.

(251) Zhang, K.; Mo, X.; Huang, C.; He, C.; Wang, H. Electrospun Scaffolds from Silk Fibroin and their Cellular Compatibility. *J. Biomed. Mater. Res., Part A* **2010**, *93A*, 976-983.

(252) Zhang, X.; Baughman, C. B.; Kaplan, D. L. *In Vitro* Evaluation of Electrospun Silk Fibroin Scaffolds for Vascular Cell Growth. *Biomaterials* **2008**, *29*, 2217-2227.

(253) Hardy, J. G.; Pfaff, A.; Leal-Egaña, A.; Müller, A. H. E.; Scheibel, T. R. Glycopolymer Functionalization of Engineered Spider Silk Protein-based Materials for Improved Cell Adhesion. *Macromol. Biosci.* **2014**, *14*, 936-942.

(254) Sanford, K.; Kumar, M. New Proteins in a Materials World. *Curr. Opin. Biotechnol.* **2005**, *16*, 416-421.

(255) Murakami, T.; Kuroda, S.; Osawa, Z. Dynamics of Polymeric Solid Surfaces Treated with Oxygen Plasma: Effect of Aging Media after Plasma Treatment. *J. Colloid Interface Sci.* **1998**, *202*, 37-44.

(256) Walther, F.; Davydovskaya, P.; Zürcher, S.; Kaiser, M.; Herberg, H.; Gigler, A. M.; Stark, R. W. Stability of the Hydrophilic Behavior of Oxygen Plasma Activated SU-8. *J. Micromech. Microeng.* **2007**, *17*, 524-531.

(257) Jokinen, V.; Suvanto, P.; Franssila, S. Oxygen and Nitrogen Plasma Hydrophilization and Hydrophobic Recovery of Polymers. *Biomicrofluidics* **2012**, *6*, 016501.

(258) Khorasani, M. T.; MoemenBellah, S.; Mirzadeh, H.; Sadatnia, B. Effect of Surface Charge and Hydrophobicity of Polyurethanes and Silicone Rubbers on L929 Cells Response. *Colloids Surf., B* **2006**, *51*, 112-119.

(259) Numata, K.; Cebe, P.; Kaplan, D. L. Mechanism of Enzymatic Degradation of Beta-Sheet Crystals. *Biomaterials* **2010**, *31*, 2926-2933.

(260) Lee, S. Y.; Amsden, J. J.; Boriskina, S. V.; Gopinath, A.; Mitropolous, A.; Kaplan, D. L.; Omenetto, F. G.; Dal Negro, L. Spatial and Spectral Detection of Protein Monolayers with Deterministic Aperiodic Arrays of Metal Nanoparticles. *Proc. Natl. Acad. Sci. U. S. A.* **2010**, *107*, 12086-12090.

(261) Hu, X.; Kaplan, D.; Cebe, P. Determining Beta-Sheet Crystallinity in Fibrous Proteins by Thermal Analysis and Infrared Spectroscopy. *Macromolecules* **2006**, *39*, 6161-6170.

(262) Hu, X.; Kaplan, D.; Cebe, P. Dynamic Protein-Water Relationships during β-Sheet Formation. *Macromolecules* **2008**, *41*, 3939-3948.

(263) Goormaghtigh, E.; Cabiaux, V.; Ruysschaert, J. M. Secondary Structure and Dosage of Soluble and Membrane Proteins by Attenuated Total Reflection Fourier-Transform Infrared Spectroscopy on Hydrated Films. *Eur. J. Biochem.* **1990**, *193*, 409-420.

(264) Barth, A.; Zscherp, C. What vibrations tell us about proteins. *Q. Rev. Biophys.* **2002**, *35*, 369-430.

(265) Spiess, K.; Wohlrab, S.; Scheibel, T. Structural Characterization and Functionalization of Engineered Spider Silk Films. *Soft Matter* **2010**, *6*, 4168-4174.

(266) Sweeney, P. J.; Walker, J. M., Pronase (EC 3.4.24.4). In *Enzymes of Molecular Biology*, Burrell, M. M., Ed. Humana Press: Totowa, N.J., 1993; pp 271-276.

(267) Nomoto, M.; Narahashi, Y.; Murakami, M. A Proteolytic Enzyme of Streptomyces Griseus - VI. Hydrolysis of Protein by Strepomyces Griseus Protease. *J. Biochem. (Tokyo)* **1960**, *48*, 593-602.

(268) Schomburg, D.; Salzmann, M., *Clostridium histolyticum* collagenase. In *Enzyme Handbook*, Springer-Verlag: Berlin, 1990; pp 3.4.24.3, 1-5.

(269) Bond, M. D.; Vanwart, H. E. Characterization of the Individual Collagenases from Clostridium-Histolyticum. *Biochemistry* **1984**, *23*, 3085-3091.

(270) Komeili, A. Molecular Mechanisms of Compartmentalization and Biomineralization in Magnetotactic Bacteria. *FEMS Microbiol. Rev.* **2012**, *36*, 232-255.

(271) Uebe, R.; Schüler, D. Magnetosome Biogenesis in Magnetotactic Bacteria. *Nat. Rev. Microbiol.* **2016**, *14*, 621-637.

(272) Jogler, C.; Schüler, D. Genomics, Genetics, and Cell Biology of Magnetosome Formation. *Annu. Rev. Microbiol.* **2009**, *63*, 501-521.

(273) Borg, S.; Hofmann, J.; Pollithy, A.; Lang, C.; Schüler, D. New Vectors for Chromosomal Integration Enable High-Level Constitutive or Inducible Magnetosome Expression of Fusion Proteins in *Magnetospirillum gryphiswaldense*. *Appl. Environ. Microbiol.* **2014**, *80*, 2609-2616.

(274) Lang, C.; Schüler, D. Expression of Green Fluorescent Protein fused to Magnetosome Proteins in Microaerophilic Magnetotactic Bacteria. *Appl. Environ. Microbiol.* **2008**, *74*, 4944-4953.

(275) Mickoleit, F.; Schüler, D. Generation of Multifunctional Magnetic Nanoparticles with Amplified Catalytic Activities by Genetic Expression of Enzyme Arrays on Bacterial Magnetosomes. *Adv. Biosyst.* **2018**, *2*, 1700109.

(276) Hull, M. C.; Cambrea, L. R.; Hovis, J. S. Infrared Spectroscopy of Fluid Lipid Bilayers. *Anal. Chem.* **2005**, *77*, 6096-6099.

(277) Humenik, M.; Smith, A. M.; Arndt, S.; Scheibel, T. Ion and Seed Dependent Fibril Assembly of a Spidroin Core Domain. *J. Struct. Biol.* **2015**, *191*, 130-138.

(278) Humenik, M.; Magdeburg, M.; Scheibel, T. Influence of Repeat Numbers on Self-Assembly Rates of Repetitive Recombinant Spider Silk Proteins. *J. Struct. Biol.* **2014**, *186*, 431-437.

5. Darstellung des Eigenanteils

Die in der vorliegenden Dissertation vorgestellten Ergebnisse wurden in Zusammenarbeit mit Kooperationspartnern erzielt und bereits in den unten aufgeführten Journalen veröffentlicht. Nachfolgend werden die einzelnen Beiträge aller Autoren zu den jeweiligen Veröffentlichungen genau angegeben,

I. **C. B. Borkner**, M. B. Elsner, T. Scheibel, Coatings and Films Made of Silk Proteins. *ACS Applied Materials and Interfaces* **2014**, *6*, 15611-15625.

Die Konzeption des Artikels wurde von Martina B. Schierling (geb. Elsner), Thomas Scheibel und mir erarbeitet. Das Manuskript wurde von Martina B. Schierling und mir in Zusammenarbeit verfasst. Martina B. Schierling (geb. Elsner) war an der Verfassung des *Kapitels 3.1. Tissue Engineering and Medical Applications* maßgeblich beteiligt. Thomas Scheibel war in wissenschaftlicher Diskussion eingebunden und an der Fertigstellung des Manuskripts beteiligt.

II. **C. B. Borkner**, S. Wohlrab, E. Möller, G. Lang, T. Scheibel, Surface Modification of Polymeric Biomaterials Using Recombinant Spider Silk Proteins. *ACS Biomaterials Science & Engineering* **2017**, *3*, 767-775.

Der Beschichtungsprozess wurde von mir entwickelt und alle Beschichtungen von mir hergestellt. Die Untersuchungen zu den Oberflächeneigenschaften der Beschichtungen sowie der Beschichtungsstabilität wurden von mir durchgeführt und ausgewertet. Stefanie Wohlrab war in wissenschaftlicher Diskussion sowie mit der Planung der Zellkulturversuche zur Adhäsion (24 h) von BALB/3T3 Fibroblasten beteiligt und führte diese durch. Eva Möller war an der Planung der Zellkulturversuche zur Adhäsion (6 d) sowie der Durchführung des Proliferationstests (BALB/3T3) beteiligt und führte diese durch. Die Mikroskopie der Zellkulturversuche wurde von mir durchgeführt. Gregor Lang war in wissenschaftlicher Diskussion beteiligt. Thomas Scheibel betreute das Projekt und war in wissenschaftlicher Diskussion und an der Fertigstellung des Manuskripts beteiligt.

III. **C. B. Borkner***, S. Lentz*, M. Müller, A. Fery, T. Scheibel, Ultrathin Spider Silk Films: Insights into Spider Silk Assembly on Surfaces. *ACS Applied Polymer Materials* **2019**, *1*, 3366-3374.
* gleichberechtigte Co-Autorenschaft

Die Projektidee wurde durch Thomas Scheibel und mir, die Konzeption des Artikels wurde von Andreas Fery, Thomas Scheibel und mir und die Methodik von Sarah Lentz, Martin Müller, Andreas Fery, Thomas Scheibel und mir erarbeitet. Die Experimente wurden von Sarah Lentz im Rahmen einer von mir betreuten Masterarbeit, von Martin Müller und von mir durchgeführt. Das Manuskript wurde von mir und Sarah Lentz verfasst. Der finale Artikel wurde von Sarah Lentz, Martin Müller, Andreas Fery und Thomas Scheibel überprüft und editiert. Visualisierungen im Artikel wurde von Sarah Lentz und mir durchgeführt. Betreuung und Finanzierung erfolgte durch Andreas Fery und Thomas Scheibel.

IV. F. Mickoleit, **C. B. Borkner**, M. Toro-Nahuelpan, H. M. Herold, D. S. Maier, J. M. Plitzko, T. Scheibel, D. Schüler, *In vivo* Coating of Bacterial Magnetic Nanoparticles by Magnetosome Expression of Spider Silk-Inspired Peptides. *Biomacromolecules* **2018**, *19*, 962-972.

Der Artikel wurde von Frank Mickoleit, Dirk Schüler und Thomas Scheibel konzeptioniert. Von Frank Mickoleit wurden die Spinnenseiden-Expressionstämme hergestellt und die Kultivierungsexperimente, die Magnetosomenisolierung, Sedimentationsversuche, Elektronenmikroskopie und Zetasizer-Messungen durchgeführt sowie die erhaltenen Daten analysiert und interpretiert. QCM-D und ATR-FTIR Experimente wurden von mir konzeptioniert, durchgeführt und optimiert und die erhaltenen Daten analysiert. Mauricio Toro-Nahuelpan führte die Cryo-Elektronentomographieexperimente durch, analysierte die Daten mit Jürgen M. Plitzko und erstellte das 3D-Rendering der tomagraphierten Zellen für die Filmsequenz. Die Fibrillisationsexperimente wurden von Heike M. Herold und Gelelektrophorese sowie Western Blots wurden von Denis M. Maier durchgeführt. Das Manuskript wurde von Frank Mickoleit verfasst. Alle Autoren waren durch kritische Diskussion an der Fertigstellung der Forschungsarbeit, der Analyse und des Manuskripts beteiligt.

6. Teilarbeiten

Teilarbeit I

Die Ergebnisse dieses Kapitels wurden bereits in *ACS Applied Materials & Interfaces* veröffentlich als:

Coatings and Films Made of Silk Proteins.

Christian B. Borkner, Martina B. Elsner und Thomas Scheibel

Mit Genehmigung abgedruckt aus C. B. Borkner, M. B. Elsner, T. Scheibel, Coatings and Films Made of Silk Proteins. *ACS Applied Materials and Interfaces* **2014**, *6*, 15611-15625. Copyright 2014 American Chemical Society.

Reprinted with permission from C. B. Borkner, M. B. Elsner, T. Scheibel, Coatings and Films Made of Silk Proteins. *ACS Applied Materials and Interfaces* **2014**, *6*, 15611-15625. Copyright 2014 American Chemical Society.

ACS APPLIED MATERIALS & INTERFACES
Review
www.acsami.org

Coatings and Films Made of Silk Proteins

Christian B. Borkner,[†] Martina B. Elsner,[†] and Thomas Scheibel*,[†,‡,§,∥,⊥]

[†]Lehrstuhl Biomaterialien, Fakultät für Ingenieurwissenschaften, [‡]Bayreuther Zentrum für Kolloide und Grenzflächen (BZKG), [§]Institut für Bio-Makromoleküle (bio-mac), [∥]Bayreuther Zentrum für Molekulare Biowissenschaften (BZMB), and [⊥]Bayreuther Materialzentrum (BayMAT), Universität Bayreuth, Universitätsstrasse 30, 95440 Bayreuth, Germany

ABSTRACT: Silks are a class of proteinaceous materials produced by arthropods for various purposes. Spider dragline silk is known for its outstanding mechanical properties, and it shows high biocompatibility, good biodegradability, and a lack of immunogenicity and allergenicity. The silk produced by the mulberry silkworm *B. mori* has been used as a textile fiber and in medical devices for a long time. Here, recent progress in the processing of different silk materials into highly tailored isotropic and anisotropic coatings for biomedical applications such as tissue engineering, cell adhesion, and implant coatings as well as for optics and biosensors is reviewed.

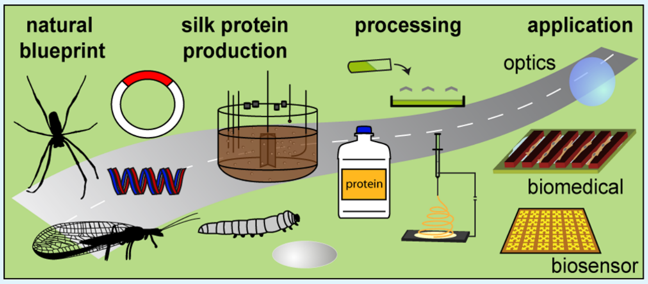

KEYWORDS: *spider silk, silkworm silk, processing, biomedical application, biosensor, optics*

1. INTRODUCTION

Silks, like keratins and collagens,[1−3] are based on a class of structural proteins with highly repetitive amino acid sequences. The proteins are stored in a soluble state and are assembled into solid extracorporeal fibers when sheared or "spun". Humans have exploited silkworm silk (from *Bombyx mori*) for millennia, primarily for textiles. Silks produced by spiders have also been used for centuries, for example by Polynesians for fishing and by Romans and Greeks as wound dressing and sutures.[4,5] Because of the outstanding mechanical properties of spider silk compared to other synthetic and natural fibers,[6−10] their biocompatibility and good biodegradability and lack of immunogenicity and allergenicity, many more technical and biomedical applications are conceivable. Importantly, unlike in nature, spider silk proteins (either regenerated from silk fibers or recombinantly produced) can also be technically processed into nonfibrous morphologies. Here, we highlight recent work on the processing and applications of proteins derived from spider silk (e.g., *Araneus diadematus*, *Nephila clavipes*), mulberry silkworm (*B. mori*), and lacewing silk (e.g., *Chrysopa carnea*, *Mallada signata*, and *Chrysopa flava*) into β-sheet-rich coatings and films.

1.1. β-Crystalline Silks. Almost all arthropods can produce silk, each with a specific structural feature (e.g., helical, coiled-coil, β-sheet, etc.) tailored to specific purposes. This review focuses on β-crystalline silks, which are produced by larvae of mulberry silkworms (*B. mori*), lacewings (*Chrysopidae*), and orb weaving spiders (*Araneae*).

1.1.1. Silkworm Silk. *B. mori* silk has been well characterized, and there exist numerous reviews on its properties[6,11] and applications.[12−14] During metamorphosis, silkworms produce silk cocoons for protection. The silk fibers are composed of two silk fibroins (SF), the heavy chain (325 kDa) and the light chain (25 kDa), which are connected by a disulfide bond[15] and complexed by the small glycoprotein P25 (30 kDa).[16] The proteins have been thoroughly investigated and reviewed.[17−19] The main structural elements of this material are repeats of the GAGAGS motif, which forms antiparallel β-sheet structures because of intra- and intermolecular hydrogen bonding.[20] The fibers are coated with the glue-like glycoprotein sericin, which has to be removed (degumming)[21−23] prior to processing for use in medical applications because it can cause immunoreactions.[24−27] It is advantageous that silkworms can be reared in captivity, and the silk can be obtained in great quantities.

1.1.2. Lacewing Silk. To protect their eggs from predators, female lacewings lay their eggs on the ends of silk stalks attached to substrates such as the lower side of leaves. These fibers show unusual bending stiffness based on the structural features of the underlying silk proteins (see also section 1.1.4.).[28] The amino acid composition[29] and the cross-β-structure[30] of egg stalk silk were first described in the 1950s. Fifty years later, researchers from Tara Sutherland's group analyzed the lacewing silk of *M. signata* and identified two proteins: MalXB1 (109 kDa) and MalXB2 (67 kDa). MalXB1 is the main component of egg stalk silk and comprises a serine-, alanine- and glycine-rich tandem repeat.[31] In another lacewing species (*C. carnea*), at least five individual proteins were identified in the egg stalk silk dope.[32]

1.1.3. Spider Silk. Web spinning spiders (*Araneae*) are probably the best-evolved β-crystalline silk producers with the most specialized silk fibers. Female orb-weaving spiders, such as *Nephila clavipes* and the European garden spider *Araneus diadematus*, can produce up to seven different types of silk with task dependent properties.[33] There exist numerous reviews and

Received: February 10, 2014
Accepted: July 8, 2014
Published: July 8, 2014

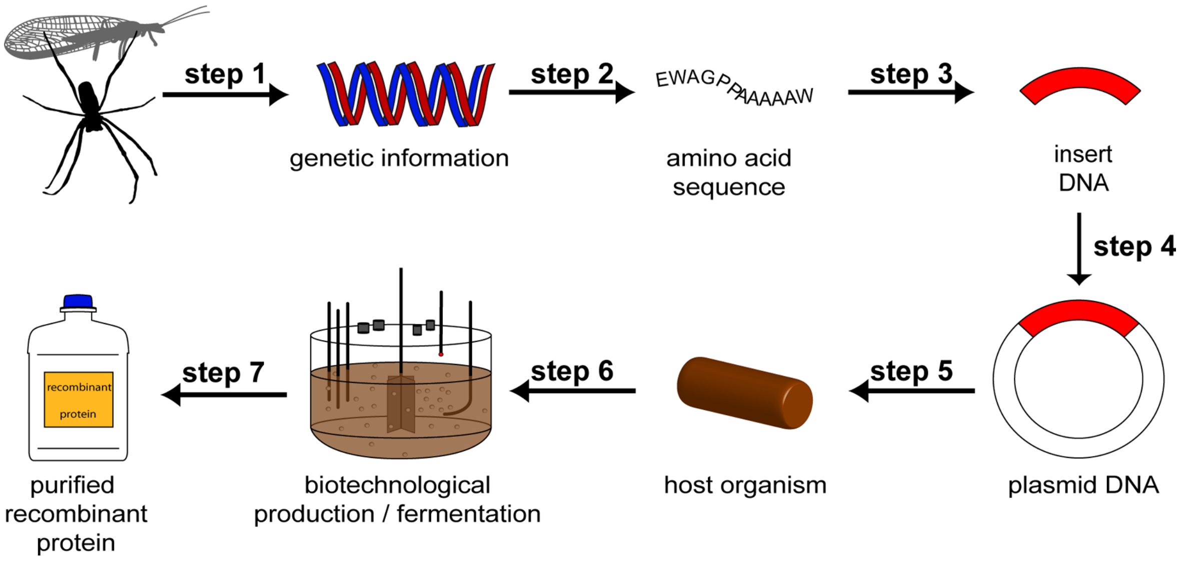

Figure 1. Scheme of recombinant silk production. Step 1, extracting genetic information; step 2, decoding the extracted DNA; step 3, reverse translation and gene engineering; step 4, ligation of insert DNA into the plasmid DNA; step 5, transfer of plasmid into host organism; step 6, fermentation; step 7, purification.

articles summarizing the biology,[11,34,35] structure[36,37] and mechanical properties[6,38−40] of spider silk. Here, we focus on major ampullate (MA) silk, which is produced in the MA gland. This MA silk is used as the outer frame and radii of a spider's web and as its lifeline.[41] MA silk has a very high tensile strength and the highest toughness of all known natural as well as synthetic fibers.[3,6,38,42−44] MA silk is mainly composed of spidroins (**spid**er *fib***roin**) and is divided into two classes (MaSp1 and MaSp2) according to its proline content. MaSp1 has a low proline content and MaSp2 is proline-rich. The physical and related mechanical properties, such as breaking strain, of MA silk are directly influenced by the proline content.[45] MA spidroins generally contain a repetitive core with individual amino acid motifs repeated up to 100 times accounting for over 90% of the sequences.[46] The core domain is flanked by nonrepetitive amino- and carboxy-terminal domains, which are highly conserved between different silks and between spider species. These terminal domains mediate the storage and assembly of the spider silk proteins.[47,48] MA silk fibers are coated with a very thin shell of glycosylated proteins, lipids, minor ampullate spidroins and other proteins.[49,50] However, these shell compounds are, in contrast to sericin from *B. mori*,[51] not immunogenic, making MA silk an interesting biomaterial for biomedical applications.

1.1.4. Comparison of β-Crystallinity in Silkworm, Lacewing, and Spider MA Silk. The β-sheet content of MA silk (11−46% *N. clavipes*,[20,52,53] 34−35% *A. diadematus*,[54] 46% *Nephila edulis*[55]) is similar to that of *B. mori* silk (40−55%).[20,52] Both silk materials form antiparallel β-sheets aligned along the thread axis. The β-sheets form crystalline-like regions embedded in an amorphous matrix, but also the presence of a so-called interphase was proposed. In contrast to *B. mori* and MA silk, Lacewing egg stalk silk shows an unusual β-sheet structure (content: 20−40%)[28,32] called cross-β structure, where β-strands are aligned perpendicular to the fiber axis.[30] The evidence for two different types of β-sheets in *N. clavipes* MA silk and *B. mori* silk was shown by hydrogen−deuterium exchange experiments. Crystalline β-sheets are D_2O-inaccessible and the β-sheets building the interphase are D_2O-accessible. The water-accessible interphase consists of weaker hydrogen bonded β-sheets. MA and *B. mori* silk differ in the fraction of the interphase which is significantly higher in case of MA silk (27 ± 3%) than in *B. mori* silk (8 ± 3%).[53] In the case of *B. mori* silk, crystalline as well as interphase β-sheets are likely formed by GAGAGS motifs. In MA silk, crystalline β-sheets are formed by polyalanine (A_n) regions, and AG and GGA blocks flanking the A_n regions are suggested to be present in β-sheets also.[52,53] The interphase probably contains GXG (X = Q, Y, L, R) motifs. A three-phase model was postulated where the crystalline regions are flanked by an interphase which is assumed to act as a transition zone between crystalline β-sheets and the surrounding amorphous phase.[53,56] The structural organization allows to describe the properties of spider silk using a hierarchical model.[57]

1.2. Natural vs Recombinant Silk Production. To exploit the manifold properties of silk, it can be advantageous to investigate the isolated underlying proteins. Silks can be harvested from their natural sources (i.e., for example of *B. mori* cocoons). The silk is degummed by boiling the cocoons in 0.02 M Na_2CO_3, and the degummed fibers are dissolved in strong chaotropic agents (e.g., 9.3 M LiBr), yielding soluble silk fibroins called regenerated silk fibroin (RSF). Because *B. mori* silk has been produced by sericulture (silk farming) for centuries, RSF has been available for investigations for decades.

In contrast, spiders cannot be farmed because they are typically territorial and cannibalistic[13,47−50] and produce silk of lower quality when held in captivity.[8,34,58] Although lacewings are bred commercially (they are used as pest control), the quantity of silk produced by each individual is too small for practical applications. In both cases, as an alternative to obtaining silk proteins from natural sources, recombinant strategies for producing silk proteins have been developed, but only a short overview is given here. For more detailed information on natural and synthetic spider silk genes, the reader is referred to Heidebrecht and Scheibel and references therein.[59] Different approaches for producing silk proteins in different host organisms have failed mainly because of the repetitive character of the gene sequences rich in guanine and

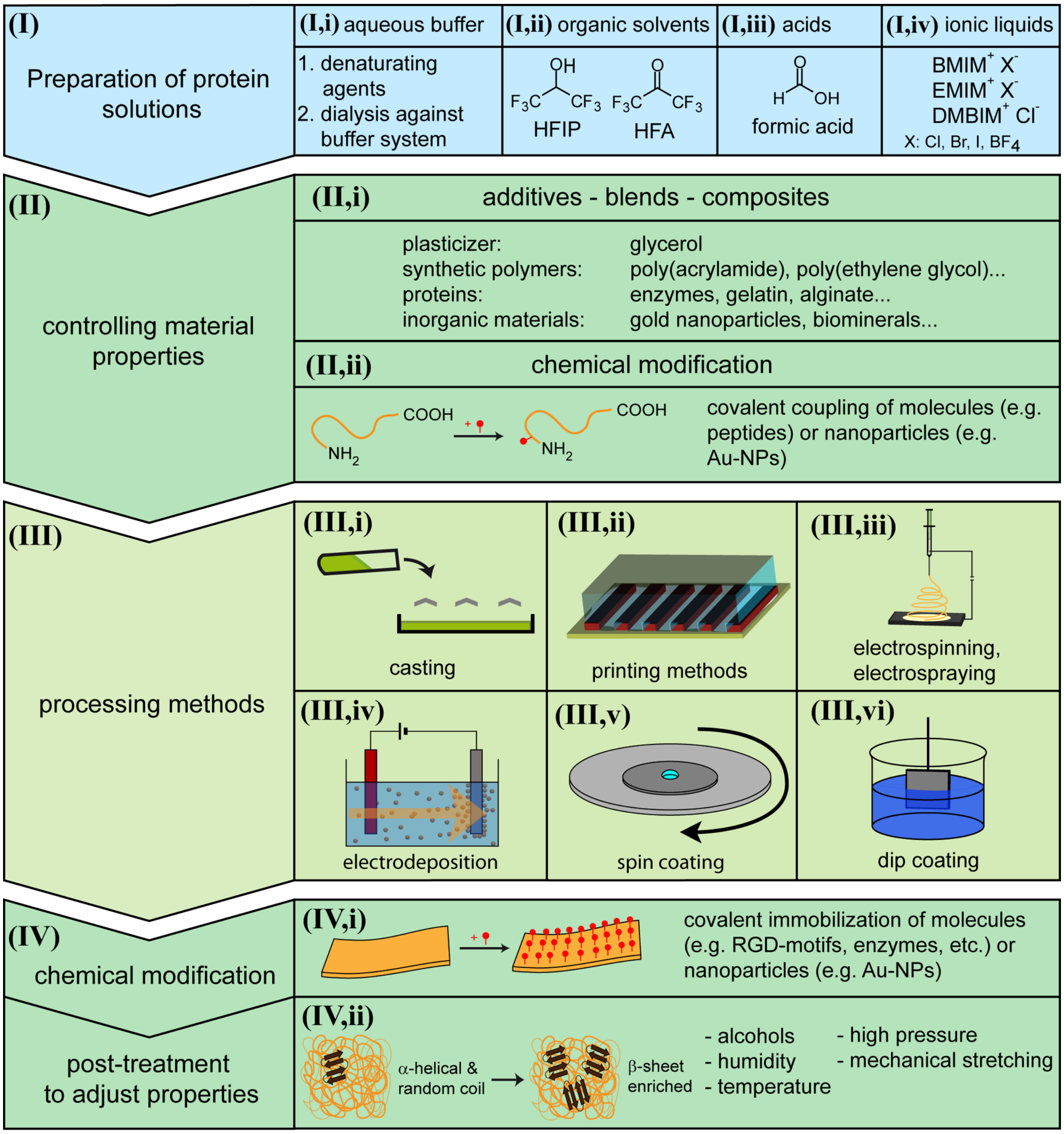

Figure 2. Schematic overview of silk processing. After (I) preparing the silk solutions, the materials properties can be controlled (II) before and (IV) after (III) further processing steps.

cytosine. A successful approach was the construction of synthetic sequences based on natural motifs (Figure 1, step 1−2) and adapting the gene sequences to the codon usage of different host systems like bacteria (e.g., *Escherichia coli*) or yeast (e.g., *Pichia pastoris*) (Figure 1, step 3−5).[60−63] A similar strategy was performed for a recombinant egg stalk protein (RESP).[32] The biotechnological production (Figure 1, step 6) yields silk proteins as primary material for further processing (Figure 1, step 7), but also allows the modification of proteins genetically. Synthetic analogues can be produced with targeted modifications to get desired material characteristics,[64] giving access to a broad range of applications.

2. PROCESSING OF SILK PROTEINS

The processing of silk proteins includes preparation of silk protein solutions (Figure 2 (I)), controlling materials properties (Figure 2 (II) & (IV)) and processing methods (Figure 2 (III)). Regenerated silk fibroin (RSF), recombinant egg stalk proteins (RESP) and recombinant spider silk proteins (RSSP) can be easily processed into different morphologies like nonwoven mats, films and coatings.

2.1. Preparation of Silk Solutions. At first, silk proteins are dissolved in a denaturating agent to prepare processable silk protein solutions (Figure 2 (I)). Such denaturating agents are chaotropic salts like lithium bromide (LiBr), lithium thiocyanate (LiSCN), guanidinium thiocyanate (GdmSCN), or guanidinium hydrochloride (GdmHCl). Chaotropic salts can easily be exchanged via dialysis (Figure 2 (I,i)). Alternatively,

Table 1. Overview of Synthetic Polymers, Biopolymers and Inorganic Materials for Silk-Based Composite Materials and Blends[a]

synthetic polymer		biopolymers		inorganic materials	
nonbiodegradable	biodegradable	proteins	polysaccharides	particles	biominerals
carbon nanotubes	poly(aspartic acid)	collagen	alginate	silver nanoparticles	calcium carbonate
nylon66	poly(ε-caprolactone)	enzymes	cellulose	gold nanoparticles	calcium phosphate
polyacrylamide	poly(ε-caprolactone-*co*-D,L-lactide)	fibroins	cellulose xanthate (viscose)	transition metal oxides and sulfides	silica
polyacrylonitrile	poly(carbonate-urethane)	gelatin	chitin		
polyallylamine	poly(lactic-*co*-glycolic acid)	green fluorescent protein	chitosan		
polyepoxide	poly(lactic acid)	growth factors	hyaluronic acid		
poly(ethylene glycol)	polyurethane	keratin			
polypyrrole		sericin			
polystyrene		spidroins			
poly(vinyl alcohol)					

[a] For details about silk composite materials, the reader is referred to Hardy et al.[70]

silk proteins can be dissolved in fluorinated organic solvents like hexafluoroisopropanol (HFIP) and hexafluoroacetone (HFA) (Figure 2 (I,ii)) or acids like formic acid (FA) (Figure 2 (I,iii)). Also, ionic liquids like 1-butyl-3-methylimidazolium chloride (BMIM Cl), 1-ethyl-3-methylimidazolium chloride (EMIM Cl), and 1-butyl-2,3-dimethylimidazolium chloride (DMBIM Cl) can act as denaturating agents (Figure 2 (I,iv)).[65,66]

2.2. Additives for Controlling Silk Properties. After preparing the initial silk protein solution, additional substances like plasticizers (e.g., glycerol[67−69]), polymers or proteins can be added before or during processing the silk materials (Figure 2 (II,i)). A broad range of material blends and composite materials containing silk proteins have been analyzed in the past, including synthetic polymers, biopolymers, and inorganic materials as additives. An overview on additives is given in Table 1. For details concerning composite materials based on silk the reader is referred to Hardy et al.[70]

2.3. Processing Methods of Silk and Silk Blends. Silk proteins and blended silk materials can be processed into films and coatings using various processing techniques (Figure 2 (III)) resulting in different morphologies. Films can be cast or printed e.g. using lithography[71] yielding 2D and 3D structured isotropic or anisotropic micro- or nanopatterned surfaces.[72] Thin coatings can easily be prepared by dip or spin coating.[73,74] Using spin coating, the silk proteins can self-assemble due to shear-forces as described for native SF.[75] Zeplin and co-workers used dip coating to modify the surface of breast implants using RSSP (for details see part 3.1).[76] Other methods for generating thin silk films are for example the Langmuir−Blodgett (LB) technique[77] and layer-by-layer (LbL) techniques.[78]

Nonwoven mats represent a completely different type of silk coating which can be produced e.g. by electrospinning[79,80] out of different solvents.[81−84] The silk protein solution or material blend is extruded from a syringe, and an electric field between the syringe and the collector plate accelerates the solution and the solvent evaporates. The resulting fibers can be deposited directly on any kind of substrate that is placed on the collector plate. Particles, too, can be deposited on substrates by electrophoretic deposition.[85−87]

Besides homogeneous films and coatings, materials with gradually changing properties, as found in biological systems (e.g., mussel byssus), are useful for various applications.[88] Fibroin/gelatin blends show a wide range of Young's moduli depending on the mixing ratio.[12,70] Gradient films were cast using glycerol-plasticized gelatin and 0−40% RSF, leading to a gradient material on a centimeter scale with a highly reproducible and smooth mechanical gradient with moduli from 160 to 550 MPa.[89]

2.3.1. Influence of Solvent and Post-Treatment on Silk Film Properties. Films can be cast from different solvents such as aqueous buffers, organic or ionic liquids (Figure 2 (III,i)) and obtained through simple solvent evaporation. The secondary structure of the silk proteins is dependent on the initial solvent and is, therefore, controllable. Fluorinated solvents induce α-helical structure in silk proteins. Films cast out of HFIP show a high amount of α-helical structures (RSF;[90] RSSP[91−93]), whereas films cast out of formic acid or water show higher β-sheet content.[90,94−97] RESP dissolved in HFA also has primarily α-helical structure, and therefore, films cast from these solutions have to be post-treated to yield more stable structures.[32] In case of RSSP, the initial solvent has no influence on the thermal stability of films made of a recombinantly produced engineered *A. diadematus* fibroin (eADF4(C16)[62]), where thermal decomposition starts around 270 °C. In contrast, the initial solvent showed a clear impact on the mechanical properties of the films.[98]

Furthermore, surface hydrophobicity can be controlled by casting conditions as shown in the following experiments with films made of RSSP. eADF4(C16) films with a thickness of 9−11 μm were cast out of aqueous buffer (10 mM NH_4HCO_3), HFIP, and FA on poly(tetrafluoroethylene) (PTFE; Teflon), polystyrene (PS) and glass at 30% relative humidity and 20 °C. The films showed different surface hydrophobicities depending on the hydrophobicity of the substrate used to cast the films on. After post-treatment with methanol, the surface hydrophobicity was analyzed by contact angle measurements at the film−air interface. Films cast on hydrophilic glass substrates were more hydrophobic at that surface in comparison to films cast on hydrophobic PS and PTFE substrates (Figure 3A). A structural model of microphase separation of silk proteins based on the amphiphilic nature of the silk protein was generated, in which nonhydrophilic polyalanine stretches are arranged into packed β-sheet crystallites causing water exclusion, and hydrophilic

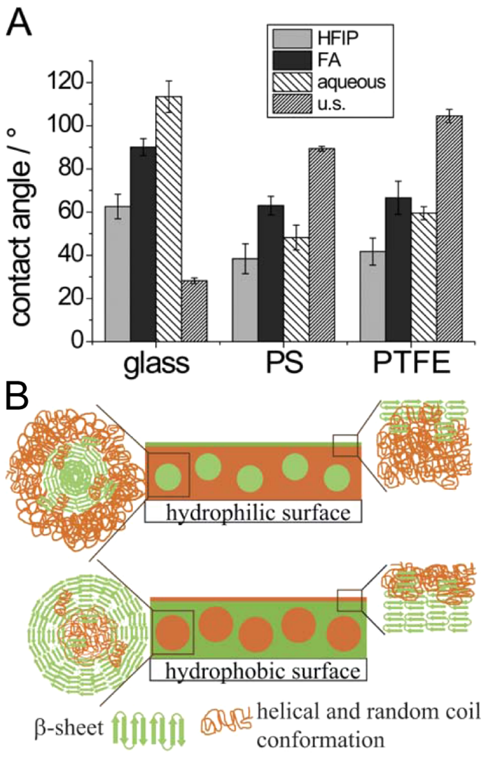

Figure 3. (A) Surface hydrophobicity of eADF4(C16) films dependent on the substrate and the solvent used, determined by water contact angle measurements. Uncoated substrates (u.s.) were measured as reference. (B) Influence of the template on the secondary structure of eADF4(C16). Reproduced with permission from ref 99. Copyright 2012 The Royal Society of Chemistry.

glycine-rich motifs remain in unstructured or helical conformations (Figure 3B).[99] On hydrophilic templates like glass, hydrophilic silk regions are oriented toward the substrate, and the hydrophobic polyalanine stretches are organized into micellar-like structures or oriented away from the hydrophilic bulk to the silk-air interface, inducing a hydrophobic film surface. On hydrophobic templates, e.g., PTFE, the hydrophobic silk regions are oriented toward the substrate, and the hydrophilic blocks are organized into micellar-like structures or oriented away from the hydrophobic bulk to the silk-air interface.[99] Microphase separation is a common effect of block copolymers, and RSF can also be described as multiblock polymer composed of crystallizable and uncrystallizable blocks. β-sheet crystallization is therefore spatially limited by microphase separation of the two different blocks.[100] Furthermore, Cebe et al. performed fast scanning chip calorimetry with RSF and reported the first reversible melting of β-sheet crystals similar to the behavior of lamellar crystals composed of synthetic polymers.[101]

In the case of RSF, Lawrence and co-workers demonstrated the influence of RSF film hydration on material properties depending on the processing technique. Methanol treated RSF films showed a less-ordered secondary structure arrangement than water annealed RSF films. The methanol treated films had a higher water absorbing capacity and reached higher oxygen permeability rates.[102]

2.3.2. *Processing Techniques for Adopting Different Surface Topographies.*

It is possible to produce structured micro- and nanopatterned silk protein surfaces by common micro- and nanopatterning methods. For example, RSF microstructures have been assembled by rapid transfer-based micropatterning and dry etching[103] and RSSP microstructures by solvent-assisted microcontact molding and capillary transfer lithography.[104] Micropatterned films made of RSF were cast on poly(dimethylsiloxane) PDMS replica molds to transfer surface structures of patterned surfaces to silk films,[105,106] and micropatterned films made of RSSP and RESP have also been processed for controllable cell adhesion, cell growth and cell orientation (for details, see section 3.1.1).[9] The RSSP/RESP patterns were made using photolithographically produced silicon templates to generate a microstructured PDMS negative which was placed on a smooth cast silk protein film (RSSP or RESP). Then, the second silk solution was soaked into the molds by capillary forces. After evaporation of the solvent, the PDMS stamp was removed yielding a patterned silk film.[9]

2.3.3. *Influencing Silk Film Properties Using Chemical Modifications.*

Various coupling reactions can be used for chemical modification (Figure 2 (II,ii) & (IV,i)) of silk proteins depending on their amino acid composition i.e. the number and type of functional groups. In the case of *B. mori* SF, the most abundant reactive amino acid residues of the heavy chain are threonine, serine, tyrosine, aspartic acid and glutamic acid. Common coupling reactions used for chemical modification of these amino acids are cyanuric chloride-activated coupling, carbiodiimide coupling, and reaction with glutaraldehyde. Further, amino acids can be modified by arginine masking and sulfation and azo-modification of tyrosine. For details about these chemical modifications the reader is referred to Murphy and Kaplan and references therein.[107]

Huemmerich and co-workers modified films made of the RSSP eADF4(C16) by carbodiimide activation of the carboxy groups of glutamate residues and the carboxy-terminus (overall 17 reactive sites) for reaction with amines in solution. The coupling of fluorophores and of the enzyme β-galactosidase was successfully shown with RSSP.[92] For biomedical applications cell binding properties can be influenced by cell binding peptides like RGD-motifs which were coupled by thiol chemistry to RSSP (eADF4(C16)) films and by carbodiimide coupling to RSF films to improve cell adhesion (see section 3.1.1.).[107,108] In the case of RSSPs, like eADF4(C16) which do not have cysteine residues in their sequence, the protein can be genetically modified during production (see chapter 1.2), for example, with a cysteine-containing tag at the amino-terminus. The eADF4(C16)$^{\mathrm{ntagCys}}$-film surfaces expose the thiol groups of the cysteines, allowing controlled and specific modification with reagents containing a maleimido function.[74] Maleimido-fluorescein, biotin maleimide, RGD-motifs, β-galactosidase and monomaleimido-nanogold (d = 1.4 nm) could be successfully coupled to the silk film surface.[74] It was also possible to covalently attach sulfonic acid groups to tyrosine of RSF using diazonium coupling. The negatively charged and hydrophilic sulfonic acid groups can selectively promote pyrrole absorption to sulfonic acid modified RSF films, yielding conductive polypyrrole patterns on silk surfaces by printing or stamping inks made of sulfonic acid-modified RSF on RSF films. Pyrrole adheres selectively to the acid modified RSF and sets up conductive structures out of polypyrrole after polymerization.[109]

2.4. Post-Treatment.

Post-treatment of processed silk proteins (Figure 2 (IV,ii)) can be used to increase the β-sheet content of a silk material resulting in more stable and water insoluble protein materials.[80,110,111] The structural change from

α-helical and random coil structures to β-sheets and can be induced by temperature,[112] alcohols (e.g., methanol, ethanol, 2-propanol),[92,93,95,111] humidity and water vapor,[113] high pressure,[114] mechanical stretching,[115] and cosmotropic salt solutions (e.g., 1 M potassium phosphate).[93,116] Anisotropic materials can also be produced by post-treatment leading to alignment of the underlying structural elements. Both types of processing influence the mechanical properties of the resulting materials.[13,20,117]

3. APPLICATIONS OF SILK FILMS, COATINGS, AND NONWOVEN MATS

3.1. Tissue Engineering and Medical Applications. Silk shows interesting features such as biodegradability and biocompatibility (reviewed in Leal-Egaña and Scheibel[14]),[118,119] and nothing has been reported concerning allergies against pure silk materials, probably based on low or no inflammatory responses when in contact with animals and humans.[119] Nonwoven mats have been applied as wound dressings, coatings, or scaffolds,[120,121] and silk films have been investigated as coatings and wound dressings as well as drug delivery systems.[122]

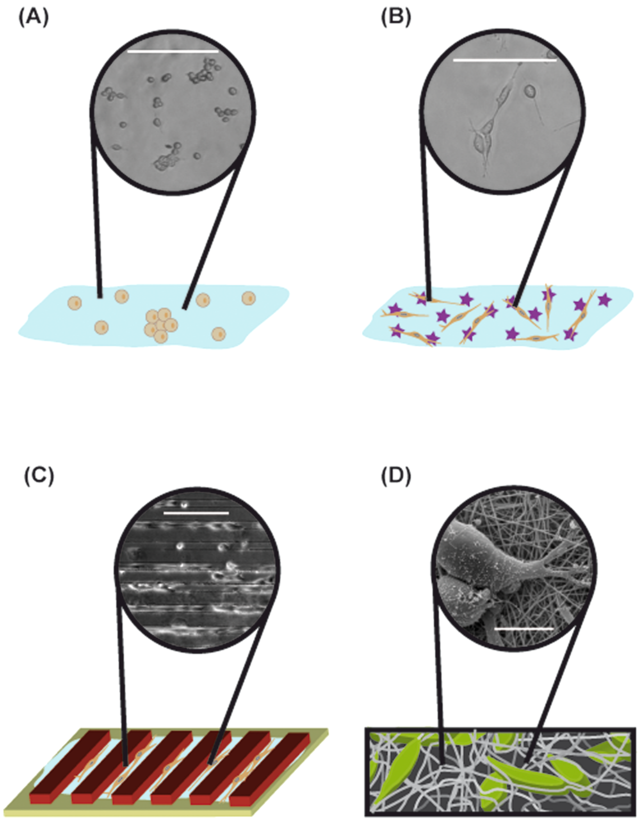

Figure 4. Cell adhesion on different silk morphologies and on modified silk films. (A) Cells were seeded on flat RSSP (eADF4(C16) films cast from HFIP). Low cell adhesion and round-shaped cell morphologies of BALB/3T3 fibroblasts are detected. (B) RGD-modified eADF4(C16) films show improved cell adhesion and cell spreading. The surface topography can be altered (C) with patterning or (D) by creating nonwoven meshes. Both approaches have a large impact on cell adhesion and orientation.[9,106,120,139,146,151,152] Scale bars: (A–C) 200 μm; (D) 10 μm.

B. mori silk has been reported to cause allergic reactions and immune responses when using so-called "virgin silk" (silk directly obtained from the silkworm), whereas removing sericin from the silk fibers (i.e., degumming) yields a material that causes no allergic reaction and/or immune response.[24−27,123−127] MA spider silk is not coated with glue, therefore, MA silk causes no allergic reactions/immune response like virgin silk. In the case of lacewing egg stalk silk, it is currently not known if it causes allergic reactions and/or immune responses because not all the proteins have been identified and tested yet.

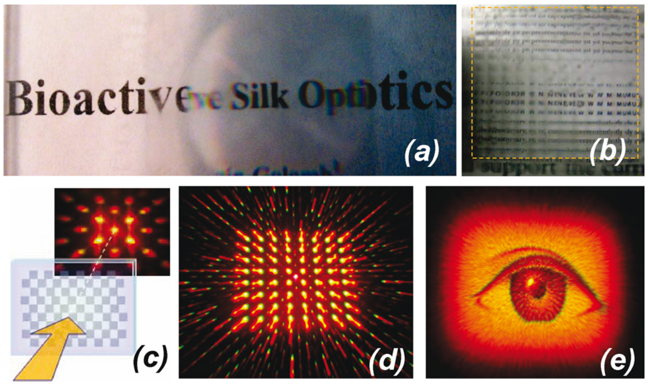

Figure 5. Optical elements made of silk. (a) silk lens, (b) 12 × 12 silk lens array, (c) scheme showing the approach for generating images, (d, e) different projected patterns obtained from propagation of a white light laser source through 2D, 64 phase level diffraction patterns. The images are taken in the far field at a distance of 10 cm from the silk optical element. (Masters from Digital Optics Inc., Tessera Corporation). Reproduced with permission from ref 168. Copyright 2008 American Chemical Society.

The properties of silk films (hydrophobicity, water-contact-angle, secondary structure, etc.) differ because of the protein used, the solvent, template surface, post-treatment, and film thickness as mentioned above,[98,99,113,128,129] with dramatic impact on cell organization, adhesion, and proliferation when used as a scaffold. Cell interactions with surfaces or other cells are mainly mediated by the integrin protein family.[130] Binding motifs recognized by integrins are present in proteins of the extracellular matrix (ECM) (e.g., laminin, collagen, fibronectin).[130−132] Therefore, it is also of great importance how such ECM proteins interact with a "technical" surface (such as in silk scaffolds). Below we will give an overview of general aspects of cell−silk surface interactions followed by a more detailed description of recent results (from the last 10 years) concerning putative medical applications of silk scaffolds.

3.1.1. Cell−silk Surface Interactions and Silk Surface Modifications for Improved Cell Binding. Generally, weak cell attachment has been detected on RSF, RSSP, and RESP films (Figure 4A), such as for osteoblast-like cells SaOs-2 on RSF[133] or BALB/3T3 fibroblasts on eADF4(C16) RSSP and RESP films.[9,108,120] Cells on these silk films are round and form cell aggregates (i.e., cell−cell interactions instead of cell−matrix interactions).[108,120,134] SaOs-2 cells up-regulated the production of ECM proteins (100%) such as collagen type *I-*α or alkaline phosphatase on RSF films, whereas fibroblasts up-regulated collagen-I on RSSP (eADF4(C16)) films as a result of weak attachment.[120,135] Weak cell attachment can be partly explained by the absence of cell recognition motifs.[136] Furthermore, RSF and RSSP (eADF4(C16)) are negatively charged proteins under cell culture conditions, which is also not conducive for cell attachment because cell surfaces are also negatively charged.[137,138] In contrast, films made of the

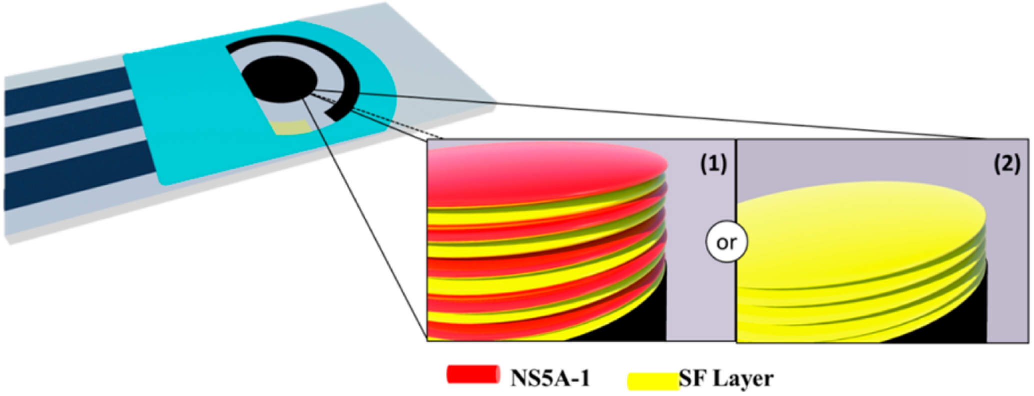

Figure 6. Schematic representation of five-layer LbL film of SF/NS5A-1 (1) and RSF (2) assembled onto carbon screen-printed electrodes. Reproduced with permission from ref 176.

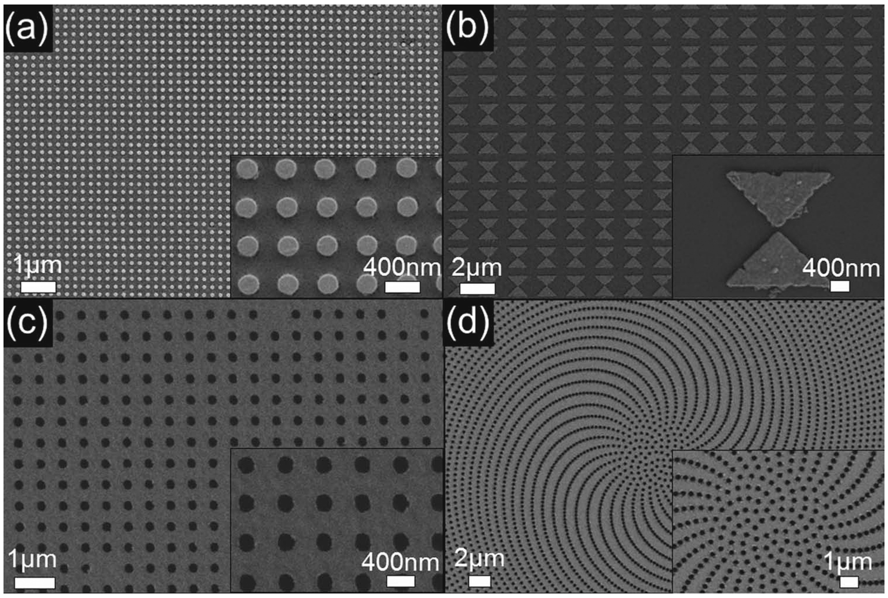

Figure 7. SEM images of transfer imprinted plasmonic nanodot arrays on doped silk fibroin films: (a) Periodic pattern of a = 400 nm and (b) bow tie structures with gaps of 40 nm. SEM images of transfer imprinted plasmonic nanohole arrays on doped silk fibrion films: (c) Periodic pattern of a = 600 nm and (d) α_2 spiral array with a_{ave} = 308 nm. Reproduced with permission from ref 182. Copyright 2012 Wiley–VCH.

positively charged RSSP (4RepCT) allowed cell attachment similar to control plates.[139] But on RESP (N[AS]$_8$C) films, also consisting of a positively charged protein, cell adhesion is quite low and the few cells detected on these films show a round morphology.[9]

One strategy to improve poor cell–silk surface interactions is to modify silk surfaces with recognition motifs (i.e., peptides) like the integrin binding motif RGD from fibronectin (Figure 4B).[22,108,133,140,141] Silk proteins can be modified genetically (in case of recombinant versions) or coupled chemically in all cases with RGD motifs. Here, a few examples will highlight the usability of such experimental set-ups. RGD-modified silk surfaces showed improved cell adhesion properties, and this effect could be detected for films made of negatively as well as for positively charged silk proteins.[108,142] In this context, researchers have created different blended RSF films with a synthetic RGD-containing spidroin for the analysis of osteoblastic differentiation,[143] analyzing the adhesion, proliferation and differentiation of an osteoblast precursor cell line (MC3T3-E1) on blended films (different RGD content accompanied by a different crystallinity). Increased crystallinity stabilizes the film and results in increased numbers of adherent cells, but no dependency of cellular differentiation was noted due to the β-sheet content. A ratio of 90:10 RSF to RGD-spidroin was optimal for the increased film stability and cell attachment. Another strategy to improve cell binding can be the coupling of macromolecules from the ECM (e.g., glycopolymers) to silk films.[144,145] RSSP films (e.g., eADF4(C16)) modified this way showed improved cell adhesion, and the morphology of the cells changed from round (unmodified films) to spread (modified films).[144]

Other peptides can be also suitable for increasing cell interactions with scaffolds and can lead to bone regeneration. Foo et al.[146] for example, modified the surface of RSSP 15mer films and electrospun fibers (nonwoven meshes) with the cell recognition motif RGD or a R5 peptide (a silicification inducing domain), which could be beneficial in the field of bone regeneration. Silicification could be only detected in the presence of the R5 peptide. Mieszawska and co-workers[152,153] were interested in silk-silica composite films and the behavior of human mesenchymal stem cells (hMSCs) seeded thereon. The RSF solution and silica solution (containing silica particles of

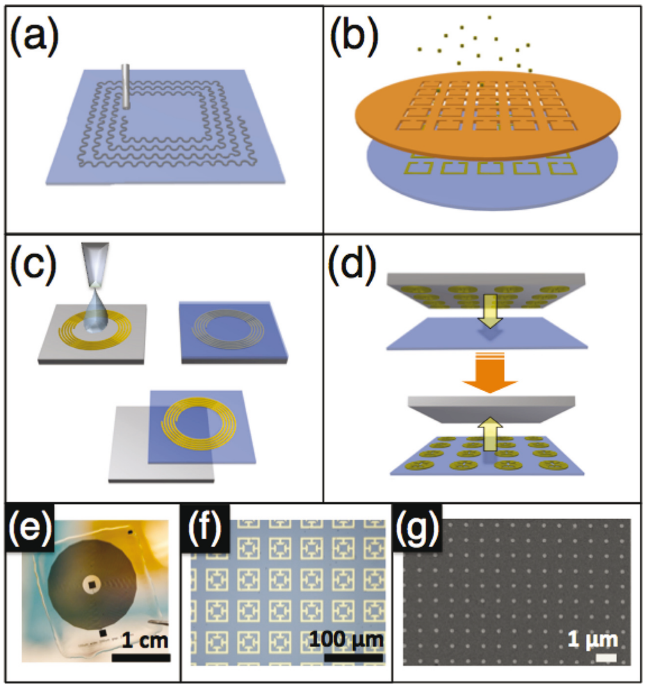

Figure 8. Schematics of fabrication processes for passive silk sensors. (a) Inkjet printing of functional components directly on the silk substrate. (b) Shadow-mask transfer. c) Casting-lift-off process. Functional components are fabricated directly on silanized silicon wafers. Silk is cast directly onto the silicon substrate, and the functional components are transferred onto the silk surface after drying under ambient conditions. (d) Direct transfer. Functionalized surfaces are applied to the silk substrate along with heat and pressure. Removal of the original substrate leaves the functional components on the surface of the silk substrate. (e) Example of a GHz resonant coil on silk, fabricated using the silk transfer applied micropatterning process (STAMP). (f) THz resonant silk metamaterial array, fabricated via shadow mask deposition. (g) Au nanoparticle array on silk, fabricated using direct transfer. Reproduced with permission from ref 184. Copyright 2012 Wiley−VCH.

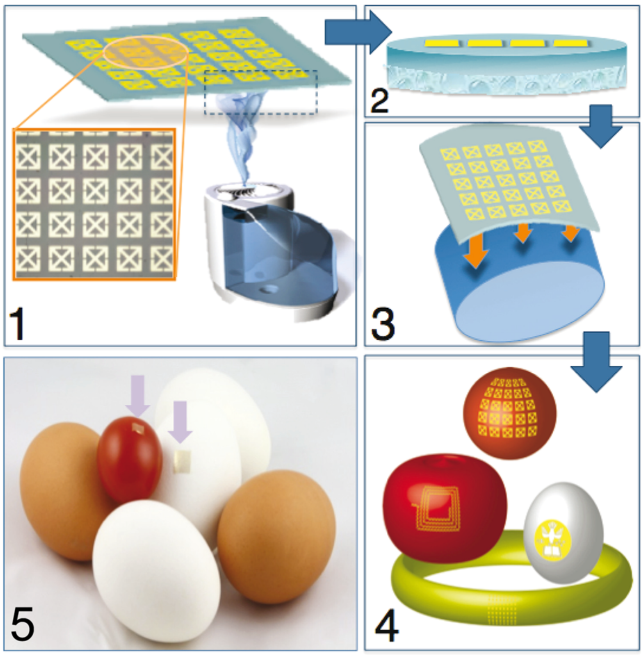

Figure 9. Rapid transfer of silk antennas onto curved substrates. (1) Water vapor is applied to the back of noncrystalline functionalized silk films, yielding (2) a functionalized film of which the back surface of the film has been partially molten. (3) The quasi-molten surface is conformally applied to arbitrary surfaces, yielding (4, 5) functional sensors thereon. Reproduced with permission from ref 184. Copyright 2012 Wiley−VCH.

24 nm, 500 nm, or 2 μm in diameter) were cast together on a cell culture plate and post-treated with methanol, yielding good proliferation rates of hMSCs as well as high cell densities. Osteogenic markers were up-regulated, and an increased formation of collagen/calcium phosphate was detected in the ECM, indicating osteoinductive properties of RSF/silica films.[147,148]

Cell attachment and proliferation, the polarity, morphology and cytoskeleton reorganization of bound cells, can be influenced by cell recognition motifs and the topography of a silk film's surface.[149,150] On flat films made of RSSP (eADF4(C16)) or RESP (N[AS]$_8$C), BALB/3T3 fibroblast adhesion was very weak.[9,108] BALB/3T3 fibroblasts as well as C2C12 myoblasts seeded on patterned films of eADF4(C16)/N[AS]$_8$C, with eADF4(C16) being the bottom layer, adhered in the grooves and proliferated better than on films of each individual protein. The cells aligned within the grooves and myoblasts even started to form myotubes, which is an important first step toward skeletal muscle regeneration (Figure 4C). Surprisingly, RGD-modified RSSP (eADF4(C16)) films as a ground layer did not result in significantly increased cell binding.[9]

An alternative to changing surface topography of silk films is the production of silk nonwoven meshes as a coating of substrates (Figure 4D). Nonwoven meshes with fiber diameters of 10−70 μm of RSSP (4RepCT) did not show improved cell adhesion and proliferation compared to smooth films.[139] However, hybrid matrices made of a bottom film layer on which a nonwoven mesh (diameter of fibers: 10−70 μm) was applied showed improved cell adhesion compared to smooth films or nonwoven meshes alone.[139] Cells like the vascular cell line HAECs or HCASMCs as well as endothelian cell line PIEC grew better on RSF nonwoven meshes (fiber diameter: 1016 nm[151] and 377 nm ±77 nm[152]) than on smooth RSF films.[151,152] Similar results were obtained by seeding BALB/3T3 fibroblasts on RSSP (eADF4(C16)) nonwoven meshes.[120] Nonwoven meshes with different fiber diameters (between 150 and 680 nm) were produced, and fibroblasts seeded thereon. The adhesion and proliferation rate of the cells increased with increasing fiber diameter likely due to the relation of cytoskeleton organization and space between the fibers of the mesh.

Patterned RSF films of different widths and depths were also used to orient mesenchymal stem cells (MSC) for compact bone regeneration.[106] One pattern in particular (3500 nm width/500 nm depth) induced osteogenic differentiation, a robust cell alignment and also ECM production similar to native cortical bone.

Neural stem cells were also cultured on films made of the positively charged RSSP (4RepCT). Cell adhesion and proliferation was comparable to the positive control (cell culture plates specifically treated for nerve cell cultivation).[153] Patterned films of negatively charged RSF with electrodes incorporated for axon alignment and outgrowth stimulation yielded varying results.[154] Stimulating the cells and monitoring over 3−5 days showed that the neural stem cells (P19) were growing, orientating along the grooves, and their axons aligned and grew out. However, after several days, the cells started to detach from the RSF surfaces. Not only RSF films but also fibers were used for nerve regeneration, which are not discussed further here. However, RSF fibers with a quite small diameter (400 nm) are more favorable to the development and maturation of neurons.[105]

3.1.2. Implants Made of or Coated with Silk. Animals with implants coated with silk generally show low levels of inflammation markers like cytokines.[76,119,155] Zeplin and co-workers coated silicone breast implants with RSSP with the aim of reducing the risk of capsular fibrosis.[76] Fibroblasts, which are critically involved in fibrosis, show decreased proliferation rates on spider silk coated silicone implants in comparison to uncoated ones. Primary human monocytes involved in fibrosis showed a significantly reduced differentiation into CD68-positive macrophages (histiocytes). Upon implantation into subcutaneous pockets of Spraque-Dawley rats, the coated implants were well-tolerated, and no wound healing disorders were detectable. Importantly, no liver granulomas and alterations of lymph nodes were detected, excluding the presence of infections or epitopic inflammation. After explantation, histological examinations of the uncoated implants showed periprosthetic tissue rich in fibroblasts and histiocytes organized in multiple cell layers, whereas silk-coated implants were surrounded by significantly fewer cells organized in only two layers. Additionally, the expression levels of several other fibrosis/inflammatory markers were significantly reduced.

For specific biomedical applications, enzymes and proteins can be coupled to silk films. Several specific proteins can be used for bone or dentin regeneration and some selected examples are explained in detail. The bone morphogenetic protein 2 (BMP-2) stimulates osteogenesis and was covalently bound to RSF films. BMP-2 silk films were more efficient in inducing osteogenic differentiation of bMSCs (bone mesenchymal stem cells) than free BMP-2 or a control silk film without BMP-2.[156] The dentin matrix protein 1 (DMP-1) is involved in nucleation and orients crystallization of hydroxyapatite within teeth, which is a prerequisite for their remarkable toughness and hardness.[157] Recently, RSSP/DMP-1 hybrids were analyzed versus plain RSSP films concerning biomineralization, i.e., the growth of hydroxyapatite crystals on the film surfaces. Films containing the DMP-1 protein were biomineralized, whereas films without DMP-1 did not induce biomineralization. Biomineralized RSF scaffolds were also used as bone grafts to repair canine inferior mandibular border defects.[158] The combination of bMSCs and apatite silk scaffolds led to fully repaired mandible defects in large animals, whereas the scaffold or bMSC alone showed incomplete bone repair 6 months after implantation. Furthermore, RSF can be processed directly into bone screws for fixation devices.[159] For better bone ingrowth into these implants or healing regulation, the RSF screws could be easily modified with BMP-2 protein or antibiotics to prevent infections.

For peripheral nerve repair Gu and co-workers fabricated a chitosan/RSF based scaffold.[55] For creation of a Schwann cell (SCs)-derived coating they were seeded on RSF/chitosan conduits for 14 days. By implanting the SC-derived ECM chitosan/RSF scaffold into rats the scaffold supported axonal outgrowth at an early regenerative stage and nerve regeneration. Although the new composite scaffold was not better than the acellular scaffold, it provided several advantages like pathogen-free production.

For application of silk scaffolds or coatings of implants in vivo, sometimes antibiotics or an antibacterial surface are required. Therefore, silver ions, known to be antimicrobial, were bound through a silver binding peptide to RSSP to yield antimicrobial silk surfaces.[160] In another series of experiments, antibiotics were loaded into RSF films which were incubated with *E. coli* and *Staphylococcus aureus*.[161] The antibiotic-loaded RSF films suppressed bacterial growth completely. RSSP films coupled with antimicrobial peptides also showed antimicrobial properties in tests with *E. coli* and *S. aureus*, whereas the simultaneously tested cell line (SaOs-2) was not affected.[162]

3.2. Silk Optics and Biosensors. Silk films and coatings can also be used in optical devices or biosensors and various applications mainly using *B. mori* fibroin have been reported, and some of them are highlighted herein. The oxygen permeability of RSF membranes is similar to that of hydrogel membranes which are used for soft contact lenses. Due to its biocompatibility, optical properties (e.g., high transparency) and oxygen permeability, RSF membranes are applicable as contact lens material.[163−165] Silk materials can also be processed into morphologies (e.g., by nanoimprinting, casting, spinning) useful in optical, photonic, electronic, and optoelectronic applications.[166] By nano- and micropatterning of optically transparent biocompatible RSF films, 3D diffraction patterns with a high fidelity were obtained.[167] Lawrence and co-workers used RSF to produce highly tailored structures and morphologies for optical devices (Figure 5).[168]

Curved rodlike optical waveguides have been produced by direct ink writing using RSF "ink" containing 28−38% RSF, followed by methanol post-treatment showing controlled structure and composition.[169] Photoactivation of drugs in silk structures is also possible, because silk biomaterials provide a perfect matrix for stabilizing enzymes because of their thermal, chemical, and mechanical robustness. Different approaches for immobilizing enzymes in silk protein materials were successful, conserving enzyme activity over months to years e.g. for their use in biosensors.[170−172] Lu and co-workers blended glucose oxidase (GOx), horseradish peroxidase (HRP) or lipase with RSF and cast the blended material into films.[173] Demura[171] and Asakura and co-workers[174] immobilized glucose oxidase (GOx) for biosensing of glucose. HRP or lipase immobilized in RSF films were used for the determination of hydrogen peroxide and uric acid in a flow injection system.[173] Tao and co-workers used a microstructured multifunctional RSF optical element for simultaneous drug delivery and feedback response.[175]

Antigens as disease detecting biosensors were also immobilized on RSF membranes.[176,177] The peptide NS5A-1 (PPLLESWKDPDYVPPWHG) derived from the hepatitis C virus (HCV) was immobilized on RSF films coating carbon screen-printed electrodes using a layer-by-layer technique (Figure 6).[176] Although plain RSF films showed no significant response, the immunosensor made of SF/NS5A-1 LbL-films showed a signal in presence of the anti-HCV (1 μg/mL), thus establishing a highly sensitive immunosensor.[176]

Other types of sustainable sensors made of silk are photonic crystals.[178,179] Three-dimensional photonic crystals were fabricated by pouring RSF solution over a mask of a close packed self-assembled colloidal crystal of poly(methyl methacrylate) (PMMA) spheres. After a drying step, PMMA is dissolved and the silk inverse opal (SIO) is obtained. The color can be controlled by changing the size of the PMMA spheres and by filling the voids with liquids like acetone. Because of their intrinsic structural color and biocompatibility, these silk materials are suitable for microscale implantable biosensing and targeted therapeutics.[178,179] Further work generated silk-protein based hybrid photonic-plasmonic crystals (HPPC), incorporating a 3D SIO and a 2D plasmonic crystal formed on top of the SIO to combine the properties of these two structures (2D SIO & 3D pseudophotonic band gap) making it suitable as a multispectral refractive index sensor.[180] Diao et al. produced SIOs with bistructural colors at UV and visible, UV and IR, and visible and IR wavelengths. The SIOs showed a linear relation between humidity and the wavelength of the reflected light, which gives rise to optical humidity sensors.[181]

Lin and co-workers demonstrated a direct transfer of subwavelength plasmonic nanostructures on bioactive RSF films, overcoming problems of integrating plasmonic metallic nanostructures into biopolymeric ones.[182] A direct transfer nanofabrication technique (based on nanotransfer printing) was used for the fabrication of large-scale metallic nanoparticles (plasmonic nanodots) and perforated metallic films (plasmonic nanoholes) on RSF films, obtaining a high fidelity sequential transfer of plasmonic nanoparticles, optical bow tie nanoantennas, and nanohole arrays with periodic and nonperiodic geometries, preserving the functionality of the imprinted biopolymer. Some examples of the structures obtained are shown in Figure 7.

Silk films also can be used to produce curvilinear electronics for different applications like biointegrated electronics for diagnosing, treating disease, or improving brain/machine interfaces;[183] adhesive and edible food sensors;[184] and to attach graphene-based biosensors onto biomaterials like tooth enamel as fully biointerfaced nanosensors.[185] Silk-based conformal, adhesive, and edible food sensors made of RSF described by Tao et al. are also a good example for such sensors.[184] Different methods can be used to produce/transfer micro- and nanopatterns onto silk substrates, and Figure 8a–d shows the most common methods used by Tao and coworkers. Examples of the fabricated structures are GHz resonators, THz metamaterials and nanopatterned Au-nanoparticle plasmonic arrays on silk (Figure 8e–g).

To attach the structures to surfaces for biosensing applications, the noncrystalline (not post-treated) carrier RSF film is exposed to water vapor to be softened. The adhesive thin layer of silk acts as "glue" and can be used to adhere the antenna to the target surface without damaging the antennas. The attachment process is shown in Figure 9.

An interesting application of this technology is the monitoring of the fruit ripening process. The resonant frequency of a banana's surface was measuered over 9 days while ripening, showing an initial resonance at day 0 of 36.1 MHz, which increased constantly to higher frequencies (up to 42.6 MHz at day 9) during ripening.

4. CONCLUSION AND FUTURE PERSPECTIVES

Silks are proteinaceous materials with a long history of use by humans. In recent decades, the structure and composition of several silk proteins of different animals have been characterized, and biotechnological protein production strategies give rise to high yields of pure proteins. The silk protein materials are biocompatible and biodegradable, but are not immunogenic, allergenic, or toxic. There are various possibilities to control the properties of silk materials, and though various processing methods (e.g., casting, printing, electrospinning, dip coating, etc.) result in a broad range of structures (e.g., films, nonwoven mats, coatings, etc.). The properties of the fabricated materials, like material stability, surface hydrophobicity, oxygen permeability and optical properties, vary depending on the silk protein used, the processing method and the processing conditions (e.g., solvents, additives, post-treatments). Cell binding properties can be improved by modifying the surface topographies and introducing cell binding motifs. Other proteins and enzymes can be coupled to or immobilized in silk materials by chemical and genetic modification or blending. Enzymes, for instance, show high long-time stability when incorporated in silk materials. Understanding the structure–function relationship of silk proteins allows the design of sustainable and more complex and highly tailored silk-based structures like photonic nanostructures, silk inverse opals (SIO), LbL films, curvilinear electronics, optoelectronics, and biosensors.

AUTHOR INFORMATION

Corresponding Author

*E-mail: thomas.scheibel@bm.uni-bayreuth.de.

Notes

The authors declare no competing financial interest.

ACKNOWLEDGMENTS

We thank Joschka Bauer, Martin Humenik, Eileen Lintz, Kristin Schacht and Stefanie Wohlrab for helpful discussions on the manuscript and Sarah Fischer for technical help with the figures and artwork. Special thanks go to Gregor Lang for nonwoven meshes pictures of spider silk. This work is supported by the SFB 840 TP A8.

REFERENCES

(1) Craig, C. L. Evolution of Arthropod Silks. *Annu. Rev. Entomol.* **1997**, *42*, 231–267.

(2) Sutherland, T. D.; Young, J. H.; Weisman, S.; Hayashi, C. Y.; Merritt, D. J. Insect Silk: One Name, Many Materials. *Annu. Rev. Entomol.* **2010**, *55*, 171–188.

(3) Vollrath, F.; Porter, D. Spider Silk as Archetypal Protein Elastomer. *Soft Matter* **2006**, *2*, 377–385.

(4) Newman, J.; Newman, C. Oh What a Tangled Web: The Medicinal Uses of Spider Silk. *Int. J. Dermatol.* **1995**, *34*, 290–292.

(5) Gerritsen, V. B. The Tiptoe of an Airbus. *Protein Spotlight* **2002**, *24*, 1–2.

(6) Gosline, J. M.; Guerette, P. A.; Ortlepp, C. S.; Savage, K. N. The Mechanical Design of Spider Silks: From Fibroin Sequence to Mechanical Function. *J. Exp. Biol.* **1999**, *202*, 3295–3303.

(7) Heim, M.; Keerl, D.; Scheibel, T. Spider Silk: From Soluble Protein to Extraordinary Fiber. *Angew. Chem., Int. Ed.* **2009**, *48*, 3584–3596.

(8) Madsen, B.; Shao, Z. Z.; Vollrath, F. Variability in the Mechanical Properties of Spider Silks on Three Levels: Interspecific, Intraspecific and Intraindividual. *Int. J. Biol. Macromol.* **1999**, *24*, 301–306.

(9) Bauer, F.; Wohlrab, S.; Scheibel, T. Controllable Cell Adhesion, Growth and Orientation on Layered Silk Protein Films. *Biomater. Sci.* **2013**, *1*, 1244–1249.

(10) Bauer, F.; Bertinetti, L.; Masic, A.; Scheibel, T. Dependence of Mechanical Properties of Lacewing Egg Stalks on Relative Humidity. *Biomacromolecules* **2012**, *13*, 3730–3735.

(11) Gührs, K.-H.; Weisshart, K.; Grosse, F. Lessons from Nature – Protein Fibers. *Rev. Mol. Biotechnol.* **2000**, *74*, 121–134.

(12) Altman, G. H.; Diaz, F.; Jakuba, C.; Calabro, T.; Horan, R. L.; Chen, J.; Lu, H.; Richmond, J.; Kaplan, D. L. Silk-Based Biomaterials. *Biomaterials* **2003**, *24*, 401–416.

(13) Hardy, J. G.; Römer, L. M.; Scheibel, T. R. Polymeric Materials Based on Silk Proteins. *Polymer* **2008**, *49*, 4309–4327.

(14) Leal-Egaña, A.; Scheibel, T. Silk-Based Materials for Biomedical Applications. *Biotechnol. Appl. Biochem.* **2010**, *55*, 155−167.

(15) Sehnal, F.; Sutherland, T. Silks Produced by Insect Labial Glands. *Prion* **2008**, *2*, 145−153.

(16) Inoue, S.; Tanaka, K.; Arisaka, F.; Kimura, S.; Ohtomo, K.; Mizuno, S. Silk Fibroin of *Bombyx mori* Is Secreted, Assembling a High Molecular Mass Elementary Unit Consisting of H-Chain, L-Chain, and P25, with a 6:6:1 Molar Ratio. *J. Biol. Chem.* **2000**, *275*, 40517−40528.

(17) Zhou, C.-Z.; Confalonieri, F.; Jacquet, M.; Perasso, R.; Li, Z.-G.; Janin, J. Silk Fibroin: Structural Implications of a Remarkable Amino Acid Sequence. *Proteins: Struct., Funct., Genet.* **2001**, *44*, 119−122.

(18) Craig, C. L.; Riekel, C. Comparative Architecture of Silks, Fibrous Proteins and Their Encoding Genes in Insects and Spiders. *Comp. Biochem. Physiol., Part B: Biochem. Mol. Biol.* **2002**, *133*, 493−507.

(19) Lintz, E. S.; Scheibel, T. R. Dragline, Egg Stalk and Byssus: A Comparison of Outstanding Protein Fibers and Their Potential for Developing New Materials. *Adv. Funct. Mater.* **2013**, *23*, 4467−4482.

(20) Fu, C.; Shao, Z.; Vollrath, F. Animal Silks: Their Structures, Properties and Artificial Production. *Chem. Commun.* **2009**, 6515−6529.

(21) Freddi, G.; Mossotti, R.; Innocenti, R. Degumming of Silk Fabric with Several Proteases. *J. Biotechnol.* **2003**, *106*, 101−112.

(22) Yanagisawa, S.; Zhu, Z.; Kobayashi, I.; Uchino, K.; Tamada, Y.; Tamura, T.; Asakura, T. Improving Cell-Adhesive Properties of Recombinant *Bombyx mori* Silk by Incorporation of Collagen or Fibronectin Derived Peptides Produced by Transgenic Silkworms. *Biomacromolecules* **2007**, *8*, 3487−3492.

(23) Earland, C.; Robins, S. P. Isolation and Characterization of a Cystine-Containing Octapeptide from Silk. *Experientia* **1969**, *25*, 905.

(24) Dewair, M.; Baur, X.; Ziegler, K. Use of Immunoblot Technique for Detection of Human IgE and IgG Antibodies to Individual Silk Proteins. *J. Allergy Clin. Immunol.* **1985**, *76*, 537−542.

(25) Kurosaki, S.; Otsuka, H.; Kunitomo, M.; Koyama, M.; Pawankar, R.; Matumoto, K. Fibroin Allergy. IgE Mediated Hypersensitivity to Silk Suture Materials. *J. Nippon Med. Sch.* **1999**, *66*, 41−44.

(26) Wen, C. M.; Ye, S. T.; Zhou, L. X.; Yu, Y. Silk-Induced Asthma in Children: A Report of 64 Cases. *Ann. Allergy* **1990**, *65*, 375−378.

(27) Soong, H. K.; Kenyon, K. R. Adverse Reactions to Virgin Silk Sutures in Cataract Surgery. *Ophthalmology* **1984**, *91*, 479−483.

(28) Weisman, S.; Trueman, H. E.; Mudie, S. T.; Church, J. S.; Sutherland, T. D.; Haritos, V. S. An Unlikely Silk: The Composite Material of Green Lacewing Cocoons. *Biomacromolecules* **2008**, *9*, 3065−3069.

(29) Lucas, F.; Shaw, J. T. B.; Smith, S. G. Amino-Acid Composition of the Silk of *Chrysopa* Egg-Stalks. *Nature* **1957**, *179*, 906−907.

(30) Parker, K. D.; Rudall, K. M. Structure of the Silk of *Chrysopa* Egg-Stalks. *Nature* **1957**, *179*, 905−906.

(31) Weisman, S.; Okada, S.; Mudie, S. T.; Huson, M. G.; Trueman, H. E.; Sriskantha, A.; Haritos, V. S.; Sutherland, T. D. Fifty Years Later: The Sequence, Structure and Function of Lacewing Cross-Beta Silk. *J. Struct. Biol.* **2009**, *168*, 467−475.

(32) Bauer, F.; Scheibel, T. Artificial Egg Stalks Made of a Recombinantly Produced Lacewing Silk Protein. *Angew. Chem., Int. Ed.* **2012**, *51*, 6521−6524.

(33) Stauffer, S. L.; Coguill, S. L.; Lewis, R. V. Comparison of Physical Properties of 3 Silks from *Nephila Clavipes* and *Araneus Gemmoides*. *J. Arachnol.* **1994**, *22*, 5−11.

(34) Vollrath, F. Biology of Spider Silk. *Int. J. Biol. Macromol.* **1999**, *24*, 81−88.

(35) Winkler, S.; Kaplan, D. L. Molecular Biology of Spider Silk. *Rev. Mol. Biotechnol.* **2000**, *74*, 85−93.

(36) Römer, L.; Scheibel, T. The Elaborate Structure of Spider Silk − Structure and Function of a Natural High Performance Fiber. *Prion* **2008**, *2*, 154−161.

(37) Eisoldt, L.; Thamm, C.; Scheibel, T. Review the Role of Terminal Domains During Storage and Assembly of Spider Silk Proteins. *Biopolymers* **2012**, *97*, 355−361.

(38) Gosline, J.; Lillie, M.; Carrington, E.; Guerette, P.; Ortlepp, C.; Savage, K. Elastic Proteins: Biological Roles and Mechanical Properties. *Philos. Trans. R. Soc., B* **2002**, *357*, 121−132.

(39) Cranford, S. W.; Tarakanova, A.; Pugno, N. M.; Buehler, M. J. Nonlinear Material Behaviour of Spider Silk Yields Robust Webs. *Nature* **2012**, *482*, 72−76.

(40) Elices, M.; Plaza, G. R.; Pérez-Rigueiro, J.; Guinea, G. V. The Hidden Link between Supercontraction and Mechanical Behavior of Spider Silks. *J. Mech. Behav. Biomed. Mater.* **2011**, *4*, 658−669.

(41) ap Rhisiart, A.; Vollrath, F. Design Features of the Orb Web of the Spider *Araneus diadematus*. *Behav. Ecol.* **1994**, *5*, 280−287.

(42) Blackledge, T. A.; Summers, A. P.; Hayashi, C. Y. Gumfooted Lines in Black Widow Cobwebs and the Mechanical Properties of Spider Capture Silk. *Zoology* **2005**, *108*, 41−46.

(43) Thiel, B. L.; Viney, C. Beta Sheets and Spider Silk. *Science* **1996**, *273*, 1480−1481.

(44) Viney, C. Natural Silks: Archetypal Supramolecular Assembly of Polymer Fibres. *Supramol. Sci.* **1997**, *4*, 75−81.

(45) Liu, Y.; Sponner, A.; Porter, D.; Vollrath, F. Proline and Processing of Spider Silks. *Biomacromolecules* **2008**, *9*, 116−121.

(46) Ayoub, N. A.; Garb, J. E.; Tinghitella, R. M.; Collin, M. A.; Hayashi, C. Y. Blueprint for a High-Performance Biomaterial: Full-Length Spider Dragline Silk Genes. *PLoS One* **2007**, *2*, e514.

(47) Garb, J. E.; Ayoub, N. A.; Hayashi, C. Y. Untangling Spider Silk Evolution with Spidroin Terminal Domains. *BMC Evol. Biol.* **2010**, *10:243*, 1−16.

(48) Eisoldt, L.; Smith, A.; Scheibel, T. Decoding the Secrets of Spider Silk. *Mater. Today* **2011**, *14*, 80−86.

(49) Sponner, A.; Vater, W.; Monajembashi, S.; Unger, E.; Grosse, F.; Weisshart, K. Composition and Hierarchical Organisation of a Spider Silk. *PLoS One* **2007**, *2*, e998.

(50) Hakimi, O.; Knight, D. P.; Knight, M. M.; Grahn, M. F.; Vadgama, P. Ultrastructure of Insect and Spider Cocoon Silks. *Biomacromolecules* **2006**, *7*, 2901−2908.

(51) Rising, A.; Widhe, M.; Johansson, J.; Hedhammar, M. Spider Silk Proteins: Recent Advances in Recombinant Production, Structure−Function Relationships and Biomedical Applications. *Cell. Mol. Life Sci.* **2011**, *68*, 169−184.

(52) Lefèvre, T.; Rousseau, M.-E.; Pézolet, M. Protein Secondary Structure and Orientation in Silk as Revealed by Raman Spectromicroscopy. *Biophys. J.* **2007**, *92*, 2885−2895.

(53) Paquet-Mercier, F.; Lefèvre, T.; Auger, M.; Pézolet, M. Evidence by Infrared Spectroscopy of the Presence of Two Types of β-Sheets in Major Ampullate Spider Silk and Silkworm Silk. *Soft Matter* **2013**, *9*, 208−215.

(54) Keerl, D.; Scheibel, T. Characterization of Natural and Biomimetic Spider Silk Fibers. *Bioinspired, Biomimetic Nanobiomater.* **2012**, *1*, 83−94.

(55) Ene, R.; Papadopoulos, P.; Kremer, F. Quantitative Analysis of Infrared Absorption Coefficient of Spider Silk Fibers. *Vib. Spectrosc.* **2011**, *57*, 207−212.

(56) Anton, M. A.; Kossack, W.; Gutsche, C.; Figuli, R.; Papadopoulos, P.; Ebad-Allah, J.; Kuntscher, C.; Kremer, F. Pressure-Dependent FTIR-Spectroscopy on the Counterbalance between External and Internal Constraints in Spider Silk of *Nephila Pilipes*. *Macromolecules* **2013**, *46*, 4919−4923.

(57) Papadopoulos, P.; Sölter, J.; Kremer, F. Hierarchies in the Structural Organization of Spider Silk - a Quantitative Model. *Colloid Polym. Sci.* **2009**, *287*, 231−236.

(58) Guehrs, K.-H.; Schlott, B.; Grosse, F.; Weisshart, K. Environmental Conditions Impinge on Dragline Silk Protein Composition. *Insect Mol. Biol.* **2008**, *17*, 553−564.

(59) Heidebrecht, A.; Scheibel, T. Recombinant Production of Spider Silk Proteins. *Adv. Appl. Microbiol.* **2013**, *82*, 115−153.

(60) Vendrely, C.; Scheibel, T. Biotechnological Production of Spider-Silk Proteins Enables New Applications. *Macromol. Biosci.* **2007**, *7*, 401−409.

(61) Scheibel, T. Spider Silks: Recombinant Synthesis, Assembly, Spinning, and Engineering of Synthetic Proteins. *Microb. Cell Fact.* **2004**, *3*, 14.

(62) Huemmerich, D.; Helsen, C. W.; Quedzuweit, S.; Oschmann, J.; Rudolph, R.; Scheibel, T. Primary Structure Elements of Spider Dragline Silks and Their Contribution to Protein Solubility. *Biochemistry* **2004**, *43*, 13604−13612.

(63) Rammensee, S.; Slotta, U.; Scheibel, T.; Bausch, A. R. Assembly Mechanism of Recombinant Spider Silk Proteins. *Proc. Natl. Acad. Sci. U.S.A.* **2008**, *105*, 6590−6595.

(64) Sanford, K.; Kumar, M. New Proteins in a Materials World. *Curr. Opin. Biotechnol.* **2005**, *16*, 416−421.

(65) Phillips, D. M.; Drummy, L. F.; Conrady, D. G.; Fox, D. M.; Naik, R. R.; Stone, M. O.; Trulove, P. C.; De Long, H. C.; Mantz, R. A. Dissolution and Regeneration of *Bombyx mori* Silk Fibroin Using Ionic Liquids. *J. Am. Chem. Soc.* **2004**, *126*, 14350−14351.

(66) Gupta, M. K.; Khokhar, S. K.; Phillips, D. M.; Sowards, L. A.; Drummy, L. F.; Kadakia, M. P.; Naik, R. R. Patterned Silk Films Cast from Ionic Liquid Solubilized Fibroin as Scaffolds for Cell Growth. *Langmuir* **2007**, *23*, 1315−1319.

(67) Kawahara, Y.; Furukawa, K.; Yamamoto, T. Self-Expansion Behavior of Silk Fibroin Film. *Macromol. Mater. Eng.* **2006**, *291*, 458−462.

(68) Dai, L.; Li, J.; Yamada, E. Effect of Glycerin on Structure Transition of PVA/SF Blends. *J. Appl. Polym. Sci.* **2002**, *86*, 2342−2347.

(69) Lu, S.; Wang, X.; Lu, Q.; Zhang, X.; Kluge, J. A.; Uppal, N.; Omenetto, F.; Kaplan, D. L. Insoluble and Flexible Silk Films Containing Glycerol. *Biomacromolecules* **2010**, *11*, 143−150.

(70) Hardy, J. G.; Scheibel, T. R. Composite Materials Based on Silk Proteins. *Prog. Polym. Sci.* **2010**, *35*, 1093−1115.

(71) del Campo, A.; Arzt, E. Fabrication Approaches for Generating Complex Micro- and Nanopatterns on Polymeric Surfaces. *Chem. Rev.* **2008**, *108*, 911−945.

(72) Tawfick, S.; De Volder, M.; Copic, D.; Park, S. J.; Oliver, C. R.; Polsen, E. S.; Roberts, M. J.; Hart, A. J. Engineering of Micro- and Nanostructured Surfaces with Anisotropic Geometries and Properties. *Adv. Mater.* **2012**, *24*, 1628−1674.

(73) Junghans, F.; Morawietz, M.; Conrad, U.; Scheibel, T.; Heilmann, A.; Spohn, U. Preparation and Mechanical Properties of Layers Made of Recombinant Spider Silk Proteins and Silk from Silk Worm. *Appl. Phys. A: Mater. Sci. Process.* **2006**, *82*, 253−260.

(74) Spiess, K.; Wohlrab, S.; Scheibel, T. Structural Characterization and Functionalization of Engineered Spider Silk Films. *Soft Matter* **2010**, *6*, 4168−4174.

(75) Greving, I.; Cai, M.; Vollrath, F.; Schniepp, H. C. Shear-Induced Self-Assembly of Native Silk Proteins into Fibrils Studied by Atomic Force Microscopy. *Biomacromolecules* **2012**, *13*, 676−682.

(76) Zeplin, P. H.; Maksimovikj, N. C.; Jordan, M. C.; Nickel, J.; Lang, G.; Leimer, A. H.; Römer, L.; Scheibel, T. Spider Silk Coatings as a Bioshield to Reduce Periprosthetic Fibrous Capsule Formation. *Adv. Funct. Mater.* **2014**, *24*, 2658−2666.

(77) Zasadzinski, J. A.; Viswanathan, R.; Madsen, L.; Garnaes, J.; Schwartz, D. K. Langmuir-Blodgett-Films. *Science* **1994**, *263*, 1726−1733.

(78) Decher, G. Fuzzy Nanoassemblies: Toward Layered Polymeric Multicomposites. *Science* **1997**, *277*, 1232−1237.

(79) Greiner, A.; Wendorff, J. H. Electrospinning: A Fascinating Method for the Preparation of Ultrathin Fibres. *Angew. Chem., Int. Ed.* **2007**, *46*, 5670−5703.

(80) Zhang, X.; Reagan, M. R.; Kaplan, D. L. Electrospun Silk Biomaterial Scaffolds for Regenerative Medicine. *Adv. Drug Delivery Rev.* **2009**, *61*, 988−1006.

(81) Zhu, J.; Shao, H.; Hu, X. Morphology and Structure of Electrospun Mats from Regenerated Silk Fibroin Aqueous Solutions with Adjusting PH. *Int. J. Biol. Macromol.* **2007**, *41*, 469−474.

(82) Zhou, S.; Peng, H.; Yu, X.; Zheng, X.; Cui, W.; Zhang, Z.; Li, X.; Wang, J.; Weng, J.; Jia, W.; Li, F. Preparation and Characterization of a Novel Electrospun Spider Silk Fibroin/Poly(D,L-Lactide) Composite Fiber. *J. Phys. Chem. B* **2008**, *112*, 11209−11216.

(83) Park, W. H.; Jeong, L.; Yoo, D. I.; Hudson, S. Effect of Chitosan on Morphology and Conformation of Electrospun Silk Fibroin Nanofibers. *Polymer* **2004**, *45*, 7151−7157.

(84) Zhang, F.; Zuo, B.; Fan, Z.; Xie, Z.; Lu, Q.; Zhang, X.; Kaplan, D. L. Mechanisms and Control of Silk-Based Electrospinning. *Biomacromolecules* **2012**, *13*, 798−804.

(85) Boccaccini, A. R.; Keim, S.; Ma, R.; Li, Y.; Zhitomirsky, I. Electrophoretic Deposition of Biomaterials. *J. R. Soc., Interface* **2010**, *7*, S581−S613.

(86) Maniglio, D.; Bonani, W.; Bortoluzzi, G.; Servoli, E.; Motta, A.; Migliaresi, C. Electrodeposition of Silk Fibroin on Metal Substrates. *J. Bioact. Compat. Polym.* **2010**, *25*, 441−454.

(87) Zhang, Z.; Jiang, T.; Ma, K.; Cai, X.; Zhou, Y.; Wang, Y. Low Temperature Electrophoretic Deposition of Porous Chitosan/Silk Fibroin Composite Coating for Titanium Biofunctionalization. *J. Mater. Chem.* **2011**, *21*, 7705−7713.

(88) Claussen, K. U.; Giesa, R.; Scheibel, T.; Schmidt, H.-W. Learning from Nature: Synthesis and Characterization of Longitudinal Polymer Gradient Materials Inspired by Mussel Byssus Threads. *Macromol. Rapid Commun.* **2012**, *33*, 206−201.

(89) Claussen, K. U.; Lintz, E. S.; Giesa, R.; Schmidt, H.-W.; Scheibel, T. Protein Gradient Films of Fibroin and Gelatine. *Macromol. Biosci.* **2013**, *13*, 1396−1403.

(90) Zhao, C.; Yao, J.; Masuda, H.; Kishore, R.; Asakura, T. Structural Characterization and Artificial Fiber Formation of *Bombyx mori* Silk Fibroin in Hexafluoro-Iso-Propanol Solvent System. *Biopolymers* **2003**, *69*, 253−259.

(91) Stephens, J. S.; Fahnestock, S. R.; Farmer, R. S.; Kiick, K. L.; Chase, D. B.; Rabolt, J. F. Effects of Electrospinning and Solution Casting Protocols on the Secondary Structure of a Genetically Engineered Dragline Spider Silk Analogue Investigated via Fourier Transform Raman Spectroscopy. *Biomacromolecules* **2005**, *6*, 1405−1413.

(92) Huemmerich, D.; Slotta, U.; Scheibel, T. Processing and Modification of Films Made from Recombinant Spider Silk Proteins. *Appl. Phys. A: Mater. Sci. Process.* **2006**, *82*, 219−222.

(93) Slotta, U.; Tammer, M.; Kremer, F.; Koelsch, P.; Scheibel, T. Structural Analysis of Spider Silk Films. *Supramol. Chem.* **2006**, *18*, 465−471.

(94) Ha, S.-W.; Tonelli, A. E.; Hudson, S. M. Structural Studies of *Bombyx mori* Silk Fibroin During Regeneration from Solutions and Wet Fiber Spinning. *Biomacromolecules* **2005**, *6*, 1722−1731.

(95) Um, I. C.; Kweon, H. Y.; Park, Y. H.; Hudson, S. Structural Characteristics and Properties of the Regenerated Silk Fibroin Prepared from Formic Acid. *Int. J. Biol. Macromol.* **2001**, *29*, 91−97.

(96) Vasconcelos, A.; Freddi, G.; Cavaco-Paulo, A. Biodegradable Materials Based on Silk Fibroin and Keratin. *Biomacromolecules* **2008**, *9*, 1299−1305.

(97) Min, B.-M.; Jeong, L.; Nam, Y. S.; Kim, J.-M.; Kim, J. Y.; Park, W. H. Formation of Silk Fibroin Matrices with Different Texture and Its Cellular Response to Normal Human Keratinocytes. *Int. J. Biol. Macromol.* **2004**, *34*, 223−230.

(98) Spiess, K.; Ene, R.; Keenan, C. D.; Senker, J.; Kremer, F.; Scheibel, T. Impact of Initial Solvent on Thermal Stability and Mechanical Properties of Recombinant Spider Silk Films. *J. Mater. Chem.* **2011**, *21*, 13594−13604.

(99) Wohlrab, S.; Spieß, K.; Scheibel, T. Varying Surface Hydrophobicities of Coatings Made of Recombinant Spider Silk Proteins. *J. Mater. Chem.* **2012**, *22*, 22050−22054.

(100) Hu, X.; Lu, Q.; Kaplan, D. L.; Cebe, P. Microphase Separation Controlled *β*-Sheet Crystallization Kinetics in Fibrous Proteins. *Macromolecules* **2009**, *42*, 2079−2087.

(101) Cebe, P.; Hu, X.; Kaplan, D. L.; Zhuravlev, E.; Wurm, A.; Arbeiter, D.; Schick, C. Beating the Heat - Fast Scanning Melts Silk Beta Sheet Crystals. *Sci. Rep.* **2013**, *3:1130*, 1−7.

(102) Lawrence, B. D.; Wharram, S.; Kluge, J. A.; Leisk, G. G.; Omenetto, F. G.; Rosenblatt, M. I.; Kaplan, D. L. Effect of Hydration on Silk Film Material Properties. *Macromol. Biosci.* **2010**, *10*, 393−403.

(103) Tsioris, K.; Tao, H.; Liu, M.; Hopwood, J. A.; Kaplan, D. L.; Averitt, R. D.; Omenetto, F. G. Rapid Transfer-Based Micropatterning and Dry Etching of Silk Microstructures. *Adv. Mater.* **2011**, *23*, 2015−2019.

(104) Young, S. L.; Gupta, M.; Hanske, C.; Fery, A.; Scheibel, T.; Tsukruk, V. V. Utilizing Conformational Changes for Patterning Thin Films of Recombinant Spider Silk Proteins. *Biomacromolecules* **2012**, *13*, 3189−3199.

(105) Gil, E. S.; Park, S.-H.; Marchant, J.; Omenetto, F.; Kaplan, D. L. Response of Human Corneal Fibroblasts on Silk Film Surface Patterns. *Macromol. Biosci.* **2010**, *10*, 664−673.

(106) Tien, L. W.; Gil, E. S.; Park, S.-H.; Mandal, B. B.; Kaplan, D. L. Patterned Silk Film Scaffolds for Aligned Lamellar Bone Tissue Engineering. *Macromol. Biosci.* **2012**, *12*, 1671−1679.

(107) Murphy, A. R.; Kaplan, D. L. Biomedical Applications of Chemically-Modified Silk Fibroin. *J. Mater. Chem.* **2009**, *19*, 6443−6450.

(108) Wohlrab, S.; Müller, S.; Schmidt, A.; Neubauer, S.; Kessler, H.; Leal-Egaña, A.; Scheibel, T. Cell Adhesion and Proliferation on RGD-Modified Recombinant Spider Silk Proteins. *Biomaterials* **2012**, *33*, 6650−6659.

(109) Romero, I. S.; Schurr, M. L.; Lally, J. V.; Kotlik, M. Z.; Murphy, A. R. Enhancing the Interface in Silk-Polypyrrole Composites through Chemical Modification of Silk Fibroin. *ACS Appl. Mater. Interfaces* **2013**, *5*, 553−564.

(110) Wilson, D.; Valluzzi, R.; Kaplan, D. Conformational Transitions in Model Silk Peptides. *Biophys. J.* **2000**, *78*, 2690−2701.

(111) Metwalli, E.; Slotta, U.; Darko, C.; Roth, S. V.; Scheibel, T.; Papadakis, C. M. Structural Changes of Thin Films from Recombinant Spider Silk Proteins Upon Post-Treatment. *Appl. Phys. A: Mater. Sci. Process.* **2007**, *89*, 655−661.

(112) Hu, X.; Kaplan, D.; Cebe, P. Dynamic Protein-Water Relationships During Beta-Sheet Formation. *Macromolecules* **2008**, *41*, 3939−3948.

(113) Jin, H.-J.; Park, J.; Karageorgiou, V.; Kim, U.-J.; Valluzzi, R.; Cebe, P.; Kaplan, D. L. Water-Stable Silk Films with Reduced Beta-Sheet Content. *Adv. Funct. Mater.* **2005**, *15*, 1241−1247.

(114) Peng, H.; Zhou, S.; Jiang, J.; Guo, T.; Zheng, X.; Yu, X. Pressure-Induced Crystal Memory Effect of Spider Silk Proteins. *J. Phys. Chem. B* **2009**, *113*, 4636−4641.

(115) Jin, H.-J.; Kaplan, D. L. Mechanism of Silk Processing in Insects and Spiders. *Nature* **2003**, *424*, 1057−1061.

(116) Chen, X.; Knight, D. P.; Shao, Z.; Vollrath, F. Conformation Transition in Silk Protein Films Monitored by Time-Resolved Fourier Transform Infrared Spectroscopy: Effect of Potassium Ions on *Nephila* Spidroin Films. *Biochemistry* **2002**, *41*, 14944−14950.

(117) Hardy, J. G.; Scheibel, T. Production and Processing of Spider Silk Proteins. *J. Polym. Sci., Part A: Polym. Chem.* **2009**, *47*, 3957−3963.

(118) Tang, X.; Ding, F.; Yang, Y.; Hu, N.; Wu, H.; Gu, X. Evaluation on *in vitro* Biocompatibility of Silk Fibroin-Based Biomaterials with Primarily Cultured Hippocampal Neurons. *J. Biomed. Mater. Res., Part A* **2009**, *91A*, 166−174.

(119) Meinel, L.; Hofmann, S.; Karageorgiou, V.; Kirker-Head, C.; McCool, J.; Gronowicz, G.; Zichner, L.; Langer, R.; Vunjak-Novakovic, G.; Kaplan, D. L. The Inflammatory Responses to Silk Films *in vitro* and *in vivo*. *Biomaterials* **2005**, *26*, 147−155.

(120) Leal-Egaña, A.; Lang, G.; Mauerer, C.; Wickinghoff, J.; Weber, M.; Geimer, S.; Scheibel, T. Interactions of Fibroblasts with Different Morphologies Made of an Engineered Spider Silk Protein. *Adv. Eng. Mater.* **2012**, *14*, B67−B75.

(121) Min, B.-M.; Lee, G.; Kim, S. H.; Nam, Y. S.; Lee, T. S.; Park, W. H. Electrospinning of Silk Fibroin Nanofibers and Its Effect on the Adhesion and Spreading of Normal Human Keratinocytes and Fibroblasts in Vitro. *Biomaterials* **2004**, *25*, 1289−1297.

(122) Sugihara, A.; Sugiura, K.; Morita, H.; Ninagawa, T.; Tubouchi, K.; Tobe, R.; Izumiya, M.; Horio, T.; Abraham, N. G.; Ikehara, S. Promotive Effects of a Silk Film on Epidermal Recovery from Full-Thickness Skin Wounds. *Proc. Soc. Exp. Biol. Med.* **2000**, *225*, 58−64.

(123) Rossitch, E., Jr.; Bullard, D. E.; Oakes, W. J. Delayed Foreign-Body Reaction to Silk Sutures in Pediatric Neurosurgical Patients. *Childs Nerv. Syst.* **1987**, *3*, 375−378.

(124) Zaoming, W.; Codina, R.; Fernández-Caldas, E.; Lockey, R. F. Partial Characterization of the Silk Allergens in Mulberry Silk Extract. *J. Invest. Allergol. Clin. Immunol.* **1996**, *6*, 237−241.

(125) Morrow, F. A.; Kogan, S. J.; Freed, S. Z.; Laufman, H. *In vivo* Comparison of Polyglycolic Acid, Chromic Catgut and Silk in Tissue of the Genitourinary Tract: An Experimental Study of Tissue Retrieval and Calculogenesis. *J. Urol.* **1974**, *112*, 655−658.

(126) Nebel, L.; Rosenberg, G.; Tobias, B.; Nathan, H. Autograft Suture in Peripheral Nerves. *Eur. Surg. Res.* **1977**, *9*, 224−234.

(127) Peleg, H.; Rao, U. N. M.; Emrich, L. J. An Experimental Comparison of Suture Materials for Tracheal and Bronchial Anastomoses. *Thorac. Cardiovasc. Surg.* **1986**, *34*, 384−388.

(128) Yucel, T.; Cebe, P.; Kaplan, D. L. Structural Origins of Silk Piezoelectricity. *Adv. Funct. Mater.* **2011**, *21*, 779−785.

(129) Jiang, C.; Wang, X.; Gunawidjaja, R.; Lin, Y.-H.; Gupta, M. K.; Kaplan, D. L.; Naik, R. R.; Tsukruk, V. V. Mechanical Properties of Robust Ultrathin Silk Fibroin Films. *Adv. Funct. Mater.* **2007**, *17*, 2229−2237.

(130) Lutolf, M. P.; Hubbell, J. A. Synthetic Biomaterials as Instructive Extracellular Microenvironments for Morphogenesis in Tissue Engineering. *Nat. Biotechnol.* **2005**, *23*, 47−55.

(131) Engler, A. J.; Humbert, P. O.; Wehrle-Haller, B.; Weaver, V. M. Multiscale Modeling of Form and Function. *Science* **2009**, *324*, 208−212.

(132) Vogel, V. Mechanotransduction Involving Multimodular Proteins: Converting Force into Biochemical Signals. *Annu. Rev. Biophys. Biomol. Struct.* **2006**, *35*, 459−488.

(133) Sofia, S.; McCarthy, M. B.; Gronowicz, G.; Kaplan, D. L. Functionalized Silk-Based Biomaterials for Bone Formation. *J. Biomed. Mater. Res., Part A* **2001**, *54*, 139−148.

(134) Gao, Z.; Wang, S.; Zhu, H.; Su, C.; Xu, G.; Lian, X. Using Selected Uniform Cells in Round Shape with a Micropipette to Measure Cell Adhesion Strength on Silk Fibroin-Based Materials. *Mater. Sci. Eng., C* **2008**, *28*, 1227−1235.

(135) Kim, J.-Y.; Choi, J.-Y.; Jeong, J.-H.; Jang, E.-S.; Kim, A.-S.; Kim, S.-G.; Kweon, H. Y.; Jo, Y.-Y.; Yeo, J.-H. Low Molecular Weight Silk Fibroin Increases Alkaline Phosphatase and Type I Collagen Expression in Mg63 Cells. *BMB Rep.* **2010**, *43*, 52−56.

(136) Salber, J.; Gräter, S.; Harwardt, M.; Hofmann, M.; Klee, D.; Dujic, J.; Jinghuan, H.; Ding, J.; Kippenberger, S.; Bernd, A.; Groll, J.; Spatz, J. P.; Möller, M. Influence of Different ECM Mimetic Peptide Sequences Embedded in a Nonfouling Environment on the Specific Adhesion of Human-Skin Keratinocytes and Fibroblasts on Deformable Substrates. *Small* **2007**, *3*, 1023−1031.

(137) Vogler, E. A. Structure and Reactivity of Water at Biomaterial Surfaces. *Adv. Colloid Interface Sci.* **1998**, *74*, 69−117.

(138) Vogler, E. A. Water and the Acute Biological Response to Surfaces. *J. Biomater. Sci., Polym. Ed.* **1999**, *10*, 1015−1045.

(139) Widhe, M.; Bysell, H.; Nystedt, S.; Schenning, I.; Malmsten, M.; Johansson, J.; Rising, A.; Hedhammar, M. Recombinant Spider Silk as Matrices for Cell Culture. *Biomaterials* **2010**, *31*, 9575−9585.

(140) Scheller, J.; Henggeler, D.; Viviani, A.; Conrad, U. Purification of Spider Silk-Elastin from Transgenic Plants and Application for Human Chondrocyte Proliferation. *Transgenic Res.* **2004**, *13*, 51−57.

(141) Bini, E.; Foo, C. W. P.; Huang, J.; Karageorgiou, V.; Kitchel, B.; Kaplan, D. L. RGD-Functionalized Bioengineered Spider Dragline Silk Biomaterial. *Biomacromolecules* **2006**, *7*, 3139−3145.

(142) Widhe, M.; Johansson, U.; Hillerdahl, C.-O.; Hedhammar, M. Recombinant Spider Silk with Cell Binding Motifs for Specific Adherence of Cells. *Biomaterials* **2013**, *34*, 8223−8234.

(143) Morgan, A. W.; Roskov, K. E.; Lin-Gibson, S.; Kaplan, D. L.; Becker, M. L.; Simon, C. G., Jr. Characterization and Optimization of RGD-Containing Silk Blends to Support Osteoblastic Differentiation. *Biomaterials* **2008**, *29*, 2556−2563.

(144) Hardy, J. G.; Pfaff, A.; Leal-Egaña, A.; Müller, A. H. E.; Scheibel, T. R. Glycopolymer Functionalization of Engineered Spider Silk Protein-Based Materials for Improved Cell Adhesion. *Macromol. Biosci.* **2014**, DOI: 10.1002/mabi.201400020.

(145) Das, S.; Pati, D.; Tiwari, N.; Nisal, A.; Sen Gupta, S. Synthesis of Silk Fibroin-Glycopolypeptide Conjugates and Their Recognition with Lectin. *Biomacromolecules* **2012**, *13*, 3695−3702.

(146) Foo, C. W. P.; Patwardhan, S. V.; Belton, D. J.; Kitchel, B.; Anastasiades, D.; Huang, J.; Naik, R. R.; Perry, C. C.; Kaplan, D. L. Novel Nanocomposites from Spider Silk-Silica Fusion (Chimeric) Proteins. *Proc. Natl. Acad. Sci. U.S.A.* **2006**, *103*, 9428−9433.

(147) Mieszawska, A. J.; Fourligas, N.; Georgakoudi, I.; Ouhib, N. M.; Belton, D. J.; Perry, C. C.; Kaplan, D. L. Osteoinductive Silk-Silica Composite Biomaterials for Bone Regeneration. *Biomaterials* **2010**, *31*, 8902−8910.

(148) Mieszawska, A. J.; Nadkarni, L. D.; Perry, C. C.; Kaplan, D. L. Nanoscale Control of Silica Particle Formation via Silk-Silica Fusion Proteins for Bone Regeneration. *Chem. Mater.* **2010**, *22*, 5780−5785.

(149) Bettinger, C. J.; Langer, R.; Borenstein, J. T. Engineering Substrate Topography at the Micro- and Nanoscale to Control Cell Function. *Angew. Chem., Int. Ed.* **2009**, *48*, 5406−5415.

(150) Biggs, M. J.; Richards, R. G.; Gadegaard, N.; McMurray, R. J.; Affrossman, S.; Wilkinson, C. D. W.; Oreffo, R. O. C.; Dalby, M. J. Interactions with Nanoscale Topography: Adhesion Quantification and Signal Transduction in Cells of Osteogenic and Multipotent Lineage. *J. Biomed. Mater. Res., Part A* **2009**, *91A*, 195−208.

(151) Zhang, K.; Mo, X.; Huang, C.; He, C.; Wang, H. Electrospun Scaffolds from Silk Fibroin and Their Cellular Compatibility. *J. Biomed. Mater. Res., Part A* **2010**, *93A*, 976−983.

(152) Zhang, X.; Baughman, C. B.; Kaplan, D. L. *In vitro* Evaluation of Electrospun Silk Fibroin Scaffolds for Vascular Cell Growth. *Biomaterials* **2008**, *29*, 2217−2227.

(153) Lewicka, M.; Hermanson, O.; Rising, A. U. Recombinant Spider Silk Matrices for Neural Stem Cell Cultures. *Biomaterials* **2012**, *33*, 7712−7717.

(154) Hronik-Tupaj, M.; Raja, W. K.; Tang-Schomer, M.; Omenetto, F. G.; Kaplan, D. L. Neural Responses to Electrical Stimulation on Patterned Silk Films. *J. Biomed. Mater. Res., Part A* **2013**, *101A*, 2559−2572.

(155) Dal Prà, I.; Petrini, P.; Charini, A.; Bozzini, S.; Farè, S.; Armato, U. Silk Fibroin-Coated Three-Dimensional Polyurethane Scaffolds for Tissue Engineering: Interactions with Normal Human Fibroblasts. *Tissue Eng.* **2003**, *9*, 1113−1121.

(156) Karageorgiou, V.; Meinel, L.; Hofmann, S.; Malhotra, A.; Volloch, V.; Kaplan, D. Bone Morphogenetic Protein-2 Decorated Silk Fibroin Films Induce Osteogenic Differentiation of Human Bone Marrow Stromal Cells. *J. Biomed. Mater. Res., Part A* **2004**, *71*, 528−537.

(157) He, G.; Dahl, T.; Veis, A.; George, A. Nucleation of Apatite Crystals in Vitro by Self-Assembled Dentin Matrix Protein, 1. *Nat. Mater.* **2003**, *2*, 552−558.

(158) Zhao, J.; Zhang, Z.; Wang, S.; Sun, X.; Zhang, X.; Chen, J.; Kaplan, D. L.; Jiang, X. Apatite-Coated Silk Fibroin Scaffolds to Healing Mandibular Border Defects in Canines. *Bone* **2009**, *45*, 517−527.

(159) Perrone, G. S.; Leisk, G. G.; Lo, T. J.; Moreau, J. E.; Haas, D. S.; Papenburg, B. J.; Golden, E. B.; Partlow, B. P.; Fox, S. E.; Ibrahim, A. M.; Lin, S. J.; Kaplan, D. L. The Use of Silk-Based Devices for Fracture Fixation. *Nat. Commun.* **2014**, *5*, 1−9.

(160) Currie, H. A.; Deschaume, O.; Naik, R. R.; Perry, C. C.; Kaplan, D. L. Genetically Engineered Chimeric Silk-Silver Binding Proteins. *Adv. Funct. Mater.* **2011**, *21*, 2889−2895.

(161) Pritchard, E. M.; Valentin, T.; Panilaitis, B.; Omenetto, F.; Kaplan, D. L. Antibiotic-Releasing Silk Biomaterials for Infection Prevention and Treatment. *Adv. Funct. Mater.* **2013**, *23*, 854−861.

(162) Gomes, S.; Gallego-Llamas, J.; Leonor, I. B.; Mano, J. F.; Reis, R. L.; Kaplan, D. L. In Vivo Biological Responses to Silk Proteins Functionalized with Bone Sialoprotein. *Macromol. Biosci.* **2013**, *13*, 444−454.

(163) Minoura, N.; Tsukada, M.; Nagura, M. Physicochemical Properties of Silk Fibroin Membrane as a Biomaterial. *Biomaterials* **1990**, *11*, 430−434.

(164) Minoura, N.; Tsukada, M.; Nagura, M. Fine-Structure and Oxygen Permeability of Silk Fibroin Membrane Treated with Methanol. *Polymer* **1990**, *31*, 265−269.

(165) Mori, H.; Tsukada, M. New Silk Protein: Modification of Silk Protein by Gene Engineering for Production of Biomaterials. *J. Biotechnol.* **2000**, *74*, 95−103.

(166) Tao, H.; Kaplan, D. L.; Omenetto, F. G. Silk Materials - a Road to Sustainable High Technology. *Adv. Mater.* **2012**, *24*, 2824−2837.

(167) Perry, H.; Gopinath, A.; Kaplan, D. L.; Dal Negro, L.; Omenetto, F. G. Nano- and Micropatterning of Optically Transparent, Mechanically Robust, Biocompatible Silk Fibroin Films. *Adv. Mater.* **2008**, *20*, 3070−3072.

(168) Lawrence, B. D.; Cronin-Golomb, M.; Georgakoudi, I.; Kaplan, D. L.; Omenetto, F. G. Bioactive Silk Protein Biomaterial Systems for Optical Devices. *Biomacromolecules* **2008**, *9*, 1214−1220.

(169) Parker, S. T.; Domachuk, P.; Amsden, J.; Bressner, J.; Lewis, J. A.; Kaplan, D. L.; Omenetto, F. G. Biocompatible Silk Printed Optical Waveguides. *Adv. Mater.* **2009**, *21*, 2411−2415.

(170) Zhang, Y.-Q. Natural Silk Fibroin as a Support for Enzyme Immobilization. *Biotechnol. Adv.* **1998**, *16*, 961−971.

(171) Demura, M.; Asakura, T. Immobilization of Glucose Oxidase with *Bombyx mori* Silk Fibroin by Only Stretching Treatment and Its Application to Glucose Sensor. *Biotechnol. Bioeng.* **1989**, *33*, 598−603.

(172) Zhang, Y.-Q.; Zhu, J.; Gu, R.-A. Improved Biosensor for Glucose Based on Glucose Oxidase-Immobilized Silk Fibroin Membrane. *Appl. Biochem. Biotechnol.* **1998**, *75*, 215−233.

(173) Lu, S.; Wang, X.; Lu, Q.; Hu, X.; Uppal, N.; Omenetto, F. G.; Kaplan, D. L. Stabilization of Enzymes in Silk Films. *Biomacromolecules* **2009**, *10*, 1032−1042.

(174) Asakura, T.; Kitaguchi, M.; Demura, M.; Sakai, H.; Komatsu, K. Immobilization of Glucose Oxidase on Nonwoven Fabrics with *Bombyx mori* Silk Fibroin Gel. *J. Appl. Polym. Sci.* **1992**, *46*, 49−53.

(175) Tao, H.; Kainerstorfer, J. M.; Siebert, S. M.; Pritchard, E. M.; Sassaroli, A.; Panilaitis, B. J. B.; Brenckle, M. A.; Amsden, J. J.; Levitt, J.; Fantini, S.; Kaplan, D. L.; Omenetto, F. G. Implantable, Multifunctional, Bioresorbable Optics. *Proc. Natl. Acad. Sci. U.S.A.* **2012**, *109*, 19584−19589.

(176) Moraes, M. L.; Lima, L. R.; Silva, R. R.; Cavicchioli, M.; Ribeiro, S. J. L. Immunosensor Based on Immobilization of Antigenic Peptide NS5A-1 from HCV and Silk Fibroin in Nanostructured Films. *Langmuir* **2013**, *29*, 3829−3834.

(177) Lu, Q.; Wang, X.; Zhu, H.; Kaplan, D. L. Surface Immobilization of Antibody on Silk Fibroin through Conformational Transition. *Acta Biomater.* **2011**, *7*, 2782−2786.

(178) Kim, S.; Mitropoulos, A. N.; Spitzberg, J. D.; Tao, H.; Kaplan, D. L.; Omenetto, F. G. Silk Inverse Opals. *Nat. Photonics* **2012**, *6*, 818−823.

(179) MacLeod, J.; Rosei, F. Photonic Crystals: Sustainable Sensors from Silk. *Nat. Mater.* **2013**, *12*, 98−100.

(180) Kim, S.; Mitropoulos, A. N.; Spitzberg, J. D.; Kaplan, D. L.; Omenetto, F. G. Silk Protein Based Hybrid Photonic-Plasmonic Crystal. *Opt. Express* **2013**, *21*, 8897−8903.

(181) Diao, Y. Y.; Liu, X. Y.; Toh, G. W.; Shi, L.; Zi, J. Multiple Structural Coloring of Silk-Fibroin Photonic Crystals and Humidity-Responsive Color Sensing. *Adv. Funct. Mater.* **2013**, *23*, 5373−5380.

(182) Lin, D.; Tao, H.; Trevino, J.; Mondia, J. P.; Kaplan, D. L.; Omenetto, F. G.; Dal Negro, L. Direct Transfer of Subwavelength Plasmonic Nanostructures on Bioactive Silk Films. *Adv. Mater.* **2012**, *24*, 6088−6093.

(183) Kim, D.-H.; Viventi, J.; Amsden, J. J.; Xiao, J.; Vigeland, L.; Kim, Y.-S.; Blanco, J. A.; Panilaitis, B.; Frechette, E. S.; Contreras, D.; Kaplan, D. L.; Omenetto, F. G.; Huang, Y.; Hwang, K.-C.; Zakin, M. R.; Litt, B.; Rogers, J. A. Dissolvable Films of Silk Fibroin for Ultrathin Conformal Bio-Integrated Electronics. *Nat. Mater.* **2010**, *9*, 511−517.

(184) Tao, H.; Brenckle, M. A.; Yang, M.; Zhang, J.; Liu, M.; Siebert, S. M.; Averitt, R. D.; Mannoor, M. S.; McAlpine, M. C.; Rogers, J. A.;

Kaplan, D. L.; Omenetto, F. G. Silk-Based Conformal, Adhesive, Edible Food Sensors. *Adv. Mater.* **2012**, *24*, 1067−1072.

(185) Mannoor, M. S.; Tao, H.; Clayton, J. D.; Sengupta, A.; Kaplan, D. L.; Naik, R. R.; Verma, N.; Omenetto, F. G.; McAlpine, M. C. Graphene-Based Wireless Bacteria Detection on Tooth Enamel. *Nat. Commun.* **2012**, *3*, 1−8.

Teilarbeit II

Die Ergebnisse dieses Kapitels wurden bereits in *ACS Biomaterials Science & Engineering* veröffentlich als:

Surface Modification of Polymeric Biomaterials Using Recombinant Spider Silk Proteins.

Christian B. Borkner, Stefanie Wohlrab, Eva Möller, Gregor Lang und Thomas Scheibel

Mit Genehmigung abgedruckt aus C. B. Borkner, S. Wohlrab, E. Möller, G. Lang, T. Scheibel, Surface Modification of Polymeric Biomaterials Using Recombinant Spider Silk Proteins. *ACS Biomaterials Science & Engineering* **2017**, *3*, 767-775. Copyright 2016 American Chemical Society.

Reprinted with permission from C. B. Borkner, S. Wohlrab, E. Möller, G. Lang, T. Scheibel, Surface Modification of Polymeric Biomaterials Using Recombinant Spider Silk Proteins. *ACS Biomaterials Science & Engineering* **2017**, *3*, 767-775. Copyright 2016 American Chemical Society.

ACS Biomaterials Science & Engineering
Article
pubs.acs.org/journal/abseba

Surface Modification of Polymeric Biomaterials Using Recombinant Spider Silk Proteins

Christian B. Borkner,[†] Stefanie Wohlrab,[†,◆] Eva Möller,[†] Gregor Lang,[†,‡] and Thomas Scheibel*,[†,§,∥,⊥,#,△]

[†]Lehrstuhl Biomaterialien, Fakultät für Ingenieurwissenschaften, [‡]Professur für Biopolymerverarbeitung, Fakultät für Ingenieurwissenschaften, [§]Bayerisches Polymerinstitut (BPI), [∥]Bayreuther Zentrum für Kolloide und Grenzflächen (BZKG), [⊥]Institut für Bio-Makromoleküle (bio-mac), [#]Bayreuther Zentrum für Molekulare Biowissenschaften (BZMB), and [△]Bayreuther Materialzentrum (BayMAT), Universität Bayreuth, Universitätsstraße 30, 95440 Bayreuth, Germany

Ⓢ *Supporting Information*

ABSTRACT: The performance of biomaterials largely depends on the materials biocompatibility, which is directly related to unwanted side effects like foreign body responses and inflammation, and the potential of interaction of cells with its surface, for example, cell adhesion. In the distinct application of catheters, low or even no cell adhesion is eligible. To influence the properties of existing and commonly used biomaterials and to further increase their biocompatibility, a coating with a recombinantly produced spider silk protein as outer layer was applied on three selected catheter polymers (polyurethane, polytetrafluoroethylene, silicone) and evaluated based on cell adhesion. The tested cell types, HaCaT keratinocytes (epidermal cells), B50 neuronal cells, C2C12 myoblasts (muscle cells) and BALB/3T3 fibroblasts (connective tissue), exhibited low or no adhesion on the silk-coated materials. In combination with the lack of toxicity, the good biocompatibility, and the low body response, it could be shown that silk coatings have a high potential as a biomedical coating material, e.g., for catheters.

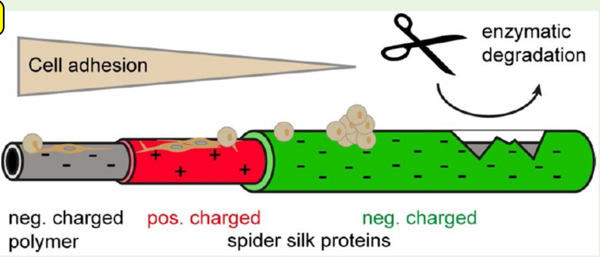

KEYWORDS: *recombinant spider silk proteins, biomaterial coating, cell adhesion, biodegradation, catheter*

1. INTRODUCTION

Various synthetic polymeric materials, especially polyurethanes (PU), fluorinated hydrocarbons like polytetrafluoroethylene (PTFE), and silicones, are used as biomaterials. Common fields of application for PU are artificial pacemaker lead insulation, catheters, vascular grafts, heart assist balloon pimps, artificial heart bladders, and wound dressings; for PTFE catheters, ligament replacement and sutures; and for silicone, membranes and tubings (extracorporeal equipment), orthopedic implants like foot and hand joints, catheters, drains and shunts, as well as aesthetic and reconstructive implants.[1−5] Unwanted side effects include foreign body responses and inflammation as a reaction to the implanted biomaterial, for example, during long-term application of silicone implants. Further, it is reported that the biocompatibility of the implanted material plays a significant role for encapsulation, whereas infections, postoperative hematomas or seromas can be attributed to clinical malpractice.[6] The most prominent and specific complication is periprostetic capsular fibrosis, which occurs most frequently within the first year after surgery.[7,8] Thrombosis is another common complication that is typically linked to the use of central venous catheters in long-term application.[9,10]

Recombinantly produced spider silk has been shown to be a promising material for implant coatings because of its biocompatibility,[11] as well as the low/none inflammatory response of both animals and human hosts.[12] The here used recombinant spider silk protein eADF4(C16) is based on the consensus sequence of the core domain of *Araneus diadematus* fibroin 4 (ADF4) of the dragline silk of the European garden spider *A. diadematus*. The amino acid consensus motif is called C-module (GSSAAAAAAAAS GPGGY GPENQGPS GPGGY GPGGP) and it is repeated 16 times in the engineered *A. diadematus* fibroin 4 (eADF4(C16)). eADF4(C16) is β-sheet rich with the β-sheets mainly formed by polyalanine (A_n) regions embedded in a glycine-rich amorphous matrix. If all glutamate residues of the negatively charged eADF4(C16) are exchanged with lysine residues (E → K) the positively charged eADF4(κ16) is obtained.[13] It has been shown that both recombinant silk proteins can be processed into different morphologies like films, coatings, and nonwoven mats.[14] Spider silk films, relevant for this study, made out of aqueous solution show an average roughness (R_a) of 8.27−27.50 nm.[15] In general, only weak attachment of mouse fibroblasts (BALB/3T3) but good cell vitality has been detected on eADF4(C16) films, and, as a consequence, cells were round shaped and formed cell aggregates. In contrast, films made of the

Special Issue: Designer Protein Biomaterials

Received: June 2, 2016
Accepted: August 9, 2016
Published: August 9, 2016

DOI: 10.1021/acsbiomaterials.6b00306
ACS Biomater. Sci. Eng. 2017, 3, 767−775

engineered variant eADF4(C16)-RGD additionally comprising the cell-binding peptide RGD showed a significantly increased fibroblast adhesion compared to that of eADF4(C16) films.[16−18] Importantly, cells do not proliferate on eADF4(C16) films,[17] which have already been used as coating material for silicone breast implants to reduce capsular fibrosis. The efficiency thereof could be shown in Sprague−Dawley rats in vivo. Acting as a bioshield, the eADF4(C16) coating improved the biocompatibility of the implant and significantly decreased the foreign body response and reduced the periprostetic fibrous capsule formation.[19,20] Up to 12 months after implantation, an eADF4(C16) coating was detectable on the explanted silicone implants.[20] In another study, it has been shown that silk materials provide good blood compatibility.[21]

Here, eADF4(C16) films were evaluated regarding, e.g., biodegradability and cell adhesion as coating material of different polymeric biomaterials, e.g., for use as catheters to enable new applications.

2. MATERIALS AND METHODS

2.1. Materials. If not stated otherwise, all chemicals were purchased from Roth (Karlsruhe, Germany) in analytical grade. eADF4(C16) was purchased from AMSilk GmbH (Planegg/München, Germany). Polydimethylsiloxane (Sylgard 184 Silicone Elastomer) was purchased from Dow Corning (Wiesbaden, Germany). Polyethylenimine (PEI, branched, MW ~ 25 000 by LS, M_n 10 000 by GPC), protease mixture (PXIV) from *Streptomyces griseus* (type XIV) and collagenase (CHC) from *Clostridium histolyticum* (type IA) were purchased from Sigma-Aldrich (Munich, Germany). 5/6-carboxy-tetramethyl-rhodamine succinimidyl ester (NHS-rhodamine) and 5/6-carboxyfluorescein succinimidyl ester (NHS-fluoresceine) was purchased from ThermoFischer Scientific (Darmstadt, Germany). CellTiter-Blue reagent was purchased from Promega (Madison, USA). Polytetrafluoroethylene catheters BD Venflon G14 (d = 2.0 mm) were purchased from BD (Heidelberg, Germany), polyurethane catheters Cavafix Certo 375 (d = 1.7 mm) were purchased from BBraun (Melsungen, Germany), and silicone catheters Rüsch Brillant (silicone, CH22, d = 7.3 mm) were purchased from Teleflex Medical (Kernen, Germany). Dimethylformamide and ethanol were purchased from VWR (Darmstadt, Germany). The used water was ultrapure (Milli-Q) and obtained by using a Merck Millipore system (Billerica, MA, USA).

2.2. Production of eADF4(κ16) and eADF4(C16)-RGD. Silk proteins were expressed in *Escherichia coli* (BL21 gold) and cells were grown in a fermenter using the fed batch technique.[22] The proteins were purified using a heat step and ammonium sulfate precipitation as described previously.[22] The genetically modified recombinant spider silk protein eADF4(C16)-RGD consists of eADF4(C16) and the additional C-terminal GGAGG**RGD**SPG sequence and was produced as reported previously.[17] Further, eADF4(κ16), in which the glutamic acid residues of eADF4(C16) are replaced by lysine residues, was produced as reported before.[13]

2.3. Protein Labeling. eADF4(κ16) and eADF4(C16) were denatured in 6 M GdnSCN and dialyzed against 20 mM HEPES (pH 7.1). A 10-fold molar excess of the NHS-fluorophore (NHS-rhodamine, NHS-fluorescein) was dissolved in DMF and added to the protein solution (1 h, rt). The labeled proteins were precipitated in the presence of 1 M phosphate (K-Pi, pH 7.0) overnight (4 °C) and then thoroughly washed with Milli-Q/DMF (1:1, v/v) and Milli-Q followed by freeze-drying. Labeling was confirmed by UV/Vis analysis (Nanodrop ND 1000, ThermoScientific, Waltham, MA, USA), and the degree of labeling n(fluorophore)/n(protein) was in a range of 1.0−1.2 for fluorescein-labeled eADF4(C16) and 1.2−1.6 for rhodamine-labeled eADF4(κ16).

2.4. Preparation of Protein Solutions and Coating Process. All proteins were denatured in 6 M GdnSCN. eADF4(C16) was dialyzed against ammonium bicarbonate buffer (20 mM, pH 9.0). Ammonium bicarbonate was chosen as it decomposes into the volatile components NH_3, CO_2, and H_2O. eADF4(κ16) was dialyzed against Tris/HCl buffer (20 mM, pH 7.5) due to the higher protein stability of eADF4(κ16) at pH 7.5. Catheter samples were cut in four segments (6 mm in length). The samples were cleaned with ethanol p.a. in an ultrasonic bath for 5 min, dried in air and then treated with an oxygen plasma (5 min, 100 W, 0.2 mbar) (MiniFlecto, plasma technology, Herrenberg-Gültstein, Germany). The plasma-treated samples were directly immersed in 1% (w/v) PEI or 1 mg/mL eADF4(κ16) for 1 h and then thoroughly washed with Milli-Q water. To stabilize the coatings, we immersed the samples in 75% (v/v) ethanol to induce β-sheet structure as reported previously.[23] PEI and eADF4(κ16) coated samples were then dip-coated in a 10 mg/mL eADF4(C16) solution for 2 min using an automatic dip-coating device (WPTL5−0.01, MIT, Richmond, CA, USA). After drying, the coated samples were dipped into 75% (v/v) ethanol for 2 min and dried in air. Fluorophore-labeled samples were analyzed by fluorescence microscopy (DMI 3000B, Leica, Wetzlar, Germany). The coating thickness was evaluated by ellipsometry (SE850 Ellipsometer, Sentech Instruments GmbH, Berlin, Germany) on flat silicone surfaces (Sylgard 184 Silicone Elastomer, Dow Corning, Wiesbaden, Germany).

2.5. Atomic Force Microscopy. For surface morphology characterization the coated catheter surfaces were analyzed in tapping mode using a Dimension 3100 Nanoscope V (Bruker, Karlsruhe, Germany). Si_3N_4 cantilevers (Olympus, Tokyo, Japan) were used with a force constant of 42 N m^{-1}. The average roughness R_a was calculated in an area of 25 μm^2.

2.6. Water Contact Angle. To analyze wettability, we measured static contact angles of water on catheter materials using the OCA contact angle system (DataPhysics Instruments GmbH, Filderstadt, Germany). Contact angles were determined using the SCA20 software (DataPhysics Instruments GmbH, Filderstadt, Germany) and a Laplace Young fit.

2.7. Bending Stability Test. The general mechanical stability during a putative application of the eADF4(κ16)/eADF4(C16) coatings on silicone catheters was tested by bending the samples along their longitudinal axis up to 180° for three times by hand to simulate the stress of material handling during application. The test was performed under ambient conditions. The surface was then investigated by SEM regarding damage to the coating like cracks and delamination.

2.8. Enzymatic Degradation. Degradation experiments were performed according to Müller-Herrmann and Scheibel.[24] Experiments were performed in TCNB buffer (50 mM Tris/HCl, 10 mM $CaCl_2$, 150 mM NaCl, 0.05% Brij 35, pH 7.5) at room temperature, and the eADF4(κ16)-rhodamine/eADF4(C16)-fluorescein coated silicone catheter samples were incubated in 200 μL of PXIV or CHC solution (175 μg/mL in TCNB buffer) for 15 days. Control experiments without enzymes were conducted in 200 μL TCNB buffer. Buffers and enzyme solutions were changed every 24 h. The experiments were performed in sextuplicates, and the fluorescence intensity of the supernatant was measured every day using a Mithras LB940 plate reader system (Berthold Technologies, Bad Wildbad, Germany) (Fluorescein: λ_{ex} = 485 nm, λ_{em} = 535 nm; rhodamine: λ_{ex} = 530 nm, λ_{em} = 600 nm). To calculate the protein concentration in the supernatant and to determine the degraded mass of the protein a calibration curve of the labeled proteins was calculated. Samples were evaluated after 1, 3, 6, 10, and 15 days. Samples were washed with TCNB buffer twice and with Milli-Q water three times, air-dried and analyzed by SEM.

2.9. Cell Culture Experiments. BALB/3T3 mouse fibroblasts, C2C12 mouse myoblasts, HaCaT human adult low-calcium, high-temperature keratinocytes, and B50 neuroblastoma rat cells were cultured in DMEM media (Biochrom, Berlin, Germany) supplemented with 10% fetal bovine serum (Biochrom, Berlin, Germany), 1% (v/v) GlutaMAX (Gibco, Grand Island, USA) and 0.1% (v/v) gentamicin sulfate (Sigma-Aldrich, Seelze, Germany) at a controlled atmosphere (5% CO_2, 95% humidity). Catheter samples were placed in nontreated cell culture plates (48 well, polystyrene, Nunc, Langenselbold, Germany). In control experiments cells were seeded

DOI: 10.1021/acsbiomaterials.6b00306
ACS Biomater. Sci. Eng. 2017, 3, 767−775

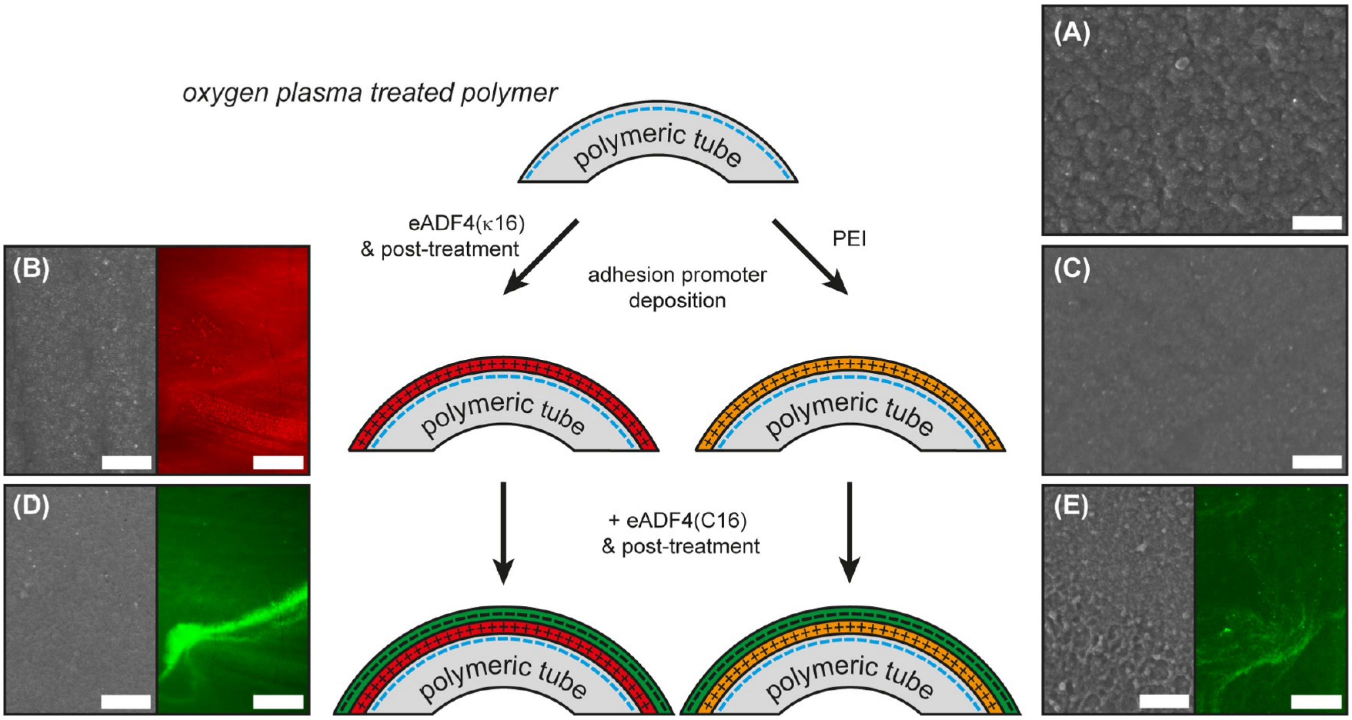

Figure 1. Schematic illustration of the layer-by-layer (lbl) strategy to coat polymeric biomaterial tubes with recombinant spider silk proteins. Scanning electron microscopy (SEM) and fluorescence microscopy images of processed silicone surfaces are shown according to the processing steps. (A) silicone surface, (B) eADF4(κ16) coating, (C) PEI coating, (D) eADF4(κ16)/eADF4(C16) coating, and (E) PEI/eADF4(C16) coating. For fluorescence imaging eADF4(κ16) was labeled with NHS-rhodamine (red fluorescence) and eADF4(C16) was labeled with NHS-fluorescein (green fluorescence). Fluorescence images B and D are of the same sample region. Scale bars: 1 μm (SEM pictures), 100 μm (fluorescence microscopy pictures).

on nontreated (weak adhesion, NTCP) and treated (strong adhesion, TCP) cell culture plates (Nunc, Langenselbold, Germany). For 24 h of cell culture experiments 100 000 cells/well and for 6 days of cell culture experiments 5000 cells/well were seeded (A_{well} = 1 cm^2). Medium was changed every 2 days. Samples were analyzed by bright field microscopy after one, three, and 6 days. For the metabolic cell proliferation assay cell culture plates (NTCP, 48 well, polystyrene, Nunc, Langenselbold, Germany) were coated with PDMS (Sylgard 184 Silicone Elastomer). For adhesion promoter deposition surfaces were incubated with 1% (w/v) PEI or 1 mg/mL eADF4(κ16) directly after plasma treatment for 1 h and washed with 200 μL Milli-Q water three times. eADF4(k16) was post-treated with 75% (v/v) ethanol. For eADF4(C16) deposition 200 μL eADF4(C16) solution (10 mg/mL) were added into the well plates, incubated for 2 min, then the silk solution was removed with a pipet and the coatings were air-dried. After drying, the coatings were post-treated with 75% (v/v) ethanol. Cell proliferation was measured for 6 days with an initial cell density of 5000 cells/cm^2 (BALB/3T3 mouse fibroblasts. To measure the metabolic activity, we washed cells with phosphate buffered saline (PBS) (Sigma-Aldrich, St. Louis, USA) two times to remove non adherent or dead fibroblasts, followed by addition of fresh medium. After incubation for 2.5 h in the presence of 10% (v/v) CellTiter-Blue reagent (Promega, Madison, USA), the transformation of the blue nonfluorescent dye resazurin into the red fluorescent resorufin (λ_{ex} = 530 nm; λ_{em} = 590 nm) was measured spectroscopically using a Mithras LB940 plate reader system (Berthold Technologies, Bad Wildbad, Germany) (λ_{ex} = 530 nm, λ_{em} = 600 nm).

2.10. Scanning Electron Microscopy (SEM). Scanning electron microscopy was performed using a Leo 1530 Gemini (Zeiss, Oberkochen, Germany) at an accelerating voltage of 3 kV. Samples were dried and then sputtered with 1.3 nm platinum.

3. RESULTS AND DISCUSSION

Different polymeric biomaterials typically used in catheters such as polyurethane (PU), polytetrafluoroethylene (PTFE) and silicone were coated with recombinantly produced engineered (polyanionic) spider silk protein eADF4(C16) using a dip-coating process. Since first direct coating attempts were not fully satisfactory the hydrophobic polymeric tubes were oxygen plasma treated to increase the surface wettability and to gain a homogeneous and complete coverage with coating solution during the dip coating process (Figure 1). Because of the plasma treatment, the hydrophobic surfaces turned hydrophilic but also negatively charged. Therefore, a polycationic adhesion promoter had to be introduced on the polymer surfaces to allow eADF4(C16) adhesion, otherwise the coating was again not satisfactory due to electrostatic repulsion. In order to show the feasibility of such process polyethylenimine (PEI) was used as a model substance. PEI is commonly used as gene carrier or to improve cell adhesion to surfaces. However, PEI shows increasing toxicity and cytotoxicity with increasing molecular weight.[25−27] To circumvent toxicity problems and to increase the biocompatibility of the coating, the recently developed polycationic spider silk protein eADF4(κ16) was used as novel alternative to PEI. SEM and fluorescence microscopy analysis showed the successful coating of a silicone surface (Figure 1A–E). The surface became significantly smoother upon coating with eADF4(κ16) (Figure 1B) or PEI (Figure 1C), both of which worked equally well. If the sample is only dipped partially into eADF4(C16) solution the border can be clearly seen between the coated and uncoated surface area (Figure S1A). Fluorescence microscopy images of rhodamine labeled eADF4-(κ16) on the silicone surface indicate a complete coverage of the surface (Figure 1B, Figure S1B). The adsorbed fluorescein-coupled eADF4(C16) layer can be seen on top of the eADF4(κ16)-layer by green fluorescence, and occurring eADF4(κ16) aggregates are covered by the eADF4(C16) layer (Figure 1D, and Figure S1C). The flat and homogeneous protein coatings ($d_{\text{PEI/eADF4(C16)}}$ = 43.1 nm ± 9.7 nm; $d_{\text{eADF4(}\kappa\text{16)/eADF4(C16)}}$ = 46.0 nm ± 11.4 nm) completely masked the silicone structure. The surface roughness (R_a) was R_a = 13.5 nm ± 2.5 nm for PEI/eADF4(C16) coatings and R_a = 13.7 nm ± 2.9 nm for eADF4(κ16)/eADF4(C16) coatings as evaluated by atomic force microscopy (Figure S2) in agreement with previously published results of spider silk films prepared from aqueous solutions.[15]

Water contact angle measurements showed that all eADF4-(C16)-coated surfaces had the same surface properties independent of the polymer or adhesion promoter in the used setup (Figure 2). Water contact angles of the cleaned polymer surfaces of the catheters (θ_{PTFE} = 110.6 ± 1.9°, θ_{PU} = 93.4 ± 0.7°, θ_{silicone} = 104.1 ± 0.5°) were in the same range as reported in literature ($\theta_{\text{PTFE, lit.}}$ = 112°, $\theta_{\text{PU, lit.}}$ = 90°, $\theta_{\text{PDMS, lit.}}$ = 105°).[28−31] Upon oxygen plasma treatment the surface contact angles significantly decreased ($\theta_{\text{PTFE, plasma}}$ = 79.0 ± 2.3°, $\theta_{\text{PU, plasma}}$ = 42.9 ± 2.1°, $\theta_{\text{silicone, plasma}}$ = 53.5 ± 5.5°). Polar functional groups were introduced, and the surfaces were made hydrophilic. After PEI/eADF4(C16) coating the water contact angle on all surfaces had mean values between 66° and 68°. Additionally, eADF4(κ16) and eADF4(κ16)/eADF4(C16) coatings were tested on silicone, resulting in contact angles of 66.5 ± 4.0° and 69.2 ± 6.2°, respectively, in agreement with previous results.[15] By evaluating the surface roughness and the surface wetting properties it could be shown that the surface properties of the silk coatings were independent of the used polymeric substrate as well as the adhesion promoter in the chosen setup.

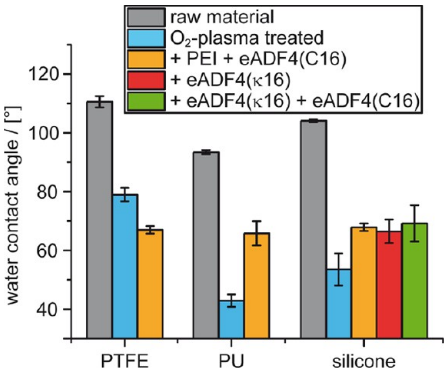

Figure 2. Wettability of silk-coated polymeric tubes in contrast to uncoated tubes determined by water contact angle measurements. Plasma-treated samples were measured directly after plasma treatment. All silk-coated tubes showed comparable water contact angles, independent of the tube material and adhesion promoter used. PEI, polyethylenimine; PU, polyurethane; PTFE, polytetrafluoroethylene.

Because all silk surfaces showed indistinguishable properties independent of the polymer material, all further experiments were performed with coatings on silicone. First, to investigate the bending stability of the silk-coated samples, the surface integrity of bended samples was analyzed by SEM (Figure 3, Figure S3). After bending in the dry state, raw silicone tubing had no defects (Figure 3A, Figure S3A). On eADF4(κ16)-coated surfaces, only a few nanocracks could be observed (Figure 3C, Figure S3C). The PEI/eADF4(C16) coatings shown in Figure 3B and Figure S3B, as well as eADF4(κ16)/eADF4(C16) coatings shown in Figure 3D and Figure S3D, revealed submicrometer cracks and no delamination, indicating a stable, well-adhered protein coating on the polymer surface/adhesion promoter.

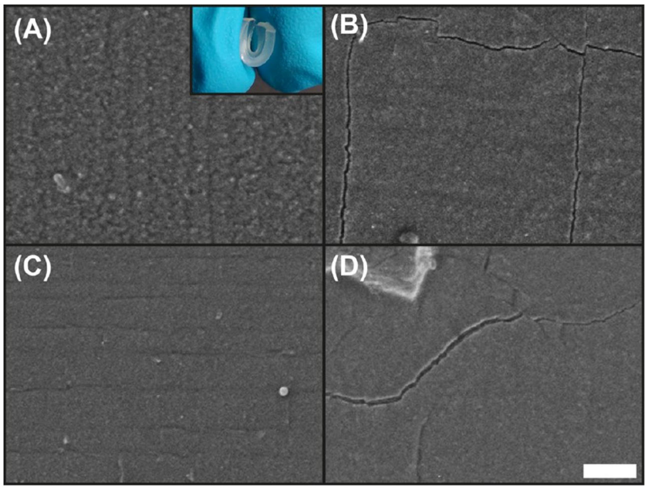

Figure 3. Representative SEM pictures of a (A) silicone tube surface (control), (B) PEI/eADF4(C16) on silicone tube, (C) eADF4(κ16) on silicone tube, and (D) eADF4(κ16)/eADF4(C16) on silicone tube after bending. All coatings showed good adhesion, and no delamination of the coatings could be detected. The insert in A illustrates the bending procedure. SEM scale bar: 2 μm.

To investigate the coating stability and biodegradation of eADF4(κ16)/eADF4(C16) coatings, we incubated the samples for 15 days in TCNB buffer or in TCNB buffer with the model enzymes collagenase type IA (CHC, *Clostridium histolyticum*) or protease mix XIV (PXIV, *Streptomyces griseus*) as previously used for degradation studies of silk scaffolds.[24,32] It has been shown that these model enzymes are well-suited to analyze eADF4(C16) degradation. PXIV is acting as model protease mix for digestive enzymes, and CHC as model protease mix for a wound healing environment.[24,32] Coatings made of both proteins, eADF4(κ16) and eADF4(C16), had good stability over 15 days in buffer. SEM pictures indicated that incubation in the presence of TCNB had a negligible effect on the coating, and the surfaces showed nearly no changes in morphology besides some aggregate formation (Figure 4E). Further, no significant protein loss was detectable. The degradation of eADF4(C16) in the presence of PXIV was finished within the first 6 days (Figure 4A), and that of eADF4(κ16) by day four (Figure 4B), but in the latter case it has to be taken into account that also the detection limit was reached faster due to the smaller amount of protein on the surface. SEM images illustrate the time dependent proteolysis (Figure 4C). After 1 day of incubation in PXIV solution holes in the coating could be detected (Figure 4C-i). At day six, when the plateau was reached, only small silk protein patches remained on the polymeric biomaterials surface, and the initial silicone structure could be visualized again (Figure 4C-ii). At day 10, only a few protein aggregates/structures were left on the surface (Figure 4C-iii), and at day 15 the initial silicone surface was seen again by SEM (Figure 4C-iv) leading to the assumption that 100% degradation was achieved in the presence of PXIV after 15 days. The degradation of eADF4(C16) in the presence of CHC was significantly slower than in the presence of PXIV, and after 15

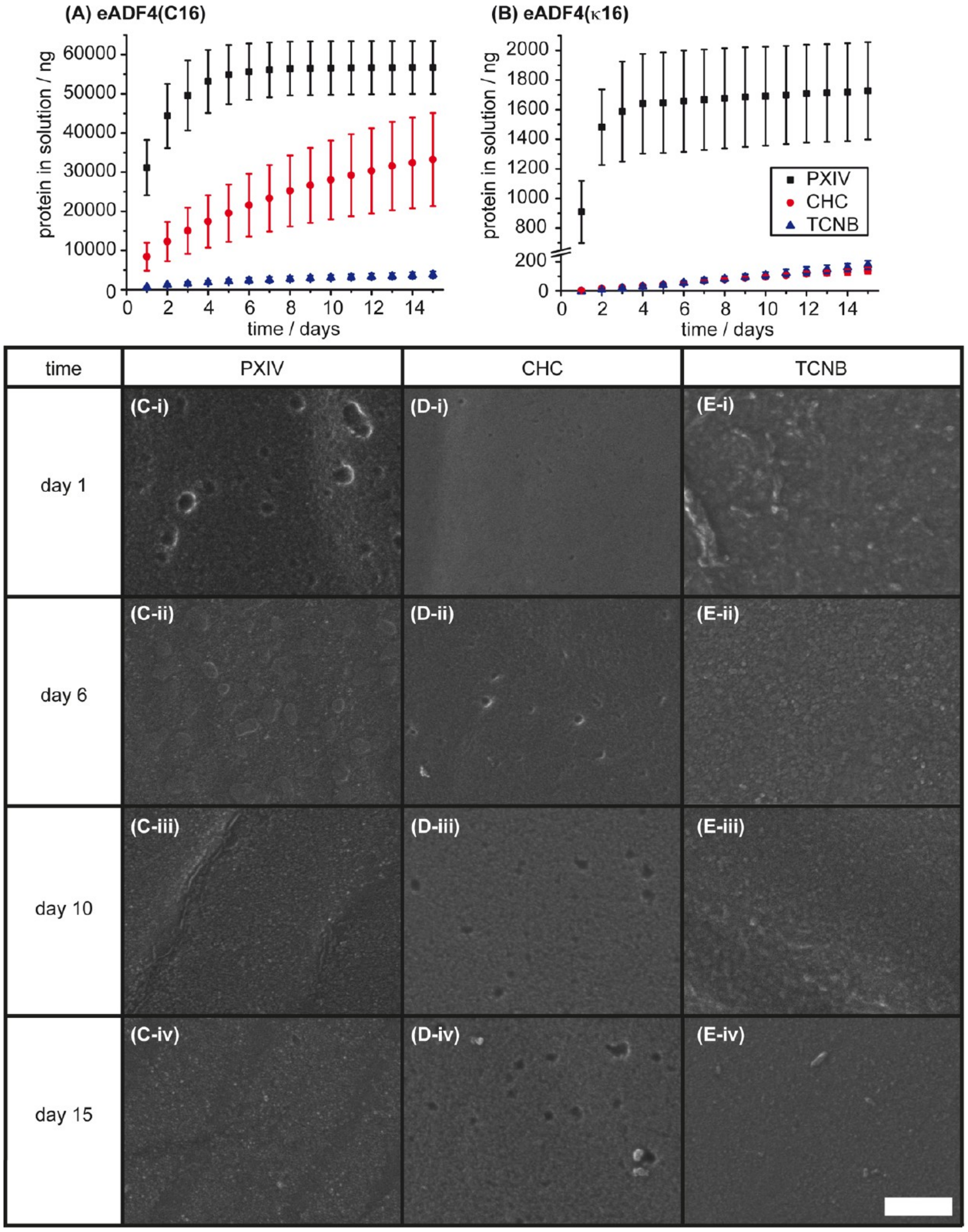

Figure 4. Enzymatic degradation of eADF4(*κ*16)/eADF4(C16) coatings on silicone catheters in the presence of the model enzymes protease-mix XIV (PXIV, *Streptomyces grieseus*) and collagenase type IA (CHC, *Clostridium histolyticum*) over 15 days. Time-dependent degradation of (A) eADF4(C16) and (B) eADF4(*κ*16) (black squares, PXIV; red circles, CHC; blue triangles, TCNB). SEM pictures of eADF4(*κ*16)/eADF4(C16) coatings on silicone degraded in the presence of (C) PXIV, (D) CHC, and (D) TCNB buffer after (i) 1 day, (ii) 6 days, (iii) 10 days, and (iv) 15 days of incubation. Scale bar: 1 *μ*m.

days only approximately 60% of the coating was degraded (Figure 4A–D), which is in agreement with previous findings.[32] After one day, small submicrometer-sized holes appeared in the coating (Figure 4D-i). The size of these holes increased over time, and at day 10 the surface became spongy in appearance (Figure 4D-iii). After 15 days (Figure 4D-iv), the surface looked similar to the surface degraded in the presence of PXIV after 1 day. In contrast, eADF4(*κ*16) showed no apparent degradation in the presence of CHC within the first 15 days. Altogether, these results indicated a good stability and compatibility in biological environments in combination with a time-dependent biodegradation.

Nonfouling surfaces exhibit weak protein adsorption properties as well as weak to no cell adhesion properties (which actually depends on protein adsorption), thus being an important prerequisite for certain biomedical applications. Here, the adhesion of BALB/3T3 mouse fibroblast on all silk-coated materials (PTFE, PU and silicone tubes) was characterized. In a first experiment, cell adhesion was analyzed after 24 h of incubation (Figure 5). On PTFE, fibroblasts did not adhere and exhibited a round morphology and formed cell aggregates (Figure 5A) similar to cells on nontreated cell culture plates (NTCP) (Figure 5L). On PEI/eADF4(C16) coated PTFE fibroblasts showed a similar adhesion behavior as on raw PTFE with cell aggregates and no spreading (Figure 5C). On raw PU most cells were found at the bottom of the cell culture plate. Only some cells adhered to the PU surface, but in such case they were well-spread (Figure 5D), and good adhesion and cell spreading was observed on the treated cell culture plates (TCP) (Figure 5K). On PEI/eADF4(C16)

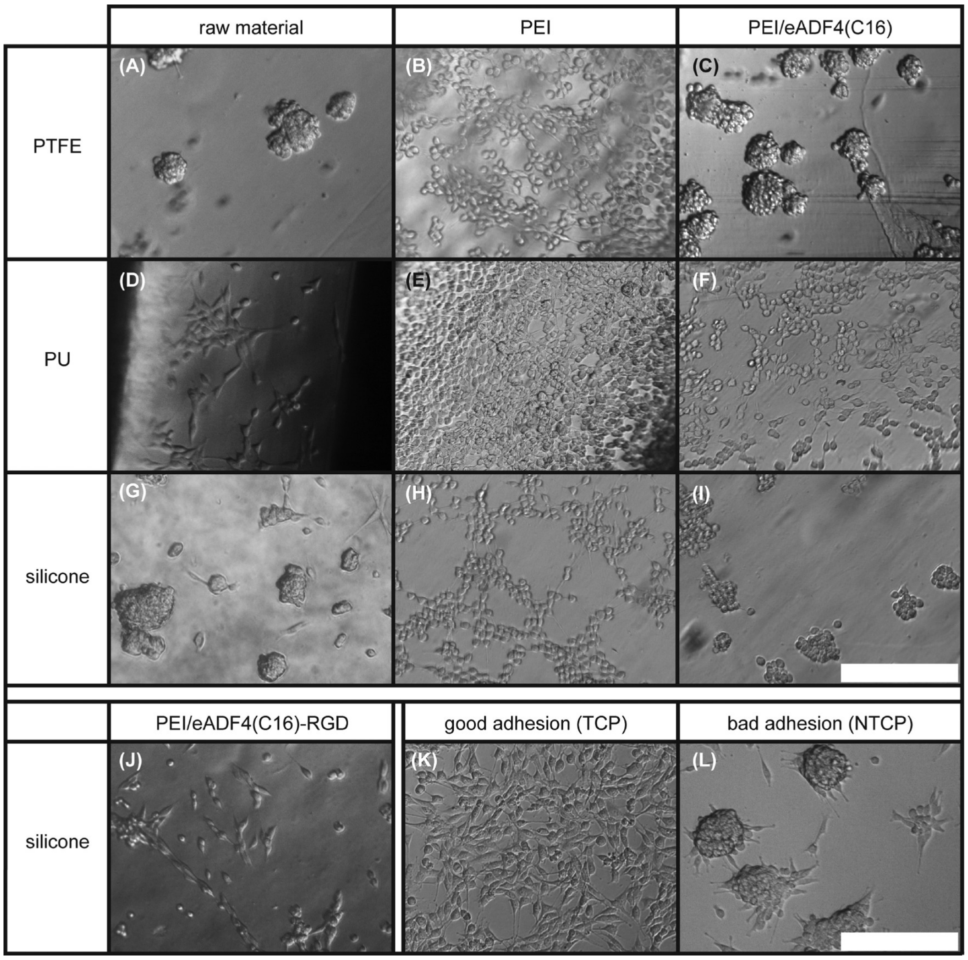

Figure 5. Fibroblast (BALB/3T3) adhesion on PTFE (A) raw material, (B) PEI, and (C) PEI/eADF4(C16)-coated PTFE; on PU (D) raw material, (E) PEI, and (F) PEI/eADF4(C16)-coated PU; on silicone (G) raw material, (H) PEI, (I) PEI/eADF4(C16)-coated silicone; (J) PEI/eADF4(C16)-RGD-coated silicone. (K) TCP (treated cell culture plate) control (good adhesion); (L) NTCP (nontreated cell culture plate) control (bad adhesion). Fibroblasts (100 000 cells/cm^2) were cultivated for 24 h in all cases. PEI, polyethylenimine, PTFE, polytetrafluoroethylene, PU, polyurethane. Scale bars: 250 μm.

coated PU, more cells than on raw PU were detected, but these cells were less spread (Figure 5F). On raw silicone, cells formed mainly cell aggregates with few adherent cells (Figure 5G). On PEI/eADF4(C16) coated silicone, fibroblasts did not adhere to the tube surface and formed small cell aggregates (Figure 5I and Figure S4). To evaluate the influence of PEI on the cells we coated all materials with PEI only to obtain a reference surface. Not surprisingly, the cells adhered much better on such PEI coating due to its positive charge (Figure 5B, E, H). In case of an additional silk layer on top of PEI the influence of PEI was diminished in the PEI/eADF4(C16) coatings (Figure 5C, F, I). The microscopy picture (Figure S4) shows a PEI/eADF4(C16)-rhodamine coating, and the difference in cell behavior on a PEI and a silk surface can be compared on the same sample, because the sample was completely covered with PEI and then partly dip-coated with eADF4(C16) (Figure S4A). At the resulting border (green dotted line) between the eADF4(C16) area (left) and the PEI coating (right) (Figure S4B) the fibroblasts only adhered at the PEI-coated area but not on the PEI/eADF4(C16) coated area (Figure S4C, D). To confirm that cells adhere less because of the surface properties of eADF4(C16), we used the genetically modified eADF4(C16)-RGD as an additional coating material with indistinguishable physicochemical properties but comprising an engineered cell binding motif (RGD-peptide). On such coatings, cell adhesion and spreading was significantly increased, and the cells built pseudopodia (Figure 5J) in accordance to previous findings.[33−35]

In a further experiment, adhesion of BALB/3T3 fibroblasts (Figure 6), B50 neuronal cells (Figure S5), HaCaT keratinocytes (Figure S6), and C2C12 myoblasts (Figure S7) was analyzed on silicone surfaces coated with eADF4(κ16) or eADF4(κ16)/eADF4(C16) over 6 days of incubation. As seen previously, fibroblasts did not adhere to the uncoated silicone surface. On eADF4(κ16), cell adhesion was improved as indicated by cell spreading. On eADF4(κ16)/eADF4(C16) coatings low cell adhesion could be detected. Only a small number of round shaped fibroblasts in cell aggregates were found at the surface. The same behavior was observed by light microscopy for B50, HaCaT, and C2C12 cells, confirming that different cell types, i.e., epidermal cells, neuronal cells, muscle cells, and connective tissue cells, showed low or no adhesion on the eADF4(C16) surface. These results are in agreement with the metabolic cell proliferation assay (Alamar Blue) (Table 1), which shows an increased cell proliferation (BALB/3T3 mouse fibroblasts) on PEI and eADF4(κ16)-coated PDMS surfaces compared to proliferation on raw PDMS and a much lower cell proliferation on eADF4(C16) coatings.

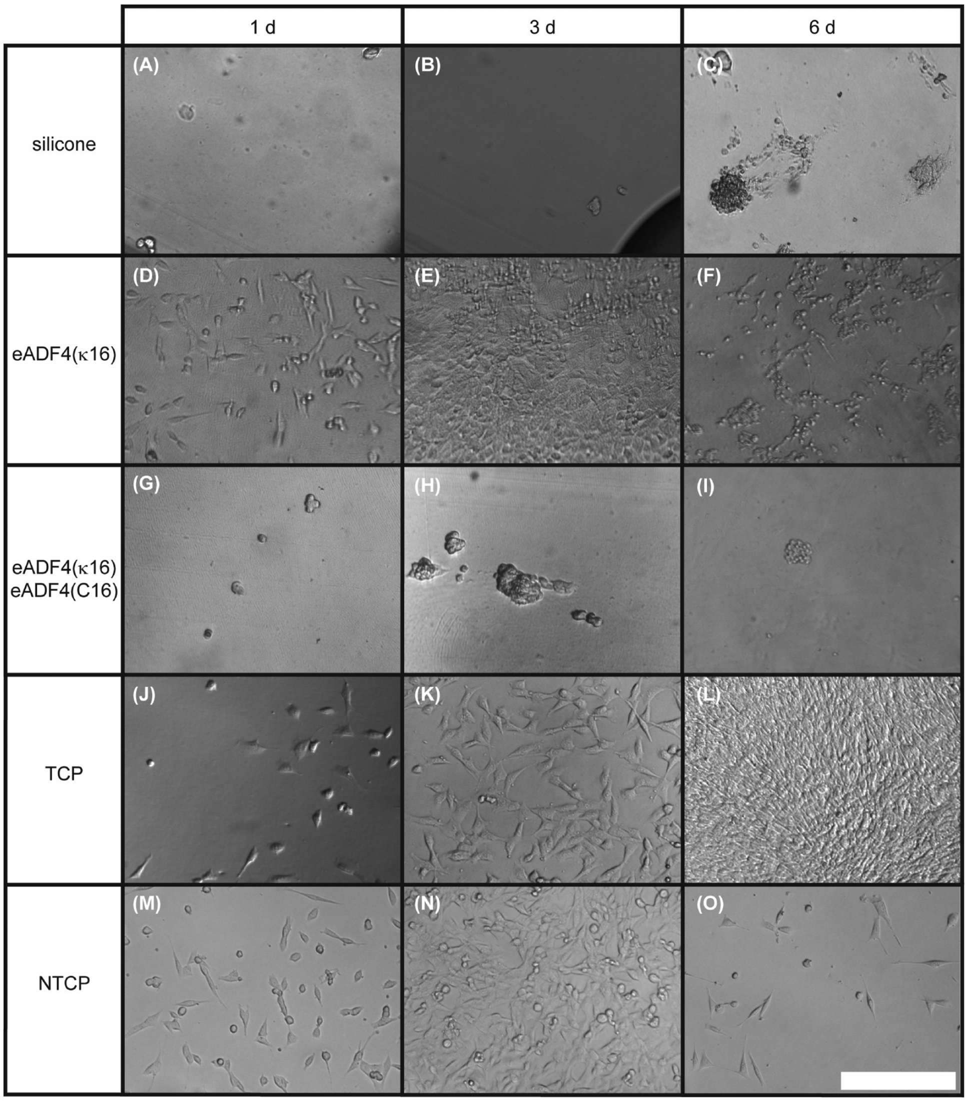

Figure 6. Fibroblast (BALB/3T3) adhesion (5000 cells/cm^2 seeded) on silicone catheters after 1, 3, and 6 days. Bright-field microscopy pictures of cells on (A–C) silicone; (D–F) eADF4(κ16)-coated silicone; (G–I) eADF4(κ16)/eADF4(C16)-coated silicone; (J–L) TCP, treated cell culture plate ("good adhesion" control); (M–O) NTCP, nontreated cell culture plate ("bad adhesion" control). Scale bar: 250 μm.

Table 1. Proliferation of BALB/3T3 Fibroblasts (5000 cells/cm^2 seeded) on Silk Coatings and Reference Surfaces after 6 days in Relation to the Treated Cell Culture Plate (TCP ≙ 100%)

entry	surface	proliferation (% of TCP)
1	PDMS	0.3
2	PEI	49.0
3	eADF4(κ16)	57.5
4	PEI/eADF4(C16)	21.4
5	eADF4(κ16)/eADF4(C16)	27.5

4. CONCLUSION AND OUTLOOK

The aim of this study was to provide a surface coating for different polymeric biomaterials (PTFE, PU, silicone) made of the recombinant polyanionic spider silk protein (eADF4-(C16)). Independent of the coated polymer material, the surface characteristics of such silk coatings were almost indistinguishable. The coatings showed good stability in a wound-like environment, and in combination with low cell adhesion such coatings might show beneficial effects upon exposure to living tissue (i.e., in catheter applications), because none of the tested cell types (HaCaT keratinocytes, BALB/3T3 fibroblasts, C2C12 myoblasts, B50 neuronal cells) significantly adhered to the polyanionic silk surface. In addition to the previously described in vitro blood stability and compatibility of silks,[21] eADF4(C16) was the first reported coating material which could effectively reduce critical side effects such as postoperative inflammation and body response especially in the critical time period in which fibrosis on implant surfaces occurs.[19,20] Nevertheless, depending on the possible fields of application and the related physiological environment of different types of catheters further studies have to be performed *in vivo*, for example studies of urinary catheters considering the development of an urinary calculus and detailed studies of such coatings exposed to blood flow.

■ ASSOCIATED CONTENT

Ⓢ Supporting Information

The Supporting Information is available free of charge on the ACS Publications website at DOI: 10.1021/acsbiomaterials.6b00306.

AFM images and average surface roughness of silk-coated silicone catheter surfaces, additional SEM pictures of the bending test, fluorescence microscopy pictures of catheter coatings, and fibroblast adhesion (BALB/3T3) on PEI/eADF4(C16)-coated silicone tubes, 6d cell culture experiments (B50 neuronal cell, HaCaT keratinocytes, C2C12 myoblasts) (PDF)

AUTHOR INFORMATION

Corresponding Author

*E-mail: thomas.scheibel@bm.uni-bayreuth.de.

Present Address

◆S.W. is currently at Roche Diagnostics GmbH, Nonnenwald 2, 82377 Penzberg, Germany

Author Contributions

The manuscript was written through contributions of all authors. All authors have given approval to the final version of the manuscript.

Notes

The authors declare no competing financial interest.

ACKNOWLEDGMENTS

We thank Hendrik Bargel, Martin Humenik, Elise DeSimone, Joschka Bauer, and Tamara Aigner for helpful discussion on the manuscript and Martina Heider and Beate Förster for technical assistance performing the SEM measurements. We also thank Sarah Lentz for AFM support. This work is supported by the SFB 840 TP A8.

ABBREVIATIONS

AFM	atomic force microscopy
CHC	collagenase type IA from *Clostridium histolyticum*
DMEM	Dulbecco's modified Eagle's medium
DMF	dimethylformamide
eADF4	engineered *Araneus diadematus* Fibroin 4
GdnSCN	guanidinium thiocyanate
GPC	gel permeation chromatography
HEPES	2-[4-(2-hydroxyethyl)-1-piperzin-yl]ethanesulfonic acid
K-Pi	potassium sulfate buffer
LS	lights scattering
M_n	number-average molecular weight
MW	average molecular weight
NHS	*N*-hydroxysuccinimide
NTCP	nontreated cell culture plate
PDMS	polydimethylsiloxane
PEI	polyethylenimine
PTFE	polytetrafluoroethylene
PU	polyurethane
PXIV	protease mixture XIV from *Streptomyces griseus*
RGD	arginine-glycine-aspartic acid cell binding peptide
SEM	scanning electron microscopy
TCP	treated cell culture plate
Tris	Tris(hydroxymethyl)aminomethane

REFERENCES

(1) Bolton, C. W.; Bruchman, W. C. The GORE-TEX Expanded Polytetrafluoroethylene Prosthetic Ligament - An *In Vitro* and *In Vivo* Evaluation. *Clin. Orthop. Relat. Res.* **1985**, *196*, 202−213.

(2) Heath, D. E.; Cooper, S. L., Polyurethanes. In *Biomaterials Science*, 3rd ed.; Rattner, B. D., Hoffman, A. S., Schoen, F. J., Lemons, J. E., Eds.; Elsevier Academic Press: San Diego, CA, 2013; pp 79−82.

(3) Curtis, J.; Colas, A., Medical Applications of Silicones. In *Biomaterials Science*, 3rd ed.; Rattner, B. D., Hoffman, A. S., Schoen, F. J., Lemons, J. E., Eds.; Elsevier Academic Press: San Diego, CA, 2013; pp 1106−1116.

(4) Ramakrishna, S.; Mayer, J.; Wintermantel, E.; Leong, K. W. Biomedical applications of polymer-composite materials: a review. *Compos. Sci. Technol.* **2001**, *61*, 1189−1224.

(5) Rattner, B. D.; Hoffman, A. S.; Schoen, F. J.; Lemons, J. E., Biomaterials Science: An Evolving, Multidisciplinary Endeavor. In *Biomaterials Science*, 3rd ed.; Rattner, B. D., Hoffman, A. S., Schoen, F. J., Lemons, J. E., Eds.; Elsevier Academic Press: San Diego, CA, 2013; pp XXV−XXXIX.

(6) Schreml, S.; Heine, N.; Eisenmann-Klein, M.; Prantl, L. Bacterial Colonization Is of Major Relevance for High-Grade Capsular Contracture After Augmentation Mammaplasty. *Ann. Plast. Surg.* **2007**, *59*, 126−130.

(7) Dancey, A.; Nassimizadeh, A.; Levick, P. Capsular contracture - What are the risk factors? A 14 year series of 1400 consecutive augmentations. *J. Plast. Reconstr. Aesthet. Surg.* **2012**, *65*, 213−218.

(8) Henriksen, T. F.; Fryzek, J. P.; Hölmich, L. R.; McLaughlin, J. K.; Kjøller, K.; Høyer, A. P.; Olsen, J. H.; Friis, S. Surgical Intervention and Capsular Contracture After Breast Augmentation - A Prospective Study of Risk Factors. *Ann. Plast. Surg.* **2005**, *54*, 343−351.

(9) Geerts, W. Central venous catheter-related thrombosis. *Hematology Am. Soc. Hematol. Educ. Program* **2014**, *2014*, 306−311.

(10) Agnelli, G.; Verso, M. Therapy Insight: venous-catheter-related thrombosis in cancer patients. *Nat. Clin. Pract. Oncol.* **2006**, *3*, 214−222.

(11) Spiess, K.; Lammel, A.; Scheibel, T. Recombinant Spider Silk Proteins for Applications in Biomaterials. *Macromol. Biosci.* **2010**, *10*, 998−1007.

(12) Leal-Egaña, A.; Scheibel, T. Silk-based materials for biomedical applications. *Biotechnol. Appl. Biochem.* **2010**, *55*, 155−167.

(13) Doblhofer, E.; Scheibel, T. Engineering of Recombinant Spider Silk Proteins Allows Defined Uptake and Release of Substances. *J. Pharm. Sci.* **2015**, *104*, 988−994.

(14) Borkner, C. B.; Elsner, M. B.; Scheibel, T. Coatings and Films Made of Silk Proteins. *ACS Appl. Mater. Interfaces* **2014**, *6*, 15611−15625.

(15) Wohlrab, S.; Spieß, K.; Scheibel, T. Varying surface hydrophobicities of coatings made of recombinant spider silk proteins. *J. Mater. Chem.* **2012**, *22*, 22050−22054.

(16) Bauer, F.; Wohlrab, S.; Scheibel, T. Controllable cell adhesion, growth and orientation on layered silk protein films. *Biomater. Sci.* **2013**, *1*, 1244−1249.

(17) Wohlrab, S.; Müller, S.; Schmidt, A.; Neubauer, S.; Kessler, H.; Leal-Egaña, A.; Scheibel, T. Cell adhesion and proliferation on RGD-modified recombinant spider silk proteins. *Biomaterials* **2012**, *33*, 6650−6659.

(18) Leal-Egaña, A.; Lang, G.; Mauerer, C.; Wickinghoff, J.; Weber, M.; Geimer, S.; Scheibel, T. Interactions of Fibroblasts with Different Morphologies Made of an Engineered Spider Silk Protein. *Adv. Eng. Mater.* **2012**, *14*, B67−B75.

(19) Zeplin, P. H.; Berninger, A.-K.; Maksimovikj, N. C.; van Gelder, P.; Scheibel, T.; Walles, H. Improving the Biocompatibility of Silicone Implants Using Spider Silk Coatings: Immunohistochemical Analysis of Capsule Formation. *Handchir. Mikrochir. Plast. Chir.* **2015**, *46*, 336−341.

(20) Zeplin, P. H.; Maksimovikj, N. C.; Jordan, M. C.; Nickel, J.; Lang, G.; Leimer, A. H.; Römer, L.; Scheibel, T. Spider Silk Coatings as a Bioshield to Reduce Peroprosthetic Fibrous Capsule Formation. *Adv. Funct. Mater.* **2014**, *24*, 2658−2666.

(21) Hao, Y.; Sun, D.; Wang, Q.; Dong, F.; Zhang, G.; Wang, J. In vitro blood compatibility evaluation of silk fibroin by chemical crosslinking. *Mater. Technol.* **2015**, *30*, 327−331.

(22) Huemmerich, D.; Helsen, C. W.; Quedzuweit, S.; Oschmann, J.; Rudolph, R.; Scheibel, T. Primary Structure Elements of Spider Dragline Silks and Their Contribution to Protein Solubility. *Biochemistry* **2004**, *43*, 13604−13612.

(23) Huemmerich, D.; Slotta, U.; Scheibel, T. Processing and modification of films made from recombinant spider silk proteins. *Appl. Phys. A: Mater. Sci. Process.* **2006**, *82*, 219−222.

(24) Müller-Herrmann, S.; Scheibel, T. Enzymatic Degradation of Films, Particles, and Nonwoven Meshes Made of a Recombinant Spider Silk Protein. *ACS Biomater. Sci. Eng.* **2015**, *1*, 247−259.

(25) Ihm, J. E.; Krier, I.; Lim, J. M.; Shim, S.; Han, D. K.; Hubbell, J. A. Improved Biocompatibility of Polyethylenimine (PEI) as a Gene Carrier by Conjugating Urocanic Acid: *In vitro* and *In vivo*. *Macromol. Res.* **2015**, *23*, 387−395.

(26) Neu, M.; Fischer, D.; Kissel, T. Recent advances in rational gene transfer vector design based on poly(ethylene imine) and its derivatives. *J. Gene Med.* **2005**, *7*, 992−1009.

(27) Peluso, G.; Petillo, O.; Ambrosio, L.; Nicolais, L. Polyetherimide as biomaterial: preliminary *in vitro* and *in vivo* biocompatibility testing. *J. Mater. Sci.: Mater. Med.* **1994**, *5*, 738−742.

(28) Dann, J. R. Forces Involved in the Adhesive Process: I. Critical Surface Tensions of Polymeric Solids as Determined with Polar Liquids. *J. Colloid Interface Sci.* **1970**, *32*, 302−320.

(29) Busscher, H. J.; Van Pelt, A. W. J.; De Jong, H. P.; Arends, J. Effect of Spreading Pressure on Surface Free-Energy Determinations by Means of Contact-Angle Measurements. *J. Colloid Interface Sci.* **1983**, *95*, 23−27.

(30) Wu, J.; Lee, N. Y. One-step surface modification for irreversible bonding of various plastics with a poly(dimethylsiloxane) elastomer at room temperature. *Lab Chip* **2014**, *14*, 1564−1571.

(31) Slepička, P.; Kasálková, N. S.; Stránská, E.; Bačáková, L.; Švorčík, V. Surface characterization of plasma treated polymers for applications as biocompatible carriers. *eXPRESS Polym. Lett.* **2013**, *7*, 535−545.

(32) Schacht, K.; Vogt, J.; Scheibel, T. Foams Made of Engineered Recombinant Spider Silk Proteins as 3D Scaffolds for Cell Growth. *ACS Biomater. Sci. Eng.* **2016**, *2*, 517−525.

(33) Hwang, D. S.; Sim, S. B.; Cha, H. J. Cell adhesion biomaterial based on mussel adhesive protein fused with RGD peptide. *Biomaterials* **2007**, *28*, 4039−4046.

(34) Ito, Y. Tissue engineering by immobilized growth factors. *Mater. Sci. Eng., C* **1998**, *6*, 267−274.

(35) Schaffner, P.; Meyer, J.; Dard, M.; Wenz, R.; Nies, B.; Verrier, S.; Kessler, H.; Kantlehner, M. Induced tissue integration of bone implants by coating with bone selective RGD-peptides *in vitro* and *in vivo* studies. *J. Mater. Sci.: Mater. Med.* **1999**, *10*, 837−839.

DOI: 10.1021/acsbiomaterials.6b00306
ACS Biomater. Sci. Eng. 2017, 3, 767−775

Supporting Information for

Surface modification of polymeric biomaterials using recombinant spider silk proteins

Christian B. Borkner[a]*, Stefanie Wohlrab*[a,†]*, Eva Möller*[a]*, Gregor Lang*[a,b]*, Thomas Scheibel*[a,c,d,e,f,g,*]

a – Lehrstuhl Biomaterialien, Fakultät für Ingenieurwissenschaften, Universität Bayreuth, Universitätsstr. 30, 95440 Bayreuth, Germany

b – Professur für Biopolymerverarbeitung, Fakultät für Ingenieurwissenschaften, Universität Bayreuth, Universitätsstr. 30, 95440 Bayreuth, Germany

c – Bayerisches Polymerinstitut (BPI), Universität Bayreuth, Universitätsstr. 30, 95440 Bayreuth, Germany

d – Bayreuther Zentrum für Kolloide und Grenzflächen (BZKG), Universität Bayreuth, Universitätsstraße 30, 95440 Bayreuth, Germany

e – Institut für Bio-Makromoleküle (bio-mac), Universität Bayreuth, Universitätsstr. 30, 95440 Bayreuth, Germany

f – Bayreuther Zentrum für Molekulare Biowissenschaften (BZMB), Universität Bayreuth, Universitätsstr. 30, 95440 Bayreuth, Germany g – Bayreuther Materialzentrum (BayMAT), Universität Bayreuth, Universitätsstr. 30, 95440 Bayreuth, Germany

Present Address: † Roche Diagnostics GmbH, Nonnenwald 2, 82377 Penzberg, Germany

* Corresponding Author: thomas.scheibel@bm.uni-bayreuth.de

Supporting information consists of 9 pages and 7 figures.

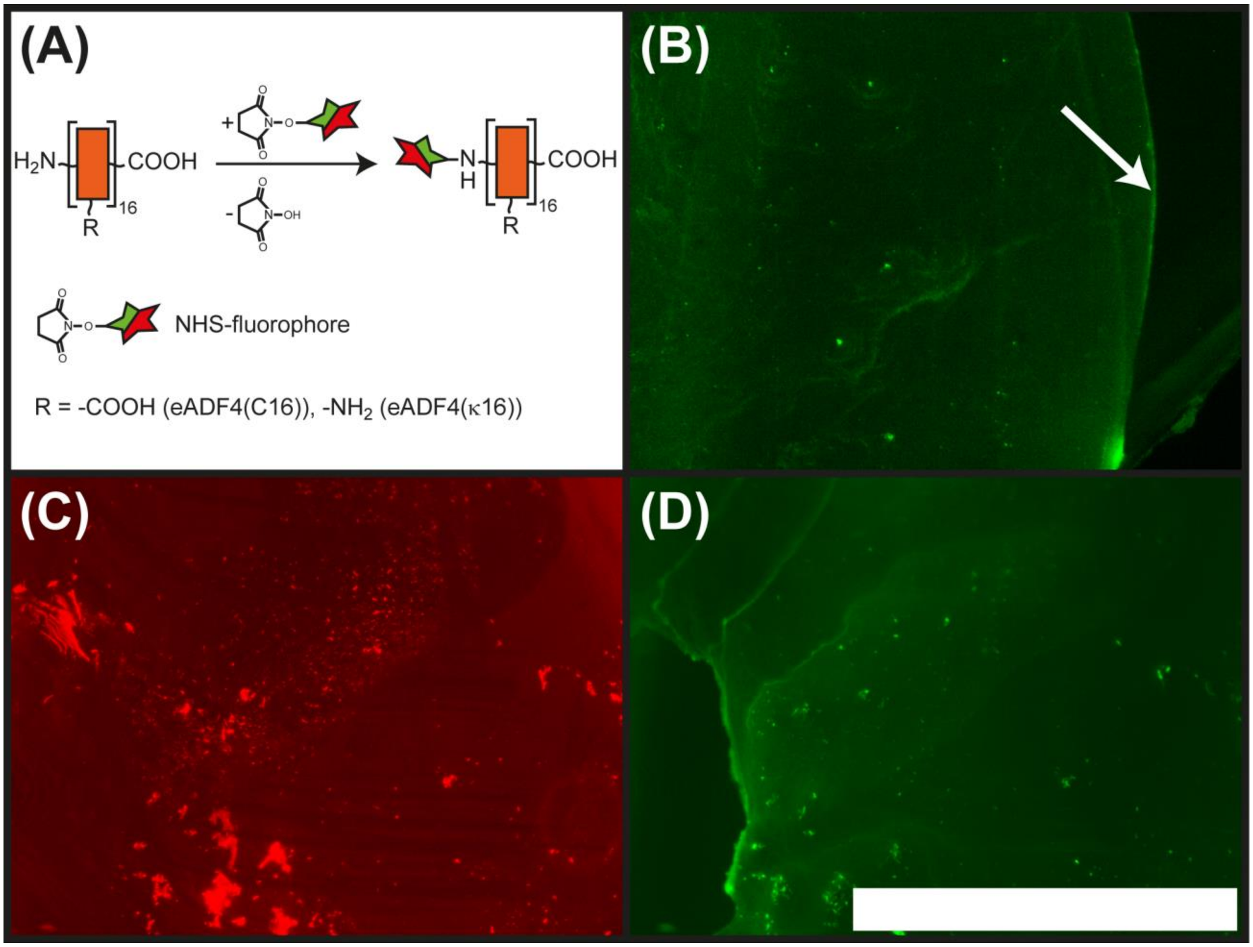

Figure S1. Schematic illustration of fluorophore coupling to proteins (A) and fluorescence microscopy images of coated silicone catheters (B-D). Catheters were coated with (B) PEI/eADF4(C16) and (C, D) eADF4(κ16)/eADF4(C16). The sample in (B) was not completely dipped into eADF4(C16) so that a sharp coating border can be seen on the right hand side (arrow). (C) and (D) show the same area on one sample. eADF4(κ16) forms the first coating layer (C). The top layer made of eADF4(C16) covers the initial eADF4(κ16) structures (D). The eADF4(κ16)/eADF4(C16) coated sample was completely dipped into eADF4(C16) solution, and only the area on the left hand side was covered by the holding clamp of the dip coater (D). eADF4(κ16) is labeled with NHS-rhodamine (red fluorescence) and eADF4(C16) is labeled with NHS-fluorescein (green fluorescence). The NHS fluorophores bind to amino groups present in the protein. Scale bar: 750 µm. PEI: polyethyleneimine.

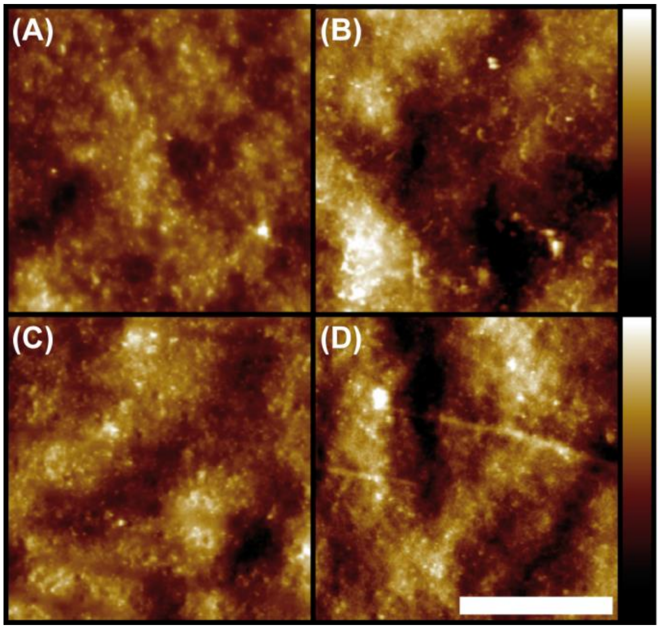

(E)

Entry	Coating	R_a / nm
1	PEI	9.6 ± 1.5
2	PEI/eADF4(C16)	13.5 ± 2.5
3	eADF4(κ16)	12.2 ± 2.7
4	eADF4(κ16)/ eADF4(C16)	13.7 ± 2.9

Figure S2. Tapping mode atomic force microscopy images showing the topography of silicone catheter surfaces coated with (A) PEI, (B) PEI/eADF4(C16), (C) eADF4(κ16) and (D) eADF4(κ16)/eADF4(C16). The average surface roughness R_a was calculated at an area of 25 µm^2 (E). Scale bar: 5 µm, height bars: 120 nm. PEI: polyethyleneimine.

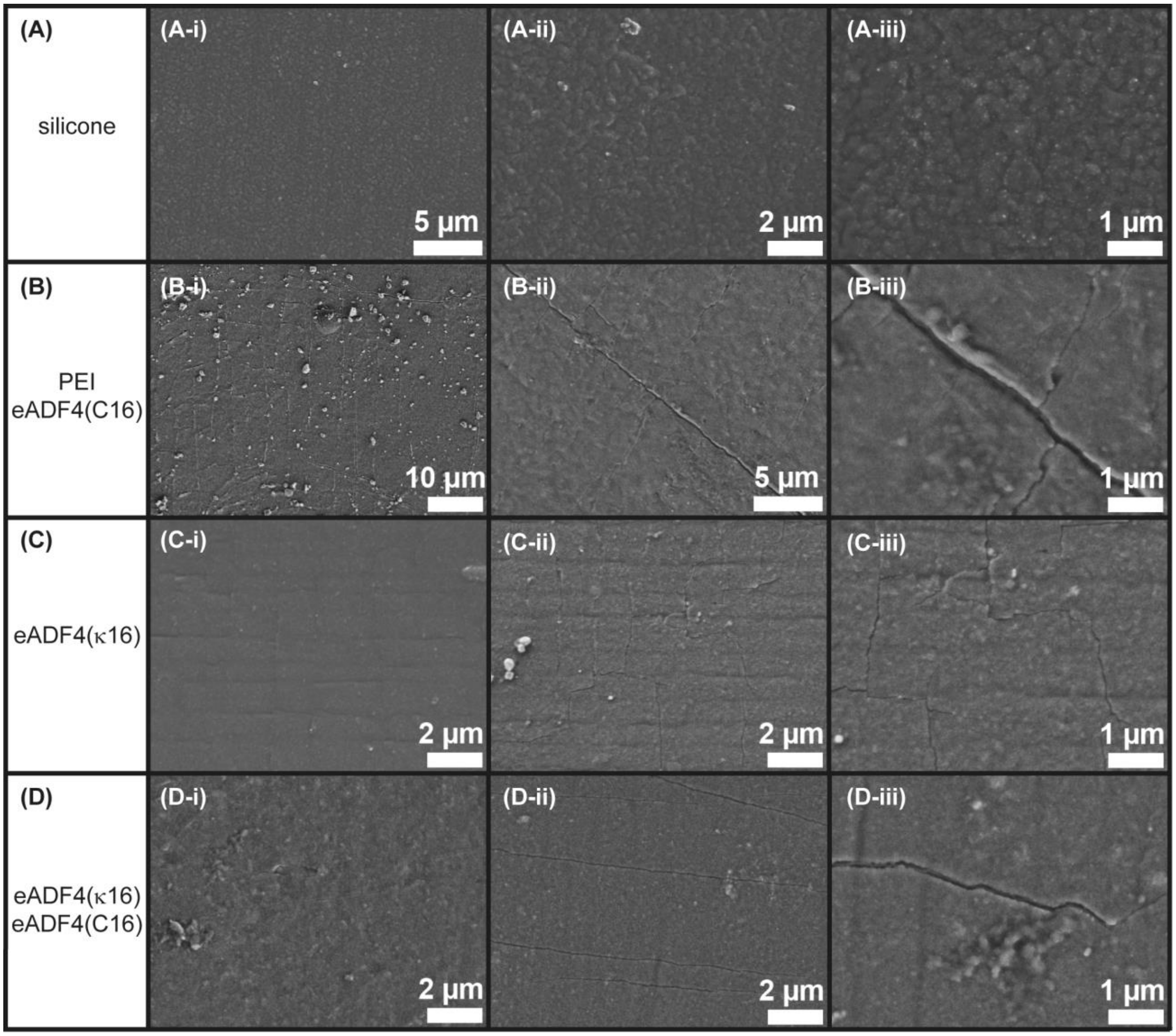

Figure S3. SEM pictures of (A) silicone (control), (B) PEI/eADF4(C16) coating, (C) eADF4(κ16) coating and (D) eADF4(κ16)/eADF4(C16) coating on silicone after bending tests (n = 3). (A-i, ii, iii) showing zoom-in pictures of the same sample area. (B-i) and (B-ii, B-iii), (C-i) and (C-ii, C-iii), (D-i) and (D-ii, D-iii) showing two different areas with (B-iii, C-iii, D-iii) being a zoom-in of (B-ii, C-ii, D-ii). PEI: polyethyleneimine.

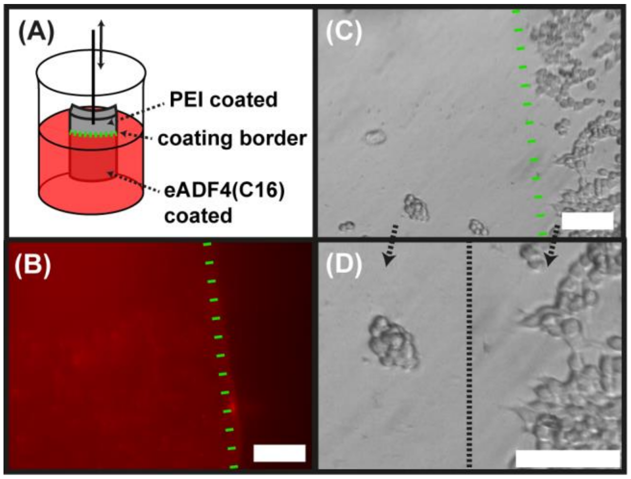

Figure S4. Fibroblast (BALB/3T3) adhesion on PEI/eADF4(C16)-coated silicone tubes illustrated by (A) a schematic of the coating procedure pointing out the border (green dotted line) between the PEI- and eADF4(C16)-coated area, (B) fluorescence microscopy image showing red fluorescence of the eADF4(C16)-rhodamine-coated area, while the PEI-coated area shows no fluorescence, and (C) light microscopy image of fibroblasts at the same area. (D) shows a 200% zoom-in of a fibroblast agglomerate at the eADF4(C16)-coated area (left) and adherent fibroblasts at the PEI-coated area (right). Fibroblasts (100,000 cells/cm^2) were cultivated for 24 h. Scale bars: 100 µm. PEI: polyethyleneimine.

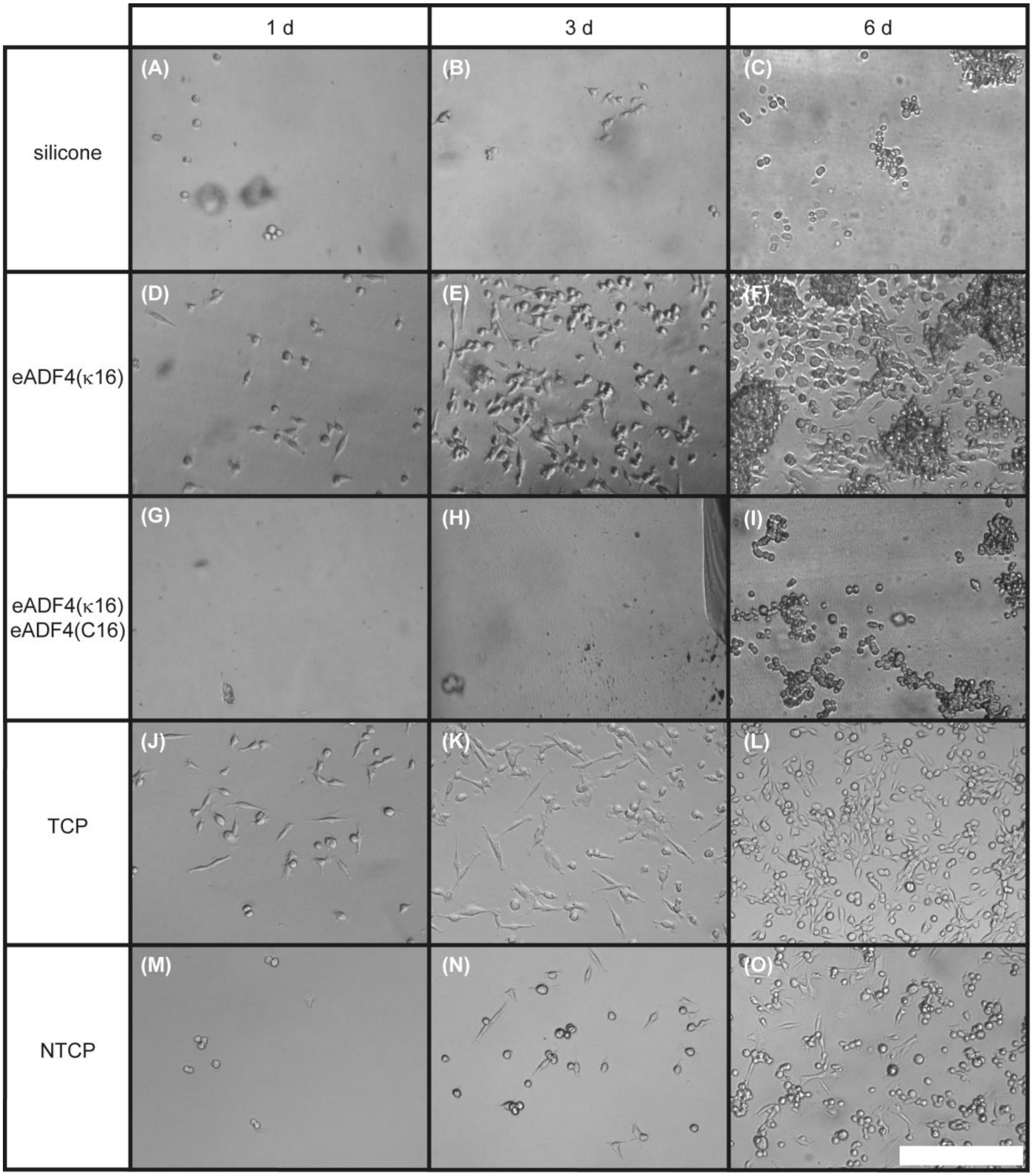

Figure S5. Neuronal cell (B50) adhesion (5,000 cells/cm² seeded) on silicone catheters after 1 d, 3 d and 6 d. Bright field microscopy pictures of cells on silicone (A-C), eADF4(κ16)-coated silicone (D-F), eADF4(κ16)/eADF4(C16)-coated silicone (G-I). TCP: treated cell culture plate ("good adhesion" control) (J-L), NTCP: non treated cell culture plate ("bad adhesion" control) (M-O). Scale bar: 250 µm.

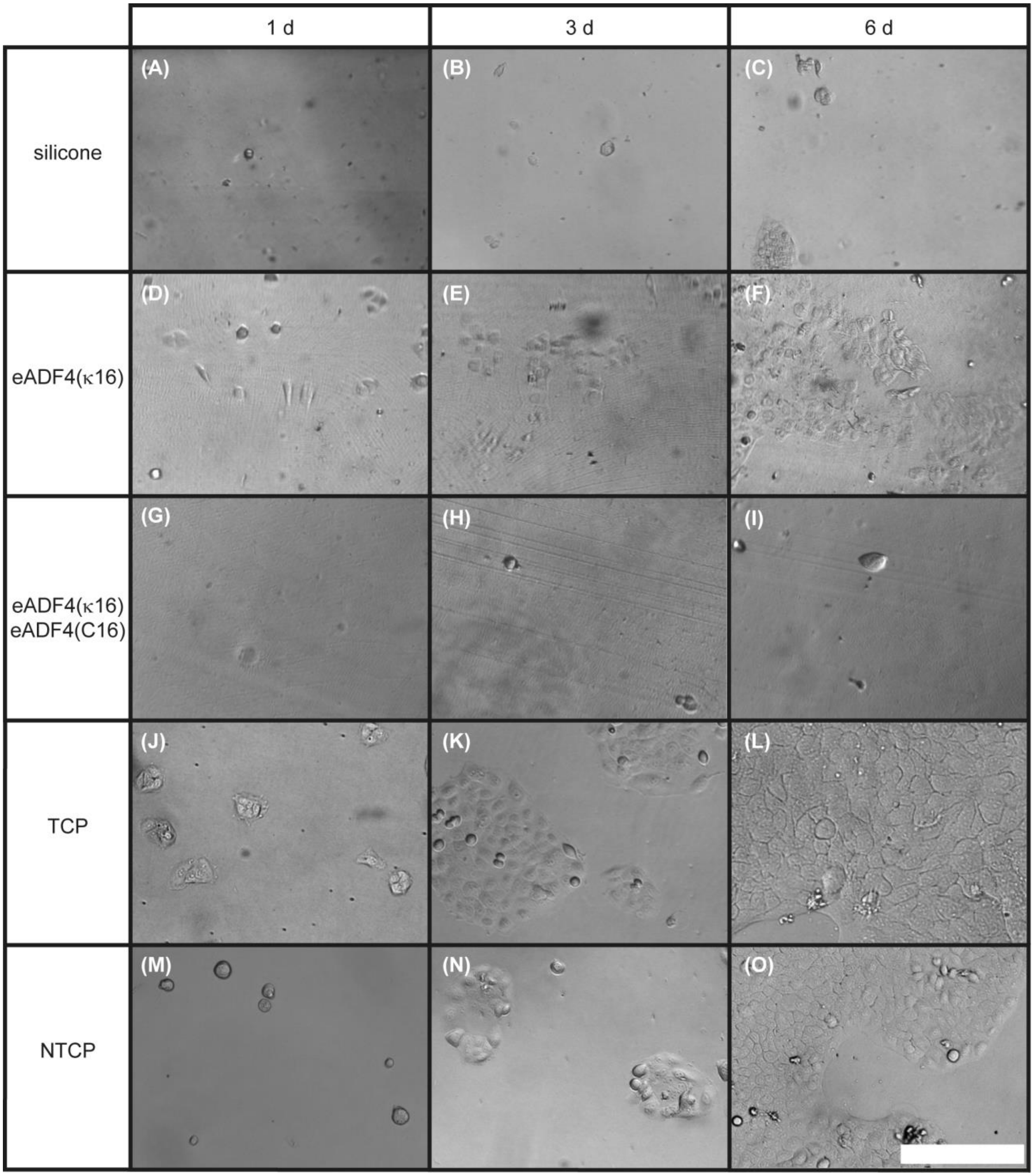

Figure S6. Keratinocyte (HaCaT) adhesion (5,000 cells/cm² seeded) on silicone catheters after 1 d, 3 d and 6 d. Bright field microscopy pictures of cells on silicone (A-C), eADF4(κ16)-coated silicone (D-F), eADF4(κ16)/eADF4(C16)-coated silicone (G-I). TCP: treated cell culture plate ("good adhesion" control) (J-L), NTCP: non treated cell culture plate ("bad adhesion" control) (M-O). Scale bar: 250 µm.

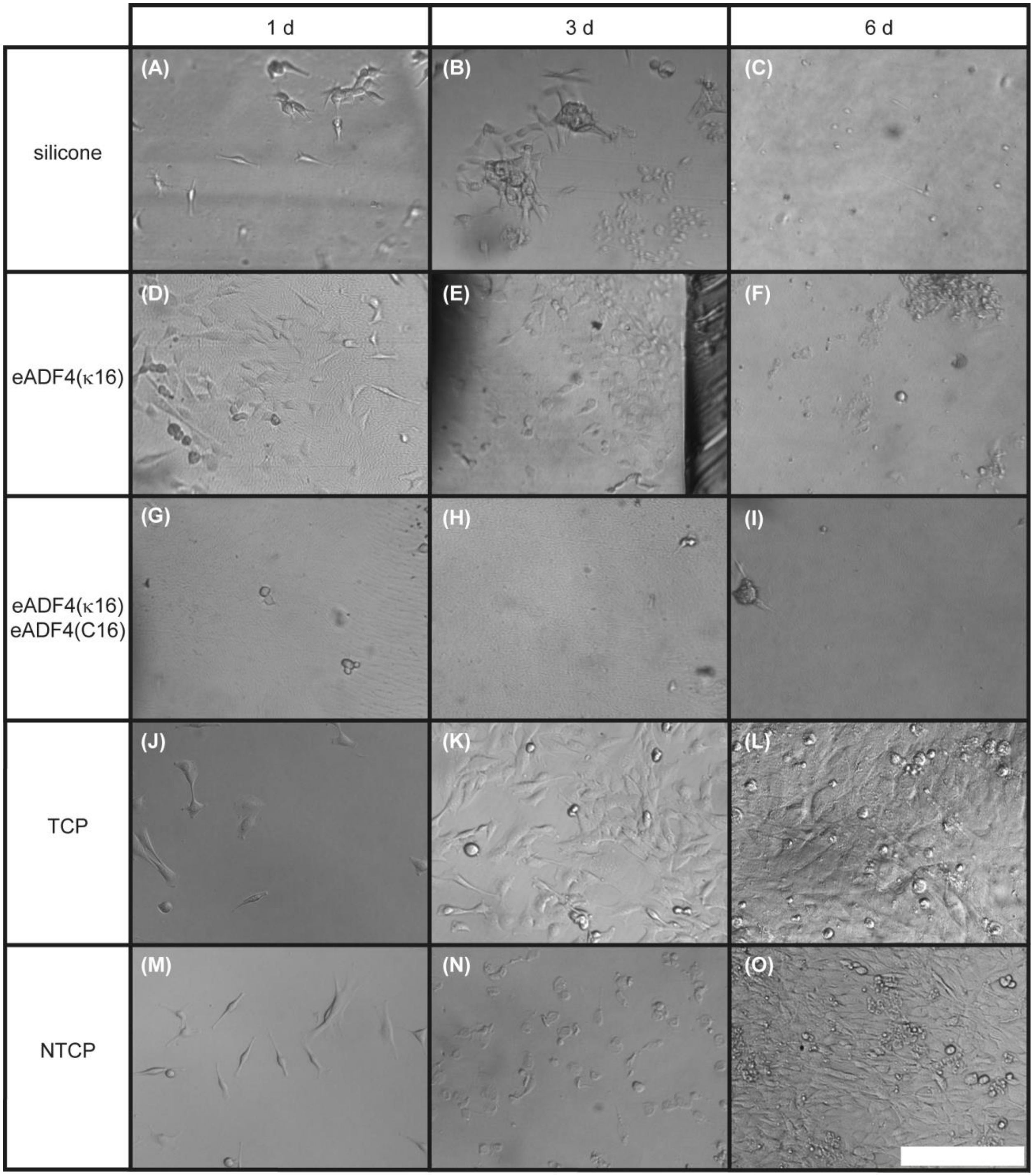

Figure S7. Myoblast (C2C12) adhesion (5,000 cells/cm² seeded) on silicone catheters after 1 d, 3 d and 6 d. Bright field microscopy pictures of cells on silicone (A-C), eADF4(κ16)-coated silicone (D-F), eADF4(κ16)/eADF4(C16)-coated silicone (G-I). TCP: treated cell culture plate ("good adhesion" control) (J-L), NTCP: non treated cell culture plate ("bad adhesion" control) (M-O). Scale bar: 250 µm.

Teilarbeit III

Die Ergebnisse dieses Kapitels wurden bereits in *ACS Applied Polymer Materials* veröffentlich als:

Ultrathin Spider Silk Films: Insights into Spider Silk Assembly on Surfaces.

Christian B. Borkner*, Sarah Lentz*, Martin Müller, Andreas Fery und Thomas Scheibel

* gleichberechtigte Co-Autorenschaft

Mit Genehmigung abgedruckt aus C. B. Borkner, S. Lentz, M. Müller, A. Fery, T. Scheibel, Ultrathin Spider Silk Films: Insights into Spider Silk on Surfaces. *ACS Applied Polymer Materials* **2019**, *1*, 3366-3374. Copyright 2019 American Chemical Society.

Reprinted with permission from C. B. Borkner, S. Lentz, M. Müller, A. Fery, T. Scheibel, Ultrathin Spider Silk Films: Insights into Spider Silk Assembly on Surfaces. *ACS Applied Polymer Materials* **2019**, *1*, 3366-3374. Copyright 2019 American Chemical Society.

ACS APPLIED POLYMER MATERIALS
Article
Cite This: ACS Appl. Polym. Mater. 2019, 1, 3366−3374
pubs.acs.org/acsapm

Ultrathin Spider Silk Films: Insights into Spider Silk Assembly on Surfaces

Christian B. Borkner,[†,¶] Sarah Lentz,[†,¶] Martin Müller,[‡,○] Andreas Fery,[‡,◆] and Thomas Scheibel[*,†,§,∥,⊥]

[†]Lehrstuhl Biomaterialien, Fakultät für Ingenieurwissenschaften, Universität Bayreuth, Prof.-Rüdiger-Bormann-Strasse 1, 95447 Bayreuth, Germany

[‡]Leibniz-Institut für Polymerforschung Dresden (e.V.), Institute of Physical Chemistry and Polymer Physics, Hohe Strasse 6, D-01069 Dresden, Germany

[○]Technische Universität Dresden, Chair for Physical Chemistry of Polymeric Materials, 01069 Dresden, Germany

[◆]Technische Universität Dresden, Chair for Macromolecular Chemistry, 01062 Dresden, Germany

[§]Bayerisches Polymerinstitut (BPI), Bayreuther Zentrum für Kolloide und Grenzflächen (BZKG), [∥]Bayreuther Zentrum für Molekulare Biowissenschaften (BZMB), [⊥]Bayreuther Materialzentrum (BayMAT), Universität Bayreuth, Universitätsstrasse 30, 95440 Bayreuth, Germany

Supporting Information

ABSTRACT: β-Sheets in natural spider dragline silk proteins are typically formed by polyalanine (A_n) as well as alanine-glycine (AG) and GGA sequences flanking these A_n regions. The hydrophobic β-sheet-rich regions are embedded in a hydrophilic amorphous matrix, and this phenomenon can be reflected as microphase separation, similar to that of block copolymers. Microphase separation occurs not only in fibers but also in cast spider silk films. Micellar-like structures form within the bulk of the film, while substrate surface as well as the film/air interface trigger explicit secondary structure formation in these layers. So far, only limited information is available concerning the mechanism of film assembly and microphase separation of spider silk proteins on surfaces. In this work, self-assembly and folding of eADF4(C16) was analyzed on steady silicon surfaces, dependent on the spider silk layer number and thickness. Based on the results, a model for structural features of spider silk films is proposed, combining block copolymer microphase separation theory with folding properties of recombinant eADF4(C16).

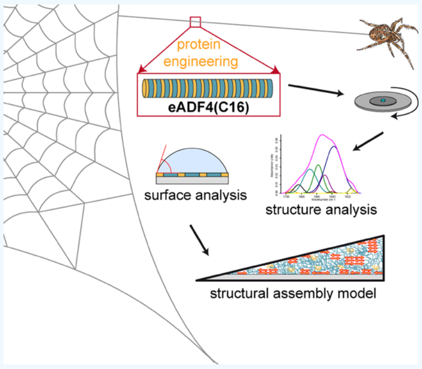

KEYWORDS: *spider silk, protein structure, self-assembly, spin-coating, microphase separation*

1. INTRODUCTION

Silks, like keratin and collagen,[1−3] are protein fibers, and the underlying proteins have highly repetitive amino acid sequences. Among silk producers, web-spinning spiders (*Araneae*) have probably the highest variety of specialized silk materials. Female orb-weaving spiders such as the European garden spider *Araneus diadematus* can produce up to seven different types of silk with task-dependent properties, up to five of which are utilized in their webs.[4]

The engineered spider silk protein eADF4(C16) is based on the consensus sequence of the core domain of *A. diadematus* fibroin 4 (ADF4), which belongs to the class of major ampullate spidroin 2 (MaSp2), characterized by proline-rich sequences. Figure 1 illustrates the key elements of the primary structure of amphiphilic eADF4(C16) and the related secondary structure elements upon processing.[5] The amino acid consensus motif of the core domain of ADF4 is called C-module (sequence: GSSAAAAAAAAS GPGGY GPENQGPS GPGGY GPGGP) and is repeated 16 times in the recombinant protein.[6] eADF4(C16) is an amphiphilic protein with polyalanine stretches reflecting hydrophobic and glycine-rich regions reflecting hydrophilic blocks. These polyalanine stretches (pAla; A_n) fold into β-sheets upon fiber assembly.[7,8] Therein, antiparallel β-sheets are formed by assembly of several individual pAla β-strands. The surrounding elastin-like sequences (GPGGX, X = Y, P) and glutamic acid containing motifs (GPENQGPS) form an amorphous phase.[8−14] From a polymer perspective, recombinant spider silk can be regarded as a semicrystalline material where β-sheets from several protein chains form β-sheet crystallites, which are embedded in an amorphous matrix.[15,16] Micrometer-thick films cast of eADF4(C16) show a secondary structure similar to that of natural spider silk fibers and have a β-sheet content (B) between 34 and 52% depending on parameters like solvent, post-treatment, and substrate material on which the films are cast.[17−20]

Received: August 24, 2019
Accepted: October 30, 2019
Published: October 30, 2019

DOI: 10.1021/acsapm.9b00792
ACS Appl. Polym. Mater. 2019, 1, 3366−3374

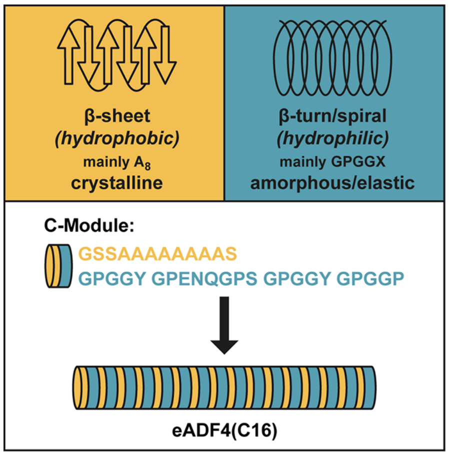

Figure 1. Primary structure (amino acid sequence) of the amphiphilic C-module and corresponding secondary structure elements in recombinant spider silk protein eADF4(C16). The two-color code indicates the block-copolymer-like structure where the hydrophobic part of the amino acid sequence is shown in yellow and the hydrophilic part is shown in blue.

Unlike synthetic polymers, recombinant proteins have a polydispersity index of 1.0. eADF4(C16) can be considered as a block copolymer with the motif $(AB)_{16}$, where block A is hydrophobic and block B is hydrophilic (illustrated in Figure 1 by a two-color code of sequence stretches, A: yellow, B: blue).[16] Block copolymers can in principle undergo microphase separation. Therein, similar blocks try to maximize and dissimilar blocks try to minimize their interaction, yielding separation into microdomains.[21−24] Such microphase separation behavior has indeed been previously reported for silk proteins, including eADF4(C16),[18,25,26] *Bombyx mori* silkworm silk fibroin,[27,28] multiblock copolymers based on *B. mori* and other spider silk proteins,[29,30] as well as other protein-based block copolymers.[31] Microphase separation occurs in diluted solutions, lyotropic liquid crystalline phases, and in the solid phase.[22,23] Phase separation and the structure of silk proteins were first described in the 1990s for the silk of the domestic silkworm *B. mori* at the water/air interface.[32−34]

Recently, recombinant spider silk proteins based on primary structure elements of spider silk proteins of the MaSp1 class (having a low proline content) were analyzed concerning their behavior when processed into films. The used proteins, named HBA_x (x = 1, 2, 6), comprised a histidine-tag (H) for purification, a pAla/glycine-rich block (A) forming hydrophobic β-sheets, and a noncrystalline glycine-rich block (B).[35] The proteins were processed into Langmuir Blodget films showing microphase separation of the hydrophilic and hydrophobic blocks at the air/silk and silk/substrate interfaces depending on the surface pressure[36] and a sequence-dependent secondary structure formation (β-sheets) in cast films of HBA_3 and HAB_3 due to the varying number of blocks.[30,37,38]

When eADF4(C16) was cast into microfilms with a thickness of 1−2 μm, microphase separation occurred depending on the hydrophobicity of the substrate and the film thickness. On hydrophilic substrates, the hydrophilic blocks were oriented toward the substrate and hydrophobic pAla patches toward the film/air interface. Within the bulk of the film, pAla β-sheets formed β-sheet crystallites embedded in a hydrophilic Gly-rich matrix.[18]

Here, spider silk films of eADF4(C16) were produced by spin-coating, yielding homogeneous thin silk films with low surface roughness.[39−41] The aim of this study was to identify the influence of the increasing number of silk layers (starting with a monolayer) on protein structure and surface properties of respective spider silk films. The term monolayer refers to the thinnest possible homogeneous layer of spider silk protein (3−4 nm). This film thickness matches with the previously reported monolayer thickness of *B.mori* silk fibroin films.[42] Lee et al. investigated the colorimetric fingerprints of aperiodic nanopattternd silk fibroin monolayers with the dimensions for β-sheets of 5 nm and corresponding β-strands of 2 nm.[42] Zha et al. assembled eADF4(C16) into nanofibers using simultaneous supramolecular assembly and adsorption in a one-pot approach.[43,44] The thinnest possible coating with nanofibrils was observed with dimensions of 2−3 nm thickness and 10 nm width.[43,44]

The present study enabled a deeper insight into structure formation and microphase separation properties of spider silk layers starting at the nanoscale, passing the mesoscale, and reaching the bulk (i.e., the microscale).

2. RESULTS

2.1. Processing of Ultrathin Spider Silk Films.

Homogenous thin eADF4(C16) films were prepared using spin-coating.[45,46] Figure 2A shows exemplary atomic force microscopy (AFM) images (topography) of eADF4(C16) films made of 1, 2, 10, and 50 mg/mL eADF4(C16) solutions.

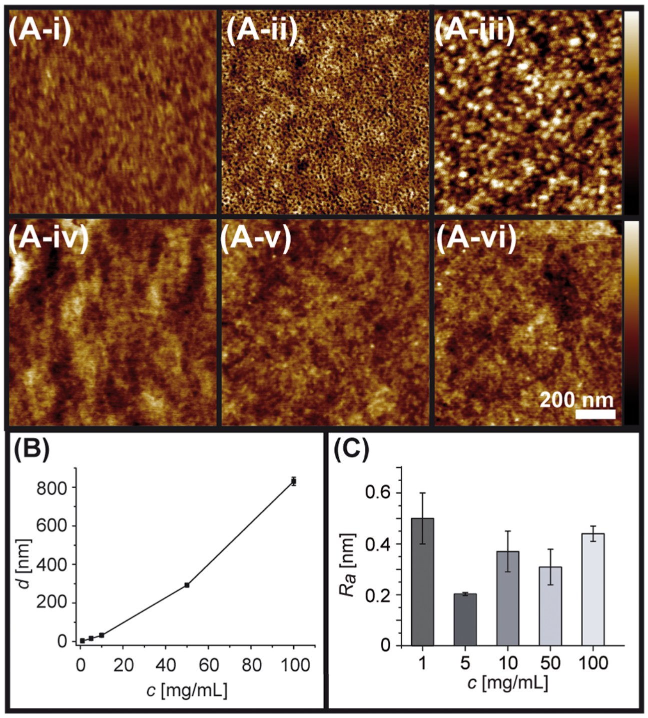

Figure 2. (A) AFM height images of thin eADF4(C16) films made using spin-coating exemplarily shown for solutions containing (i) 1, (ii) 2, (iii) 5, (iv) 10, (v) 50, and (vi) 100 mg/mL eADF4(C16) (height bar: 2 nm) on a silicon wafer. (B) Protein concentration dependency (1, 5, 10, 50, and 100 mg/mL) of the film thickness using constant spin-coating parameters. (C) Average roughness (R_a) of films prepared at protein concentrations of 1, 5, 10, 50, and 100 mg/mL (3−800 nm, respectively) on silicon measured in an area of 25 μm^2.

Additional AFM images are shown in the Supporting Information (Figure S1). Figure 2B illustrates the concentration dependence of the coating thickness in a range of 1–100 mg/mL, leading to film thicknesses from 3 to 800 nm with an average surface roughness (R_a) of <1.0 nm for all prepared films (Figure 2C). Thus, spin-coating allowed controlled processing of ultrathin silk films by simply varying the silk concentration in solution. Observation of microphase separation in thin silk films by AFM was limited by the small size of hydrophilic (23 amino acids) and hydrophobic (12 amino acids) blocks combined with the similar physical properties (stiffness/softness; adhesion between tip and surface) of the two different blocks in the C-module. The spider silk film processed from 1 mg/mL protein solution showed vertically aligned segments (Figure 2A-i), whereas the 2 mg/mL film showed mesophasic features and a smooth surface (Figure 2A-ii). Through further increase of the protein concentration to 10 and 50 mg/mL eADF4(C16), the structural features of the films became more blurred and cloudier (Figure 2A-iii and A-iv).

2.2. Secondary Structure and Contact Angle Analysis.

In the following, nanofilms are depicted as films with a thickness of 1 to ~100 nm; films in the range of 100 nm to ~999 nm are called submicrofilms, and films thicker than 1 μm are called microfilms. The relative β-sheet content (B) of spin-coated nano- and (sub)microfilms (d = 3–800 nm) after spin-coating and before (bpt) or after (apt) post-treatment with methanol vapor was determined using grazing angle attenuated total reflectance (GATR)-Fourier transform infrared (FTIR) spectroscopy measurements and data treatment using Fourier self-deconvolution (FSD) and curve fitting of the amide I band, yielding the β-sheet content shown in Figure 3A (see Supporting Information, Figure S3 and S4). The amide I band is mainly a superposition of C=O stretching vibrations from the amide groups of the protein backbone, and they are influenced considering their vibration energy by intra- and intermolecular coupling due to their specific/defined secondary structural surroundings.[47,48] In eADF4(C16) nanofilms (d = 3–4 nm), a relative β-sheet content of $B_{bpt} = 14.2 \pm 2.7\%$ was obtained before post-treatment. The thickness of the thinnest prepared eADF4(C16) nanofilm was similar to the thickness of β-sheet platelets and nanofilaments reported for silkworm silk fibroin and eADF4 nanofibrils (d = 2–5 nm).[41,43,49] When the film thickness was increased, B_{bpt} also increased. A steady increase in B_{bpt} could be observed with an increasing film thickness of nano- and (sub)microfilms until a saturation was reached with a relative β-sheet content of B_{bpt} = 18–21% at d > 65 nm.

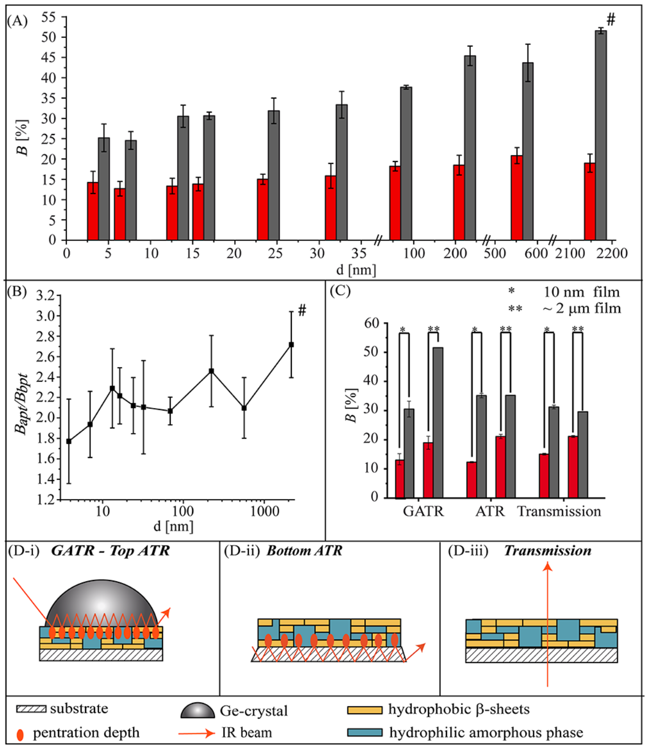

Figure 3. (A) β-sheet content B of spin-coated eADF4(C16) films before (bpt) and after post-treatment (apt, gray) in methanol atmosphere dependent on film thickness d (red). (B) Ratio of the relative average β-sheet content after (B_{apt}) and before post-treatment (B_{bpt}) reflects the increase in B due to post-treatment in a methanol atmosphere. Connecting lines are auxiliary lines to guide the eye. Microfilms with a thickness of ~2 μm were prepared by drop-casting. (C) β-sheet content B before (bpt, red) and after post-treatment (apt, gray) in a methanol atmosphere measured using three different FTIR techniques, namely GATR, ATR, and transmission. (D) Schematic representation of different FTIR techniques: (i) shows the GATR setup, where the film is measured on the surface facing the air. (ii) The complementary measurement setup. There, the substrate/film interface is measured using attenuated total reflection with the ATR mode. (iii) Representation of a transmission measurement, where parts of the IR beam penetrate the entire sample. Signals derived from the spin-coated eADF4(C16) films depended on the used FTIR technique.

The steady increase of B_{bpt} from mono- to bilayered nanofilms to (sub)microfilms can be explained by the intra- and intermolecular interactions of the protein and the interaction of eADF4(C16) molecules with the silicon wafer surface. Due to the fast evaporation of formic acid, which was used as solvent for eADF4(C16), the silk molecules were frozen in a metastable partially unstructured state and did not have time for folding into secondary structures like β-sheets. In the thinnest produced nanofilm, the silk molecules had no protein neighbor in the z-direction, and interactions with other molecules were only possible in the xy-plane. The B_{bpt} determined in the films when d < 10 nm can be explained by interactions of the protein backbone with the surface of the substrate. If the molecules were forced to the surface in a monolayer, the carbonyl group (C=O) could only interact with the silicon oxide (SiO_2) layer, which covered the silicon wafer surface. However, the probability to form pAla–pAla interactions increased in a multilayer. The increase in layer thickness raised the probability (gain in the degree of freedom of translation) to form inter- and intramolecular interactions (pAla–pAla; β-sheets), leading to a rise of B_{bpt}. The volume phase also increased with the layer thickness. An increasing volume phase caused a higher degree of the amorphous silk phase, in which β-crystallites could more readily grow with less confinement from the silicon/silk and the silk/air interface.

Post-treatment of spider silk films in methanol atmosphere led to an increasing β-sheet content (rearrangement of pAla stretches into β-sheets) due to dehydration (Figure 3A and Supporting Information, Figures S3 and S4)).[39,50–52] The post-treatment in methanol vapor led to temporary swelling of the spider silk films.[53] Here, we assume that the differences in B_{apt} in nano and (sub-)microfilms occur from the limited diffusion of methanol vapor to the bulk of the microfilm because the conversion of pAla-patches to β-sheet starts at the

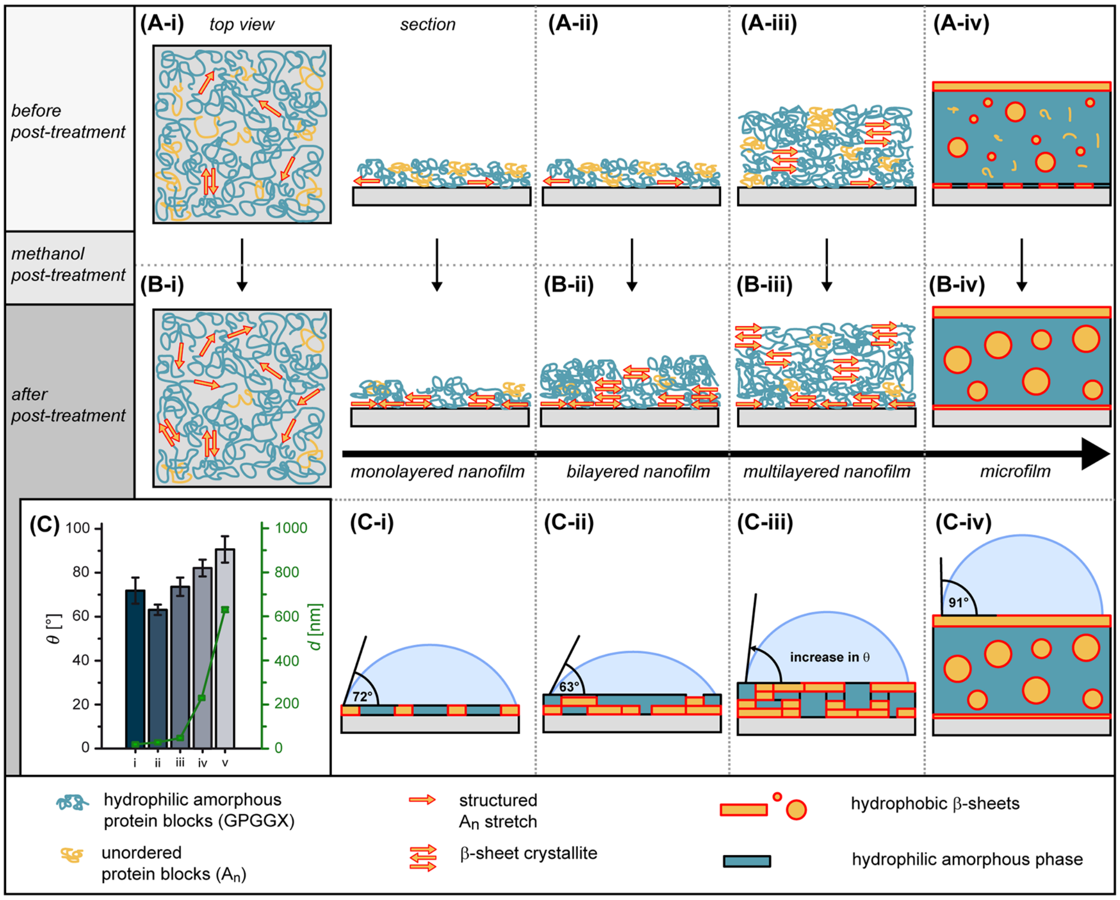

Figure 4. Structural assembly model for eADF4(C16) films dependent on the film thickness from the nano- to microscale. A detailed structural model for films (A) directly after spin-coating and drying and (B) after post-treatment with methanol. (C) Static water contact angle on post-treated spider silk films with simplified separation scheme and illustrated wetting behavior. In all panels (A−C): (i) monolayered nanofilms showed 2D separation of the hydrophilic and hydrophobic phases, (ii) bilayered nanofilms showed a pAla-enriched phase at the silicon substrate surface leading to exposition of the hydrophilic phase at the protein/air interface, (iii) multilayered nanofilms yielded pAla-rich surface/protein interfaces and β-sheet-rich protein/air interfaces, which are hydrophobic,[18] and (iv) microfilms showed microphase separation in the bulk film as previously reported by Wohlrab et al., in which β-sheet crystallites are separated at the protein/air interface as well as embedded as micelle-like inclusions in the amorphous matrix.[18]

interface and therefore limits the diffusion of the methanol vapor to the deeper layers of the film. After the post-treatment in methanol, the films were stored in air to allow the methanol to evaporate completely. B_{apt} was always measured with dry films. The film thickness was only temporarily influenced by the post-treatment.[53] At the beginning, Hu et al. stated that structural water can act as a "mobility enhancer" and increases the flexibility and the extensibility, but exposure to nonaqueous solvents yields in β-sheet formation. In all cases, post-treatment led to an increase in B. Figure 3B shows the ratio (B_{apt}/B_{bpt}) of the β-sheet content after (B_{apt}) and before post-treatment (B_{bpt}). The lowest rise in B upon post-treatment was observed for spider silk monolayers ($d \approx 4$ nm) ($B_{apt}/B_{bpt} = 1.8 \pm 0.4$). The error of B_{apt}/B_{bpt} was calculated using Gauß law of propagation. If the layer thickness was doubled ($d \approx 8$ nm), B_{apt}/B_{bpt} increased to 1.9 ± 0.3 and reached 2.3 ± 0.4 at $d \approx 13$ nm. In the case of the monolayer ($d < 5$ nm), the β-sheet content increased from 14.2 ± 2.7 to $25.2 \pm 3.4\%$ upon post-treatment, which was only half of the B_{apt} for eADF4(C16) microfilms because the number of pAla/pAla interactions was limited in the monolayer. Intra- and intermolecular pAla interactions could be formed only in the xy-direction, which significantly decreased the probability for these interactions. In comparison, B_{bpt} and B_{apt} of drop-cast eADF4(C16) films with a thickness of ∼2 μm on silicon were also investigated (Figure S2), where B increased from $B_{bpt} = 19.0 \pm 2.2\%$ to $B_{apt} = 51.6 \pm 0.7\%$ with $B_{apt}/B_{bpt} = 2.7 \pm 0.3$. This reflects the maximum relative β-sheet content $B_{max,apt}$ of post-treated eADF4(C16) films reported in literature (on glass: $35.7 \pm 1.7\%$;[18] on polystyrene: $41.0 \pm 0.3\%$,[18] 45.2%[19] by post-treatment with methanol, and 52.1%[20] by post-treatment with $K_xH_{3-x}PO_4$). As stated above, in the case of films before post-treatment, the carbonyl group (C=O) could interact only with the silicon oxide layer. When the film thickness was increased, the conformational freedom, increasing volume phase, and the probability for each molecule/pAla stretch to form β-sheets increased due to the increasing number of interaction partners in each layer (z-direction). This led to an increase in B with increasing film thickness until the maximum in B_{bpt} and B_{apt} was reached at a film thickness of about 90−220 nm.

The high B_{apt} of microfilms on silicon indicates the separation of the hydrophobic β-sheet structures at the protein/air interface, considering the theoretical penetration depth d_p of the IR-irradiation during GATR-ATR measurements of 313 nm at 1590 cm^{-1} and 292 nm at 1705 cm^{-1} (see

Supporting Information, Table S1 and FTIR spectra Figures S3 and S4)).

Due to the limited penetration depth of the IR beam, two additional FTIR methods were used besides GATR-FTIR to gain a deeper insight into the distribution of β-sheet structures in eADF4(C16) nano- (d = 10 nm) and microfilms (d = 1 μm). Schematic setups of the three different measuring modes are shown in Figure 3C. With the GATR-FTIR setup, the air/silk interface was measured (Figure 3D-i). With the ATR-FTIR setup, it was possible to measure the spider silk film structure at the silicon/silk interface (Figure 3D-ii). The third setup measured the transmission of the FTIR beam through the whole silk film (Figure 3D-iii, Supporting Information Table S2). The results from these three setups showed that, depending on which interface (silicon/silk or silk/air) was investigated, different β-sheet contents were observed. B_{bpt} showed in all three setups similar values for nano- and (sub)microfilms as shown in detail for the GATR setup (Figure 3A, see FTIR spectra Supporting Information, GATR Figures S3 and S4, ATR Figure S5, and transmission Figure S6). In contrast to B_{bpt}, the proportions of signals at the silicon/silk interface (ATR-FTIR) resulted in different values for B_{apt}. Nano- and microfilms contained the same amount of β-sheets (B_{10nm}= 35.2 ± 0.7%; $B_{1\mu m}$ = 35.2 ± 0.5%). This could be explained by limited diffusion of methanol during the post-treatment process for the (sub-) microfilms because the β-sheets on the interface air/film formed a more compact layer through which the methanol vapor could no longer diffuse freely. Therefore, the bulk (middle) and lower part of the film showed less β-sheet content (see Supporting Information, Figure S7).

Transmission FTIR provided the overall β-sheet content of the films. Interestingly, B of the nanofilms doubled (B_{bpt} = 15.1 ± 0.3% to B_{apt} = 31.2 ± 0.6%) upon methanol post-treatment, whereas B_{bpt} in microfilms was already 21.1 ± 0.4% and only slightly increased to B_{apt} = 29.6 ± 0.2% after methanol post-treatment.

3. DISCUSSION

Structural Assembly of Spider Silk Proteins on Surfaces Depends on the Number of Layers/Film Thickness. An interesting observation was the increase in B until saturation by increasing the spider silk film thickness. Analysis of B combined with the surface wetting properties of the spin-coated thin spider silk films led to a structural assembly model for eADF4(C16) films depending on the number of protein layers (Figure 4).

Blocks in polymers (here: hydrophobic and hydrophilic sequence motifs of the C-module) are only miscible if they interact through specific interactions such as hydrogen bonds, charge−charge, and hydrophobic interactions, which yields structuring/folding of the protein. In eADF4(C16), the hydrophilic Gly-rich blocks do not significantly interact with the more hydrophobic pAla blocks, and therefore, interactions between identical blocks are preferred. Due to the covalent connection (i.e., the polypeptide backbone) of the hydrophilic and the hydrophobic block, the molecules could not undergo macroscopic phase separation in the solid-state, i.e., in contact with a substrate's surface. If one considers eADF4(C16) an amphiphilic block copolymer with the architecture $(AB)_{16}$, it is possible to calculate the volume fraction ϕ_A for the hydrophobic block and ϕ_B for the hydrophilic block. The amino acid sequence of the C-module (Figure 1) is divided into 12 amino acids which correspond to the hydrophobic block A and 23 amino acids which correspond to the amorphous, hydrophilic block B. For $(AB)_{16}$ polymers, the ratio of block A to the total number of aa in the sequence is a value for the expected type of microphase formation. It results in ϕ_A = 0.34 for the hydrophobic block, which is also the theoretical β-sheet content of eADF4(C16). At ϕ_A = 0.35−0.65, alternating lamellar structures for A and B would be observed.[54] In contrast, at $0.2 < \phi_A < 0.35$, cylindrical structures would be observed for the hydrophobic block.[54] These theoretical volume fractions fit very well with the observed B as obtained from the transmission FTIR measurements (Figure 3D). There, the overall B was 31.2 ± 0.6% for the 8 nm nanofilm and 29.6 ± 0.2% for the 2 μm microfilm. Interestingly, B_{apt} of the 2 μm eADF4(C16) film was significantly higher when measuring in the GATR mode. These led to the assumption that microphase separation is the driving force for the increase of β-sheet content after post-treatment. The methanol cannot diffuse deeply into the film, and therefore, the bulk phase of the (sub)microfilm has less β-sheet content than the surface where the methanol can convert the pAla patches into β-sheets.

In contrast to cast films, where the silk molecules formed bigger β-sheet crystallites during the drying process, spin-coating of eADF4(C16) out of formic acid led to metastable and mainly unstructured silk films due to the fast evaporation of the solvent during the spin-coating process. In thin films, the microstructure was also influenced by the protein/substrate (surface field) and protein/air interface as well as the thickness (i.e., the number of layers) of the protein film.[55−57]

Surface wetting properties of post-treated eADF4(C16) films were analyzed as an indicator of the structural properties of the protein/air interphase. Due to the low crystallinity (low β-sheet content) of the metastable silk films, it was not possible to determine the water contact angle before post-treatment. The eADF4(C16) monolayer was composed of statistically distributed and mainly unfolded hydrophilic and hydrophobic blocks (Figure 4A-i). Upon post-treatment, the β-sheet content was increased, and the films turned water-stable because methanol induced refolding and restructuring at the surface. The hydrophobic pAla stretches further interacted with the substrate and were surrounded by the hydrophilic phase, but microphase separation could only occur in the xy-direction (Figure 4B-i). Figure 4C shows the static water contact angle θ of post-treated eADF4(C16) films, dependent on the film thickness. Water contact angle measurements of as-cast films (bpt) are not possible due to their water solubility.[39] The statistical distribution of hydrophobic and hydrophilic blocks at the protein/air interface in monolayers yielded an "intermediate" contact angle of 72 ± 6°, and Figure 4C-i illustrates the contact angle dependence on the statistical distribution of hydrophilic and hydrophobic blocks in the monolayer. At $5 < d < 10$ nm, the protein layer at the substrate/protein interface could interact with the substrate in a monolayer-like manner, and the protein layer at the protein/air interface was mainly unstructured Figure 4A-ii. Upon post-treatment, β-sheets also formed in the z-direction between the layers. The morphology of thin block copolymer films, in general, depends on the influence of the surface field on the biopolymer/protein and the film thickness. The morphology and the microstructure in thin films can significantly differ from the structure in the bulk, which explains the observed results.[58] The silk system changed its properties upon increasing the film thickness due to the interplay of folding and microphase separation. At $5 < d < 10$ nm, microphase separation was mainly influenced by the surface field, while in thicker films, additional protein folding processes took place independent of the surface. For as-spin-coated films, the probability of forming β-sheets further increased with thickness/number of layers (Figure 4A-iii). Accordingly, the β-sheet content increased with increasing film thickness before as well as after post-treatment. In post-treated multilayered films, the hydrophilic and hydrophobic blocks could also form bigger volumes of individual blocks during microphase separation (Figure 4B-iii). The hydrophobic β-sheets oriented toward the protein/air interface with increasing film thickness (Figure 4C-iii). On top of the initial pAla-rich layer at the substrate/protein interface, a hydrophilic phase was formed in which hydrophobic patches were embedded if a critical film thickness between 90 and 250 nm was reached. In the latter, the β-sheet amount before (B_{bpt}) and after (B_{apt}) post-treatment reached its maximum. In this film thickness range, the β-sheet content was more or less constant, but the surface water contact angle at the protein/air interface still increased until a film thickness of 600 nm was reached. This can be explained by the formation of hydrophobic β-sheet-rich patches (increasing micellar character[18]) with increasing film thickness. Before post-treatment, only smaller hydrophobic patches were formed (Figure 4A-iii), and post-treatment led to the formation of bigger β-sheet crystallites as well as to increased separation of hydrophobic blocks at the protein/air interface (Figure 4B-iii). A more distinct separation of hydrophilic and hydrophobic blocks occurred in thick films (~2 μm produced by drop casting) as previously reported by Wohlrab et al.[18] Exposition of hydrophobic β-crystallites at the protein/air interface led to a hydrophobic surface (Figure 4A-iv, B-iv, C-iv). The GATR measurements (Figure 3D-i) as well as the ATR-FTIR measurements indicated that the 2 μm film showed a very high β-sheet content at the protein/air interface ($B_{apt} = 51.6 \pm 0.7\%$, $d_p \sim 300$ nm), which confirmed the proposed microphase separation model (Figure 4A-iv, B-iv, C-iv). More than 85% of the overall β-sheet content (29.6 ± 0.2%) was oriented toward both surfaces (silicon/protein and protein/air). Hence, in the center of the films, only approximately 15% of the formed β-sheets were located and generated a micellar-like phase, as detected previously. For the 8 nm film, where all three FTIR setups can detect the entire signal of the film, B_{apt} was nearly identical for all setups ($B_{apt} \sim 32\%$), which fits very well to the theoretically calculated maximum β-sheet content ($\phi_A = 0.35$, $B_{apt,max} = 35\%$).

4. CONCLUSION

Spin-coating of eADF4(C16) allowed controlling film thickness by simply varying the concentration of the protein in solution while keeping all other spin-coating parameters constant. The resulting films showed low average surface roughness ($R_a < 1$ nm). Secondary structure and surface properties (surface hydrophilicity) of eADF4(C16) films changed upon varying the number of silk layers/film thickness and post-treatment. In eADF4(C16) films, different physical properties of the hydrophilic and hydrophobic amino acid sequence blocks led to microphase separation. β-Sheet structures mainly occurred at the substrate/protein interface, especially in very thin films. When the film thickness was increased (and more protein layers were added), the proteins could interact in all three directions. The β-sheet content (B_{bpt}, B_{apt}) reached its maximum for spin-coated eADF4(C16) films at a film thickness of ~100 nm, but the surface properties (protein/air interface) of silk films changed until a film thickness of $d > 600$ nm, where the water contact angle was identical to that of cast bulk silk films.

5. EXPERIMENTAL SECTION

Materials. If not stated otherwise, all chemicals were purchased from Roth (Karlsruhe, Germany) in analytical grade. eADF4(C16) (salt-free) was purchased from AMSilk GmbH (Planegg/München, Germany). The used water was ultrapure and obtained by using a Merck Millipore system (Billerica, MA, United States).

Processing of eADF4(C16) into Nano- and (Sub)microfilms. Polished (111) silicon wafers (CrysTec GmbH, Berlin, Germany) were cut into 1 × 1 cm pieces and cleaned by rinsing with acetone and heating using snow-jetting prior to coating. eADF4(C16) was dissolved in formic acid at desired concentrations. Silk solutions ($V = 20$ μL) were placed in the center of the substrate and spin-coated ($f_{rot} = 4000$ rpm, $a_{rot} = 1800$ rpm/s, $t = 30$ s) using a 1-EC 101 DT-19456 Spin-Coater (Headway Research Inc., Garland, United States). Silk microfilms with a thickness of $d \sim 2$ μm were prepared by casting. The silk solution was cast on silicon wafers at 1 mg/cm^2 and dried overnight at ambient conditions. For post-treatment, samples were placed in a desiccator with 20 mL methanol at the bottom. The desiccator was evacuated ($p = 10-1$ mbar) to generate a saturated methanol atmosphere, and samples were incubated overnight.

Atomic Force Microscopy. For surface morphology characterization film, surfaces were analyzed in tapping mode using a Dimension 3100 Nanoscope V (Bruker, Karlsruhe, Germany) with a resolution of 512 by 512 data points at 0.5 to 1 Hz. Silicon cantilevers (OTESPA-R3, Bruker, Karlsruhe, Germany) were used with a force constant of 26 N m^{-1}. The average roughness R_a was calculated in an area of 25 μm^2.

Film Thickness Measurements. For thickness measurements of spin-coated films, samples were scratched using a sharp tweezer, and the scratched area was measured perpendicular to the direction of the scratch. For analysis of the film thickness, STEP and DEPTH routine of Nanoscope Analysis 1.5 Software (Bruker, Karlsruhe, Germany) was used. Silk microfilms were cast on the polished side (top) of silicon wafers. To generate a sharp breaking edge, the silicon wafer substrate was scratched underneath and broken afterward. The defined breaking edge was analyzed by scanning electron microscopy (SEM) using a Leo 1530 Gemini (Zeiss, Oberkochen, Germany) at an accelerating voltage of 3 kV. Samples were sputtered with 1.3 nm platinum.

GATR-FTIR. Fourier transform infrared spectroscopy was performed using the VariGATR grazing angle attenuated total reflection accessory (Harrick Scientific Products Inc., Pleasantville, United States) using a Bruker Tensor 27 FTIR-spectrometer with an MCT detector (Bruker, Rheinstetten, Germany). For absorbance measurements, a grazing angle of 62° was used. One-hundred and forty scans from 4000 cm^{-1} to 800 nm^{-1} were averaged at a resolution of 2 cm^{-1}. The penetration depth d_p of the evanescent wave depends on the refractive indices of the germanium crystal (n_1) and of the sample (n_2, silk film at the silicon wafer), angle of incidence (α), and the wavelength of the incident light (λ_i), as shown in eq 1.[59]

$$d_p = \frac{\lambda}{2\pi n_1\left(\sin^2(a) - \left(\frac{n_2}{n_1}\right)^2\right)^{1/2}} \qquad (1)$$

For $\alpha = 62°$ (1,0821 rad), $n_1 = 4$ of germanium crystal ($T = 20$ °C, $\lambda_{IR} = 6$ μm),[60] and $n_2 = 1.5$ of silk proteins,[40] the penetration depth d_p was calculated in the amide I region ($\nu = 1705$ to 1590 cm^{-1}) to be $d_p = 293-313$ nm (Supporting Information Table S1).

The relative error $\sigma_{B_d^\delta}/B_d^\delta$ (with $B_d^\delta = B_{apt}/B_{bpt}$, $\sigma_{B_d}^\delta$: absolute error of B_d^δ) for specific film thicknesses d was calculated using the Gauß law of error propagation using eq 2. $\sigma_{B_{x,d}}$ (x = apt, bpt) is the standard deviation of $B_{x,d}$ (x = apt, bpt) for a specific film thicknesses d.

$$\left(\frac{\sigma_{B_d^\delta}}{B_d^\delta}\right)^2 = \left(\frac{\sigma_{B_{\mathrm{apt,d}}}}{B_{\mathrm{apt,d}}}\right)^2 + \left(\frac{\sigma_{B_{\mathrm{bpt,d}}}}{B_{\mathrm{bpt,d}}}\right)^2 \qquad (2)$$

Preparation of Films for ATR and Transmission FTIR Measurements. eADF4(C16) was dissolved in formic acid at desired concentrations. Thin spider silk films ($\ll$1 μm) were prepared by spin coating. Therefore, diluted silk solutions (V = 200 μL, $c \geq 1$ mg/mL) were placed in the center of trapezoidal silicon (Si) internal reflection elements (IRE, 50 × 20 × 2 mm^3, see below) and spin-coated (f_{rot} = 4500 rpm, t = 30 s) using a commercial Spin-Coater (SCT-10, LOT ORIEL, Darmstadt, Germany). The Spin-coater was equipped with a home-built rotating plate (Al), in which a mount (deepening) for fixation of the IRE was milled. After spin-coating, the total area of Si IRE and the lower half area of the silicon crystal (50 × 10 mm^2) was cleaned with water using a tissue. Thick silk films (~2 μm) were prepared by casting, i.e., placing a concentrated silk solution ($V \geq 10$ μL, $c \geq 50$ mg/mL) as spot in the middle of the upper half area (50 × 10 mm^2) of Si IRE followed by drying under gentle N_2 gas stream optionally using a heatable metal support at T = 50 °C. For post-treatment (vapor phase), samples (silk coated IREs) were placed on a base in a closed crystallizing dish filled with 250 μL of methanol not directly contacting the sample. Samples were incubated overnight.

ATR and Transmission FTIR Spectroscopy. An FTIR spectrometer (Tensor II, BRUKER-Optics GmbH, Ettlingen, Germany) equipped with globar source and either deuterated triglycine sulfate (DTGS) or a mercurium−cadmium−telluride (MCT) detector was used in the mid-IR range. FTIR spectra were recorded in the wavenumber range between 4000−400 cm^{-1} at 2 cm^{-1} spectral resolution, and 50 scans were done. Both modes, transmission (TRANS) FTIR and attenuated total reflection (ATR) FTIR, were used.

TRANS-FTIR was applied at silicon (Si) internal reflection elements (IRE), which were fixed in constructed sample holders (M. Ulrich, M.M., IPF Dresden). The IR beam transmitted the Si IRE at minimum focal area (<5 mm) in the FTIR sample chamber. TRANS FTIR absorbance spectra $A(\upsilon)$ were recorded from spider silk coated (spin coated or cast) Si IREs as the sample intensity $I_{S(\upsilon)}$ and clean (plasma cleaner, Harrick, Ossining, NY, United States) uncoated Si IREs as the reference intensity $I_R(\upsilon)$ and processed according to $A(\upsilon) = -\log\,[I_S(\upsilon)/I_R(\upsilon)]$.

ATR-FTIR was applied at trapezoidal Si IREs (50 × 20 × 2 mm^3, see above) allowing an incident and leaving angle of 45°. Si IREs were fixed in sample holders (M. Ulrich, M.M., IPF Dresden) located in a commercial pseudodouble-beam-ATR device (OPTISPEC, Neerach, Switzerland) operated according to the single-beam-sample-reference (SBSR) concept of Fringeli.[61] In principle, the (spin-coated or cast) silk film was located at the upper half area (50 × 10 mm^2) of the front side of Si IRE, which was achieved by cleaning the lower half area (50 × 10 mm^2) from silk material. Sample $I_S(\upsilon)$ and reference $I_S(\upsilon)$ intensities were measured by alternately shuttling the upper and lower half of the Si IRE into the IR beam using a lift, and absorbance spectra were computed similar to that of TRANS-FTIR according to $A(\upsilon) = -\log\,[I_S(\upsilon)/I_R(\upsilon)]$.

Fourier Self-Deconvolution and Curve Fitting. To determine the fractions of individual secondary structures, the amide I region (1595 cm^{-1} to 1705 cm^{-1}) was analyzed by Fourier self-deconvolution (FSD) with subsequent curve fitting according to Hu et al. using the Software Opus 6.5 (Bruker Optics Corp., Billerica, MA, United States).[47]

Water Contact Angle. To analyze surface wettability, static water contact angles on surfaces were analyzed using the OCA contact angle system (DataPhysics Instruments GmbH, Filderstadt, Germany). A water droplet of 2 μL was placed on the surface, and the contact angles were determined using the SCA 20 software (DataPhysics Instruments GmbH, Filderstadt, Germany) and a Laplace−Young fit.

■ ASSOCIATED CONTENT

Supporting Information

The Supporting Information is available free of charge on the ACS Publications website at DOI: 10.1021/acsapm.9b00792.

> AFM topography pictures of films at all concentrations showing 3 different pictures sizes (1, 9, and 625 μm^2) (Figure S1); representative SEM image of the thickness of a microfilm (Figure S2); normalized spectra of all three used FTIR methods with a magnification of the amide I band region (Figures S3−S7); values of the penetration depth of the IR beam (Table S1); summary of the values for the β-sheet content of the three FTIR methods with standard derivation (Table S2) (PDF)

■ AUTHOR INFORMATION

Corresponding Author

*E-mail: thomas.scheibel@bm.uni-bayreuth.de.

ORCID

Martin Müller: 0000-0001-8961-4604
Andreas Fery: 0000-0001-6692-3762
Thomas Scheibel: 0000-0002-0457-2423

Author Contributions

¶C.B.B. and S.L. contributed equally. Conceptualization: C.B.B., A.F., and T.S.; methodology: C.B.B., S.L., M.M., A.F., and T.S.; investigation: C.B.B., S.L., and M.M.; writing of original draft: C.B.B. and S.L.; review and editing: S.L., M.M., A.F., and T.S.; visualization: C.B.B. and S.L.; supervision: A.F. and T.S.; funding: A.F. and T.S.

Funding

This work is supported by Grants DFG SCHE603/23-1 and DFG FE600/29-1.

Notes

The authors declare no competing financial interest.

■ ACKNOWLEDGMENTS

We thank Martin Humenik for helpful discussion regarding the manuscript and Markus Hund for support during AFM measurements. We thank Birgit Urban for the ATR and the transmission FTIR measurements. We thank Prof. Laforsch for access to the Harrick VariGATR.

■ REFERENCES

(1) Craig, C. L. Evolution of arthropod silks. *Annu. Rev. Entomol.* **1997**, *42*, 231−267.

(2) Sutherland, T. D.; Young, J. H.; Weisman, S.; Hayashi, C. Y.; Merritt, D. J. Insect silk: One name, many materials. *Annu. Rev. Entomol.* **2010**, *55*, 171−188.

(3) Vollrath, F.; Porter, D. Spider silk as archetypal protein elastomer. *Soft Matter* **2006**, *2* (5), 377−385.

(4) Lintz, E. S.; Scheibel, T. R. Dragline, Egg Stalk and Byssus: A Comparison of Outstanding Protein Fibers and Their Potential for Developing New Materials. *Adv. Funct. Mater.* **2013**, *23* (36), 4467−4482.

(5) Exler, J. H.; Hummerich, D.; Scheibel, T. The amphiphilic properties of spider silks are important for spinning. *Angew. Chem., Int. Ed.* **2007**, *46* (19), 3559−3562.

(6) Huemmerich, D.; Helsen, C. W.; Quedzuweit, S.; Oschmann, J.; Rudolph, R.; Scheibel, T. Primary structure elements of spider dragline silks and their contribution to protein solubility. *Biochemistry* **2004**, *43* (42), 13604−13612.

(7) Boyle, A. L. Applications of de novo designed peptides. *Peptide Applications in Biomedicine, Biotechnology and Bioengineering* **2018**, 51−86.

(8) Boyle, A. L. 3: Applications of de novo designed peptides. In *Peptide Applications in Biomedicine, Biotechnology and Bioengineering*; Koutsopoulos, S., Ed.; Woodhead Publishing: 2018; pp 51−86.

(9) Eisoldt, L.; Smith, A.; Scheibel, T. Decoding the Secrets of Spider Silk. *Mater. Today* **2011**, *14* (3), 80−86.

(10) Brooks, A. E.; Nelson, S. R.; Jones, J. A.; Koenig, C.; Hinman, M.; Stricker, S.; Lewis, R. V. Distinct contributions of model MaSp1 and MaSp2 like peptides to the mechanical properties of synthetic major ampullate silk fibers as revealed in silico. *Nanotechnol., Sci. Appl.* **2008**, *1*, 9−16.

(11) Keten, S.; Buehler, M. J. Nanostructure and molecular mechanics of spider dragline silk protein assemblies. *J. R. Soc., Interface* **2010**, *7* (53), 1709−21.

(12) Rabotyagova, O. S.; Cebe, P.; Kaplan, D. L. Role of Polyalanine Domains in β-Sheet Formation in Spider Silk Block Copolymers. *Macromol. Biosci.* **2010**, *10* (1), 49−59.

(13) Tokareva, O.; Jacobsen, M.; Buehler, M.; Wong, J.; Kaplan, D. L. Structure-function-property-design interplay in biopolymers: Spider silk. *Acta Biomater.* **2014**, *10* (4), 1612−1626.

(14) Boyle, A. L.; Woolfson, D. N. De novo designed peptides for biological applications. *Chem. Soc. Rev.* **2011**, *40* (8), 4295−4306.

(15) Lefèvre, T.; Rousseau, M.-E.; Pézolet, M. Protein Secondary Structure and Orientation in Silk as Revealed by Raman Spectromicroscopy. *Biophys. J.* **2007**, *92* (8), 2885−2895.

(16) Pappu, R. V.; Wang, X.; Vitalis, A.; Crick, S. L. A polymer physics perspective on driving forces and mechanisms for protein aggregation. *Arch. Biochem. Biophys.* **2008**, *469* (1), 132−141.

(17) Keerl, D.; Scheibel, T. Characterization of natural and biomimetic spider silk fibers. *Bioinspired, Biomimetic Nanobiomater.* **2012**, *1* (BBN2), 83−94.

(18) Wohlrab, S.; Spieß, K.; Scheibel, T. Varying surface hydrophobicities of coatings made of recombinant spider silk proteins. *J. Mater. Chem.* **2012**, *22* (41), 22050−22054.

(19) Slotta, U.; Tammer, M.; Kremer, F.; Koelsch, P.; Scheibel, T. Structural analysis of spider silk films. *Supramol. Chem.* **2006**, *18* (5), 465−471.

(20) Spiess, K.; Lammel, A.; Scheibel, T. Recombinant Spider Silk Proteins for Applications in Biomaterials. *Macromol. Biosci.* **2010**, *10* (9), 998−1007.

(21) Darling, S. B. Directing the self-assembly of block copolymers. *Prog. Polym. Sci.* **2007**, *32* (10), 1152−1204.

(22) Förster, S.; Plantenberg, T. From self-organizing polymers to nanohybrid and biomaterials. *Angew. Chem., Int. Ed.* **2002**, *41* (5), 688−714.

(23) Mai, Y.; Eisenberg, A. Self-assembly of block copolymers. *Chem. Soc. Rev.* **2012**, *41* (18), 5969−5985.

(24) Hu, H.; Gopinadhan, M.; Osuji, C. O. Directed self-assembly of block copolymers: a tutorial review of strategies for enabling nanotechnology with soft matter. *Soft Matter* **2014**, *10* (22), 3867−89.

(25) Rammensee, S.; Slotta, U.; Scheibel, T.; Bausch, A. R. Assembly mechanism of recombinant spider silk proteins. *Proc. Natl. Acad. Sci. U. S. A.* **2008**, *105* (18), 6590−6595.

(26) Hermanson, K. D.; Huemmerich, D.; Scheibel, T.; Bausch, A. R. Engineered microcapsules fabricated from reconstituted spider silk. *Adv. Mater.* **2007**, *19* (14), 1810−1815.

(27) Hu, X.; Lu, Q.; Kaplan, D. L.; Cebe, P. Microphase Separation Controlled β-Sheet Crystallization Kinetics in Fibrous Proteins. *Macromolecules* **2009**, *42* (6), 2079−2087.

(28) Gebhardt, R.; Vendrely, C.; Burghammer, M.; Riekel, C. Characterization of the Boundary Zone of a Cast Protein Drop: Fibroin beta-Sheet and Nanofibril Formation. *Langmuir* **2009**, *25* (11), 6307−6311.

(29) Rathore, O.; Sogah, D. Y. Nanostructure formation through beta-sheet self-assembly in silk-based materials. *Macromolecules* **2001**, *34* (5), 1477−1486.

(30) Krishnaji, S. K.; Huang, W.; Cebe, P.; Kaplan, D. L. Influence of Solution Parameters on Phase Diagram of Recombinant Spider Silk-Like Block Copolymers. *Macromol. Chem. Phys.* **2014**, *215*, 1230−1238.

(31) Rabotyagova, O. S.; Cebe, P.; Kaplan, D. L. Protein-Based Block Copolymers. *Biomacromolecules* **2011**, *12* (2), 269−289.

(32) Muller, W. S.; Samuelson, L. A.; Fossey, S. A.; Kaplan, D. L. Formation and Characterization of Langmuir Silk Films. *Langmuir* **1993**, *9* (7), 1857−1861.

(33) Valluzzi, R.; Gido, S. P.; Muller, W.; Kaplan, D. L. Orientation of silk III at the air-water interface. *Int. J. Biol. Macromol.* **1999**, *24*, 237−242.

(34) Valluzzi, R.; Gido, S. P.; Zhang, W.; Muller, W. S.; Kaplan, D. L. Trigonal Crystal Structure of *Bombyx mori* Silk Incorporating a Threefold Helical Chain Conformation Found at the Air-Water Interface. *Macromolecules* **1996**, *29*, 8606−8614.

(35) Rabotyagova, O. S.; Cebe, P.; Kaplan, D. L. Self-Assembly of Genetically Engineered Spider Silk Block Copolymers. *Biomacromolecules* **2009**, *10* (2), 229−236.

(36) Krishnaji, S. T.; Huang, W.; Rabotyagova, O.; Kharlampieva, E.; Choi, I.; Tsukruk, V. V.; Naik, R.; Cebe, P.; Kaplan, D. L. Thin Film Assembly of Spider-like Block Copolymers. *Langmuir* **2011**, *27* (3), 1000−1008.

(37) Krishnaji, S. T.; Bratzel, G.; Kinahan, M. E.; Kluge, J. A.; Staii, C.; Wong, J. Y.; Buehler, M. J.; Kaplan, D. L. Sequence-Structure-Property Relationships of Recombinant Spider Silk Proteins: Integration of Biopolymer Design, Processing and Modeling. *Adv. Funct. Mater.* **2013**, *23* (23), 241−253.

(38) Tokareva, O. S.; Lin, S.; Jacobsen, M. M.; Huang, W.; Rizzo, D.; Li, D.; Simon, M.; Staii, C.; Cebe, P.; Wong, J. Y.; Buehler, M. J.; Kaplan, D. L. Effect of sequence features on assembly of spider silk block copolymers. *J. Struct. Biol.* **2014**, *186* (3), 412−9.

(39) Borkner, C. B.; Elsner, M. B.; Scheibel, T. Coatings and Films Made of Silk Proteins. *ACS Appl. Mater. Interfaces* **2014**, *6* (18), 15611−15625.

(40) Jiang, C. Y.; Wang, X. Y.; Gunawidjaja, R.; Lin, Y. H.; Gupta, M. K.; Kaplan, D. L.; Naik, R. R.; Tsukruk, V. V. Mechanical properties of robust ultrathin silk fibroin films. *Adv. Funct. Mater.* **2007**, *17* (13), 2229−2237.

(41) Tao, H.; Kaplan, D. L.; Omenetto, F. G. Silk Materials - A Road to Sustainable High Technology. *Adv. Mater.* **2012**, *24* (21), 2824−2837.

(42) Lee, S. Y.; Amsden, J. J.; Boriskina, S. V.; Gopinath, A.; Mitropolous, A.; Kaplan, D. L.; Omenetto, F. G.; Dal Negro, L. Spatial and spectral detection of protein monolayers with deterministic aperiodic arrays of metal nanoparticles. *Proc. Natl. Acad. Sci. U. S. A.* **2010**, *107* (27), 12086−12090.

(43) Huemmerich, D.; Scheibel, T.; Vollrath, F.; Cohen, S.; Gat, U.; Ittah, S. Novel Assembly Properties of Recombinant Spider Dragline Silk Proteins. *Curr. Biol.* **2004**, *14* (22), 2070−2074.

(44) Zha, R. H.; Delparastan, P.; Fink, T. D.; Bauer, J.; Scheibel, T.; Messersmith, P. B. Universal nanothin silk coatings via controlled spidroin self-assembly. *Biomater. Sci.* **2019**, *7* (2), 683−695.

(45) Metwalli, E.; Slotta, U.; Darko, C.; Roth, S. V.; Scheibel, T.; Papadakis, C. M. Structural changes of thin films from recombinant spider silk proteins upon post-treatment. *Appl. Phys. A: Mater. Sci. Process.* **2007**, *89* (3), 655−661.

(46) Junghans, F.; Morawietz, M.; Conrad, U.; Scheibel, T.; Heilmann, A.; Spohn, U. Preparation and mechanical properties of layers made of recombinant spider silk proteins and silk from silk worm. *Appl. Phys. A: Mater. Sci. Process.* **2006**, *82* (2), 253−260.

(47) Hu, X.; Kaplan, D.; Cebe, P. Determining beta-sheet crystallinity in fibrous proteins by thermal analysis and infrared spectroscopy. *Macromolecules* **2006**, *39* (18), 6161−6170.

(48) Hu, X.; Kaplan, D.; Cebe, P. Dynamic protein-water relationships during beta-sheet formation. *Macromolecules* **2008**, *41* (11), 3939−3948.

(49) Bates, F. S. Polymer-Polymer Phase-Behavior. *Science* **1991**, *251* (4996), 898−905.

(50) Cheng, Y.; Koh, L.-D.; Li, D.; Ji, B.; Han, M.-Y.; Zhang, Y.-W. On the strength of β-sheet crystallites of Bombyx mori silk fibroin. *J. R. Soc., Interface* **2014**, *11* (96), 20140305−20140305.

(51) Hu, X.; Kaplan, D.; Cebe, P. Dynamic Protein−Water Relationships during β-Sheet Formation. *Macromolecules* **2008**, *41* (11), 3939−3948.

(52) Rathore, O.; Sogah, D. Y. Self-Assembly of β-Sheets into Nanostructures by Poly(alanine) Segments Incorporated in Multiblock Copolymers Inspired by Spider Silk. *J. Am. Chem. Soc.* **2001**, *123* (22), 5231−5239.

(53) Aigner, T.; Scheibel, T. Self-Rolling Refillable Tubular Enzyme Containers Made of Recombinant Spider Silk and Chitosan. *ACS Appl. Mater. Interfaces* **2019**, *11* (17), 15290−15297.

(54) Mai, Y.; Zhang, F.; Feng, X. Polymer-directed synthesis of metal oxide-containing nanomaterials for electrochemical energy storage. *Nanoscale* **2014**, *6* (1), 106−121.

(55) Knoll, A.; Horvat, A.; Lyakhova, K. S.; Krausch, G.; Sevink, G. J. A.; Zvelindovsky, A. V.; Magerle, R. Phase behavior in thin films of cylinder-forming block copolymers. *Phys. Rev. Lett.* **2002**, *89* (3) DOI: 10.1103/PhysRevLett.89.035501.

(56) Knoll, A.; Magerle, R.; Krausch, G. Phase behavior in thin films of cylinder-forming ABA block copolymers: Experiments. *J. Chem. Phys.* **2004**, *120* (2), 1105−1116.

(57) Krausch, G.; Magerle, R. Nanostructured thin films via self-assembly of block copolymers. *Adv. Mater.* **2002**, *14* (21), 1579−1583.

(58) Karim, A.; Singh, N.; Sikka, M.; Bates, F. S.; Dozier, W. D.; Felcher, G. P. Ordering in Asymmetric Poly (Ethylene-Propylene)-Poly (Ethylethylene) Diblock Copolymer Thin-Films. *J. Chem. Phys.* **1994**, *100* (2), 1620−1629.

(59) Mirabella, F. M. *Internal Reflection Spectroscopy: Theory and Application*; Marcel Dekker, Inc.: New York, United States, 1993.

(60) Li, H. H. Refractive-Index of Silicon and Germanium and Its Wavelength and Temperature Derivatives. *J. Phys. Chem. Ref. Data* **1980**, *9* (3), 561−658.

(61) Lindon, J. C.; Tranter, G. E.; Koppenaal, D. *Encyclopedia of Spectroscopy and Spectrometry*; Academic Press: 2016.

Supporting Information

Ultra-Thin Spider Silk Films: Insights into Spider Silk Assembly on Surfaces

Christian B. Borkner[a] ‡, *Sarah Lentz*[a] ‡, *Martin Müller*[b], *Andreas Fery*[b] *and Thomas Scheibel*[a, c, d, e] *

[a] Lehrstuhl Biomaterialien, Fakultät für Ingenieurwissenschaften, Universität Bayreuth, Prof.-Rüdiger-Bormann-Str.1, 95447 Bayreuth, Germany

* Corresponding author, E-Mail: thomas.scheibel@bm.uni-bayreuth.de

[b] Leibniz Institute of Polymer Research Dresden, Institute of Physical Chemistry and Polymer Physics, Hohe Str. 6, 01069 Dresden, Germany

[c] Bayerisches Polymerinstitut (BPI), Bayreuther Zentrum für Kolloide und Grenzflächen (BZKG)

[d] Bayreuther Zentrum für Molekulare Biowissenschaften (BZMB)

[e] Bayreuther Materialzentrum (BayMAT)

[c-e] Universität Bayreuth, Universitätsstr. 30, 95440 Bayreuth, Germany

‡ contributed equally

The supporting information includes seven figures and two tables.

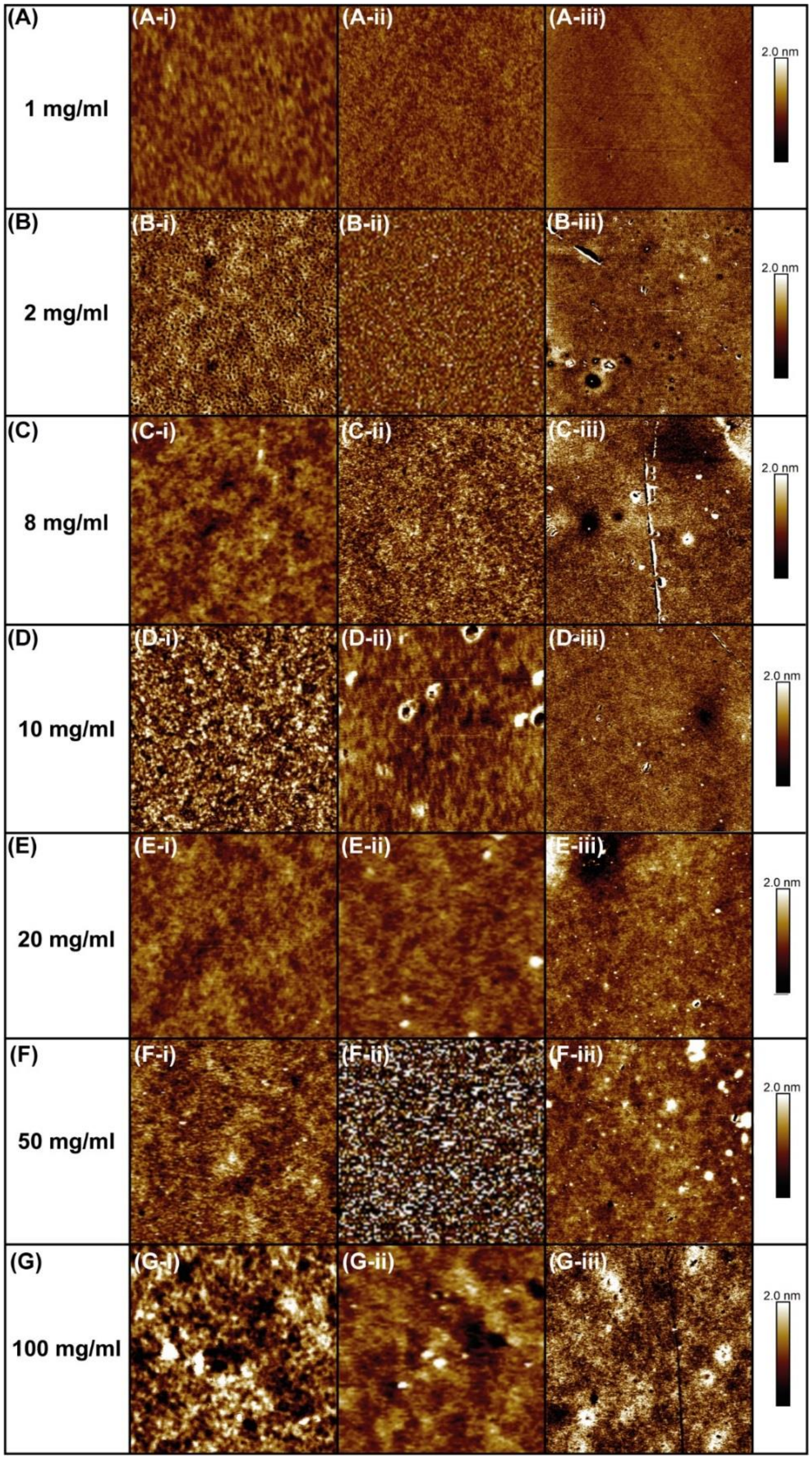

Figure S1. AFM topography images of eADF4(C16) films spin-coated with (A) 1 mg/ml, (B) 2 mg/ml, (C) 8 mg/ml, (D) 10 mg/ml, (E) 20 mg/ml, (F) 50 mg/ml and (G) 100 mg/ml eADF4(C16). Image size of (i) 1 µm x 1 µm, (ii) 3 µm x 3 µm and (iii) 15 µm x 15 µm.

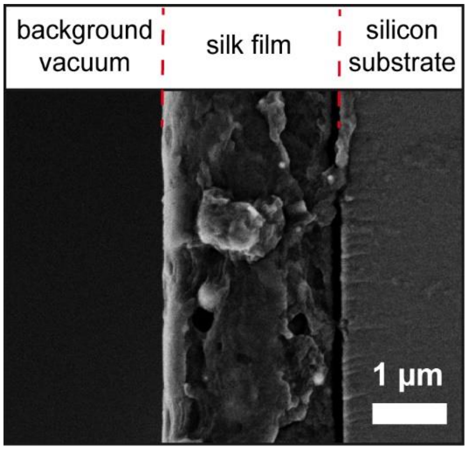

Figure S2. Exemplary SEM picture of a breaking edge of a cast eADF4(C16)-microfilm on a silicon wafer surface used for film thickness measurement.

Table S1. Calculated values of penetration depth d_p of the germanium ATR-crystal for the wave numbers υ of the amide I band.

υ, cm^{-1}	d_p, nm	υ, cm^{-1}	d_p, nm	υ, cm^{-1}	d_p, nm	υ, cm^{-1}	d_p, nm
1590	313	1619	307	1648	302	1677	296
1591	312	1620	307	1649	301	1678	296
1592	312	1621	307	1650	301	1679	296
1593	312	1622	306	1651	301	1680	296
1594	312	1623	306	1652	301	1681	296
1595	312	1624	306	1653	301	1682	295
1596	311	1625	306	1654	300	1683	295
1597	311	1626	306	1655	300	1684	295
1598	311	1627	305	1656	300	1685	295
1599	311	1628	305	1657	300	1686	295
1600	311	1629	305	1658	300	1687	295
1601	310	1630	305	1659	300	1688	294
1602	310	1631	305	1660	299	1689	294
1603	310	1632	305	1661	299	1690	294
1604	310	1633	304	1662	299	1691	294
1605	310	1634	304	1663	299	1692	294
1606	309	1635	304	1664	299	1693	294
1607	309	1636	304	1665	299	1694	293
1608	309	1637	304	1666	298	1695	293
1609	309	1638	303	1667	298	1696	293
1610	309	1639	303	1668	298	1697	293
1611	309	1640	303	1669	298	1698	293
1612	308	1641	303	1670	298	1699	293
1613	308	1642	303	1671	297	1700	292
1614	308	1643	303	1672	297	1701	292
1615	308	1644	302	1673	297	1702	292
1616	308	1645	302	1674	297	1703	292
1617	307	1646	302	1675	297	1704	292
1618	307	1647	302	1676	297	1705	291

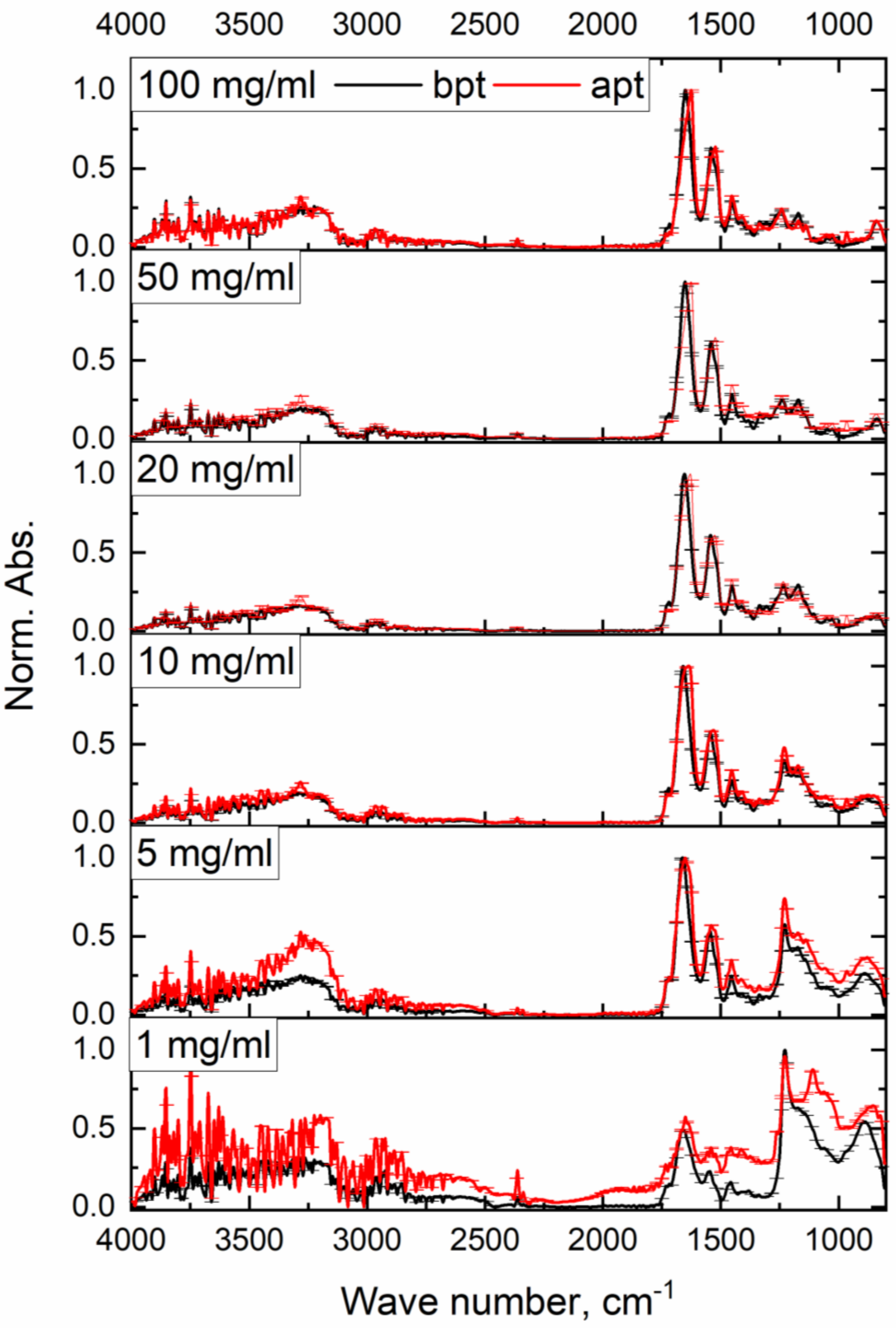

Figure S3: Averaged (n =3) and normalized (to maximum) full spectra of GATR measurements of recombinant spider silk protein films with concentrations of (1, 5, 10, 20, 50, 100) mg/ml. The black lines are the GATR-FTIR spectra before post-treatment (bpt) and the red lines represent the spectra of recombinant spider silk films after post-treatment (apt). In the interest of clarity only 150 error bars per curve are shown.

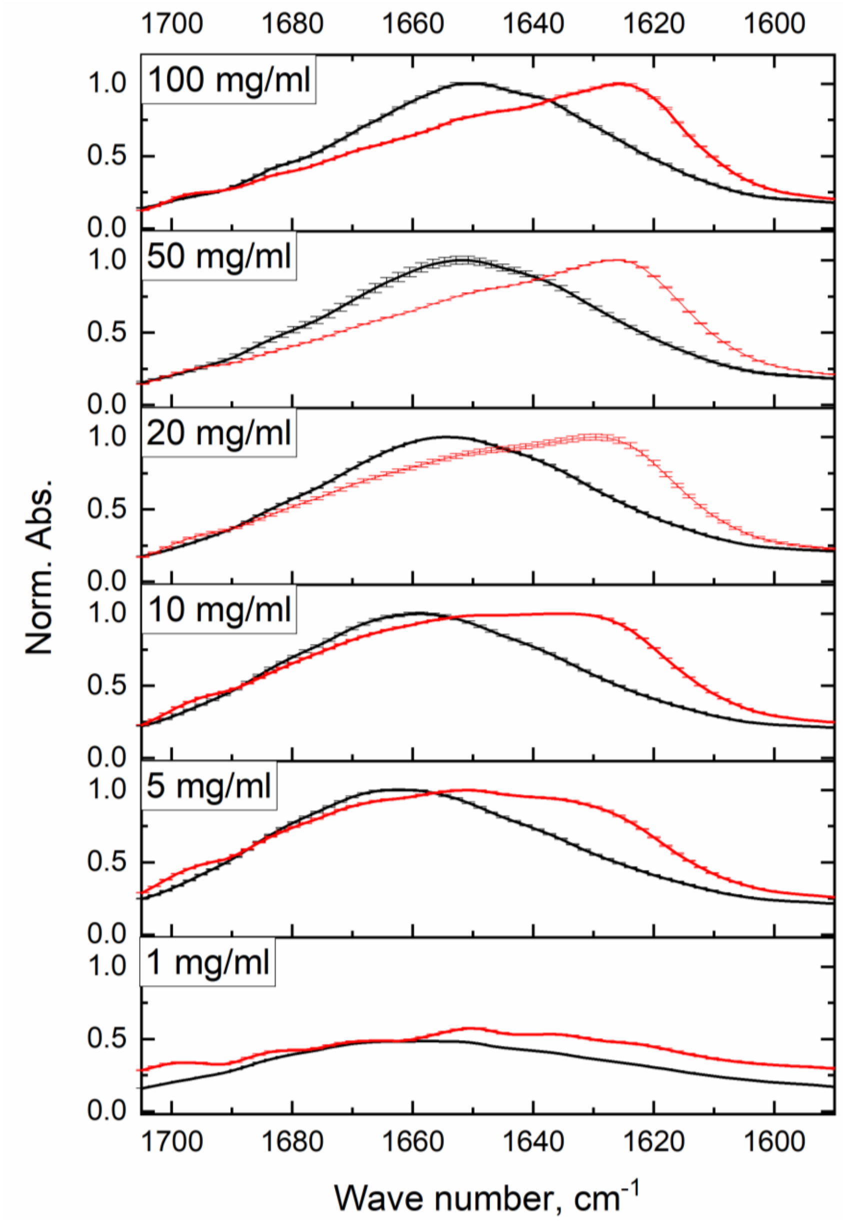

Figure S4: Averaged (n =3) and normalized (to maximum) spectra of GATR measurements of the amide I band of recombinant spider silk protein films with concentrations of (1, 5, 10, 20, 50, 100) mg/ml. The black lines are the GATR-FTIR spectra before post-treatment (bpt) and the red lines represent the spectra of recombinant spider silk films after post-treatment (apt). In the interest of clarity, only 150 error bars per curve are shown.

Table S2. B_{bpt} and B_{apt} with corresponding standard derivations (SD) of nano- and microfilms of eADF4(C16) measured using three different FTIR-setups (GATR, SBSR, and Transmission-FTIR)

FTIR	10 nm film				1 µm film			
	B_{bpt}, %	SD, %	B_{apt}, %	SD, %	B_{bpt}, %	SD, %	B_{apt}, %	SD, %
GATR	13.3	1.9	30.5	2.7	19.0	2.2	51.6	0.7
SBSR	12.3	0.2	35.2	0.7	21.1	0.7	35.2	0.5
Transmission	15.1	0.3	31.2	0.6	21.1	0.4	29.6	0.2

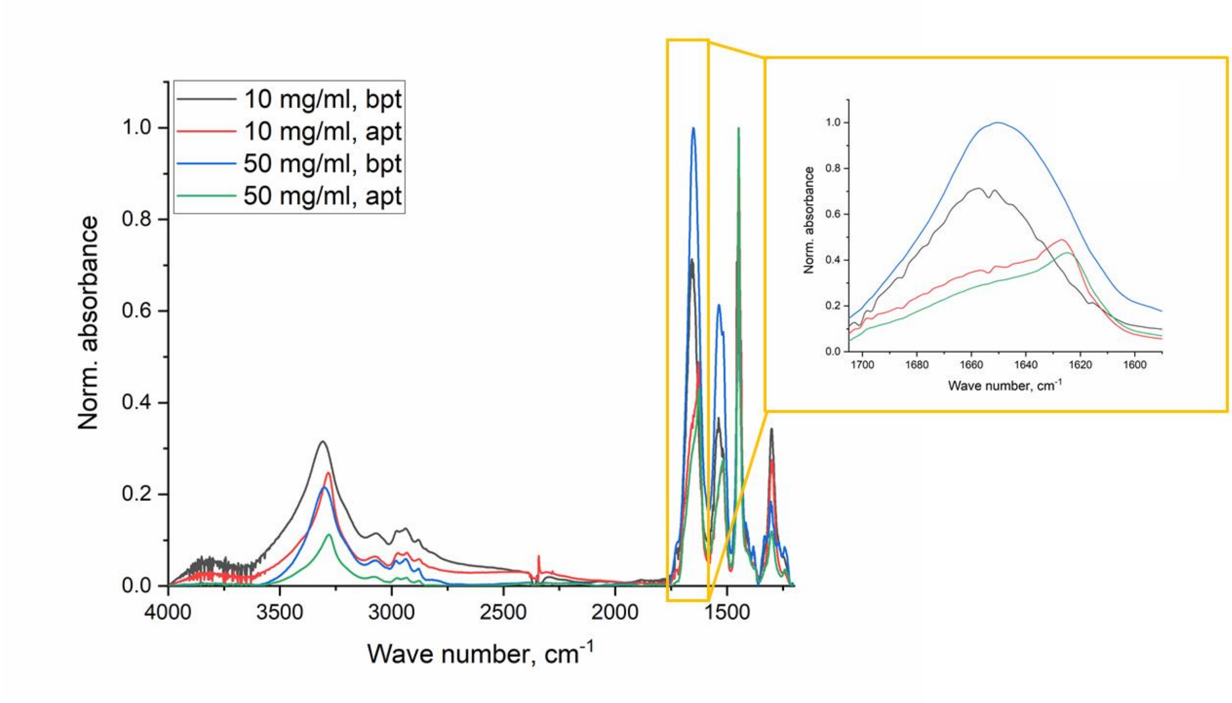

Figure S5: Normalized SBSR FTIR spectra of recombinant spider silk films with concentrations of 10 mg/ml and 50 mg/ml before (bpt) and after (apt) post-treatment with methanol.

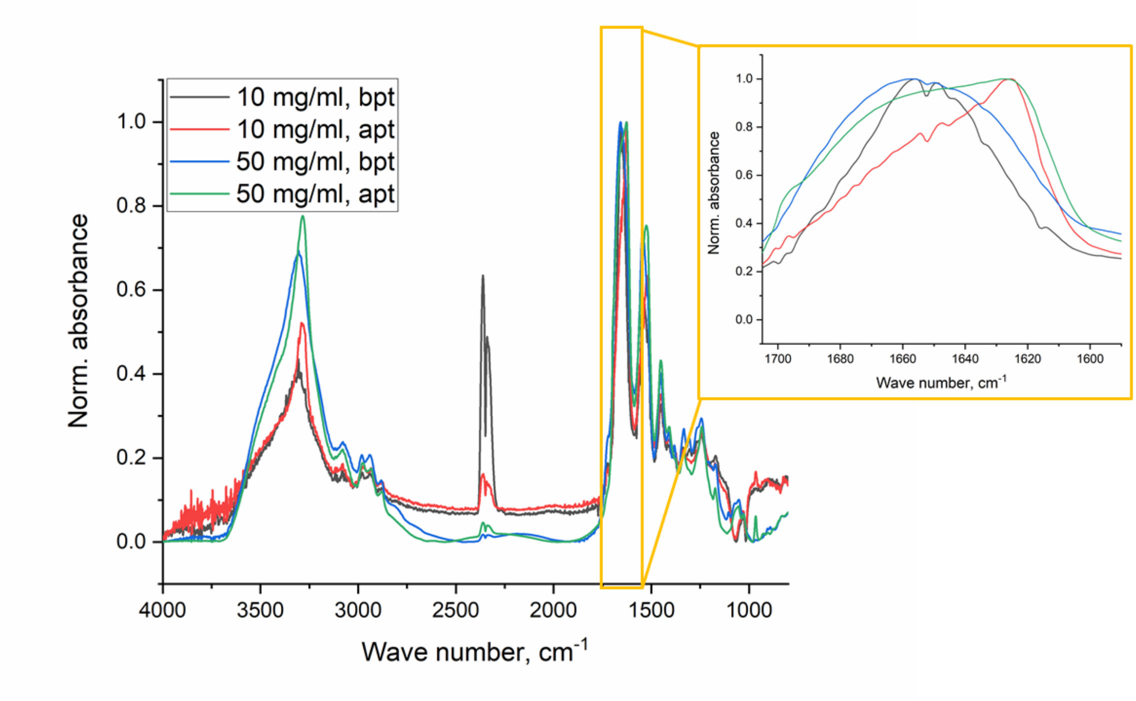

Figure S6: Normalized Transmission FTIR spectra of recombinant spider silk films with concentrations of 10 mg/ml and 50 mg/ml before (bpt) and after (apt) post-treatment with methanol.

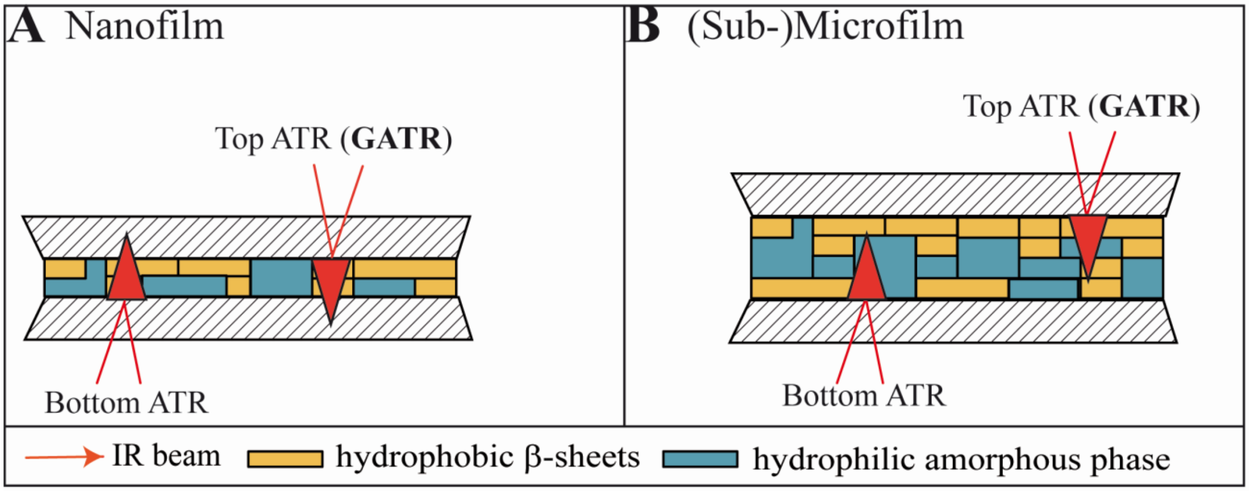

Figure S7: GATR FTIR in comparison to SBSR FTIR yields different *B* for nano- (A) and (sub) microfilms (B).

Teilarbeit IV

Die Ergebnisse dieses Kapitels wurden bereits in *Biomacromolecules* veröffentlich als:

In Vivo Coating of Bacterial Magnetic Nanoparticles by Magnetosome Expression of Spider Silk-Inspired Peptides.

Frank Mickoleit, **Christian B. Borkner**, Mauricio Toro-Nahuelpan, Heike M. Herold, Denis S. Maier, Thomas Scheibel und Dirk Schüler

Mit Genehmigung abgedruckt aus F. Mickoleit, **C. B. Borkner**, M. Toro-Nahuelpan, H. M. Herold, D. S. Maier, J. M. Plitzko, T. Scheibel, D. Schüler, *In Vivo* Coating of Bacterial Magnetic Nanoparticles by Magnetosome Expression of Spider Silk-Inspired Peptides. *Biomacromolecules* **2018**, *19*, 962-972. Copyright 2018 American Chemical Society.

Reprinted with permission from F. Mickoleit, **C. B. Borkner**, M. Toro-Nahuelpan, H. M. Herold, D. S. Maier, J. M. Plitzko, T. Scheibel, D. Schüler, *In Vivo* Coating of Bacterial Magnetic Nanoparticles by Magnetosome Expression of Spider Silk-Inspired Peptides. *Biomacromolecules* **2018**, *19*, 962-972. Copyright 2018 American Chemical Society.

Biomacromolecules

Article

Cite This: Biomacromolecules 2018, 19, 962−972

pubs.acs.org/Biomac

In Vivo Coating of Bacterial Magnetic Nanoparticles by Magnetosome Expression of Spider Silk-Inspired Peptides

Frank Mickoleit,[†] Christian B. Borkner,[‡] Mauricio Toro-Nahuelpan,[†,○] Heike M. Herold,[‡] Denis S. Maier,[†] Jürgen M. Plitzko,[○] Thomas Scheibel,[‡,§,∥,⊥,#,∇] and Dirk Schüler*[,†]

[†]Department of Microbiology, [‡]Department of Biomaterials, [§]Bayerisches Polymerinstitut (BPI), [∥]Bayreuther Zentrum für Kolloide und Grenzflächen (BZKG), [⊥]Institut für Bio-Makromoleküle (bio-mac), [#]Bayreuther Zentrum für Molekulare Biowissenschaften (BZMB), [∇]Bayreuther Materialzentrum (BayMAT), University of Bayreuth, D-95447 Bayreuth, Germany

[○]Department of Molecular Structural Biology, Max Planck Institute of Biochemistry, D-82152 Martinsried, Germany

Supporting Information

ABSTRACT: Magnetosomes are natural magnetic nanoparticles with exceptional properties that are synthesized in magnetotactic bacteria by a highly regulated biomineralization process. Their usability in many applications could be further improved by encapsulation in biocompatible polymers. In this study, we explored the production of spider silk-inspired peptides on magnetosomes of the alphaproteobacterium *Magnetospirillum gryphiswaldense*. Genetic fusion of different silk sequence-like variants to abundant magnetosome membrane proteins enhanced magnetite biomineralization and caused the formation of a proteinaceous capsule, which increased the colloidal stability of isolated particles. Furthermore, we show that spider silk peptides fused to a magnetosome membrane protein can be used as seeds for silk fibril growth on the magnetosome surface. In summary, we demonstrate that the combination of two different biogenic materials generates a genetically encoded hybrid composite with engineerable new properties and enhanced potential for various applications.

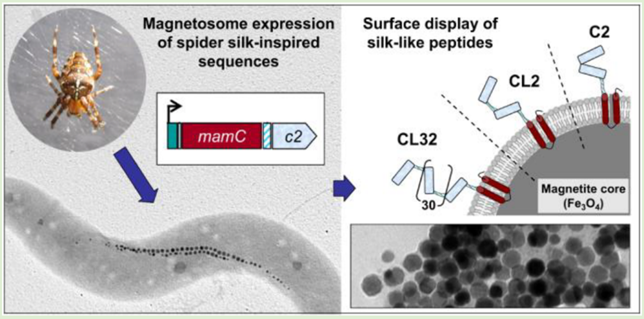

■ INTRODUCTION

Magnetosomes are membrane-enveloped magnetic nanoparticles (MNPs) biomineralized by magnetotactic bacteria, in which they serve as geomagnetic field sensors.[1,2] In the alphaproteobacterium *Magnetospirillum gryphiswaldense* they are composed of a monocrystalline magnetite (Fe_3O_4) core enveloped by the magnetosome membrane, which consists of phospholipids and a set of specific proteins.[3] Due to their highly regulated biosynthesis, magnetosomes exhibit unprecedented characteristics such as high crystallinity, strong magnetization, as well as uniform shapes and sizes.[4,5] These features make them ideal for numerous biomedical and biotechnological applications, for instance magnetic capturing of soluble analytes,[6] magnetosome-based immunoassays,[7] as nanocarriers for magnetic drug targeting,[8] magnetic hyperthermia,[9,10] and as reporters for magnetic resonance imaging (MRI)[11,12] and magnetic particle imaging (MPI).[13] For many of these applications magnetosomes have to be further functionalized by the introduction of additional moieties to the surface, or by encapsulation of the particles, especially if they are intended for the use as theranostics. As one of the most attractive features of magnetosomes both their crystal morphologies and the composition of the enveloping membrane can be engineered *in vivo* by genetic means. Abundant magnetosome membrane (Mam) proteins can be used as fusion anchors for surface display of foreign proteins and peptides. For example, both the N- and C-terminus of the 12.4-kDa MamC protein that has only a minor function in magnetite biomineralization[14−16] provide sites for covalent and highly specific attachment of foreign proteins to the magnetosome surface by genetic fusion.[17−19] MamC has been used for the magnetosome expression of the fluorophore (e)GFP,[17,18] camelid antibody fragments (nanobodies),[6,20] and enzymes such as luciferase,[21] the multisubunit chimeric bacterial RNase P,[22] or the paraoxonase Opd.[23] Using an improved expression system[18] and a recombination-impaired bacterial strain,[24] even arrays of up to five copies of the enzyme glucuronidase (GusA) fused to a terminal, codon-optimized eGFP (mEGFP) as additional reporter could be expressed on the magnetosome surface.[25] In the latter study, MamC, GusA monomers, and mEGFP were stitched together by flexible Gly_{10} linkers, which are known to allow proper folding of recombinant proteins and thus, ensure biological activity.[26] In addition, Borg and co-workers generated hybrid core−shell nanoparticles, consisting of the fluorescent magnetosome core (expressing eGFP) enclosed by a ZnO or silica shell,[27] which improved colloidal stability.

A further intriguing material suitable for coatings could be spider silk, which exhibits extraordinary properties such as a

Received: December 13, 2017
Revised: January 19, 2018
Published: January 22, 2018

DOI: 10.1021/acs.biomac.7b01749
Biomacromolecules 2018, 19, 962−972

high toughness combined with good biocompatibility[28−30] desirable for future *in vivo* applications of bacterial magnetosomes. Spider silk proteins (so-called spidroins) consist of nonrepetitive terminal domains that flank the highly repetitive core domain and often exceed a molecular weight of 150 kDa.[29] However, recombinant expression of spider silk proteins in bacteria so far has been confined to only few well-established systems such as *Escherichia coli*, *Salmonella*, and *Bacillus* sp. species.[31−33]

In this study, we explored the expression of spider silk sequences on the magnetosome surface of the magnetotactic alphaproteobacterium *M. gryphiswaldense*. The recombinant engineered spider silk protein eADF4 (engineered *Araneus diadematus* fibroin 4) is based on the consensus sequence of the highly repetitive primary structure of ADF4,[34,35] and the number of repeat units can be adjusted allowing the production of spidroins with various molecular weights.[36] The engineered consensus sequence is called module C consisting of 35 amino acids (GSSAAAAAAAASGPGGYGPENQGPSG-PGGYGPGGP).[35,37,38] We show that silk motifs (based on module C) can be conjugated to a single MamC anchor by genetic fusion. Silk expression enhanced magnetosome biosynthesis and caused the formation of a proteinaceous capsule, which increased the colloidal stability of isolated particles. Overall, this demonstrates that two different biogenic materials, spider silk and magnetosomes, can be genetically combined, thereby generating a new hybrid composite with novel properties and enhanced application potential.

MATERIALS AND METHODS

Bacterial Strains, Plasmids, and Cultivation Conditions. Bacterial strains and plasmids that were used in this study are listed in Tables S1 and S2, respectively. *M. gryphiswaldense* strains were grown microaerobically in modified flask standard medium (FSM) at 30 °C according to Heyen and Schüler.[39] Magnetite formation was ensured by applying a headspace-to-liquid ratio of approximately 1:4 with air in the headspace. Oxygen concentrations declined from high initial levels in the medium with increasing cell numbers, eventually reaching low dissolved oxygen concentrations, permitting magnetite synthesis.[17] *E. coli* strains were grown as previously described.[40] For the cultivation of *E. coli* WM3064 D,L-*α*,*ε*-diaminopimelic acid (DAP) was added to lysogeny broth (LB) medium at a final concentration of 1 mM. Strains were routinely cultured as previously described.[18] For the cultivation on solid medium 1.5% (w/v) agar was added. For strains carrying recombinant plasmids, media were supplemented with 25 μg/mL kanamycin (Km) for *E. coli* and 5 μg/mL for *M. gryphiswaldense* strains.

Molecular and Genetic Techniques. Oligonucleotides (see Table S3) were purchased from Sigma-Aldrich (Steinheim, Germany). Plasmids were constructed by standard recombinant techniques as described in detail below. All constructs were sequenced by Macrogen Europe (Amsterdam, Netherlands). Sequence data were analyzed with Geneious 8.0.5 (Biomatters Ltd.) and ApE 2.0.47 (M. Wayne Davis, 2009).

Construction of MamC Fusion Proteins. The *c2* sequence was amplified from pCS-eADF4(C2) using the primers linker1-sps fwd and sps rev. The resulting fragment was subsequently inserted into the NcoI and BamHI restriction sites of pSB9, thereby generating pFM-C2. For construction of pFM1 and pFM2, first the *cl2* and *cl32* sequences were generated via several PCR steps (Figure S1−S3). The primer combinations linker1-sps fwd and sps-linker2 rev, or linker2-sps fwd and sps rev were used to amplify the *c*-module, with pCS-eADF4(C16) serving as template. Due to the repetitive *c16* sequence, in both reactions fragments of different sizes (ranging from 105 to 10 500 bp) were obtained. The *c1* fragments (105 bp) were chosen and fused via overlap PCR, resulting in the 276 bp sequence *gly10-c1-gly10-c1*, referred to as *cl2*. After restriction with NcoI and BamHI, *cl2* was cloned into pSB9, thereby replacing *gusA* and generating pFM1. For the construction of *cl32*, the *cl2* sequence was amplified using primer combinations linker1-sps fwd/sps-linker3 rev or linker3-sps fwd/sps-linker4 rev. The resulting fragments were subjected to overlap PCR as described above, thereby generating a *cl4* fragment. The *cl32* sequence $(gly10\text{-}c1)_{32}$ was obtained by overlap PCR using *cl4* as template. Due to the repetitive *cl4* structure, *cl6*, *cl8*, *cl16* and *cl32* sequences were obtained. *cl32* was chosen and amplified using the primers linker1-sps fwd and sps rev to generate NcoI and BamHI restriction sites. After digestion, *cl32* was cloned into pSB9, thereby replacing *gusA* and generating pFM2.

pFM-C2, pFM1, or pFM2 were transferred to *M. gryphiswaldense* strains by conjugation, with the expression cassettes being chromosomally inserted by Tn5 transposition.

Determination of Iron. Iron content of cells and isolated magnetosomes were determined by flame atomic absorption spectroscopy. Magnetosomes or cells (suspensions with equal optical densities) were pelleted, resuspended in 0.5 mL 69% nitric acid and incubated at 98 °C for 3 h. The measurements were conducted with a PerkinElmer Atomic Absorption Spectrometer 1100 B (Überlingen, Germany) using the following conditions: wavelength 248 nm, gap width 0.2 nm, lamp current 20 mA.

UV/Vis Spectroscopy. Optical density (OD) and magnetic response (C_{mag}) of late exponentially phase cells were measured photometrically at 565 nm as previously reported.[41] Briefly, for C_{mag} measurements, cells were aligned parallel to the field lines of a magnetic field, resulting in a change in light scattering. The ratio of scattering intensities at different field angles relative to the light beam was used to characterize the average magnetic orientation of the cells. C_{mag} is well correlated to the average number of magnetosomes in magnetic cell populations and, thus, can be used for semiquantitative estimations of magnetosome contents.

Transmission Electron Microscopy (TEM). For TEM of whole cells and isolated magnetosomes, specimens were directly deposited onto carbon-coated copper grids. Magnetosomes were stained with 1% uranyl acetate. Transmission electron microscopy was performed on a CEM 902A (Zeiss, Oberkochen, Germany) with an acceleration voltage of 80 kV. Images were taken with a Gata Erlangshen ES500W CCD camera. Sizes of crystals were measured with ImageJ software.

Analysis of Sedimentation Behavior/Colloidal Stability. Sedimentation analyses of isolated magnetosomes were performed as previously described.[42,43] Nanoparticle dispersions were fractioned by gravity and allowed to settle for 60 min. During this incubation time, agglomerates (e.g., particles that have accidently lost their membrane) formed pellets at the bottom of the tube. The supernatants were collected and subjected to the sedimentation assay. Assuming that the dispersions contained particles with equal size distributions (at the beginning of the experiment), the sedimentation rates depended only on the aggregation process. Sedimentation profiles were obtained by measuring the optical density as a function of time at a wavelength of 508 nm. Absorption values were normalized with the absorption at the initial time of the experiment, thus allowing direct comparisons of the different dispersions.

Zetasizer Measurements. Zeta potential (ZP) values and particle sizes were determined with a Zetasizer Nano (Malvern, U.K.). Suspensions of isolated magnetosomes (wild-type or spider silk decorated particles) were pelleted and resuspended in 10 mM Hepes +1 mM EDTA buffer, pH 7.2. For ZP measurements DTS1070 folded capillary cells (Malvern, U.K.) were used. Measurements were made in triplicates.

Biochemical Methods. Isolation of bacterial magnetosomes from *M. gryphiswaldense* was performed as previously described.[17,39] Denaturing polyacrylamide gels were prepared according to the method of Laemmli,[44] modified after Fling and Gregerson.[45] Samples of isolated magnetosomes contained 32 μg Fe, and the solubilized magnetosome membrane proteins were separated by electrophoresis and subsequently transferred onto polyvinylidene difluoride (PVDF) membranes (Roth, Germany). For immunological detection, membranes were blocked/equilibrated in AP-T buffer (0.1 M Tris; 0.1 M

NaCl; 5 mM $MgCl_2 \times 6\,H_2O$; 0.05% (v/v) Tween 20; pH 7.4) for 2 h. Primary rabbit anti-MamC IgG antibody was added at a 1:3000 ratio and incubated for 2 h at room temperature. Membranes were subsequently washed 4-times with AP-T buffer for 5 min and incubated with a secondary goat antirabbit IgG antibody (1:30 000; antirabbit IgG with conjugated alkaline phosphatase [Sigma-Aldrich, Steinheim, Germany]) for 1 h. Membranes were again washed 4-times with AP-T buffer for 5 min, and finally 15 min in AP buffer (0.1 M Tris; 0.1 M NaCl; 5 mM $MgCl_2$; pH 9.5). For staining/detection, the membrane was transferred to a BCIP/NBT substrate solution and incubated until violet bands appeared. The reaction was stopped with acidified water.

Cryo-Electron Tomography (CET). *Plunge-Freezing Vitrification.* Five microliters of MSR culture mixed with 2 μL of 15 nm BSA-coated colloidal gold clusters (Sigma-Aldrich, Steinheim, Germany) was used for subsequent alignment purposes. The mixture was added on glow-discharged Quantifoil R 2/1 holey carbon molybdenum grids (Quantifoil Micro Tools GmbH, Jena, Germany), blotted, and embedded in vitreous ice by plunge freezing into liquid ethane (<−170 °C). The grids were stored in sealed boxes in liquid nitrogen until used.

CET. Tomography was performed under low-dose conditions using a Tecnai G2 Polara transmission electron microscope (FEI) equipped with a 300 kV field emission gun, and a Gatan GIF 2002 postcolumn energy filter. A 3838 × 3710 Gatan K2 Summit Direct Detection Camera operated in counting and dose-fractionation mode was used for imaging. Data collection was performed at 300 kV, with the energy filter operated in the zero-loss mode (slit width of 20 eV). Tilt series were acquired using Serial EM software.[46] The specimen was tilted about one axis with 1.5° increments over a typical total angular range of ±60°. The cumulative electron dose during the tilt series was kept below 150 $e^- Å^{-2}$. To account for the increased specimen thickness at high tilt angles, the exposure time was multiplied by a factor of $1/\cos\alpha$. Pixel size at the specimen level was 4.27 Å at an EFTEM magnification of 27500×. Images were recorded at nominal −6 μm defocus.

Tomogram Reconstruction and Segmentation. Tomograms were reconstructed in the IMOD package.[47] Tomographic reconstructions from tilt series were performed with the weighted back-projection with IMOD software using particles as a fiducial marker. Aligned images were binned to the final pixel size of 17.08 Å for WT (9 tomograms), *mamC-cl2* (8 tomograms) and *mamC-cl32* (11 tomograms) non-magnetic cells treated under low iron conditions and 25.62 Å for the *mamC-cl32* strain grown in FSM media (10 tomograms from 10 cells). For tomographic reconstruction, the radial filter options were cut off: 0.5 and fall off: 0.05. The data set for this study consisted of 38 tomograms from 38 cells. Tomograms were treated with an anisotropic nonlinear diffusion denoising algorithm to improve signal-to-noise ratio.

Segmentation of the tomogram was done with Amira software on binned volumes of magnetic cells of the *mamC-cl32* strain with a voxel size of 25.62 Å. Membrane segmentation was done using the software TomoSegMemTV and a complementary package, SynapSegTools, both for Matlab.[48] Tomograms visualization and membrane thickness measurements were performed in 3dmod software from the IMOD package.

Attenuated Total Reflection Fourier Transform Infrared Spectroscopy (ATR-FTIR). Magnetosome samples were dispersed in water at a concentration of 1.5 mg/mL, and 2 μL magnetosome dispersion were placed on the Ge crystal. The samples were dried and ATR-FTIR spectra were measured on a Ge crystal using a MIRacle Single Reflection ATR accessory (PIKE Technologies, Madison, USA) with a Bruker Tensor 27 spectrometer (Bruker, Germany) between 4000 and 800 cm^{-1}. Each measurement reflects 120 scans at a resolution of 2 cm^{-1}. Spectra are focused between 1770 and 1580 cm^{-1} to highlight relevant and significant differences in the absorbance region of C = O stretching vibrations of lipids and proteins. A baseline correction was applied using OPUS software (Bruker Optics Corp., USA) and spectra were normalized (A/A_{max}). The relation of the absorption maxima of the phospholipid/lipid band (~1750 cm^{-1} − 1710 cm^{-1}) and amide I band of proteins (~1690 cm^{-1} − 1600 cm^{-1}) was calculated by $A_{norm.}$(amide I)/$A_{norm.}$(phospholipids).

Quartz Crystal Microbalance with Dissipation Monitoring (QCM-D). *Sensor Chip Coating with eADF4(C16).* QCM-D resonators (5 MHz, AT-cut, Cr/Au; Quartz Pro Sweden AB, Järfälla, Sweden) were cleaned by a 10 min UV/ozone treatment (PSD-Pro Series, Novascan, Ames, USA) followed by spin coating (4000 rpm, 1800 rpm/s, 30s; 1-EC 101 DT 8−19456 Spin-Coater, Headway Research Inc., Garland, USA) with 30 μL eADF4(C16) (AMSilk GmbH, Planegg/München, Germany) solution (1 mg/mL) in formic acid (Sigma-Aldrich, Steinheim, Germany). The eADF4(C16)-coated sensor chips were post treated in methanol atmosphere overnight, and mounted in the standard Q-Sense flow module (QFM 401, Biolin Scientific, Västra Frölunda, Sweden).

Magnetosome Adsorption Study. All equilibration and adsorption steps were performed in Hepes buffer (10 mM Hepes, 1 mM EDTA, pH 7.2) at a volume flow of 70 mL/min at 21 °C with a Q-Sense E4 (Biolin Scientific, Västra Frölunda, Sweden). The coated sensor chips (eADF4(C16)) were equilibrated in buffer, flushed with 100 μg/mL magnetosomes (wild-type and *mamC-c2*) for 40 min followed by a 50 min buffer flow again. Frequency and dissipation data are monitored for the third overtone. The change in areal mass density $\Delta\rho_A$ for a specific overtone n is proportional to the change in frequency Δf and described by Sauerbrey eq (eq 1).[49]

$$\Delta\rho_A = -\frac{\rho_q h_q}{f_0}\frac{\Delta f}{n} = -C\frac{\Delta f}{n} \tag{1}$$

The mass sensitivity constant C depends on the density (ρ_q), the thickness (h_q) and the fundamental frequency (f_0) of the quartz crystal.[50]

Fibrillization Experiments. eADF4(C16) protein was produced as published previously.[34] Aqueous eADF4(C16) solutions were prepared by dissolving lyophilized protein in 6 M guanidinium thiocyanate (GdmSCN) followed by dialysis against 10 mM Tris/HCl, pH 7.5, with three buffer changes: twice after 2 h and once after 16 h. The protein concentration was determined using a Varian Cary 50 Bio UV−Vis spectrometer after centrifugation in a Beckman Optima ultracentrifuge at 55 000 rpm for 45 min at 20 °C. Isolated MamC-C2 or wild-type magnetosomes (0.5 mg/mL Fe) were used as seeds in fibrillization experiments and added to an eADF4(C16) solution (1 mg/mL) in the presence of 100 mM potassium phosphate (pH 7.4).

■ RESULTS AND DISCUSSION

Construction of Spider Silk Motif Expressing *M. gryphiswaldense* strains. An engineered version of *adf4* (codon-optimized for recombinant expression in *E. coli*)[34,35,51] was used as a template for the generation of repetitive spider silk sequences. By designing engineered spider silk motifs for expression on magnetosomes, two strategies were explored: (i) Glycine linkers could improve folding of recombinant fusion proteins and also reduce sterical hindrance,[26] and therefore spider silk-like constructs containing Gly_{10} linkers were designed. Single C motifs were connected by Gly_{10} , and the resulting arrays with two or 32 silk units (referred to as CL2 or CL32, respectively) were genetically fused to the magnetosome membrane protein MamC. On the other hand, previous computational analysis and *in vitro* measurements have shown that the structural properties of silks (like their unique pattern of extreme solubility inside the spider glands and complete insolubility outside) depend on their highly repetitive, uninterrupted hydrophobic regions and that their characteristics might be affected by very small changes in the protein sequence.[52] We (ii) also generated a construct with the established C2 peptide[36] connected to MamC. Translational fusions of *c2* or *cl2*/32 to *mamC* were designed as *mamC-c2* or *mamC-cl2*/32 constructs (Figure 1) under control of the

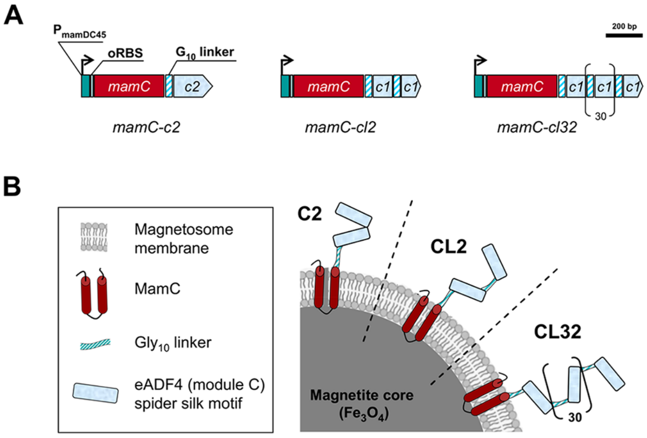

Figure 1. (A) Schematic representation showing the genetic organization of the expression cassettes for magnetosome display of spider silk motifs (MamC-C2, MamC-CL2, and MamC-CL32). (B) Schematic of spider silk motifs C2, CL2, and CL32 produced as hybrid-proteins fused to a single MamC membrane anchor. For more details, refer to the methods section (size of particle and proteins not to scale).

constitutive, optimized $P_{mamDC45}$ promotor and the optimized ribosome binding site (oRBS), which allow high-level expression of foreign proteins.[18] *mamC-c2* or *mamC-cl2/32* cassettes were inserted via Tn5 transposition at random chromosomal positions and expressed in RecA-deficient strain *M. gryphiswaldense* IK-1 to avoid homologous recombination between identical sequences.[24]

Expression of Linker-Modified, Silk-Like Constructs in *M. gryphiswaldense* Impairs Cell Division and Increases Magnetosome Biomineralization. *M. gryphiswaldense* strains *mamC-c2* and *mamC-cl2/32* grew slightly slower compared to the parental strain IK-1 (doubling times: *mamC-c2*, 6.1 h; *mamC-cl2*, 6.2 h; *mamC-cl32*, 6.5 h; IK-1, 5.9 h). The magnetic response (C_{mag}) of *mamC-c2* cells was comparable to that of IK-1 (*mamC-c2*: 0.91 ± 0.07; IK-1:0.94 ± 0.05); however, for strains *mamC-cl2* and *mamC-cl32*, C_{mag} values decreased with the number of spider silk motifs (*mamC-cl2*: 0.83 ± 0.02; *mamC-cl32*: 0.64 ± 0.09). Iron contents and total particle numbers per cell were increased for *mamC-cl2* and *mamC-cl32* by 66% and 71%, respectively, with up to 60 magnetosomes per cell on average. One can speculate that the observed reduced growth rates favor an increased magnetosome production. Nearly 40% of the cells (*mamC-cl2*: 36.2%; *mamC-cl32*: 38.3%) contained less than 20 particles, whereas more than 50% (*mamC-cl2*: 51.7%; *mamC-cl32*: 53.0%) contained more than 80 particles (*mamC-cl2*: 97 ± 14; *mamC-cl32*: 104 ± 13) partially resembling overproducer strains engineered before.[53] Only a low number of cells (6%) produced wild-type-like particle amounts (Figure 2 and Figure S5). By contrast, strain *mamC-c2* showed a wild-type-like particle number distribution and synthesized wild-type-like amounts of magnetosomes (32 ± 11 particles per cell; Figure 2 and Figure S4) arranged in one or two chains positioned at midcell.

The spatial stochastic resonance in the sequence hydrophobicities of spider silk proteins[52,54] is highly sequence dependent. Even small changes in the spider silk protein sequence, like the Gly_{10} linker introduction into constructs MamC-CL2 and MamC-CL32, might affect these resonance properties, which could be experimentally confirmed here for the first time. The Gly_{10} linkers seem to affect the properties of the resulting artificial proteins, cell division, magnetosome production and protein expression. Therefore, seamless cloning[34] of the highly repetitive sequences is essential for spider silk proteins and their properties, even if expressed in a complex system like *M. gryphiswaldense*.

Intrigued by the perturbed cell separation phenotype, we studied the *mamC-cl32* cell division sites by cryo-electron tomography, a powerful technique to investigate the subcellular ultrastructure in a near-native state. Cells of *mamC-cl32* tended to form minicell-like structures at the division sites, before becoming eventually separated. Parts of the magnetosome chains were frequently trapped in and traversing the minicells (Figure 3A−D and Figures S6 and S7), and the separation of individual cells was impaired. Hydrophobic interactions of the silk peptides might largely contribute to the forces to maintain the magnetosomes together in addition to the magnetostatic forces. The sum of both factors, the hydrophobic surface interaction and the magnetic forces, may likely lead to impairment for the cell in splitting the magnetosome chain properly, in turn generating the cell division defect, where cells seem to be caught in cytokinesis or forming minicell bridges with magnetosome chains confined inside. Even with the aid of the dynamic MamK filaments contributing to pole-to-midcell motion of the magnetosome chain,[55] the magnetosome surface hydrophobic forces are such that the cells cannot separate properly the magnetosome chain, and higher forces might be required to overcome the magnetic and other noncovalent interactions between particles. Furthermore, binding of MamJ to the MamK filament might be impaired by the silk peptides displayed on the magnetosome surface, and it can be assumed that MamJ is inaccessible due to the proteinaceous spider silk capsule.

Magnetosome Expression of Spider Silk Motifs Generates a Proteinaceous Capsule. In SDS gels, MamC-C2 magnetosomes displayed an additional band of 20 kDa (Figure 4, red boxes), equivalent to the predicted molecular weight of the MamC-C2 hybrid protein. For *mamC-cl2*, an expected band of 21 kDa (predicted molecular weight of the MamC-CL2 fusion) was absent; instead, an additional 150 kDa band could be detected. A protein of similar electrophoretic mobility was visible for *mamC-cl32*, corresponding to the predicted molecular weight of the MamC-CL32 fusion (156 kDa). In Western blots, for the wild-type and MamC-mEGFP (=control construct) bands with the expected molecular weight were detected (wild-type: 13 kDa, MamC-mEGFP: 39 kDa). For MamC-C2 particles, two bands with equal intensities but different electrophoretic mobilities (21 and 13 kDa) were obtained, corresponding to the expected molecular weight of the MamC-C2 hybrid protein and the unfused MamC (20 and 12 kDa, respectively) (Table 1). For MamC-CL32, two bands of high molecular weight (156 kDa and 144 kDa) with different intensities were detected (with the predominant band of 156 kDa corresponding to the predicted size of the MamC-CL32 fusion protein), while for the MamC-CL2 fusion, the expected band of 21 kDa was absent, and high molecular weight bands of 154 kDa, 142 kDa and 83 kDa were detected instead (Table 1). This unexpected behavior might be partly caused by an altered binding behavior of SDS to the linker-modified proteins due to the Gly_{10} sequences.

Due to their highly hydrophobic character, it is not unlikely that the produced hybrid proteins (consisting of MamC and spider silk peptides) might interact with each other. However,

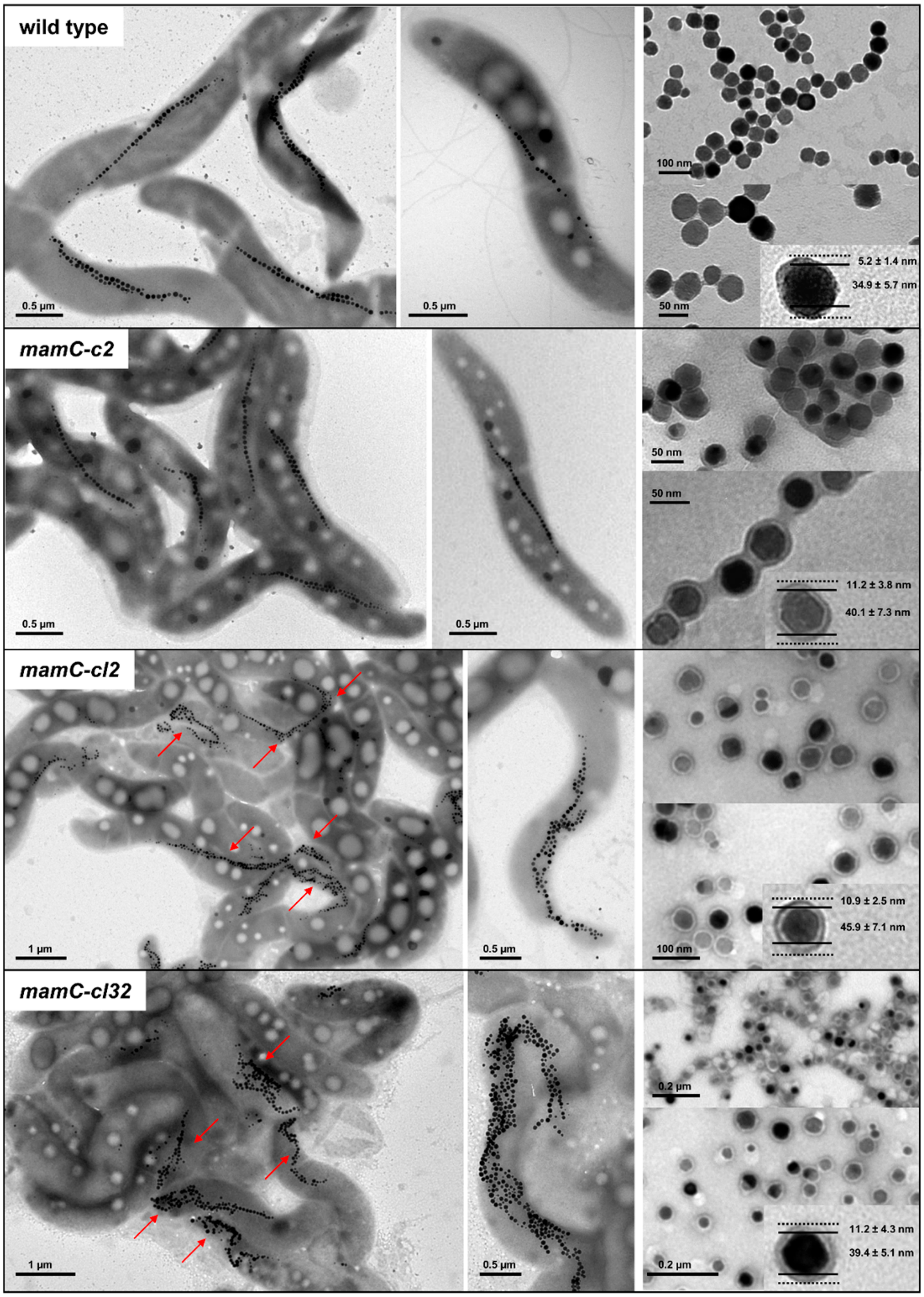

Figure 2. Transmission electron micrographs of cells and isolated, negatively stained particles from *M. gryphiswaldense* strains *mamC-c2*, *mamC-cl2*, *mamC-cl32*, and from the wild-type. The spider silk motif expressing strains *mamC-cl2* and *mamC-cl32* showed a magnetosome misdistribution with more than 50% of the cells containing 70−120 particles per cell (see also Figures S4 and S5). Furthermore, high ratios of nearly particle-free cells were visible. Arrows indicate cells overproducing magnetosomes. In contrast, *mamC-c2* cells formed wild-type-like particle amounts (about 32 particles per cell, arranged in one or two chains positioned at midcell). For all particles displaying spider silk motifs, a capsule of up to 15 nm in thickness was visible.

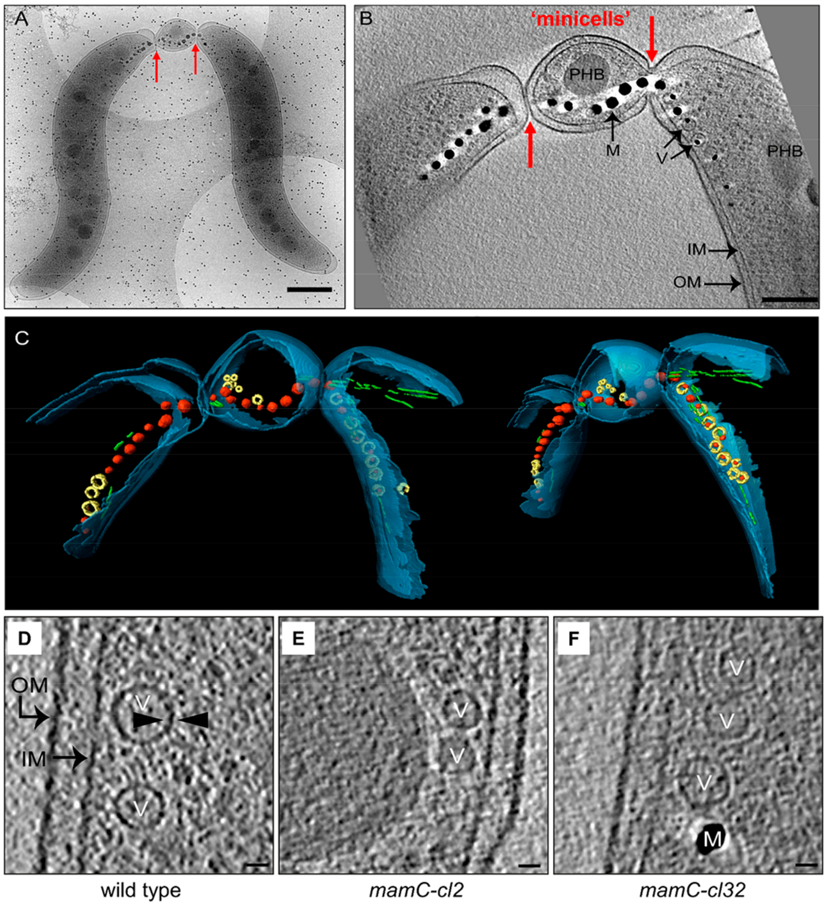

wild type *mamC-cl2* *mamC-cl32*

Figure 3. Cryo-electron tomography of selected strains. (A) Cryo-electron microscopy image of a *mamC-cl32* cell (*n* = 10) selected for tomography. Scale bar: 500 nm. (B) A 12.8 nm thick tomographic slice (average of 5 slices) displaying the division site of the cell shown in "A". Cells display impairment in cytokinesis generating bridges of minicells due to improper cell division. Division sites are indicated by red arrows. M: magnetite crystal, IM: inner membrane, OM: outer membrane, V: vesicle, PHB: polyhydroxybutyrate granule. Scale bar: 200 nm. (C) CET 3D rendering of the selected cell division site. Magnetite crystals: red, vesicles (magnetosome membrane): yellow, and MamK filament: green. The cellular envelope inner and outer membranes are depicted in blue. (D−F) Magnetosome vesicle visualization by cryo-electron tomograms. An 8.5 nm thick tomographic slice (average of 5 slices) of nonmagnetic cells of (D) wild-type (*n* = 9), (E) *mamC-cl2* (*n* = 8) and (F) *mamC-cl32* (*n* = 11) cultivated in low-iron medium for vesicle (magnetosome membrane) thickness comparison. V: vesicle (magnetosome membrane). M: magnetite crystal, OM: outer membrane, IM: inner membrane. Arrowheads indicate vesicle thickness. Scale bars: 20 nm.

the overall high abundance of magnetosome membrane proteins suggests an unusually crowded protein composition of the magnetosome membrane.[56] Therefore, we assume that the tight packing with transmembrane domains of integral proteins would interfere with the formation of specific patches in the magnetosome membrane.

Proteomics analysis of polyacrylamide gel slices (Proteomics Service, Ludwig-Maximilians-University of Munich, Planegg-Martinsried, Germany) revealed a variety of cellular (enzyme) proteins and peptides (including MamC) present in the 150 and 140 kDa region of lanes "MamC-CL2" and "MamC-CL32". However, distinct proteins with a molecular mass of 150 or 140 kDa could not be detected. An almost identical protein/peptide content pattern was obtained for gel slices from the "wild-type" lane. Thus, in particular for the MamC-CL2 fusion, these findings might argue for the presence of chimeric proteins on the particle surface, with increased molecular masses that also involve other cellular proteins and peptides. Furthermore, for both CL fusions, no unfused MamC was detectable, indicating that the latter might be incorporated in mixed assemblies with (chimeric) MamC-CL fusion proteins.

TEM micrographs revealed that magnetosomes isolated from spider silk-expressing strains were surrounded by an organic capsule of low electron density (Figure 2, Table S4). For MamC-C2, MamC-CL2, and MamC-CL32, the thickness of this layer was about 11 nm, with overall particle diameters of 52.6 and 56.8 nm, respectively. The expression of silk motifs with 32 repetitive units (MamC-CL32) also resulted in a layer of 11 nm, and therefore in similar particle sizes. Thus, particle diameters were considerably increased compared to wild-type magnetosomes (38.1 nm in diameter) or MamC-mEGFP particles (39.7 nm in diameter), which were used as an additional control because the latter display up to 200 mEGFP copies on the surface.[18] For spider silk magnetosomes, neither the presence of Gly_{10} linkers nor the number of spider silk motifs did affect layer thickness and particle diameters. A possible explanation is that linker constructs may closely adhere (in a flat layer) to the magnetosome surface and by that the surface is blocked by a protein layer. Increased particle sizes were essentially confirmed by zetasizer measurements revealing diameters of up to 63.5 ± 5.8 nm (for strain *mamC-cl32*) (Table S4).

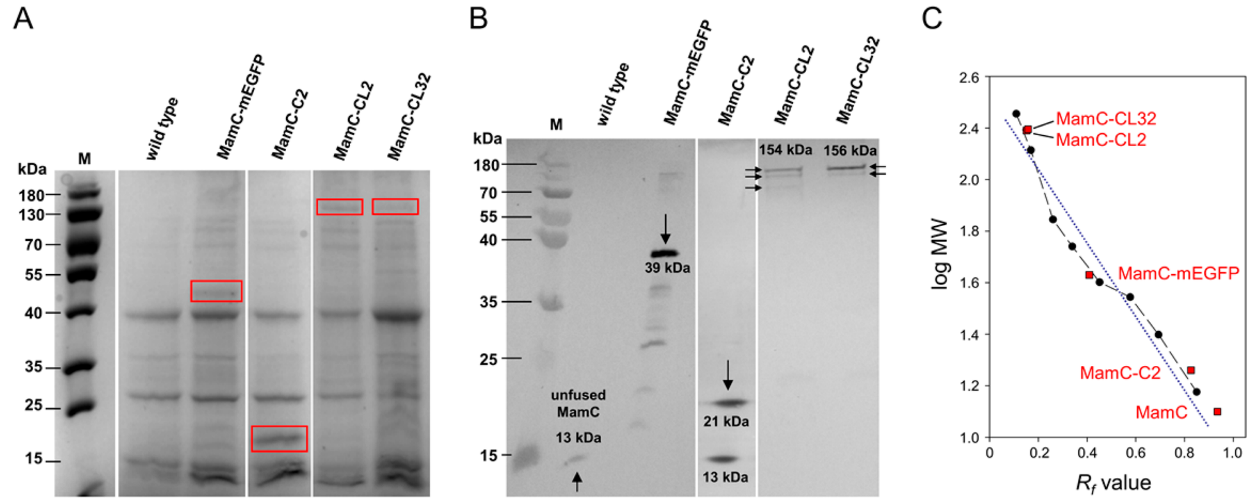

Figure 4. Magnetosome expression of spider silk motifs as translational fusions to MamC. (A) Solubilized protein fractions of isolated magnetosomes (32 μg Fe/lane) from the mutant strains *mamC-c2*, *mamC-cl2*, and *mamC-cl32* of *M. gryphiswaldense* were subjected to denaturing PAGE. Fractions from wild-type magnetosomes and from a Δ*mamC::mamC-megfp* transposon mutant (MamC-mEGFP)[18] were used as control. In the Coomassie-stained gel, similar patterns were obtained for all strains. However, depending on the proteins displayed on the magnetosome surface, additional bands (compared to the wild-type) were detected (red boxes). For Δ*mamC::mamC-megfp*, an extra band of 39 kDa was visible, which corresponds to the MamC-mEGFP fusion. (B) Western blot analysis employing an IgG antibody directed against MamC was used for the detection of MamC fusion proteins. Degradation products potentially caused by the sample preparation were detected to only minor extents. M, protein molecular weight marker. (C) Electrophoretic mobilities (and the corresponding R_f values) of the marker proteins were taken to draw a calibration curve and to estimate the molecular weight of MamC hybrid proteins.

Table 1. Molecular Weight of MamC-C2, MamC-CL2, and MamC-CL32 Hybrid Proteins on the Magnetosome Surface[a]

	MamC	MamC-mEGFP	MamC-C2	MamC-CL2	MamC-CL32
predicted molecular weight (kDa)	12	39	20	21	160
apparent molecular weight, estimated from Western blot (kDa)	13	39	21	154/142/83	156/144

[a]Denaturing PAGE with subsequent Western blotting (Figure 4) was used to estimate the molecular weight of the fusions according to their electrophoretic mobility. The obtained values are compared with the theoretical weights based on amino acid composition.

By contrast, cryo-electron tomography of iron-starved cells (mostly devoid of magnetite crystals) of the wild-type, *mamC-cl2* and *mamC-cl32* strains (C_{mag} = 0.42, 0.2 or 0.2, respectively) revealed no apparent differences in vesicle features *in situ* (i.e., same electron density, shape, diameter), with membrane thickness determined as 6.1 ± 0.1 (SEM) and 6.0 ± 0.1 (SEM) for the wild-type and *mamC-cl32*, respectively (Figure 3 and Figure S8). This can be explained as the protein layers residing on the magnetosome membrane are not sufficiently electron-dense to be detected.

Effects of the displayed silk peptides on magnetosome biosynthesis by potential misorganization of magnetosome membrane proteins (like, e.g., MamA) and/or impaired interactions with other (magnetosome) proteins are rather unlikely since it has been shown that even the magnetosome expression of large enzyme arrays (with up to 90% coverage of the particle surface) has no influence on magnetosome biomineralization.[25]

Fourier transform infrared spectroscopy (FTIR) was used to obtain further information on the organic layer on the magnetosome surface (Figure S9). Of particular interest were bands in the C═O stretch vibration regime (1780−1585 cm^{-1}), which contain information on the phospholipid portion (esters, acids: ∼1750−1710 cm^{-1}) and protein portion (amide I: ∼1690−1600 cm^{-1}). Protein to phospholipid ratios calculated from phospholipid and amide I band maxima ($A_{norm.}$(amide I)/$A_{norm.}$(phospholipids)) were 3.54 for wild-type and 3.41 for MamC-mEGFP particles, indicating the presence of proteins on the surface as expected. Similar values were obtained for particles of MamC-CL2 and MamC-CL32 magnetosomes, with ratios of 3.77 and 3.02, respectively. By contrast, for magnetosome preparations in which the native enveloping membrane was partially lost (for instance during preparation), we observed reduced protein to phospholipid ratios (MamC-CL2:0.11, MamC-CL32:0.10 and 0.41; Figure S9) revealing low protein amounts on the magnetosome surface. Therefore, ATR-FTIR can be used as qualitative method for examination of protein expression and the proper preservation of the magnetosomes membrane. For MamC-C2, a protein-to-phospholipid ratio of 6.19 was measured, indicating a high C2-expression on the magnetosome surface in agreement with the detection of this construct by Western blot and the improved compatibility with the expression system (indicated by reduced effects on cell growth and division). The amide I band is a superposition of C═O stretching vibrations of the protein backbone (peptide bond), which are influenced in their vibrational energy depending on the chemical environment. Secondary structures were assigned to specific wavenumber regions of the amide I band based on secondary structure assignment of recombinant spider silk protein eADF4(C16).[57] All samples (wild-type, MamC-mEGFP, MamC-C2, MamC-CL2 and MamC-CL32) showed a maximum in the α-helical regime (1656−1653 cm^{-1}). For MamC-mEGFP and in particular for MamC-CL2/32 constructs, an increase of the shoulder in the region from 1640−1625 cm^{-1} was visible (Figure S9). These spectra therefore indicate differences in secondary structure elements (for instance, β-sheet content). mEGFP forms β-barrel-like structures,[58,59] and

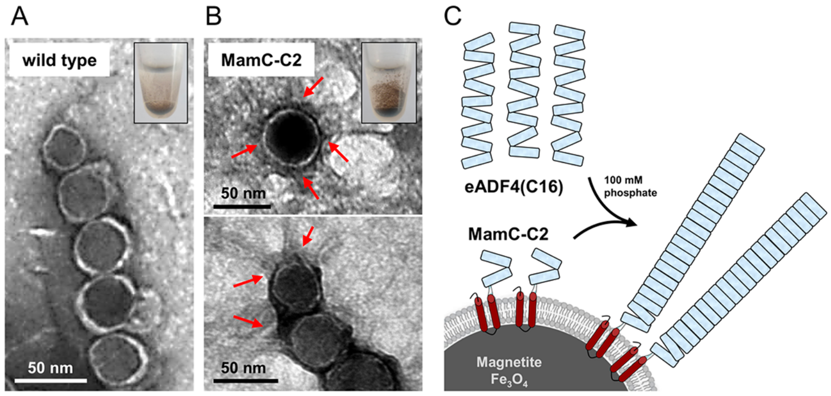

Figure 5. Assembly of nanofibrils in the presence of MamC-C2 magnetosomes. TEM micrographs of isolated wild-type particles (A) or MamC-C2 magnetosomes (B) that were incubated with 20 μM freshly dialyzed eADF4(C16) monomers in potassium phosphate buffer. For wild-type magnetosomes no indications for directed fibril growth from the particle surfaces were detectable, whereas for MamC-C2 magnetosomes fibril-like structures were visible at the particle surface (indicated by arrows), suggesting C2 triggered docking of further eADF4(16) monomers and fibril formation on the magnetosome surface (C) as it has been observed for silk particles by Humenik and co-workers.[62] Insets: During incubation with eADF4(C16) monomers, in the presence of MamC-C2 magnetosomes fibrous, network-like structures were visible in the reaction tube. These structures were not observed for wild-type magnetosomes.

compared to wild-type magnetosomes MamC-mEGFP particles exhibited a slight increase of the shoulder in the β-sheet regime. By contrast, for the MamC-C2 construct spectra were comparable to those of wild-type magnetosomes (no shoulder in the region from 1640−1625 cm^{-1}), indicating the absence of β-sheets, which is consistent with the assumption that MamC-C2 only forms a minor β-sheet portion due to the small size of the fusion and the low number of C-module repeats.

Physicochemical Characteristics of MamC-C2, MamC-CL2, and MamC-CL32 Magnetosomes. Next, we investigated the sedimentation behavior of MamC-C2, MamC-CL2, and MamC-CL32 magnetosomes (Figure S10). For wild-type magnetosomes linear sedimentation profiles were observed, reflected by absorption ratios that significantly decreased with time. MamC-C2 and MamC-CL2/32 particles also showed linear sedimentation patterns; however, absorption ratios only slightly decreased, and MamC-CL32 particle suspensions remained nearly stable (i.e., did not sediment) for more than 200 min. Although MamC-C2 and MamC-CL2 magnetosomes exhibited a higher tendency to settle down, absorption ratios were still significantly higher compared to that of wild-type particles (up to 30% for MamC-C2). Furthermore, the zeta potential (ZP) of silk motif-expressing particles shifted to more negative values (wild-type: −34.8 ± 5.3 mV; MamC-C2: −37.2 ± 3.9 mV; MamC-CL2: −37.2 ± 4.0 mV; MamC-CL32: −45.2 ± 4.5 mV). An ANOVA test confirmed that the overall difference between the means was significant ($P < 0.001$). The observed shift in the ZP values might be attributed to negatively charged amino acid residues (e.g., glutamate residues) of the silk motifs or (in case of MamC-CL2/32 linker constructs) additional unspecifically bound protein compounds. These residues would add an additional charge to the particle surface when exposed to the solvent. The theoretical pI values of C2, CL2, and CL32 were calculated[60] to be 3.79, 3.79, and 2.87 and indicate negatively charged protein species at a given pH of 7.2. Therefore, decreased sedimentation rates might be explained by electrostatic repulsion, and increased spacing between the magnetite cores (caused by the silk capsule) might lead to reduced magnetic interactions. Thus, the presence of the spider silk capsule reduced sedimentation and increased colloidal stability of the suspensions.

MamC-C2 Magnetosomes Act as Seeds for Spider Silk Fibril Growth. Although nucleation is a thermodynamically disfavored process and the rate limiting step[61] of eADF4(C16) fibril formation, it can be surpassed upon the addition of preformed seeds, which enable docking of monomers and thus, trigger fibril formation.[36,62] Humenik et al. showed that silk particles can interact with monomeric eADF4(C16),[62] resulting in fibril growth from their surface. In order to analyze potential interactions of MamC-C2 or wild-type magnetosomes with material surfaces made of eADF4(C16), QCM-D measurements were performed. MamC-C2 magnetosomes exhibited adsorption rates on eADF4(C16) films that were increased compared to that of wild-type particles. Furthermore, for MamC-C2 particles, a more linear adsorption behavior was observed, and one can assume that MamC-C2 magnetosomes interacted with eADF4(C16) by intermolecular interactions. Due to shown interaction of MamC-C2 with eADF4(C16), we further investigated whether MamC-C2 magnetosomes enabled docking of soluble eADF4(C16) on the magnetosome surface and triggered fibril formation. Therefore, MamC-C2 magnetosomes were incubated with freshly dialyzed eADF4(C16). TEM micrographs revealed the formation of fibrillar structures arising from single magnetosomes or magnetosome chains at similar rates (Figure 5B and Figure S11). By contrast, on wild-type particles no indications for directed fibril growth from the particle surfaces were detectable (Figure 5A). These findings suggest that magnetosome surface exposed spider silk peptides can function as fibrillization seeds, and thus can trigger fibril growth by recruiting eADF4(C16) out of solution (Figure 5C).

■ CONCLUSIONS

We for the first time demonstrated that recombinant spider silk peptides (MamC-C2) can be expressed in a magnetotactic bacterium. The need of a seamless cloning strategy[34] preserving the highly repetitive hydrophobic character of silk proteins[52,54] was experimentally confirmed as disturbances in the sequence, like the introduced Gly_{10} linkers (MamC-CL2, MamC-CL32), affect the silk properties and even lead to affection of cell division, magnetosome production, and protein expression. By contrast, magnetosome display of a (linker-less) C2 silk motif as hybrid protein fused to an abundant magnetosome membrane anchor in *M. gryphiswaldense* caused the formation of a proteinaceous coat with exposed spider silk features (specific interaction with materials made of eADF4(C16) as well as seeding/nucleating fibrillar growth from the surface) and thus provides a promising route for encapsulation and functionalization of bacterial nanoparticles. Since spider silk is nonimmunogenic,[63] in future applications such building blocks might improve the biocompatibility of bacterial magnetosomes and mask immunogenic compounds displayed on the particle surface. Our strategy demonstrates that the surface properties of magnetic nanoparticles can be further tuned, as particle agglomeration was reduced and the colloidal stability increased. Magnetosome expression of spider silk-inspired peptides could be used in future approaches to generate multifunctional nanoparticles combining those features with further functionalities, such as catalytic activities, and to produce magnetic silk composites that can be oriented and manipulated by an external magnetic field.[64] In summary, our results provide a route toward the generation of fully genetically encoded, functionalized hybrid composites that might be useful as novel biomaterials with enhanced properties in biotechnological and biomedical applications.

■ ASSOCIATED CONTENT

Ⓢ Supporting Information

The Supporting Information is available free of charge on the ACS Publications website at DOI: 10.1021/acs.biomac.7b01749.

> Schematics illustrating the generation of *mamC-cl2* and *mamC-cl32* constructs; charts/tables showing magnetosome distributions, cellular iron contents, particle sizes and layer thicknesses of spider silk-decorated magnetosomes; cryo-electron tomography data; normalized FTIR absorption spectra of magnetosome samples showing bands in the C═O stretch vibration regime; normalized absorption values reflecting the sedimentation behavior of spider silk coated magnetosomes; TEM micrographs illustrating the assembly of nanofibrils in the presence of MamC-C2 magnetosomes (PDF)
>
> Supplemental Movie M1: Cryo-electron tomography and three-dimensional rendering of a *mamC-cl32* cell division site, viewed through the z-stack tomogram of the division site of *mamC-cl32* connected cells by a minicell bridge at a 27 500× magnification; cellular envelope (blue), vesicles (yellow), and magnetite (red) associated to the MamK filament structure (green); Movie M1 related to Figure 3 (MPG)

■ AUTHOR INFORMATION

Corresponding Author

*E-mail: Dirk.Schueler@uni-bayreuth.de. Address: Department Microbiology, University of Bayreuth, Universitätsstraße 30, D-95447 Bayreuth, Germany. Tel.: +49-921-552728. Fax: +49-921-552727.

ORCID

Frank Mickoleit: 0000-0002-1943-3960

Author Contributions

F.M., D.S., and T.S. designed the study. F.M. generated spider silk-expressing strains and performed cultivation experiments, magnetosome isolation, sedimentation assays, electron microscopy, and zetasizer measurements; F.M. analyzed and interpreted the obtained data. C.B.B. designed, performed, and optimized QCM-D and ATR-FTIR experiments and analyzed the data. M.T.-N. performed cryo-electron tomography experiments; M.T.-N. and J.M.P. analyzed the data. M.T.-N. performed 3D rendering of tomographed cells and the corresponding movie. H.M.H. carried out fibrillization experiments. D.S.M. prepared samples for and performed gel electrophoreses and Western blotting. F.M. took the lead in writing the manuscript. All authors provided critical feedback and helped shape the research, analysis, and manuscript.

Notes

The authors declare no competing financial interest.

■ ACKNOWLEDGMENTS

We are grateful to S. Borg for providing several expression plasmids, M. Schlotter (University of Bayreuth) for expert technical assistance, and Günter Pfeifer, Rubén Fernández-Busnadiego, and Tillman Schäfer (MPI of Biochemistry) for constant support with cryo-electron tomography. Dr. M. Lehmann and J. Davydova (MSBioLMU - Proteomics Service, Planegg-Martinsried) are acknowledged for proteomics analysis on polyacrylamide gel slices. This project was funded by the Deutsche Forschungsgemeinschaft (Grants DFG SCHU 1080/15-3 and SCHU 1080/9-2 to D.S., SCHE 603/15-2 to T.S.) and the European Research Council (ERC AdG Syntomagx to D.S.).

■ REFERENCES

(1) Komeili, A. Molecular Mechanisms of Compartmentalization and Biomineralization in Magnetotactic Bacteria. *FEMS Microbiol. Rev.* **2012**, *36*, 232−255.

(2) Uebe, R.; Schüler, D. Magnetosome Biogenesis in Magnetotactic Bacteria. *Nat. Rev. Microbiol.* **2016**, *14*, 621−637.

(3) Jogler, C.; Schüler, D. Genomics, Genetics, and Cell Biology of Magnetosome Formation. *Annu. Rev. Microbiol.* **2009**, *63*, 501−521.

(4) Staniland, S. S.; Ward, B.; Harrison, A.; van der Laan, G.; Telling, N. Rapid Magnetosome Formation Shown by Real-Time X-Ray Magnetic Circular Dichroism. *Proc. Natl. Acad. Sci. U. S. A.* **2007**, *104*, 19524−19528.

(5) Staniland, S. S.; Rawlings, A. E. Crystallizing the Function of the Magnetosome Membrane Mineralization Protein Mms6. *Biochem. Soc. Trans.* **2016**, *44*, 883−890.

(6) Pollithy, A.; Romer, T.; Lang, C.; Müller, F. D.; Helma, J.; Leonhardt, H.; Rothbauer, U.; Schüler, D. Magnetosome Expression of Functional Camelid Antibody Fragments (Nanobodies) in Magnetospirillum gryphiswaldense. *Appl. Environ. Microbiol.* **2011**, *77*, 6165−6171.

(7) Tanaka, T.; Takeda, H.; Ueki, F.; Obata, K.; Tajima, H.; Takeyama, H.; Goda, Y.; Fujimoto, S.; Matsunaga, T. Rapid and Sensitive Detection of 17Beta-Estradiol in Environmental Water Using Automated Immunoassay System with Bacterial Magnetic Particles. *J. Biotechnol.* **2004**, *108*, 153−159.

(8) Lang, C.; Schüler, D.; Faivre, D. Synthesis of Magnetite Nanoparticles for Bio- and Nanotechnology: Genetic Engineering and Biomimetics of Bacterial Magnetosomes. *Macromol. Biosci.* **2007**, *7*, 144−151.

(9) Hergt, R.; Dutz, S.; Röder, M. Effects of Size Distribution on Hysteresis Losses of Magnetic Nanoparticles for Hyperthermia. *J. Phys.: Condens. Matter* **2008**, *20*, 385214.

(10) Alphandéry, E.; Guyot, F.; Chebbi, I. Preparation of Chains of Magnetosomes, Isolated from Magnetospirillum magneticum Strain AMB-1 Magnetotactic Bacteria, Yielding Efficient Treatment of Tumors Using Magnetic Hyperthermia. *Int. J. Pharm.* **2012**, *434*, 444−452.

(11) Taukulis, R.; Widdrat, M.; Kumari, M.; Heinke, D.; Rumpler, M.; Tompa, É.; Uebe, R.; Kraupner, A.; Cebers, A.; Schüler, D.; Pósfai, M.; Hirt, A. M.; Faivre, D. Magnetic Iron Oxide Nanoparticles as MRI

Contrast Agents - a Comprehensive Physical and Theoretical Study. *Magnetohydrodynamics* **2015**, *51*, 721−747.

(12) Herborn, C. U.; Papanikolaou, N.; Reszka, R.; Grünberg, K.; Schüler, D.; Debatin, J. F. Magnetosomen als biologisches Modell der Eisenbindung: Messung der Relaxivität in der MRT. *Fortschr. Röntgenstr.* **2003**, *175*, 830−834.

(13) Kraupner, A.; Eberbeck, D.; Heinke, D.; Uebe, R.; Schüler, D.; Briel, A. Bacterial Magnetosomes - Nature's Powerful Contribution to MPI Tracer Research. *Nanoscale* **2017**, *9*, 5788−5793.

(14) Grünberg, K.; Wawer, C.; Tebo, B. M.; Schüler, D. A Large Gene Cluster Encoding Several Magnetosome Proteins is Conserved in Different Species of Magnetotactic Bacteria. *Appl. Environ. Microbiol.* **2001**, *67*, 4573−4582.

(15) Scheffel, A.; Gärdes, A.; Grünberg, K.; Wanner, G.; Schüler, D. The Major Magnetosome Proteins MamGFDC are not Essential for Magnetite Biomineralization in Magnetospirillum gryphiswaldense but Regulate the Size of Magnetosome Crystals. *J. Bacteriol.* **2008**, *190*, 377−386.

(16) Grünberg, K.; Müller, E. C.; Otto, A.; Reszka, R.; Linder, D.; Kube, M.; Reinhardt, R.; Schüler, D. Biochemical and Proteomic Analysis of the Magnetosome Membrane in Magnetospirillum gryphiswaldense. *Appl. Environ. Microbiol.* **2004**, *70*, 1040−1050.

(17) Lang, C.; Schüler, D. Expression of Green Fluorescent Protein Fused to Magnetosome Proteins in Microaerophilic Magnetotactic Bacteria. *Appl. Environ. Microbiol.* **2008**, *74*, 4944−4953.

(18) Borg, S.; Hofmann, J.; Pollithy, A.; Lang, C.; Schüler, D. New Vectors for Chromosomal Integration Enable High-Level Constitutive or Inducible Magnetosome Expression of Fusion Proteins in Magnetospirillum gryphiswaldense. *Appl. Environ. Microbiol.* **2014**, *80*, 2609−2616.

(19) Nudelman, H.; Zarivach, R. Structure Prediction of Magnetosome-Associated Proteins. *Front. Microbiol.* **2014**, *5*, 9.

(20) Borg, S.; Popp, F.; Hofmann, J.; Leonhardt, H.; Rothbauer, U.; Schüler, D. An Intracellular Nanotrap Redirects Proteins and Organelles in Live Bacteria. *mBio* **2015**, *6*, e02117-14.

(21) Yoshino, T.; Matsunaga, T. Efficient and Stable Display of Functional Proteins on Bacterial Magnetic Particles Using Mms13 as a Novel Anchor Molecule. *Appl. Environ. Microbiol.* **2006**, *72*, 465−471.

(22) Ohuchi, S.; Schüler, D. In Vivo Display of a Multisubunit Enzyme Complex on Biogenic Magnetic Nanoparticles. *Appl. Environ. Microbiol.* **2009**, *75*, 7734−7738.

(23) Ginet, N.; Pardoux, R.; Adryanczyk, G.; Garcia, D.; Brutesco, C.; Pignol, D. Single-Step Production of a Recyclable Nanobiocatalyst for Organophosphate Pesticides Biodegradation Using Functionalized Bacterial Magnetosomes. *PLoS One* **2011**, *6*, e21442.

(24) Kolinko, I.; Jogler, C.; Katzmann, E.; Schüler, D. Frequent Mutations within the Genomic Magnetosome Island of Magnetospirillum gryphiswaldense are Mediated by RecA. *J. Bacteriol.* **2011**, *193*, 5328−5334.

(25) Mickoleit, F.; Schüler, D. Generation of Multifunctional Magnetic Nanoparticles with Amplified Catalytic Activities by Genetic Expression of Enzyme Arrays on Bacterial Magnetosomes. *Adv. Biosyst.* **2018**, *2*, 1700109.

(26) Sabourin, M.; Tuzon, C.; Fisher, T.; Zakian, V. A Flexible Protein Linker Improves the Function of Epitope-Tagged Proteins in Saccharomyces cerevisiae. *Yeast* **2007**, *24*, 39−45.

(27) Borg, S.; Rothenstein, D.; Bill, J.; Schüler, D. Generation of Multishell Magnetic Hybrid Nanoparticles by Encapsulation of Genetically Engineered and Fluorescent Bacterial Magnetosomes with ZnO and SiO2. *Small* **2015**, *11*, 4209−4217.

(28) Vollrath, F. Strength and Structure of Spiders' Silks. *Rev. Mol. Biotechnol.* **2000**, *74*, 67−83.

(29) Bini, E.; Knight, D. P.; Kaplan, D. L. Mapping Domain Structures in Silks from Insects and Spiders Related to Protein Assembly. *J. Mol. Biol.* **2004**, *335*, 27−40.

(30) Leal-Egaña, A.; Scheibel, T. Silk-Based Materials for Biomedical Applications. *Biotechnol. Appl. Biochem.* **2010**, *55*, 155−167.

(31) Fahnestock, S. *Novel, recombinantly produced spider silk analogs*, Int. Patent Number WO 94/29450, 1994.

(32) Heidebrecht, A.; Scheibel, T. Recombinant Production of Spider Silk Proteins. *Adv. Appl. Microbiol.* **2013**, *82*, 115−153.

(33) Widmaier, D. M.; Tullman-Ercek, D.; Mirsky, E. A.; Hill, R.; Govindarajan, S.; Minshull, J.; Voigt, C. A. Engineering the Salmonella Type III Secretion System to Export Spider Silk Monomers. *Mol. Syst. Biol.* **2009**, DOI: 10.1038/msb.2009.62.

(34) Huemmerich, D.; Helsen, C. W.; Quedzuweit, S.; Oschmann, J.; Rudolph, R.; Scheibel, T. Primary Structure Elements of Spider Dragline Silks and their Contribution to Protein Solubility. *Biochemistry* **2004**, *43*, 13604−13612.

(35) Rammensee, S.; Slotta, U.; Scheibel, T.; Bausch, A. R. Assembly Mechanism of Recombinant Spider Silk Proteins. *Proc. Natl. Acad. Sci. U. S. A.* **2008**, *105*, 6590−6595.

(36) Humenik, M.; Magdeburg, M.; Scheibel, T. Influence of Repeat Numbers on Self-Assembly Rates of Repetitive Recombinant Spider Silk Proteins. *J. Struct. Biol.* **2014**, *186*, 431−437.

(37) Exler, J. H.; Hummerich, D.; Scheibel, T. The Amphiphilic Properties of Spider Silks are Important for Spinning. *Angew. Chem., Int. Ed.* **2007**, *46*, 3559−3562.

(38) Hagn, F.; Thamm, C.; Scheibel, T.; Kessler, H. pH-Dependent Dimerization and Salt-Dependent Stabilization of the N-Terminal Domain of Spider Dragline Silk-Implications for Fiber Formation. *Angew. Chem., Int. Ed.* **2011**, *50*, 310−313.

(39) Heyen, U.; Schüler, D. Growth and Magnetosome Formation by Microaerophilic Magnetospirillum Strains in an Oxygen-Controlled Fermentor. *Appl. Microbiol. Biotechnol.* **2003**, *61*, 536−544.

(40) Sambrook, J.; Russell, D. *Molecular Cloning: A Laboratory Manual*, 3rd ed; Cold Spring Harbor Laboratory Press: New York, 2001; pp 1−44.

(41) Schüler, D.; Rainer, U.; Bäuerlein, E. A Simple Light Scattering Method to Assay Magnetism in Magnetospirillum gryphiswaldense. *FEMS Microbiol. Lett.* **1995**, *132*, 139−145.

(42) Phenrat, T.; Saleh, N.; Sirk, K.; Tilton, R. D.; Lowry, G. Aggregation and Sedimentation of Aqueous Nanoscale Zerovalent Iron Dispersions. *Environ. Sci. Technol.* **2007**, *41*, 284−290.

(43) Tiraferri, A.; Chen, K. L.; Sethi, R.; Elimelech, M. Reduced Aggregation and Sedimentation of Zero-Valent Iron Nanoparticles in the Presence of Guar Gum. *J. Colloid Interface Sci.* **2008**, *324*, 71−79.

(44) Laemmli, U. K. Cleavage of Structural Proteins During the Assembly of the Head of Bacteriophage T4. *Nature* **1970**, *227*, 680−685.

(45) Fling, S. P.; Gregerson, D. S. Peptide and Protein Molecular Weight Determination by Electrophoresis Using a High-Molarity Tris Buffer System Without Urea. *Anal. Biochem.* **1986**, *155*, 83−88.

(46) Mastronarde, D. N. Automated Electron Microscope Tomography Using Robust Prediction of Specimen Movements. *J. Struct. Biol.* **2005**, *152*, 36−51.

(47) Kremer, J. R.; Mastronarde, D. N.; McIntosh, J. R. Computer Visualization of Three-Dimensional Image Data Using IMOD. *J. Struct. Biol.* **1996**, *116*, 71−76.

(48) Martinez-Sanchez, A.; Garcia, I.; Asano, S.; Lucic, V.; Fernandez, J. J. Robust Membrane Detection Based on Tensor Voting for Electron Tomography. *J. Struct. Biol.* **2014**, *186*, 49−61.

(49) Sauerbrey, G. Use of a Quartz Vibrator from Weighing Thin Films on a Microbalance. *Eur. Phys. J. A* **1959**, *155*, 206−222.

(50) Liu, G.; Zhang, G. Chapter 1: Basic Principles of QCM-D. In *QCM-D Studies on Polymer Behavior at Interfaces*; Sharma, S. K., Ed.; Springer Briefs in Molecular Science; Springer: Heidelberg/New York/Dordrecht/London, 2013; pp 1−8.

(51) Xia, X. X.; Qian, Z. G.; Ki, C. S.; Park, Y. H.; Kaplan, D. L.; Lee, S. Y. Native-Sized Recombinant Spider Silk Protein Produced in Metabolically Engineered Escherichia coli Results in a Strong Fiber. *Proc. Natl. Acad. Sci. U. S. A.* **2010**, *107*, 14059−14063.

(52) Zbilut, J. P.; Scheibel, T.; Huemmerich, D.; Webber, C. L., Jr.; Colafranceschi, M.; Giuliani, A. Statistical Approaches for Investigating Silk Properties. *Appl. Phys. A: Mater. Sci. Process.* **2006**, *82*, 243−251.

(53) Lohße, A.; Kolinko, I.; Raschdorf, O.; Uebe, R.; Borg, S.; Brachmann, A.; Plitzko, J. M.; Müller, R.; Zhang, Y.; Schüler, D. Overproduction of Magnetosomes by Genomic Amplification of

Biosynthesis-Related Gene Clusters in a Magnetotactic Bacterium. *Appl. Environ. Microbiol.* **2016**, *82*, 3032−3041.

(54) Zbilut, J. P.; Scheibel, T.; Huemmerich, D.; Webber, C. L., Jr.; Colafranceschi, M.; Giuliani, A. Spatial Stochastic Resonance in Protein Hydrophobicity. *Phys. Lett. A* **2005**, *346*, 33−41.

(55) Toro-Nahuelpan, M.; Müller, F. D.; Klumpp, S.; Plitzko, J. M.; Bramkamp, M.; Schüler, D. Segregation of Prokaryotic Magnetosomes Organelles is Driven by Treadmilling of a Dynamic Actin-Like MamK Filament. *BMC Biol.* **2016**, *14*, 88.

(56) Raschdorf, O.; Bonn, F.; Zeytuni, N.; Zarivach, R.; Becher, D.; Schüler, D. A Quantitative Assessment of the Membrane-Integral Sub-Proteome of a Bacterial Magnetic Organelle. *J. Proteomics* **2018**, *172*, 89−99.

(57) Slotta, U.; Tammer, M.; Kremer, F.; Koelsch, P.; Scheibel, T. Structural Analysis of Spider Silk Films. *Supramol. Chem.* **2006**, *18*, 465−471.

(58) Ormö, M.; Cubitt, A. B.; Kallio, K.; Gross, L. A.; Tsien, R. Y.; Remington, S. J. Crystal Structure of the Aequorea victoria Green Fluorescent Protein. *Science* **1996**, *273*, 1392−1395.

(59) Yang, F.; Moss, L. G.; Phillips, G. N., Jr The Molecular Structure of Green Fluorescent Protein. *Nat. Biotechnol.* **1996**, *14*, 1246−1251.

(60) Gasteiger, E.; Hoogland, C.; Gattiker, A.; Duvaud, S.; Wilkins, M. R.; Appel, R. D.; Bairoch, A. Protein Identification and Analysis Tools on the ExPASy Server. In *The Proteomics Protocols Handbook*; Walker, J. M., Ed.; Humana Press: New York, 2005; pp 571−607.

(61) Jarrett, J. T.; Lansbury, P. T., Jr Seeding ″One-Dimensional Crystallization″ of Amyloid: a Pathogenic Mechanism in Alzheimer's Disease and Scrapie? *Cell* **1993**, *73*, 1055−1058.

(62) Humenik, M.; Smith, A. M.; Arndt, S.; Scheibel, T. Ion and Seed Dependent Fibril Assembly of a Spidroin Core Domain. *J. Struct. Biol.* **2015**, *191*, 130−138.

(63) Spiess, K.; Lammel, A.; Scheibel, T. Recombinant Spider Silk Proteins for Applications in Biomaterials. *Macromol. Biosci.* **2010**, *10*, 998−1007.

(64) Mayes, E. L.; Vollrath, F.; Mann, S. Fabrication of Magnetic Spider Silk and Other Silk-Fiber Composites Using Inorganic Nanoparticles. *Adv. Mater.* **1998**, *10*, 801−805.

DOI: 10.1021/acs.biomac.7b01749
Biomacromolecules 2018, 19, 962−972

Supporting Information

In vivo coating of bacterial magnetic nanoparticles by magnetosome expression of spider silk-inspired peptides

Frank Mickoleit[1], Christian B. Borkner[2], Mauricio Toro-Nahuelpan[1,3], Heike M. Herold[2], Denis S. Maier[1], Jürgen M. Plitzko[3], Thomas Scheibel[2,4,5,6,7,8] & Dirk Schüler[1]*

[1]Dept. Microbiology / [2]Dept. Biomaterials / [4]Bayerisches Polymerinstitut (BPI) /
[5]Bayreuther Zentrum für Kolloide und Grenzflächen (BZKG) /
[6]Institut für Bio-Makromoleküle (bio-mac) / [7]Bayreuther Zentrum für Molekulare Biowissenschaften (BZMB) / [8]Bayreuther Materialzentrum (BayMAT),
University of Bayreuth, D-95447 Bayreuth, Germany;
[3]Dept. Molecular Structural Biology, Max Planck Institute of Biochemistry,
D-82152 Martinsried, Germany

*Corresponding Author: Prof. D. Schüler

Department Microbiology, University of Bayreuth

Universitätsstraße 30, D-95447 Bayreuth, Germany

Tel.: +49-921-552728

Fax: +49-921-552727

E-mail: Dirk.Schueler@uni-bayreuth.de

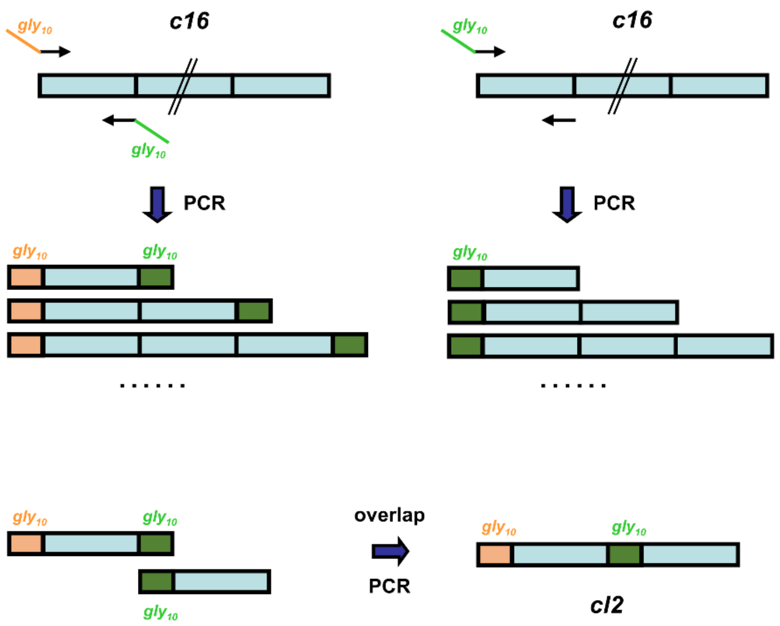

Figure S1. Scheme illustrating the construction of the *cl2* spider silk gene fusion. *c1* units were generated by PCR and fused via overlap splicing, with a *gly*$_{10}$ linker (composed of ten glycine residues) connecting both units.

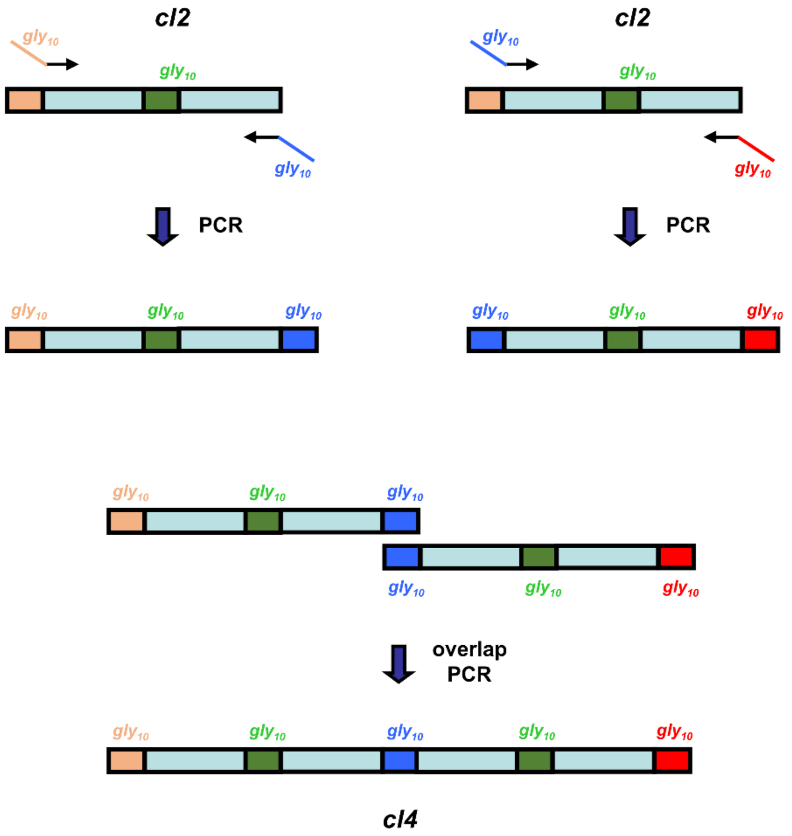

Figure S2. Scheme illustrating the generation of the *cl4* spider silk gene. *cl2* units were amplified by PCR and fused via overlap splicing, with a *gly*$_{10}$ linker (composed of ten glycine residues) connecting both units.

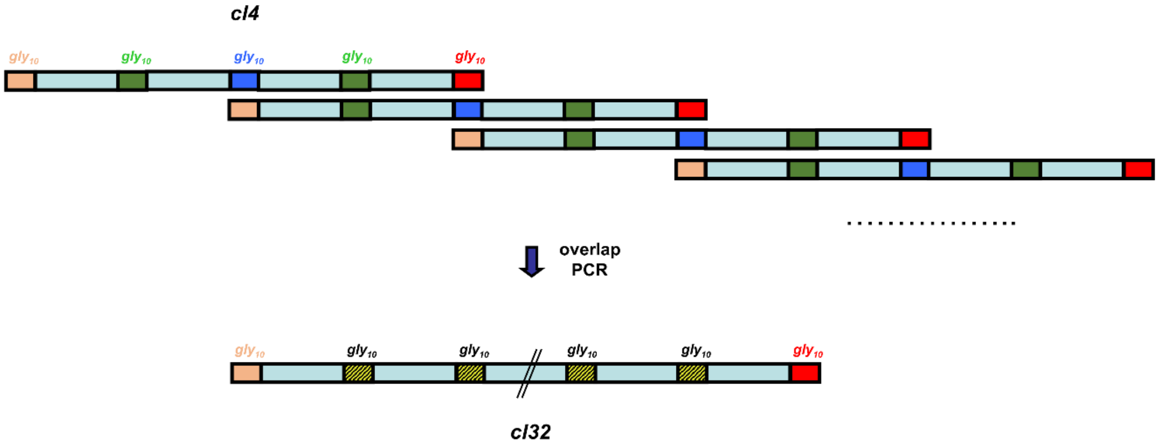

Figure S3. Construction of the *cl32* spider silk gene fusion. *cl4* units were fused via overlap splicing thereby generating fragments of different sizes, including the *cl32* gene fusion.

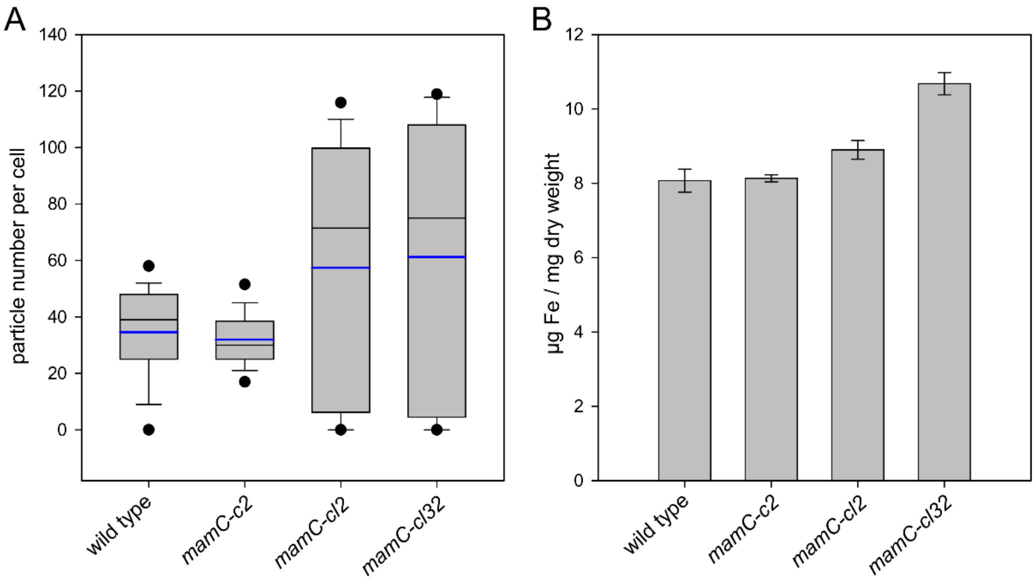

Figure S4. (A) Box plot illustrating magnetosome numbers per cell (n = 285) for the indicated *M. gryphiswaldense* strains. The boundary of each box closest to zero indicates the 25th percentile, a black line within the boxes mark the median, and the boundary of the boxes farthest from zero indicates the 75th percentile (50% central data). Whiskers above and below the boxes indicate the 90th and 10th percentiles. Outlying points represent the 95th and 5th percentiles, blue lines indicate the mean value. Whereas *mamC-c2* synthesized wild type-like amounts of magnetosomes (*mamC-c2*: 32 ± 11; wild type: 35 ± 16) arranged in one or two chains positioned ad midcell, total particle numbers were increased for *mamC-cl2* and *mamC-cl32* by 66% and 71%, respectively, with up to 60 magnetosomes per cell on average. (B) Iron contents (given as µg Fe per mg cell dry weight) of strains *mamC-c2*, *mamC-cl2*, *mamC-cl32*, and the wild type of *M. gryphiswaldense*. For cells of the wild type and strain *mamC-c2*, similar iron contents were obtained, whereas for *mamC-cl2* and *mamC-cl32* cells the number of synthesized particles and the iron contents were significantly increased (10% for *mamC-cl2* and 32% for *mamC-cl32*), which is in accordance with the particle (mis)distribution visible by transmission electron microscopy.

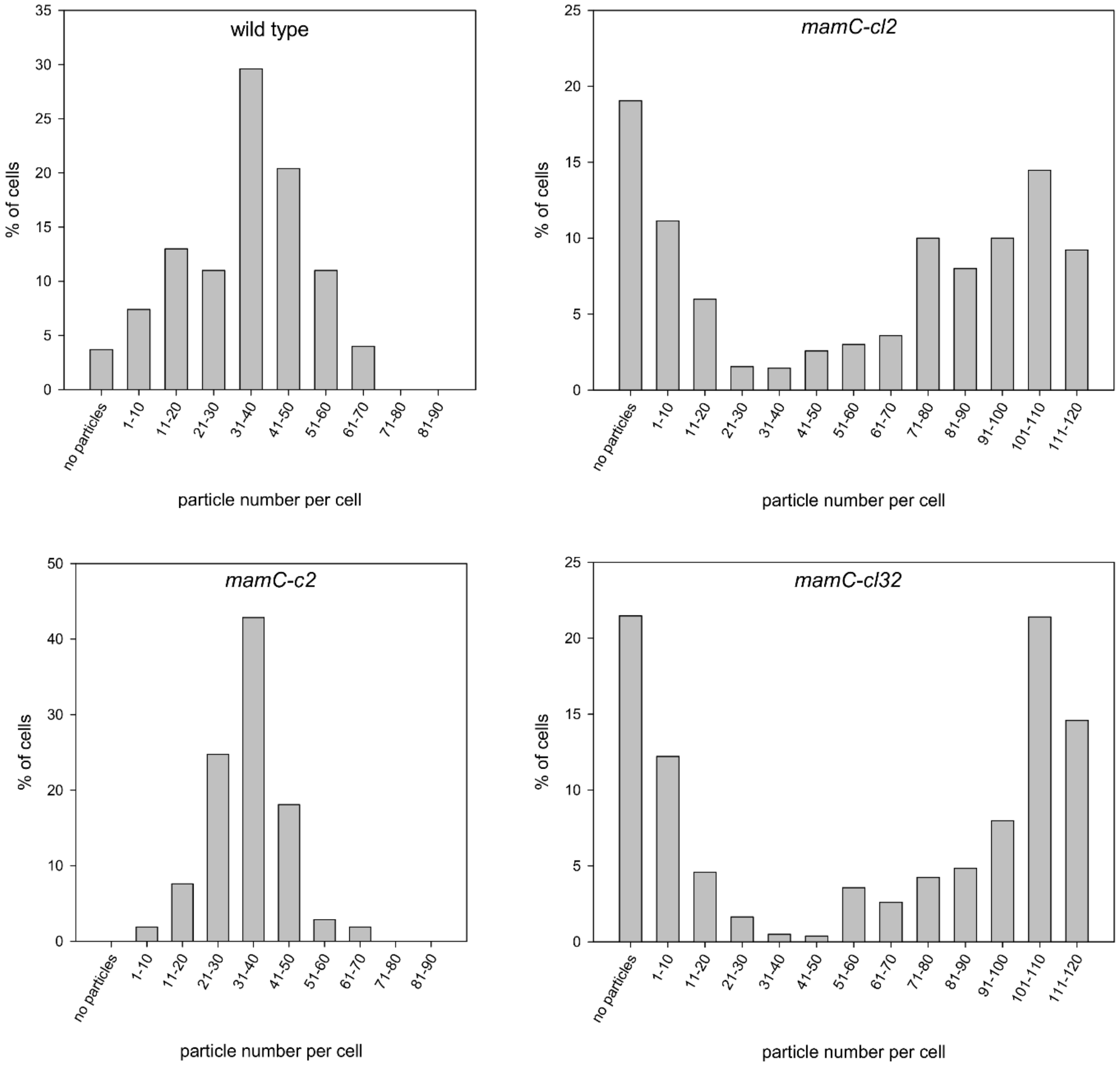

Figure S5. Magnetosome distribution of the spider silk motif expressing strains *mamC-c2*, *mamC-cl2* and *mamC-cl32*, and the wild type. The particle numbers per cell are given as percentage of the total amount of cells that were analyzed (n = 285). The bar charts visualize the particle misdistribution in strains *mamC-cl2* and *mamC-cl32*, with about 40% of the cells containing less than 20 particles, and about 50% containing more than 70 magnetosomes per cell. In contrast, cells of strain *mamC-c2* exhibit a wild type-like particle distribution.

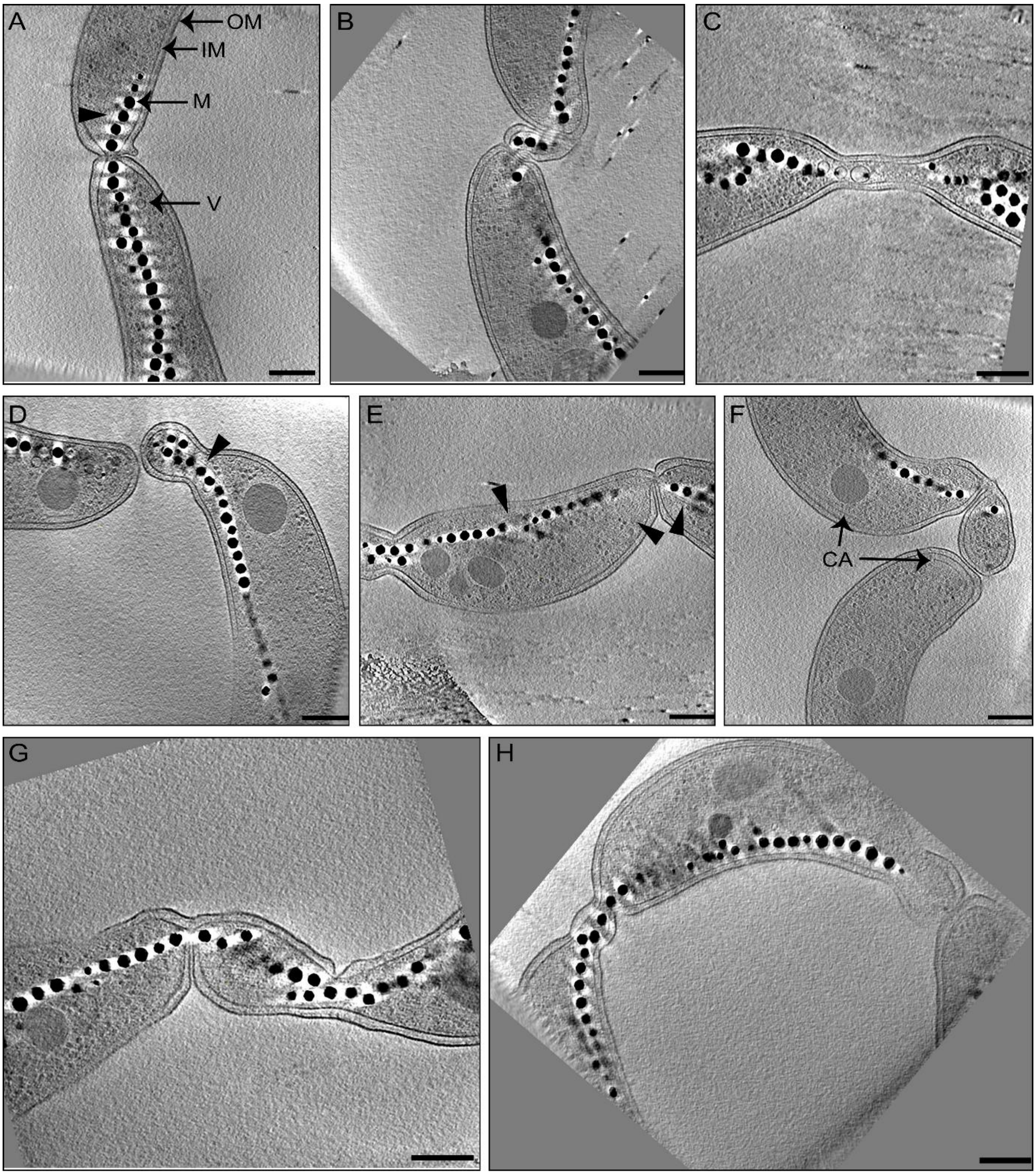

Figure S6. Cryo-electron tomography of *mamC-cl32* cells. (A-H) 12.8 nm thick slices (average of 5 slices) through the tomograms of cells undergoing cell division (n = 11). Cells display impairment in cytokinesis generating bridges of minicells due to improper cell division. (E) and (H) show slices from tomograms of bridging minicells. CA: chemoreceptor array, M: magnetite crystal, OM: outer membrane, IM: inner membrane, V: vesicle. Arrowheads indicate the presence of MamK filaments. Scale bars: 200 nm.

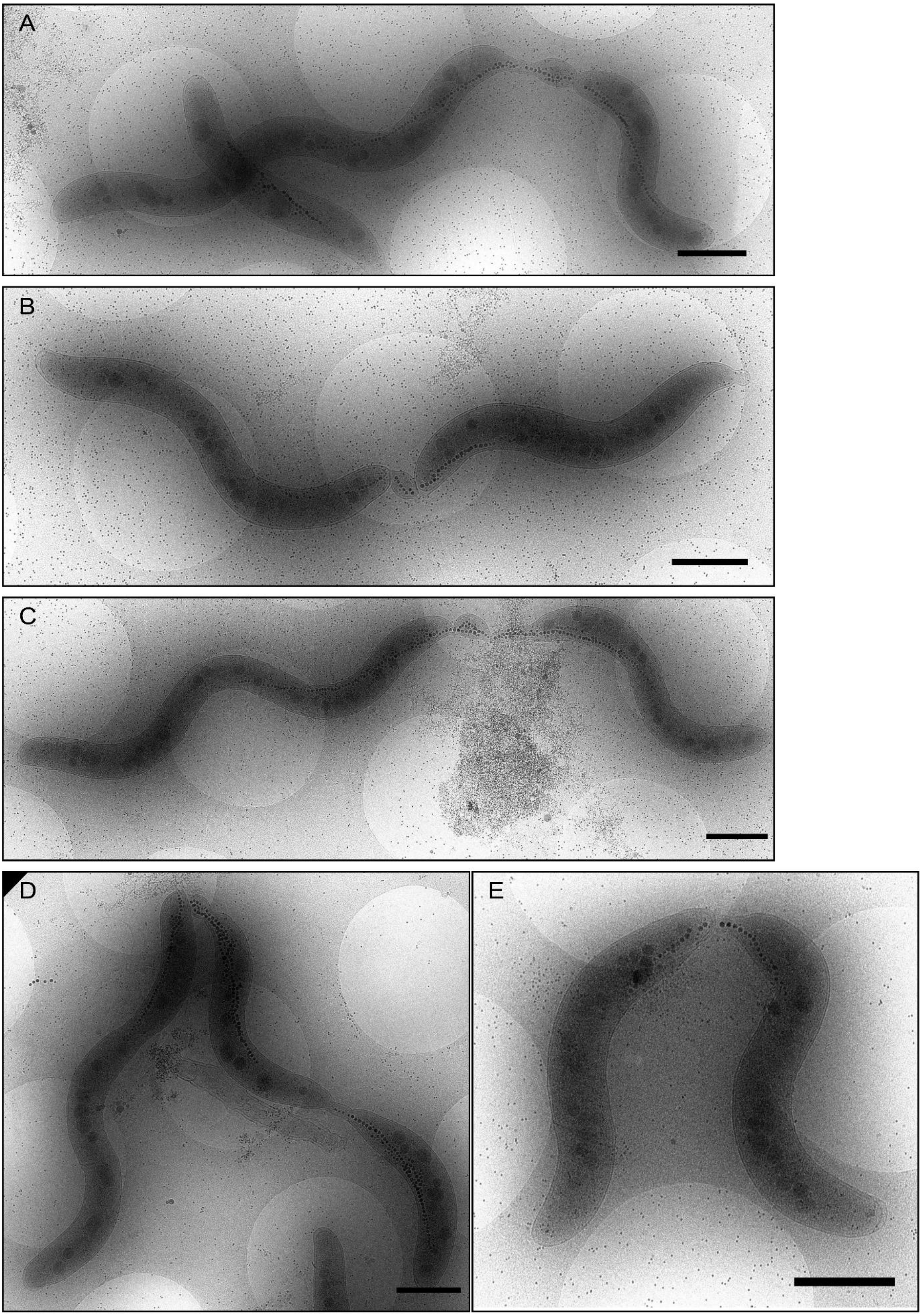

Figure S7. Overview of *mamC-cl32* strain by cryo-electron microscopy. (A-E) Cryo-electron micrographs depicting a conspicuous cell division defect present in the *mamC-cl32* strain. Scale bars: 1 µm.

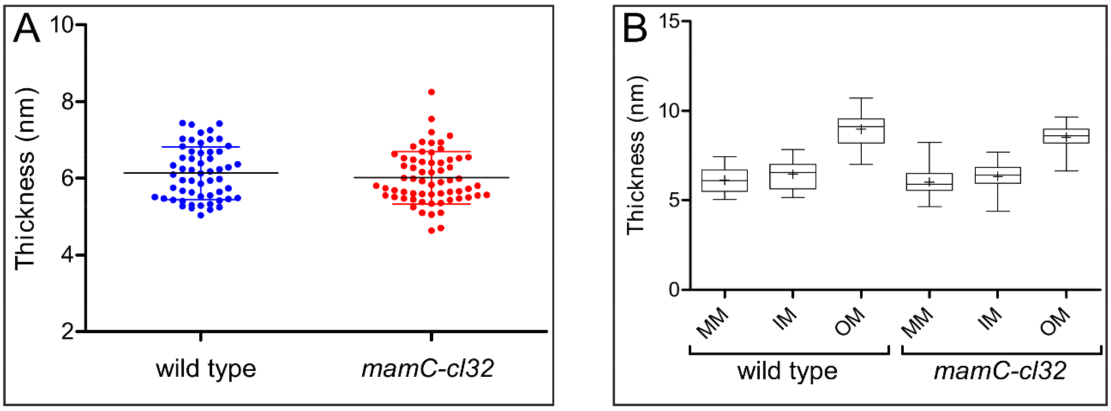

Figure S8. Magnetosome membrane thickness determined by cryo-electron tomography. Non-magnetic cells of the wild type (n = 9) and *mamC-cl32* (n = 11) were cultivated in low-iron medium to evaluate magnetosome vesicle (magnetosome membrane) thickness.
(A) Dot plot of magnetosome membrane thickness of the wild type and *mamC-cl32* strains. The line represents the average and the bars the standard deviation. (B) The thickness of the magnetosome membrane as well as the inner (cytoplasmic) and outer membranes were quantified in the wild type and *mamC-cl32* strains. The boxes encompass from the 25th to 75th percentiles (50% central data). The line inside the box represents the median and the cross the average. The whiskers display the minimum and maximum values.
MM: magnetosome membrane (vesicle), IM: inner membrane, OM: outer membrane.

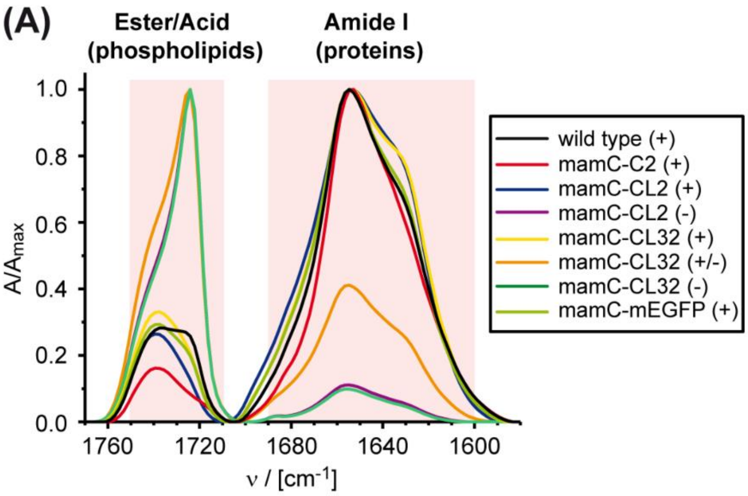

(B)

entry	sample	$A_{norm.}$(amide I) / $A_{norm.}$(phoshoplipids)
1	mamC-wt (+)	3.54
2	mamC-C2 (+)	6.19
3	mamC-CL2 (+)	3.77
4	mamC-CL2 (-)	0.11
5	mamC-CL32 (+)	3.02
6	mamC-CL32 (+/-)	0.41
7	mamC-CL32 (-)	0.10
8	mamC-mEGFP (+)	3.41

Figure S9. Representative normalized FTIR absorption spectra of magnetosome samples showing bands in the C=O stretch vibration regime. (A) C=O stretch vibration adsorption bands of phospholipid portion (esters, acids; ~1750-1710 cm^{-1}) and protein portion (amide I; ~1690-1600 cm^{-1}) of MamC-CL2 and MamC-CL32 magnetosomes for quality control measurements. (B) Protein-to-phospholipid ratios of different fermentation batches and constructs calculated from phospholipid and amide I band maxima ($A_{norm.}$(amide I)/$A_{norm.}$(phospholipids)) can be used for qualitative and empirical batch characterization. (+) high protein-to-phospholipid ratio (> 3); (+/-) intermediate protein-to-phospholipid ratio (0.2 - 3); (-) low protein-to-phospholipid ratio (< 0.2).

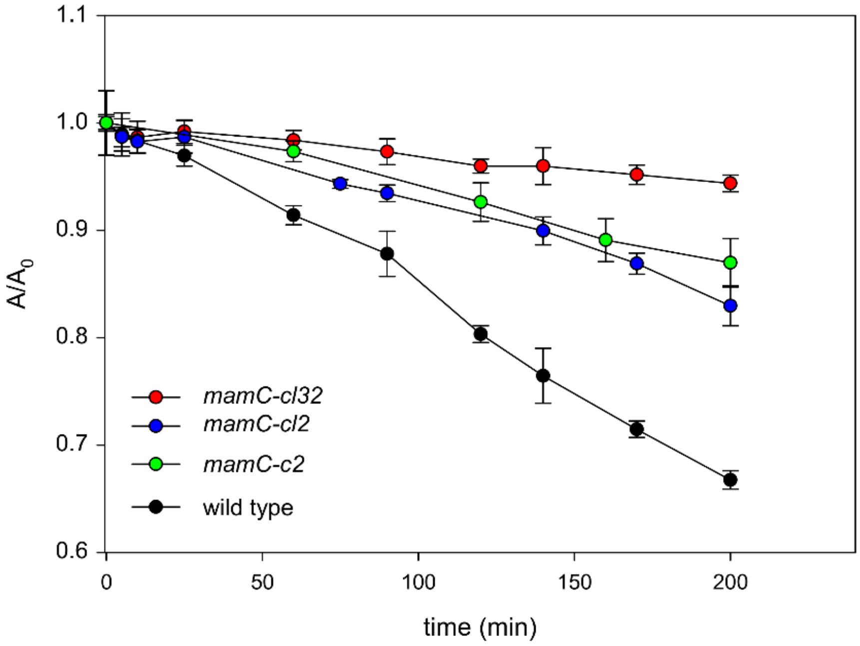

Figure S10. Normalized absorption values reflecting the sedimentation behavior of spider silk coated magnetosomes. Isolated particles of spider silk motif expressing strains *mamC-c2*, *mamC-cl2* and *mamC-cl32* and from the wild type were subjected to sedimentation assays. Sedimentation profiles are given as function of time and were normalized with the absorption at the initial time of the experiment. Standard deviations are based on at least three independent measurements.

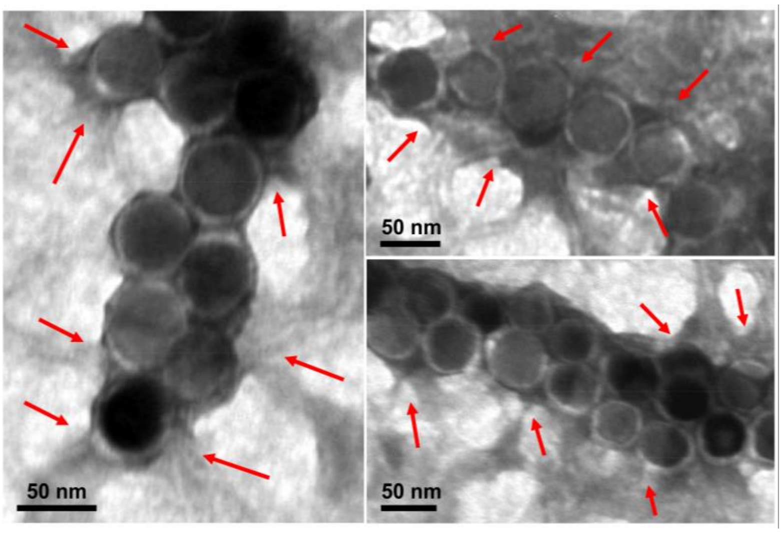

Figure S11. Assembly of nanofibrils in the presence of MamC-C2 magnetosomes. Isolated particles were incubated with 20 µM freshly dialyzed eADF4(C16) monomers in potassium phosphate buffer. In TEM micrographs, fibril-like structure were visible at the particle surface (indicated by arrows), suggesting directed fibril growth by C2 triggered docking of further eADF4(16) monomers.

Table S1. Strains used in this study

Strain	Description	Source or reference
Escherichia coli		
DH5α	F^- *sup*E44 Δ*lac*U169 (Φ80 *lac*ZDM15) *hsd*R17 *rec*A1 *end*A1 *gyr*A96 *thi*-1 *rel*A1	Invitrogen
WM3064	*thrB1004 pro thi rpsL hsdS lacZΔM15 RP4-1360 Δ(araBAD)567 ΔdapA1341::[erm pir]*	Metcalf, unpublished
Magnetospirillum gryphiswaldense		
M. gryphiswaldense MSR-1 R3/S1	Rif^R, Sm^R spontaneous mutant, lab strain	Schultheiss and Schüler 2003
M. gryphiswaldense mamC-megfp	R3/S1 Km^R, transposon mutant with inserted *mamC-megfp* from $P_{mamDC45}$	Borg et al. 2014
M. gryphiswaldense MSR-1 IK-1	R3/S1 Δ*recA*	Kolinko et al. 2011
M. gryphiswaldense mamC-c2	R3/S1 Δ*recA*, Km^R, transposon mutant with inserted *mamC-c2* from $P_{mamDC45}$	this study
M. gryphiswaldense mamC-cl2	R3/S1 Δ*recA*, Km^R, transposon mutant with inserted *mamC-cl2* from $P_{mamDC45}$	this study
M. gryphiswaldense mamC-cl32	R3/S1 Δ*recA*, Km^R, transposon mutant with inserted *mamC-cl32* from $P_{mamDC45}$	this study

Table S2. Plasmids used in this study

Plasmid name	Description	Source or reference
pCS-eADF4(C2)	Amp^R, f1_origin, pBR322_origin, *c2* sequence	Huemmerich et al. 2004
pCS-eADF4(C16)	Amp^R, f1_origin, pBR322_origin, *c16* sequence	Huemmerich et al. 2004
pBAM1	Km^R, Amp^R, oriR6K, *tnpA*	Martinez-Garcia et al. 2011
pSB9	pBAM1 with $P_{mamDC45}$, *mamC-gusA*, Km^R, Amp^R	Borg, unpublished
pFM-C2	pBAM1 with $P_{mamDC45}$, *mamC-c2,* Km^R, Amp^R	this study
pFM1	pBAM1 with $P_{mamDC45}$, *mamC-cl2*, Km^R, Amp^R	this study
pFM2	pBAM1 with $P_{mamDC45}$, *mamC-cl32*, Km^R, Amp^R	this study

Table S3. Primers and oligonucleotides used in this study. Restriction sites indicated in bold.

Primer name	Sequence (5’ - 3’)	Restriction site
linker1-sps fwd	GAATTGGC **CCATGG** AGGCGGAGGCGGTGGCGGAGGTGGCGGA **ATCGAT** GGTTCTAGCGCGGCTGCAGCCGCGGC	NcoI / ClaI
sps-linker2 rev	GCCGCGCTAGAACCGCCACCGCCACCTCCGCCGCCACCTCCACCGCCCGGACCGCCAGGACCGTAGCC	
linker2-sps fwd	CCGGGCGGTGGAGGTGGCGGCGGAGGTGGCGGTGGCGGTTCTAGCGCGGCTGCAGCCGCGGCAGCTGCGTCCGGCC	
sps-linker3 rev	GCCGCGCTAGAACCACCTCCTCCGCCACCTCCTCCGCCACCGCCGCCCGGACCGCCAGGACCGTAGCC	
linker3-sps fwd	CCGGGCGGCGGTGGCGGAGGAGGTGGCGGAGGAGGTGGTTCTAGCGCGGCTGCAGCCGCGGCAGCTGCGTCCGGCC	
sps-linker4 rev	GCCGCGCTAGAACCACCTCCTCCGCCACCTCCTCCGCCACCGCCGCCCGGACCGCCAGGACCGTAGCC	
sps rev	**GGGACCC GGATCC** TTAGCCCGGACCGCCAGGACCGTAGCC	SanDI / BamHI

Table S4. Particle size and layer thickness of magnetosomes isolated from *mamC-c2, mamC-cl2* and *mamC-cl32* mutant strains. Wild type and MamC-mEGFP magnetosomes (Borg et al. 2014) were used as controls. Particle diameters were determined by TEM (n = 150) and zetasizer measurements. For the latter, the theory of Smoluchowski was used to calculate overall diameters (Spiess et al. 2010). Particle sizes were analyzed in 10 mM Hepes/ 1 mM EDTA at pH 7.2. A one-way ANOVA test and a post-hoc Tukey test (using the wild type as control) confirmed that the overall difference between overall diameter means is statistically significant ($P < 0.05$).

Strain	Overall diameter (nm)		Diameter magnetite core	Thickness of capsule
	TEM	Zetasizer	(TEM) (nm)	(TEM) (nm)
wild type	38.1 ± 7.3	40.7 ± 4.1	34.9 ± 5.7	5.2 ± 1.4
mamC-megfp	39.7 ± 8.1	41.2 ± 7.2	38.4 ± 6.2	4.3 ± 2.1
mamC-c2	52.6 ± 6.4	59.8 ± 6.9	40.1 ± 7.3	11.2 ± 3.8
mamC-cl2	56.8 ± 9.6	61.9 ± 5.7	45.9 ± 7.1	10.9 ± 2.5
mamC-cl32	50.6 ± 9.4	63.5 ± 5.8	39.4 ± 4.3	11.2 ± 4.3

References Supporting Information

(1) Schultheiss, D.; Schüler, D. Development of a Genetic System for Magnetospirillum gryphiswaldense. *Arch. Microbiol.* **2003**, *179*, 89-94.

(2) Borg, S.; Hofmann, J.; Pollithy, A.; Lang, C.; Schüler, D. New Vectors for Chromosomal Integration Enable High-Level Constitutive or Inducible Magnetosome Expression of Fusion Proteins in Magnetospirillum gryphiswaldense. *Appl. Environ. Microbiol.* **2014**, *80*, 2609-2616.

(3) Kolinko, I.; Jogler, C.; Katzmann, E.; Schüler, D. Frequent Mutations within the Genomic Magnetosome Island of Magnetospirillum gryphiswaldense are Mediated by RecA. *J. Bacteriol.* **2011**, *193*, 5328-5334.

(4) Huemmerich, D.; Helsen, C. W.; Quedzuweit, S.; Oschmann, J.; Rudolph, R.; Scheibel, T. Primary Structure Elements of Spider Dragline Silks and their Contribution to Protein Solubility. *Biochemistry* **2004**, *43*, 13604-13612.

(5) Martinez-Garcia, E.; Calles, B.; Arevalo-Rodriguez, M.; de Lorenzo, V. pBAM1: an All-Synthetic Genetic Tool for Analysis and Construction of Complex Bacterial Phenotypes. *Bmc Microbiol.* **2011**, DOI: 10.1186/1471-2180-11-38

(6) Spiess, K.; Lammel, A.; Scheibel, T. Recombinant Spider Silk Proteins for Applications in Biomaterials. *Biosci.* **2010**, *10*, 998-1007.

7. Danksagung

Ich möchte mich an dieser Stelle bei all denjenigen bedanken, die zum Gelingen dieser Arbeit beigetragen haben.

Einen besonderen Dank widme ich meinem Doktorvater und Mentor Prof. Dr. Thomas Scheibel für die sehr interessante Themenstellung, die hervorragende Betreuung meiner Arbeit und für das mir entgegengebrachte Vertrauen. Ich habe viele Freiheiten bei der Bearbeitung der Arbeit genossen und konnte jederzeit auf seinen Rat und seine Unterstützung zählen. Insbesondere möchte ich mich für das Vertrauen durch die Übertragung der IT-Administration des Lehrstuhls und der damit verbundenen Verantwortung bedanken.

Weiterhin danke ich Prof. Dr. Andreas Greiner und Prof. Dr. Andreas Fery für die Übernahme meines Mentorats.

Ebenso möchte ich mich bei Dr. Frank Mickoleit und Prof. Dr. Dirk Schüler für die erfolgreiche und produktive Kooperation im Projekt „*In Vivo Coating of Bacterial Magnetic Nanoparticles by Magnetosome Expression of Spider Silk-Inspired Peptides*“ und vor allem für die Möglichkeit bedanken an diesem Projekt mitzuwirken.

Folgenden Personen möchte ich besonders für die Unterstützung danken:

- Dr. Hendrik Bargel und Dr. Martina Schierling für REM-Aufnahmen sowie Martina Heider und Dr. Beate Förster für die Hilfe bei der Durchführung von REM-Messungen.
- Dr. Martin Humenik, Dr. Stephanie Wohlrab und Markus Hund für die Unterstützung am AFM.
- Dr. Stefanie Wohlrab, Eva Möller und Alexandra Pellert für die Durchführung von Zellkulturexperimenten und die Hilfe bei der Mikroskopie.
- Petra Zippelius für die Unterstützung während meiner Messungen am Tensiometer und Ellipsometer.
- Eileen Lintz und Dr. Stefanie Wohlrab für die gute Einführung und Hilfe am FTIR und bei der FSD.

- Eileen Lintz, Elise DeSimone und Dr. Martin Humenik für das Korrekturlesen meiner Manuskripte.
- Meinen Praktikanten Sören Blum, Ramona Fraas, Saskia Frank, Anika Winkler, Merisa Saric, Bernd Steiger, Vivien Beyersdorfer und Sarah Lentz für die tolle Mitarbeit.
- Andreas Schmidt, Johannes Diehl, André Wetzel, Daniela Suhre, Jasmin Wickinghoff, Eva Möller, Claudia Stemmann und Alexandra Pellert für die Unterstützung im Laboralltag.
- Meiner Arbeitsgruppe „Proteinmodifikation" für viele hilfreiche Diskussionen und die schöne kameradschaftliche Atmosphäre.
- Meinen Bürokollegen Prof. Dr. Gregor Lang, Stephan Jokisch, Dr. Kristin Schacht, Dr. Stefanie Wohlrab, Dr. Martina Schierling, Dr. Christopher Thamm, Dr. Joschka Bauer, Jia Wang, Fabian Müller, Vanessa Neubauer und Annika Döbl für den wertvollen Austausch und dafür, dass mein kleiner Kamerad Loisl sich wie zu Hause fühlen durfte.
- Susanne Schramm, Andrea Bodner, Sabrina Schwägerl, Christa Vogl und Katja Weiner für die Hilfe bei organisatorischen Angelegenheiten.
- Allen aktuellen und ehemaligen Kollegen des gesamten Lehrstuhls Biomaterialien die freundliche und kollegiale Atmosphäre.

Ein besonderer Dank gilt Dr. Martin Humenik für die zahlreichen wissenschaftlichen Diskussionen, die einen wertvollen Beitrag zu dieser Arbeit geleistet haben und die gute Eigenschaft einen verirrten Doktoranden immer wieder auf den rechten Weg zu bringen. Ich danke Dr. Martin Humenik, Tamara Aigner, Sarah Fischer und Heike Herold für das Lektorat meiner Dissertation.

Bei meiner Familie bedanke ich mich für die endlose und bedingungslose Unterstützung. Meiner Partnerin und Verlobten Sarah danke ich für die großartige Unterstützung und das Verständnis, dass sie mir in der ganzen Zeit entgegenbrachte. Du bist stetiger Quell neuer Kraft für mich. Meinen Eltern Wolfgang und Annemarie danke ich für ihre bedingungslose Unterstützung auf dem von mir eingeschlagenen Weg und ihren Glauben an mich. Erst durch sie bekam ich die Möglichkeit den Weg vom Chemiestudium bis hin zur Fertigstellung dieser Arbeit einzuschlagen. Ihr seid die besten Eltern, die ich mir vorstellen kann.

8. Eidesstattliche Versicherung und Erklärungen

(§9 Satz 2 Nr. 3 PromO BayNAT)

Hiermit versichere ich eidesstattlich, dass ich die Arbeit selbständig verfasst und keine anderen als die von mir angegebenen Quellen und Hilfsmittel benutzt habe (vgl. Art. 64 Abs. 1 Satz 6 BayHSchG).

(§9 Satz 2 Nr. 3 PromO BayNAT)

Hiermit erkläre ich, dass ich die Dissertation nicht bereits zur Erlangung eines akademischen Grades eingereicht habe und dass ich nicht bereits diese oder eine gleichartige Doktorprüfung endgültig nicht bestanden habe.

(§9 Satz 2 Nr. 4 PromO BayNAT)

Hiermit erkläre ich, dass ich Hilfe von gewerblichen Promotionsberatern bzw. -vermittlern oder ähnlichen Dienstleistern weder bisher in Anspruch genommen habe noch künftig in Anspruch nehmen werde.

(§9 Satz 2 Nr. 7. PromO BayNAT)

Hiermit erkläre ich mein Einverständnis, dass die elektronische Fassung meiner Dissertation unter Wahrung meiner Urheberrechte und des Datenschutzes einer gesonderten Überprüfung unterzogen werden kann.

(§9 Satz 2 Nr. 8 PromO)

Hiermit erkläre ich mein Einverständnis, dass bei Verdacht wissenschaftlichen Fehlverhaltens Ermittlungen durch universitätsinterne Organe der wissenschaftlichen Selbstkontrolle stattfinden können.

Bayreuth, 09.02.2020

Ort, Datum, Unterschrift